



<http://researchspace.auckland.ac.nz>

## ***ResearchSpace@Auckland***

### **Copyright Statement**

The digital copy of this thesis is protected by the Copyright Act 1994 (New Zealand).

This thesis may be consulted by you, provided you comply with the provisions of the Act and the following conditions of use:

- Any use you make of these documents or images must be for research or private study purposes only, and you may not make them available to any other person.
- Authors control the copyright of their thesis. You will recognise the author's right to be identified as the author of this thesis, and due acknowledgement will be made to the author where appropriate.
- You will obtain the author's permission before publishing any material from their thesis.

To request permissions please use the Feedback form on our webpage.

<http://researchspace.auckland.ac.nz/feedback>

### **General copyright and disclaimer**

In addition to the above conditions, authors give their consent for the digital copy of their work to be used subject to the conditions specified on the [Library Thesis Consent Form](#) and [Deposit Licence](#).

### **Note : Masters Theses**

The digital copy of a masters thesis is as submitted for examination and contains no corrections. The print copy, usually available in the University Library, may contain corrections made by hand, which have been requested by the supervisor.

# Cascade and Secondary Coolant Supermarket Refrigeration Systems: Modelling and New Frost Correlations

---

**Getu Haile-Michael**

A thesis submitted in partial fulfilment of the requirements for the degree of

**Doctor of Philosophy**

Department of Mechanical Engineering

The University of Auckland

New Zealand

June 2011

# Abstract

---

Nowadays traditional (direct expansion) supermarket refrigeration systems are mostly employed in supermarket establishments for refrigerating food products and beverages in the store. However, the installations of long piping system, fittings and joints in traditional systems are causing substantial refrigerant losses. The refrigerant losses in turn bring about cost and high environmental damage in terms of ozone layer depletion and global warming potential. Additionally, defrosting of air-coils is one of the most energy consuming processes in supermarket refrigeration systems due to susceptibility of the air-coils to moisture. Hence, the frost forming on air-coils as a result of moisture transfer should be removed to keep display cabinets under the required temperature.

Various studies, though limited in scope, have been conducted both numerically and experimentally by several researchers in order to provide efficient and environmentally friendly supermarket refrigeration technologies. Empirical and mathematical expressions have also been continuously developed to quantify frost characteristics on flat plates and round tubes thereby determining the appropriate defrost periods. Cascade and secondary coolant refrigeration systems are the potential candidates to replace traditional ones due to the fact that the former can work on natural refrigerants and the latter essentially eliminates long connecting lines and environmentally damaging refrigerants. Development of empirical correlations for frost characteristics on real heat exchangers could also provide accurate prediction of defrost periods thereby eliminating unnecessary waste of energy and deterioration of food products.

The current study, therefore, presents (a) mathematical expressions for carbon dioxide-ammonia (R744-R717) cascade refrigeration system; (b) mathematical expressions for frost property and air pressure drop; and (c) a numerical model for medium-temperature secondary coolant system incorporating the new frost property correlations. The thermodynamic analysis of the cascade refrigeration system is useful for the supermarket refrigeration industry to optimize the design and operating parameters of the system. The development of the frost property correlations from experiments on a lab-scale flat-finned-tube heat exchanger is also useful for the supermarket refrigeration industry for better prediction and control of defrost periods and duration for medium-temperature air-coils. The medium-temperature secondary coolant model adopted the most appropriate heat transfer, mass transfer and pressure drop correlations obtained from the open literature. The system components such as air-coil, plate heat exchangers, distribution lines, coolant pump and compressor were modeled independently. Each component model was validated and linked to form a complete overall medium-temperature secondary coolant refrigeration system model.

The experimental results showed that COP of the Monopropylene glycol/water based medium-temperature secondary coolant refrigeration system could be 1.33, whereas the simulated results on a typical supermarket showed that COP of the system could be as high as 1.75.

The fundamental difference between the existing secondary coolant models and the current one is that frost characteristics have been incorporated in the air-coil model. In addition to this, complete independent models have been developed for plate heat exchangers based on their respective applications. Hence, the main advantage of the current medium-temperature secondary coolant refrigeration system model is that defrost periods and time span required to defrost frosted air-coils can be accurately determined to achieve energy savings and prevent product deterioration in the display cabinets. The plate heat exchanger models can also enable one to reasonably determine pressure drops thereby leading to an appropriate coolant pump selection.

Finally, a step-by-step exercise of the application of the secondary coolant model, which has been included in this project, can be used to completely design, select, evaluate and install such systems or retrofit the existing traditional direct expansion refrigeration systems in supermarkets.

# Acknowledgements

---

Conducting a PhD project normally takes a lot of time and requires commitment. Additionally, the support of other people plays an important role for the successful completion of the project. I would like to take this opportunity to express my special thanks to those who have contributed to this thesis.

I would like to thank my supervisor, Professor Pradeep Bansal for his invaluable advice, guidance, enormous amount of review work and mentoring throughout this thesis. Your patience and kind help are highly appreciated.

Many thanks to our highly experienced lab technicians, namely Alan Eaton, Martin Ryder, Derek Hobbs, Stephen Elder, Barry Fullerton and Harold Tarun for their excellent technical support and cooperation, who helped me set up the instrumentation for collecting measurements from the experimental test rig. Your cooperation and advice were very important to me.

Once again, special thanks go to Martin Ryder for your excellent support and patience for building the experimental test rig. Had it not been for your help, it could have been really difficult for me to complete this thesis.

# Table of Contents

Abstract	ii
Acknowledgements	iv
List of Figures	x
List of Tables	xiii
Nomenclature	xvi
CHAPTER 1.	1
Introduction	1
1.1. Background	1
1.2. Supermarket refrigeration systems	3
1.3. Direct expansion/multiplex refrigeration system	4
1.4. Cascade refrigeration systems	4
1.5. Secondary coolant system	5
1.6. Distributed refrigeration system	7
1.7. Scope of research	8
1.8. Refrigeration system model	10
1.9. Outline of the thesis	10
CHAPTER 2.	12
Literature Review	12
2.1. Introduction	12
2.2. Medium-temperature refrigeration systems	12
2.3. Cascade refrigeration systems	13
2.4. Frost characteristics and frosted air-coils	16
2.5. Secondary coolant systems	20
2.5.1. Selection of primary refrigerants	21
2.5.2. Selection of secondary coolants	21

CHAPTER 3.	28
Thermodynamic Analyses of an R744-R717 Cascade Refrigeration Systems	28
3.1. Introduction	28
3.2. Thermodynamic analysis of a cascade system	28
3.3. High-temperature circuit refrigerant selection	32
3.4. Results and discussion of the analysis	34
3.4.1. Effect of degree of subcooling and superheat	34
3.4.2. Effect of condensing, evaporating and differential temperatures	38
3.4.3. Effect of isentropic efficiencies of compressors	40
3.4.4. Multilinear regression analysis	43
3.5. Economic benefits of the new thermodynamic correlations	47
CHAPTER 4.	49
New Frost Property Correlations	49
4.1. Introduction	49
4.2. Test rig setup and measurements	51
4.3. Uncertainty analysis	60
4.4. Test conditions and results	63
4.4.1. Test conditions	63
4.4.2. Test results	64
4.5. Multilinear regression analysis for frost correlations	69
4.6. Comparison of measured and correlation predicted frost characteristics	75
CHAPTER 5.	78
Development of Numerical Model for Secondary Coolant Systems	78
5.1. Introduction	78
5.2. Air-coil model	79
5.2.1. General assumptions	80
5.2.2. Sequence of calculation	80

5.2.3. Inputs	80
5.2.4. Outputs	82
5.2.5. Air-side heat transfer coefficient and pressure drop	84
5.2.6. Coolant-side heat transfer coefficient and pressure drop	86
5.2.7. Effectiveness-NTU method for air-coil analysis	89
5.3. Plate heat exchanger models	99
5.3.1. General assumptions	100
5.3.2. Sub-cooler model	100
5.3.3. Intermediate heat exchanger model	111
5.3.4. Condenser model	119
5.4. Distribution line model	127
5.4.1. General assumptions	128
5.4.2. Inputs	128
5.4.3. Outputs	129
5.4.4. Coolant-side heat transfer coefficient and pressure drop	129
5.4.5. Heat transfer and coolant outlet temperature of distribution line	130
5.5. Secondary coolant pump model	132
5.6. Compressor model	133
5.6.1. General assumptions	134
5.6.2. Compressor model inputs and outputs	134
5.7. Expansion valve model	136
5.8. Overall secondary coolant refrigeration system model	138
CHAPTER 6.	142
Validation of Secondary Coolant Refrigeration System Numerical Model	142
6.1. Introduction	142
6.2. Test rig details	142
6.3. Instrumentation	143



6.3.1. Data logging	145
6.3.2. Calibration of measurement sensors	146
6.4. Uncertainty analysis and test results of the secondary coolant system	148
6.4.1. Uncertainty analysis	148
6.5. Test results of the secondary coolant system	150
6.5.1. Variation of rate of heat transfers in heat exchanger between two fluids	151
6.5.2. Coefficient of performance of the secondary coolant system	155
6.6. Validation of secondary coolant system numerical model	159
6.6.1. Air coil model validation	159
6.6.2. Intermediate heat exchanger model validation	161
6.6.3. Condenser model validation	162
6.6.4. Distribution line model validation	163
6.6.5. Secondary coolant pump model validation	164
6.6.6. Compressor model validation	165
6.6.7. Validation of sub-cooler and expansion valve models	166
6.6.8. Validation of overall secondary coolant system model	167
CHAPTER 7.	169
Application of Secondary Coolant Model for Supermarket Refrigeration Systems	169
7.1. Introduction	169
7.2. Details of supermarket selected for simulation	169
7.3. Simulation of secondary coolant refrigeration system components	174
7.3.1. Simulation of air-coil for display cabinets	174
7.3.2. Inputs and outputs of the simulated display cabinet air-coils	177
7.3.3. Simulation of plate heat exchangers	179
7.3.4. Simulation of secondary coolant distribution line	182
7.3.5. Simulation of secondary coolant pump	184
7.3.6. Simulation of compressor	185

7.3.7. Simulation of expansion valve	186
7.3.8. Simulation of overall secondary coolant refrigeration system	186
7.4. Summary of the application of secondary coolant model for supermarkets	187
7.5. Economic benefits of the new secondary coolant system model	189
CHAPTER 8.	191
Conclusions and Recommendations	191
8.1. Conclusions	191
8.1.1. Thermodynamic analysis of a cascade refrigeration system	191
8.1.2. New frost property correlations for flat-finned tube air coils	192
8.1.3. New numerical model for medium-temperature secondary coolant refrigeration system	192
8.1.4. Application of secondary coolant model for supermarket refrigeration systems	195
8.2. Recommendations for future research works	196
8.2.1. Cascade refrigeration system	196
8.2.2. Improvement in frost property correlations for flat-finned tube air coils	197
8.2.3. Improvements in medium-temperature secondary coolant refrigeration systems	198
<i>Appendix A</i>	A
<i>Appendix B</i>	D
<i>Appendix C</i>	H
<i>Appendix D</i>	N
<i>Appendix E</i>	T
<i>List of publications</i>	Z
1. Journal papers	Z
2. Conference papers	Z
<i>Vita</i>	AA

# List of Figures

---

Figure 1.1 Direct expansion/Multiplex refrigeration system. ....	4
Figure 1.2 Cascade refrigeration system [7].....	5
Figure 1.3 Secondary coolant refrigeration system [8].....	6
Figure 1.4 Distributed refrigeration system [8]. ....	7
Figure 2.1 Schematic of a two-stage cascade refrigeration system. ....	14
Figure 2.2 Variation of pressure drop and heat transfer coefficient against inlet temperatures of various types of secondary coolants. ....	22
Figure 2.3 Variation of pump power consumption against inlet temperatures of various secondary coolants. ....	24
Figure 3.1 Carbon dioxide and Ammonia cycles on T-s property plots. ....	30
Figure 3.2 Carbon dioxide and Ammonia cycles on P-h property plots. ....	31
Figure 3.3 Variation of system performance for a subcooling of 0 K and superheat of 20 K in both circuits. ....	33
Figure 3.4 Variation of system performance for subcooling of 10 K and superheat of 0 K in both circuits. ....	34
Figure 3.5 Variation of system performance for a subcooling of 0 K and superheat of 0 K in both circuits. ....	35
Figure 3.6 Variation of system performance for a subcooling of 10 K and superheat of 20 K in both circuits. ....	36
Figure 3.7 The ratio of high-temperature to low-temperature mass flow rates. ....	37
Figure 3.8 Effect of superheating and subcooling on system and individual cycles. ....	38
Figure 3.9 System performance curve for R744-R717 with variation in R717 evaporating temperature and degree of subcooling on both cycles. ....	39
Figure 3.10 Variation of R744-R717 mass ratios with change in R717 evaporating temperature and degree of subcooling in both R744 and R717 cycles. ....	40
Figure 3.11 Variation of R744-R717 system COP with change in R717 evaporating temperature and degree of superheat in both R744 and R717 cycles. ....	40
Figure 3.12 Variation of R744-R717 mass ratios with respect to change in superheat. ....	41
Figure 3.13 Effect of condensing, evaporating and differential temperatures on system performance. ....	41

Figure 3.14 Effect of condensing, evaporating and differential temperatures on mass ratio..	42
3.15 Effect of having different isentropic efficiencies in the compressors of both cycles.....	44
3.16 Effect of isentropic efficiency with change in R717 evaporating temperature assuming the same isentropic efficiency in the compressors of both cycles. ....	45
Figure 4.1 Experimental test rig. ....	49
Figure 4.2 Layout of secondary coolant system model and instrumentation. ....	50
Figure 4.3 Detail A: Test coil design for frost experiment.....	51
Figure 4.4 Positions of temperature sensors on the test coil fins and tubes. ....	52
Figure 4.5 Layout of temperature sensors on a single fin-tube arrangement. ....	53
Figure 4.6 Configuration of CCD Camera and the frosted test coil. ....	54
Figure 4.7 Frost thickness measurements.....	56
Figure 4.8 Transient and steady state parts of the frost test conditions. ....	58
Figure 4.9 Discrepancy between measured and calculated total frost masses. ....	59
Figure 4.10 Test 8: Frost growth on fins and tubes on the left side of the test coil. ....	62
Figure 4.11 Test 7: Frost growth on fins and tubes in the middle of the test coil. ....	63
Figure 4.12 Test 10: Frost growth on fins and tubes on the right side of the test coil.....	65
Figure 4.13 Comparison of measured and correlation predicted a) frost density; and b) frost thermal conductivity.....	75
Figure 4.14 Comparison of measured and correlation predicted a) frost thickness; and b) frosted coil air pressure drop. ....	76
Figure 5.1 Flowchart of medium-temperature secondary coolant refrigeration system model. ....	79
Figure 5.2 Air-coil divided into n-number of elements. ....	81
Figure 5.3 Air-coil simulation flowchart to predict frosted air-coil performance for medium-temperature secondary coolant applications.....	98
Figure 5.4 A typical brazed plate heat exchanger plate. ....	99
Figure 5.5 Sub-cooler (a) divided into n-number of elements with equal size; and (b) temperature distribution for a counterflow arrangement.....	101
Figure 5.6 Sub-cooler simulation flowchart to predict sub-cooler performance for medium-temperature secondary coolant applications.....	110
Figure 5.7 Intermediate heat exchanger a) divided into two-phase and superheated regimes; b) temperature distribution for a counterflow arrangement. ....	112
Figure 5.8 Intermediate heat exchanger simulation flowchart to predict its performance for medium-temperature secondary coolant applications. ....	119

Figure 5.9 Condenser model a) divided into two-phase and superheated regimes; b) temperature distribution for a counterflow arrangement.....	120
Figure 5.10 Condenser simulation flowchart to predict its performance for medium-temperature secondary coolant applications.....	125
Figure 5.11 Secondary coolant distribution line model. ....	127
Figure 5.12 Distribution line simulation flow chart to predict its outlet conditions for medium-temperature secondary coolant applications. ....	131
Figure 5.13 Secondary coolant pump model. ....	132
Figure 5.14 Compressor model for secondary coolant refrigeration system.....	134
Figure 5.15 Thermostatic expansion valve model. ....	136
Figure 5.16 Secondary coolant system model simulation flowchart. ....	137
Figure 6.1 Layout of temperature, pressure and mass flowrate data logging system. ....	144
Figure 6.2 Layout of frost image and dew point measurement data logging system. ....	145
Figure 6.3 Variation of rate of heat transfer on the refrigerant- and coolant-sides in the intermediate heat exchanger. ....	152
Figure 6.4 Variation of rate of heat transfer on the refrigerant- and water-sides in the condenser. ....	153
Figure 6.5 Variation of rate of heat transfer on the air- and coolant-sides in the test coil. ...	154
Figure 6.6 Coefficient of performance (COP) of the secondary coolant system for various tests.....	155
Figure 6.7 Air-coil model prediction of (a) air; and (b) coolant outlet temperatures. ....	158
Figure 6.8 Air-coil model prediction of air coil effectiveness. ....	160
Figure 6.9 Intermediate heat exchanger model prediction of coil coolant outlet temperature. ....	161
Figure 6.10 Condenser model prediction of cooling water outlet temperature. ....	162
Figure 6.11 Prediction of coolant outlet temperature from supply line of the secondary coolant circuit. ....	163
Figure 6.12 Pump model prediction of secondary coolant pump power consumption.....	164
Figure 6.13 Compressor model prediction of compressor outlet temperature. ....	165
Figure 6.14 Overall system model prediction of secondary coolant system COP. ....	167
Figure 7.1 Layout of supermarket selected for simulation.....	170
Figure 7.2 Layout of simulated secondary coolant refrigeration system for supermarkets. .	172
Figure 7.3 Piping layout of Circuit A in the selected supermarket for simulation. ....	173
Figure 7.4 Layout of display cabinet air-coil. ....	176

# List of Tables

---

Table 3.1 Calculation of thermodynamic state points of R744-R717 cascade system using EES [9]. .....	29
Table 3.2 Statistical information for Equations 3-9 through 3-12. ....	46
Table 4.1 Equations used during frost measurements in the steady state part of the test. ....	57
Table 4.2 Comparison of manually measured and approximated frost surface temperatures. 60	
Table 4.3 Results of uncertainty analysis. ....	62
Table 4.4 Steady state experimental conditions. ....	64
Table 4.5 Measured air conditions during the steady state parts of the tests. ....	66
Table 4.6 Measured frost and inlet coolant conditions during the steady state parts of the tests. ....	68
Table 4.7 Calculated parameters during the steady state parts of the tests (for the same duration as in Tables 4.4 and 4.5). ....	71
Table 4.8 Statistical information for frost thickness and density. ....	73
Table 4.9 Statistical information for frost thermal conductivity and air coil pressure drop. ..	74
Table 5.1 Calculation of thermodynamic state points of secondary coolant system using EES [9]. ....	140
Table 6.1 Results of uncertainty analysis. ....	149
Table 6.2 COP in descending order as a function of operating parameters of the secondary coolant system. ....	156
Table 7.1 Air-coil geometrical inputs for selected display cabinets (BR33, BR35 and BR36). ....	178
Table 7.2 Air- and coolant-side inputs of the display cabinet air-coils. ....	178
Table 7.3 Outputs of display cabinet air-coils. ....	179
Table 7.4 Geometrical inputs of intermediate heat exchanger and condenser. ....	180
Table 7.5 Inputs of fluid conditions for the intermediate heat exchanger and condenser. ....	181
Table 7.6 Outputs of intermediate heat exchanger and condenser. ....	182
Table 7.7 Geometrical inputs and outputs of distribution line. ....	183
Table 7.8 Fluid-side inputs and outputs of distribution line. ....	184

Table 7.9 Inputs and outputs of secondary coolant pump. ....	185
Table 7.10 Inputs and outputs of compressor. ....	185
Table 7.11 Inputs and outputs of thermostatic expansion valve. ....	186
Table 7.12 Inputs and outputs of the overall secondary coolant refrigeration system. ....	187
Table A.1 Schedule of secondary coolant system components. ....	A
Table A.2 Schedule of pipes and bends for secondary coolant system test rig. ....	B
Table A.3 Schedule of pipe and duct insulation for secondary coolant system test rig. ....	B
Table A.4 Detailed geometrical parameters and construction materials of plate heat exchangers. ....	C
Table B.1 Schedule of temperature sensors for frosted test coil fins and air stream. ....	D
Table B.2 Schedule of temperature sensors for frosted test coil tubes. ....	E
Table B.3 Schedule of secondary coolant system temperature and pressure sensors. ....	F
Table B.4 Schedule of secondary coolant system flowmeters and wattmeters. ....	G
Table C.1 Intermediate heat exchanger measurements for mono-propylene glycol/water mixture (52%/48% by weight). ....	H
Table C.2 Thermostatic expansion valve measurements for mono-propylene glycol/water mixture (52%/48% by weight). ....	I
Table C.3 Condenser measurements for mono-propylene glycol/water mixture (52%/48% by weight). ....	J
Table C.4 Subcooler measurements for mono-propylene glycol/water mixture (52%/48% by weight). ....	K
Table C.5 Test coil and pre-cooler measurements for mono-propylene glycol/water mixture (52%/48% by weight). ....	L
Table C.6 Compressor and coolant pump measurements for mono-propylene glycol/water mixture (52%/48% by weight). ....	M
Table D.1 Intermediate heat exchanger measurements for mono-ethylene glycol/water mixture (42%/58% by weight). ....	N
Table D.2 Thermostatic expansion valve measurements for mono-ethylene glycol/water mixture (42%/58% by weight). ....	O
Table D.3 Condenser measurements for mono-ethylene glycol/water mixture (42%/58% by weight). ....	P
Table D.4 Subcooler measurements for mono-ethylene glycol/water mixture (42%/58% by weight). ....	Q

Table D.5 Test coil and pre-cooler measurements for mono-ethylene glycol/water mixture (42%/58% by weight).....	R
Table D.6 Compressor and coolant pump measurements for mono-ethylene glycol/water mixture (42%/58% by weight).....	S
Table E.1 List of cabinets fed by Circuit A.....	T
Table E.2 List of cabinets fed by Circuit B.....	U
Table E.3 List of cabinets fed by Circuit C.....	V
Table E.4 List of cabinets fed by Circuit D.....	W
Table E.5 List of cabinets fed by Circuit E.....	X
Table E.6 List of cool rooms fed by separate Refrigerant Circuit.....	Y



# Nomenclature

---

A	area	[m <sup>2</sup> ]
C <sub>pma</sub>	specific heat of moist air	[kJ kg <sup>-1</sup> K <sup>-1</sup> ]
C <sub>psc</sub>	specific heat of secondary coolant	[kJ kg <sup>-1</sup> K <sup>-1</sup> ]
COP	coefficient of performance	[dimensionless]
D	diameter	[m]
D <sub>h</sub>	hydraulic diameter	[m]
f	friction factor	[dimensionless]
Fo	Fourier number	[dimensionless]
F <sub>p</sub>	fin pitch	[m <sup>-1</sup> ]
G <sub>ma</sub>	air mass flux	[kg m <sup>-2</sup> s <sup>-1</sup> ]
G <sub>m,sc</sub>	secondary coolant mass flux	[kg m <sup>-2</sup> s <sup>-1</sup> ]
h	heat transfer coefficient or enthalpy	[W m <sup>-2</sup> K <sup>-1</sup> ] or [kJ kg <sup>-1</sup> ]
h <sub>flow</sub>	Flow length	[m]
h <sub>hx</sub>	Heat exchanger length	[m]
h <sub>s</sub>	specific enthalpy calculated at suction entropy	[kJ kg <sup>-1</sup> ]
k	thermal conductivity	[W m <sup>-1</sup> K <sup>-1</sup> ]
L	length	[m]
$\dot{m}$	mass flow rate	[kg s <sup>-1</sup> ]
m <sub>fst</sub>	frost mass accumulation	[kg m <sup>-2</sup> ]
$\dot{m}_H \backslash \dot{m}_L$	ratio of high-temperature circuit mass flowrate to low-temperature circuit mass flowrate	[dimensionless]
Nu <sub>D</sub>	Nusselt number	[dimensionless]
N <sub>T</sub>	number of tubes in horizontal direction	[dimensionless]
N <sub>V</sub>	number of tubes in vertical direction	[dimensionless]
P	pressure	[kPa]
Pr <sub>D</sub>	Prandtl number	[dimensionless]
q	heat flux	[W m <sup>-2</sup> ]

$\dot{Q}$	rate of heat transfer	[kW]
R1\$	carbon dioxide	(R744)
R2\$	ammonia	(R717)
Re <sub>D</sub>	Reynolds number for circular diameter	[dimensionless]
Re <sub>Da</sub>	Reynolds number for air-coil	[dimensionless]
Re <sub>Dh</sub>	Reynolds number at hydraulic diameter	[dimensionless]
r <sub>1</sub>	tube outer radius	[m]
r <sub>2</sub>	fin tip radius	[m]
row1	first row of air-coil	[dimensionless]
row2	second row of air-coil	[dimensionless]
s	specific entropy	[kJ kg <sup>-1</sup> K <sup>-1</sup> ]
S <sub>F</sub>	fin spacing	[m]
S <sub>T</sub>	vertical distance between tubes	[m]
t	thickness	[m]
T	temperature	[°C]
U	overall heat transfer coefficient	[W m <sup>-2</sup> °C <sup>-1</sup> ]
v	velocity	[m s <sup>-1</sup> ]
$\dot{V}$	volumetric flow rate	[m <sup>3</sup> s <sup>-1</sup> ]
W	effective width	[m]
$\dot{W}$	power	[W]
W <sub>T</sub>	horizontal distance between tubes	[m]
SC\$	Secondary coolant	[MPG]/[MEG]
x	x-axis/quality	[m]/[dimensionless]

***Greek letters***

$\delta$	thickness	[m]
$\Delta$	change	[dimensionless]
$\varepsilon$	heat exchanger effectiveness	[%]
$\eta$	efficiency	[dimensionless]
$\mu$	dynamic viscosity	[kg s <sup>-1</sup> m <sup>-1</sup> ]

$\omega$	humidity ratio	[g /kg <sub>DA</sub> ]
$\rho$	density	[kg m <sup>-3</sup> ]
$\sigma$	ratio of free-flow to frontal area/standard deviation	[dimensionless]
$\tau$	time	[s]

### *Subscripts*

a	air
act	actual
avg	average
C	condenser
CAS	cascade heat exchanger
channel	channel
circuit	coolant/refrigerant circuit
CO <sub>2</sub>	carbon dioxide
com	compressor
con	concentration
coolant	secondary coolant
D	diameter
desup	desuperheating
e	element
E	evaporator
elec	electric
EXV	expansion valve
fin	fin
free	free flow
flow	fluid flow
fluid	fluid/secondary coolant
fr	frontal
fst	frost
H	high-temperature circuit

hx	heat exchanger
ice	ice
ihx	Intermediate heat exchanger
in	inlet
interface	frost-coil interface
isen	isentropic
L	low-temperature circuit
line	distribution line
MAX	maximum
meas	measured
min	minimum
MPG	monopropylene glycol
NH <sub>3</sub>	ammonia
OPT	optimum
o	Overall/Outer
out	outlet
p	pitch/port
pc	precooler
plate	plate
PUMP	pump
R	refrigerant
r,com,in	refrigerant compressor inlet
r,com,out	refrigerant compressor outlet
r,exv,in	refrigerant expansion valve inlet
r,exv,out	refrigerant expansion valve outlet
r,ihx,in	refrigerant intermediate heat exchanger inlet
r,ihx,out	refrigerant intermediate heat exchanger outlet
r,con,in	refrigerant condenser inlet

r,con,out	refrigerant condenser outlet
r,sub,in	refrigerant sub-cooler inlet
r,sub,out	refrigerant sub-cooler outlet
s	subcooling
sc,ihx,in	coolant intermediate heat exchanger inlet
sc,ihx,out	coolant intermediate heat exchanger outlet
sc,pc,out	coolant pre-cooler outlet
sc,tc,in	coolant test coil inlet
sc,tc,out	coolant test coil outlet
sub	subcooling
sup	superheating
surface	surface
system	system
total	total
tp	two phase
tr	triple point
tc	test coil
tube	tube
w	wall/water
w,con,in	water condenser inlet
w,con,out	water condenser outlet
w,sub,in	water sub-cooler inlet
w,sub,out	water sub-cooler outlet

# CHAPTER 1.

## Introduction

---

### 1.1. Background

Refrigeration is a technology which regulates and maintains temperatures lower than the surrounding. Among its applications, food storage and air condition systems are the two typical examples. Vapor compression refrigeration dates back to 1834 when Jacob Perkins received a patent for closed cycle ice machine [1]. Since the development of the vapor compression cycle, refrigeration obtained a very fast growth. From chilling and chilled storage to freezing and frozen storage, from refrigerated transport to retail distribution, accompanied by the development of air conditioning technology, refrigeration plays a vital role in the commercial sectors, especially in supermarkets. However, supermarkets are the most energy-intensive types of commercial buildings, which contain heating, cooling, and ventilation (HVAC) as well as refrigeration systems as single integrated facility. Electricity consumption in large supermarket represents about 4% of the national electric energy use in both the United States and France [2].

Supermarket refrigeration systems, mainly refrigerated display cases, consume about 50% of the total store energy [3]. According to the study conducted by Getu [4], the average power consumption of the compressors/rack systems for both the low- and medium-temperature refrigeration systems of the supermarket amounts to roughly 20% of the total energy use of the supermarket. The field (defrosting, anti-sweat resistance heaters, display cabinet lights and fans) energy consumption contributes to an additional 14%. The energy consumption due to the air-conditioning system of the building is as much as 17% of the entire energy use of the supermarket. The rest of the supermarket energy use, which is around 49% attributes to water heating and lighting systems of the establishment.

Defrosting of air-coils is also one of the most energy consuming processes in supermarket refrigeration systems. When the surface temperature of coils falls below 0°C, water vapor in the air condenses and freezes forming frost on the coils. The water vapor mainly attributes to exchange of moisture between the display cases and the store environment. Open display cases are seriously affected by the extent of moisture in the supermarket whereas the glass-door display cases are rarely susceptible by moisture transfer. Large amount of frost accumulation decreases the performance of the coils by reducing the flow of air. This consequently reduces the refrigerating capacity of the coils. Hence, frosting should be removed from air-coils when the frost grows to a certain thickness to maintain system performance and temperature control.

Nowadays, there are different types of refrigeration systems, which provide cooling to various kinds of display cabinets such as meat, dairy, delicatessen, produce and frozen food in the supermarket industry. These are direct expansion/multiplex, cascade, secondary coolant and distributed refrigeration systems. Additionally, new refrigeration technologies are emerging which could potentially reduce the environmental impacts of the conventional refrigeration systems in the food industry [5]. These are (a) sorption refrigeration technologies (e.g. absorption and adsorption) where the compressor of a vapor compression cycle is replaced by a 'thermal compressor' and a sorbent; (b) ejector refrigeration systems (thermally driven technologies) where two refrigerants (primary and secondary) are mixed in the ejector eliminating the necessity of moving parts; (c) air cycle refrigeration which produces low temperatures for refrigeration by using air in compression, constant pressure cooling and expansion to achieve a final temperature lower than the temperature at the start of compression; (d) tri-generation or CCHP (Combined Cooling, Heating and Power) which is a thermally driven refrigeration system providing cooling, electrical power, heating energy; (e) Stirling cycle refrigeration system which is a closed-cycle regenerative thermal machine working on the principle that a piston alternately compresses and expands a working gas, whereas the displacer shuttles the gas back and forth between the cold end (where heat is absorbed) and the warm end (where heat is rejected); (f) thermoelectric refrigeration (Peltier effect) which is attributable to the junction of two dissimilar metals to either cool down or warm up when a direct electric current passes through the junction depending on the direction of applied current; (g) thermo-acoustic refrigeration systems which operate by using sound waves and a non-flammable mixture of inert gas (e.g. helium, argon, air

etc) or a mixture of gases in a resonator to produce cooling; and (h) magnetic refrigeration which is based on the magneto-caloric effect (MCE), a basic property of magnetic solids characterized by a reversible temperature rise when a magnetic field is applied adiabatically.

However, direct expansion refrigeration system is the most commonly employed configuration in modern supermarkets for providing refrigeration to display cabinets located in the store. The other new refrigeration systems including the emerging refrigeration technologies need a lot of work to make them commercially attractive. Among these works, thermodynamic analysis and develop numerical models and empirical frost correlations for cascade and secondary coolant refrigeration systems, respectively, could be vital to evaluate the performance of two of the new refrigeration technologies. This is because carbon dioxide is, for example, being widely used in cascade refrigeration systems in Europe by attracting supermarket owners [5]. It was also reported by Wang et al [6] that secondary coolant refrigeration systems, especially, for medium-temperature applications are being tried in Europe, US and Canada by supermarket owners due to their minimized environmental impact and piping networks as compared to traditional ones. The following sections, in general, present brief descriptions of the direct expansion, cascade and secondary coolant supermarket refrigeration systems and the overview of the project. Interested readers can refer to reference [5] for further information on the emerging refrigeration technologies.

## **1.2. Supermarket refrigeration systems**

Supermarkets have three different types of cooling systems. The first one is air-conditioning system, which has a typical refrigerated water temperature of roughly (+) 10<sup>0</sup>C that regulates the relative humidity and temperature in an occupied store. The second one is the medium-temperature refrigeration system. It has air discharge temperature of around (–) 2<sup>0</sup>C, which provides refrigeration for fresh food such as meats, vegetables and dairy products. The last system has air discharge temperature of nearly (–) 24<sup>0</sup>C and is called low-temperature refrigeration system.



### 1.3. Direct expansion/multiplex refrigeration system

The operation of a direct expansion refrigeration system contains four processes comprising evaporation, compression, condensation and throttling. Two or more compressors operate in parallel, usually known as *rack* or *pack*, at the same saturated suction temperature, and are piped with common suction and discharge refrigeration manifolds. The advantage of having multiple compressors is that it is possible to control the compressors selectively and cycle as needed to meet the refrigeration load. These systems are called *multiplex refrigeration systems* and the configuration is shown in Figure 1.1. Heat rejection is usually carried out by air-cooled condensers.

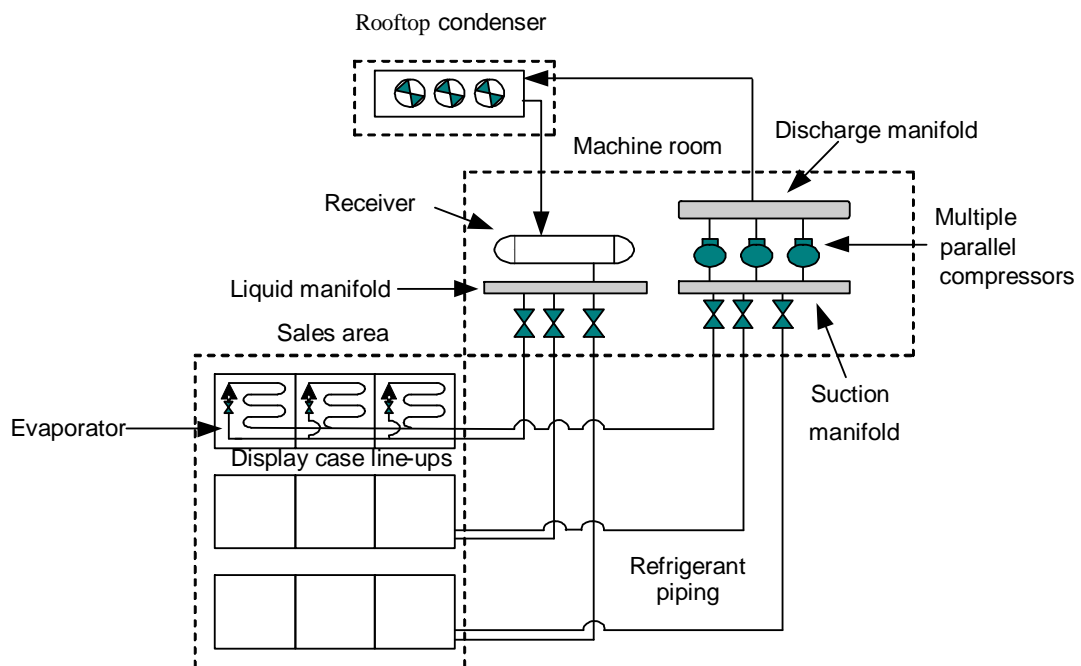


Figure 1.1 Direct expansion/Multiplex refrigeration system.

### 1.4. Cascade refrigeration systems

In cascade systems, propane or ammonia can be used as primary refrigerant, whereas carbon dioxide and glycol are used as secondary thermofluids for low- and medium-temperature refrigeration systems, respectively. Figure 1.2 describes the working principle of the cascade

refrigeration system presented by Christensen and Bertilsen [7]. Propane is compressed by one or more compressors ( $C_1$  through  $C_3$ ) and condenses in an air-cooled condenser on the roof of the supermarket. Carbon dioxide is also compressed by a small compressor ( $C_4$ ). Heat exchange between propane and carbon dioxide takes place in the cascade heat exchanger (HX2) where propane evaporates and carbon dioxide condenses. The propane also exchanges heat with glycol heat exchanger (HX1). Glycol is pumped (by brine pumps) in a secondary loop to supply the medium-temperature cabinets and cold stores. Some of the disadvantages of this system are; 1) propane is highly flammable and 2) carbon dioxide reaches a higher pressure (7.4MPa) at 31°C, leading to redesign of pipes and fittings.

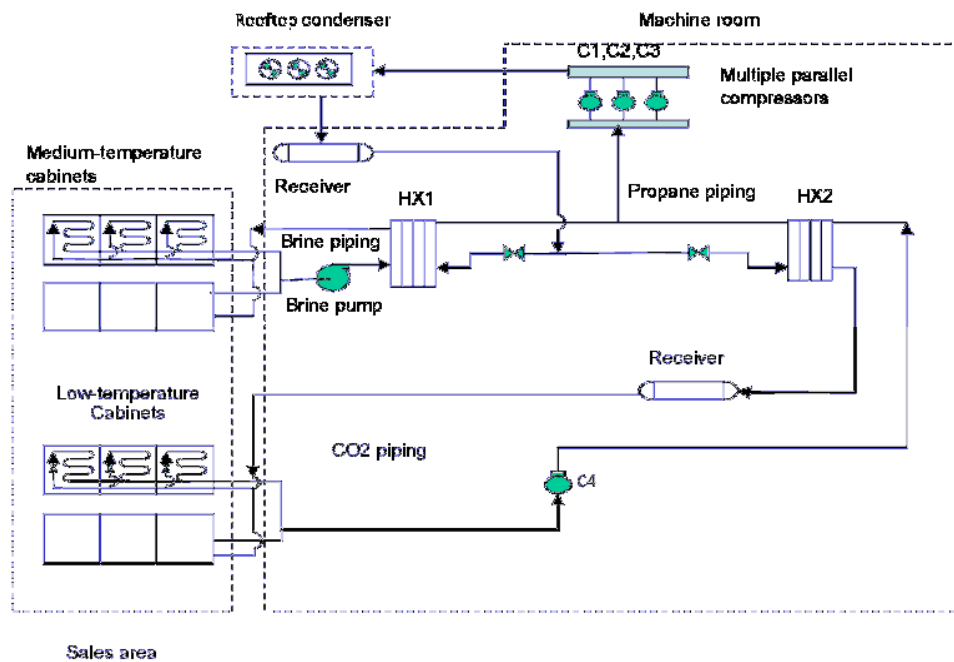


Figure 1.2 Cascade refrigeration system [7].

## 1.5. Secondary coolant system

In the case of secondary coolant refrigeration, brine loops are run between the display cases and central chiller systems. The refrigerated brine from the chiller is then circulated through the coils in the display cases where it is used to chill the air in the case. The system scheme is shown in

Figure 1.3. Central chillers are constructed as multiplex parallel racks for capacity control. High-efficiency compressors (such as reciprocating or scroll units) and coolant pumps should always be used to avoid unnecessary added energy consumption. Additionally, in the primary refrigerant loop of the secondary coolant systems, the pressure drop at the compressor inlet needs to be compensated by the compressor. This refrigeration system, however, needs certain improvements such as increasing the effectiveness of display case aircoils (heat exchangers) for the use of brine, proper brine selection in order to avoid higher energy consumption for pumping, and reducing the brine lines to minimize frictional losses. Secondary coolant systems are normally suitable for medium-temperature applications.

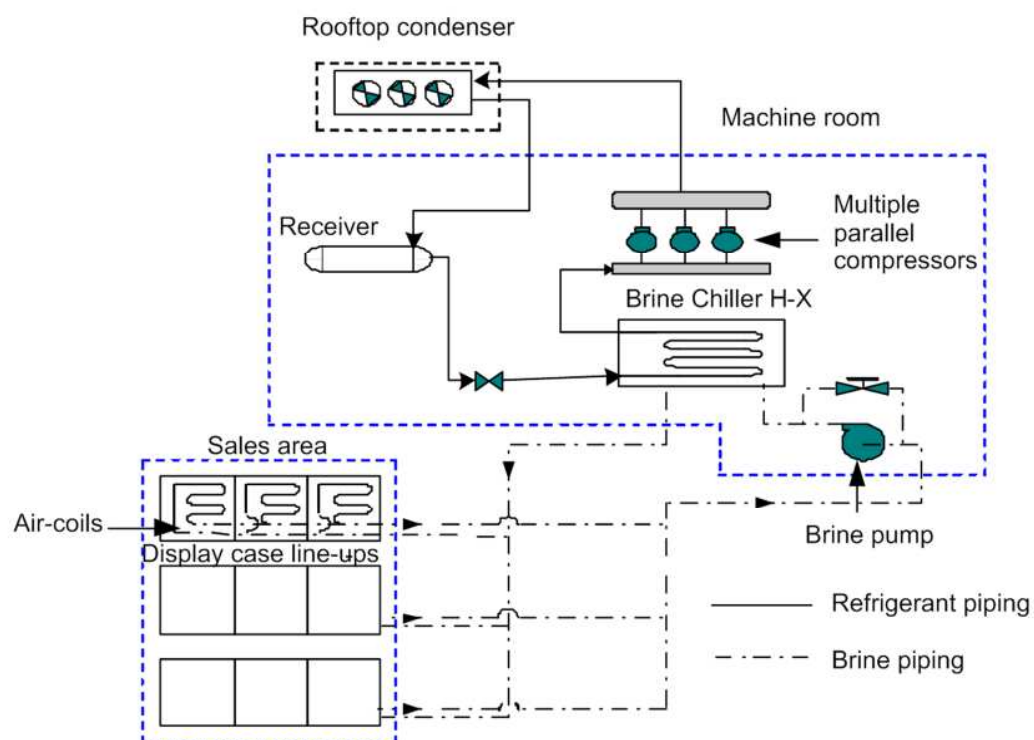


Figure 1.3 Secondary coolant refrigeration system [8].

## 1.6. Distributed refrigeration system

Unlike the direct expansion refrigeration system, in the distributed refrigeration, multiple compressors are situated in cabinets, which are in the sales area of the store. The cabinets are closely connected to the display cases and air-cooled condenser or a glycol loop is used to reject heat from the cabinets. The condensers are located on the roof above the cabinets, whereas the glycol loop connects the cabinets to a fluid cooler. In this type of refrigeration system, scroll compressors are used since they have lower noise and vibration levels. The layout of the system is shown in Figure 1.3. The advantage of this refrigeration system over direct expansion systems is the close connection between the display cases and the compressors, which considerably reduces the suction lines, thereby decreasing the pressure drop between the evaporators and the suction manifold of the compressors.

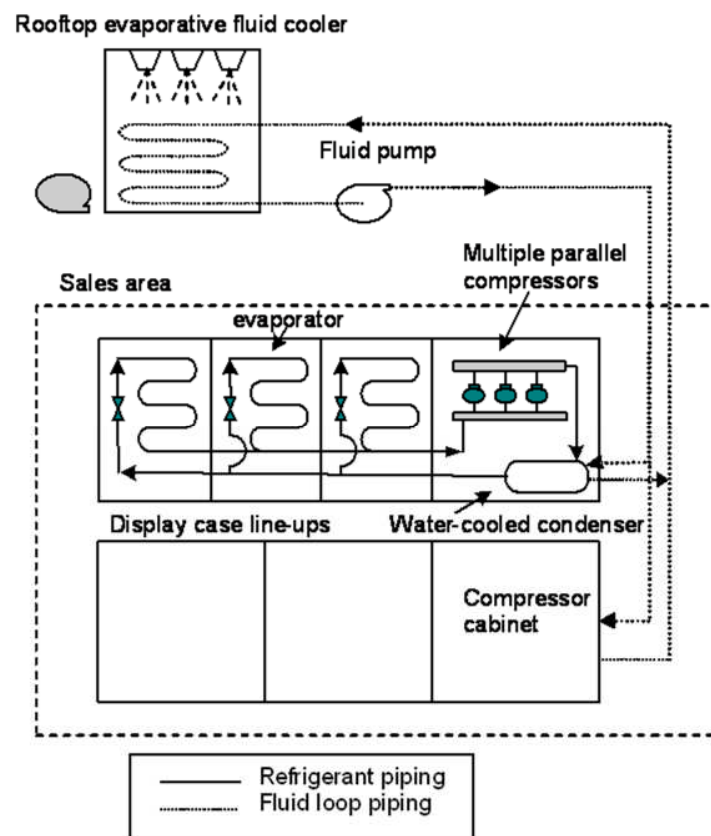


Figure 1.4 Distributed refrigeration system [8].

### **1.7. Scope of research**

In spite of the fact that new refrigeration technologies are introduced to the supermarket industry, the direct expansion refrigeration system is still a choice of many supermarket Owners. The main reason for this is that the new technologies are not yet as competitive as the traditional ones. There is limited research work available on the development of numerical models, which will be discussed later in Chapter 2, to evaluate the performance of the new technologies adequately. The development of numerical models requires selection of appropriate existing heat and mass transfer correlations. Additionally it requires development of new frost characteristic correlations for different temperature applications (e.g. medium-temperature display cabinets). It is well known that the frost characteristics are highly influenced by heat exchanger surface temperatures. Generally, the development of frost characteristic correlations for specific applications is vital for determining defrost period thereby avoiding unnecessary waste of energy and deterioration of food products due to the insulation effect of frost layers which form on the surfaces of display case air-coils.

For the benefit of the supermarket industry, it is therefore important to analyze the thermodynamic parameters of a cascade refrigeration system in order to theoretically evaluate the impact of variation of these parameters on the performance of the system as a whole. Furthermore, development of fresh frost correlations such as frost thickness, density and thermal conductivity for medium-temperature secondary coolant air-coils is essential to make defrost controls more efficient. These fresh frost correlations can then be incorporated in the newly developed robust secondary coolant model for medium-temperature applications to fill the gap existing in the supermarket industry.

In general, the main purpose of this research project is to develop 1) a thermodynamic numerical model for cascade refrigeration systems; 2) frost correlations on a real flat-finned-tube exchanger for secondary coolant air-coil; and 3) a computer model for secondary coolant refrigeration systems for medium-temperature applications. All of the above frost correlations and numerical models can then be effectively used to evaluate the performance of refrigeration systems with

respect to energy consuming operating and system variables for supermarket applications. For instance, the medium-temperature secondary coolant refrigeration system model has been employed for design; selection and evaluation of such systems for supermarkets (see Chapter 7).

The thermodynamic model of the cascade refrigeration system includes four empirical correlations by which for any given design and operating parameters such as refrigeration capacity, isentropic efficiency and various temperatures, the new correlations enable a design engineer to determine the ideal maximum COP and mass flow requirements of a carbon dioxide-ammonia (R744-R717) cascade refrigeration system. Besides, the usefulness of the freshly developed frost correlations is that a refrigeration engineer can also easily estimate the time interval between defrost cycles given fin pitch, the inlet variables of the air and surface conditions of the heat exchangers since the duration of frost build up is implicit in the frost thickness calculation. The heat and time span required for defrosting frosted heat exchangers can be estimated using frost correlations as well.

Furthermore, the secondary coolant model includes the utilization of the most appropriate heat transfer, mass transfer and pressure drop correlations. The system components such air-coil, plate heat exchangers, distribution lines, coolant pump and compressor are modeled independently so that a refrigeration engineer can evaluate the design parameters of each component for better component design and selection based on various secondary coolant and refrigerant for medium-temperature applications. In addition, the air-coil model incorporates the newly developed frost correlations for medium-temperature applications. Each component model in turn can be linked to form a complete overall secondary coolant refrigeration system model to enable a refrigeration engineer to evaluate the coefficient of performance (COP) of the system in total for additional improvements. The model results were finally validated against the measurements taken from a lab-scale secondary coolant test rig located in the Thermodynamic Laboratory, the University of Auckland, New Zealand.

## **1.8. Refrigeration system model**

All of the numerical models were written in a software package called (EES) Engineering Equation Solver [9]. It has built-in properties of many refrigerants. The package has the ability to solve systems of non-linear equations and also has a structured programming environment. The computer models can be used as convenient tools to analyze the performance of the cascade and secondary coolant refrigeration systems for various operation conditions such as temperatures, humidity ratios, pressures, mass flowrates, secondary coolants and primary refrigerants.

## **1.9. Outline of the thesis**

The thesis introduces three major original works to the refrigeration industry – 1) a thermodynamic model for a carbon dioxide-ammonia cascade refrigeration system, which has four new empirical correlations; 2) new frost property correlations such as frost thickness, frost density, frost thermal conductivity including pressured drops across frosted air-coils; and 3) a secondary coolant computer model for medium-temperature applications, which incorporates the newly developed frost property correlations. In general, the thesis comprises the following eight chapters.

1. Background
2. Literature review
3. Thermodynamic analyses of an R744-R717 cascade refrigeration systems
4. New frost property correlations
5. Development of numerical models for secondary coolant systems
6. Validation of secondary coolant refrigeration system numerical model
7. Application of secondary coolant model for supermarket refrigeration systems
8. Conclusions/Recommendations

*Chapter 2* deals with an intensive literature survey related to medium-temperature refrigeration systems in general, thermodynamic analyses of cascade refrigeration systems in particular, frost property correlations and secondary coolant systems for supermarket applications including

modeling of refrigeration systems and experimental investigation carried out by different researchers.

*Chapter 3* deals with thermodynamic analyses of a carbon dioxide-ammonia cascade refrigeration systems and introduces four brand new empirical correlations by which the best performance points of such systems can be obtained.

*Chapter 4* demonstrates the experimental techniques employed to study frost formation processes on a lab-scale flat-finned tube heat exchanger and introduces four brand new empirical frost property correlations derived from the experimental results.

*Chapter 5* illustrates the development of numerical models for secondary coolant refrigeration systems for medium-temperature applications.

*Chapter 6* this chapter describes the experimental techniques used to measure various system variables including the instrumentation mounted on a modified lab-scale test rig. The validation of component and overall secondary coolant system models is presented in detail as well.

*Chapter 7* illustrates the application of the numerical model of medium-temperature secondary coolant refrigeration system for supermarket applications.

*Chapter 8* summaries the conclusions and presents recommendations for future work.



## CHAPTER 2.

# Literature Review

---

### 2.1. Introduction

Some research has been carried out in the areas of cascade refrigeration systems and development of frost characteristics on flat plates and round tubes. There also exists some literature related to secondary coolant refrigeration systems for medium-temperature applications in the supermarket stores. Hence, this chapter discusses classification of refrigeration systems based on discharge air or evaporating/air-coil coolant temperature and extensive literature review on 1) cascade refrigeration systems; 2) correlations of frost properties and; 3) secondary coolant systems. In general, this chapter identifies a research gap in the supermarket refrigeration systems and discusses the motivation behind the project for the benefit of the supermarket industry.

### 2.2. Medium-temperature refrigeration systems

As described in Section 1.2, a medium-temperature refrigeration system operates at a discharge air temperature of around  $(-2)^{\circ}\text{C}$ , which provides refrigeration for fresh food such as meats, vegetables and dairy products. Medium-temperature cabinets have approximately  $(-10)^{\circ}\text{C}$  evaporating or lower coolant temperatures which are usually served by separate refrigeration systems from the low-temperature cabinets having evaporating or coolant temperatures of approximately  $(-40)^{\circ}\text{C}$ . Traditional direct expansion and secondary coolant refrigeration systems are the most suitable systems for medium-temperature applications due to the fact that a traditional direct expansion system for low-temperature applications (Getu and Bansal [10]) involves a large pressure lift between evaporating and condensing temperatures resulting in an increase in the compression ratio and reduction of the volumetric efficiency of the compressors. Whereas, low-temperature secondary coolant systems require high pumping power for a small

air-coil capacity due to lower coolant heat transfer coefficient and higher coolant pressure at low coolant temperatures.

Hence, because of high leakage rates and environmentally damaging primary refrigerants, secondary coolant systems are more suitable for medium-temperature applications than traditional direct expansion systems. Additionally, the secondary coolant systems effectively eliminate the long lengths of interconnection piping through which the primary refrigerant flows. However, two-stage cascade refrigeration systems are more suitable than both traditional and secondary coolant refrigeration systems for low-temperature applications where the evaporating temperature of frozen-food cabinets ranges from  $(-)\ 30^{\circ}\text{C}$  to  $(-)\ 50^{\circ}\text{C}$  (Getu and Bansal [11]). Consequently, the following sections discuss what is available in the open literature regarding cascade and secondary coolant refrigeration systems for low- and medium-temperature applications, respectively, including frost property correlations since these are the major components of the thesis.

### **2.3. Cascade refrigeration systems**

Two-stage cascade refrigeration systems (see Figure 2.1) are suitable for industrial applications, especially in the supermarket refrigeration industry, where the evaporating temperature of frozen-food cabinets ranges from  $(-)\ 30^{\circ}\text{C}$  to  $(-)\ 50^{\circ}\text{C}$  (Getu and Bansal [11]). In these systems, two single-stage units are thermally coupled through cascade condensers. The high-temperature circuit of a cascade refrigeration system could, for example, be charged with ammonia (R717), propane (R290), propylene (R1270), or R404A, whereas carbon dioxide (R744) may be used in the low-temperature circuit of the refrigeration system to take advantage of some these natural refrigerants. Ammonia is a naturally available refrigerant, but it has application constraints such as toxicity and flammability (Chaichana et al [12]). The disadvantage of propylene and propane is their high flammability. However, the risk associated with toxic and flammable refrigerants can be highly minimized by confining the high-temperature circuit to the plant room area or the rooftop of a supermarket. Carbon dioxide has a disadvantage of reaching a higher pressure

(7.4MPa) at 31°C, leading to redesign of pipes and fittings (Christensen and Bertilsen [7]). Therefore, it is economical to use R744 for low-temperature applications.

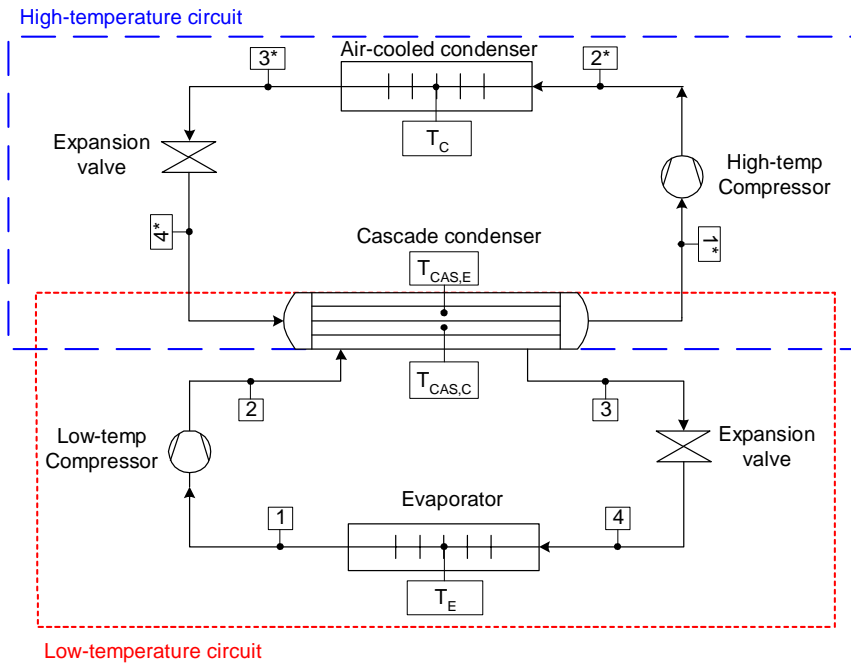


Figure 2.1 Schematic of a two-stage cascade refrigeration system.

A traditional direct expansion low-temperature refrigeration system (Getu and Bansal [10]) involves a large pressure lift between evaporating and condensing temperatures resulting in an increase in the compression ratio and reduction of the volumetric efficiency of the compressors. Furthermore, environmental issues of global warming are forcing the supermarket owners to adopt alternative technologies offering lower refrigerant charge and reduced environmental impact. Therefore, natural refrigerants are increasingly receiving attention for their use in supermarket refrigeration systems. Especially, the use of R744 in the low-temperature circuit of cascade systems is recently becoming commercially more attractive alternative. For instance, carbon dioxide-propylene (R744-R1270) cascade refrigeration system is serving frozen-food display cabinets in a newly developed store in Auckland, New Zealand [13]. A concern with cascade refrigeration systems is the initial installation cost being 10% higher than the traditional direct expansion systems (Wilson and Maier [14]). But this cost can be negated with less

refrigerant charge requirements and the environmental advantage of the cascade system due to less direct emissions as compared to single stage R404A system. High pressure ratios and hot gas temperatures should also be avoided at high temperature differences.

An improvement, which can also be observed in cascade systems (with the same fluid in both circuits) is the reduced amount of superheat in the discharge temperature of the high-temperature circuit that results in a reduced capacity of the high-temperature condenser and an increased refrigeration effect (Ratts and Brown [15]). High-temperature circuit condenser, cascade condenser and evaporator losses can also be reduced if the sizes of the heat exchangers are properly optimized. Several types of cascade condensers such as plate, shell-and-plate or shell-and-tube heat exchangers can be employed for cascade systems to couple the low-and high-temperature circuits (Sawalha [16]).

Several researchers have evaluated the thermodynamic performance of two-stage cascade refrigeration systems. Lee et al [17] analyzed a carbon dioxide-ammonia (R744-R717) cascade system thermodynamically to determine the optimum condensing temperature of R744 in the low-temperature circuit. A carbon dioxide-propane (R744-R290) cascade system was studied by Bhattacharyya et al [18], where an optimum cascade evaporating temperature of R744 in the high-temperature circuit was determined for heating applications. Bansal and Jain [19] evaluated the optimum cascade condensing temperatures of R744 for different refrigerants such as R717, R290, R1270 and R404A, which are in the high-temperature circuits of a cascade system. There have also been several studies on R744 for low temperature refrigeration systems presented by Bansal [20-22]. However, the aforementioned studies lack the main design parameters such as degree of subcooling and superheat in order to optimize the evaporating temperature of R744 and mass flow ratio for maximum COP of a two-stage carbon dioxide-ammonia (R744-R717) cascade refrigeration system. Therefore, one of the main aims of the current research, which is discussed in Chapter 3, is to conduct a thermodynamic analysis on a carbon dioxide-ammonia (R744-R717) cascade refrigeration system to optimize the evaporating temperature of R717 and mass flow ratio, which can give the maximum COP of the system. A novel multilinear regression analysis was employed to develop mathematical expressions for maximum COP,

optimum evaporating and condensing temperatures of the R717-cycle, and an optimum mass flow ratio in terms of sub-cooling, superheating, evaporating temperature, condensing temperature and temperature difference in cascade condenser of the system.

#### **2.4. Frost characteristics and frosted air-coils**

Whenever a refrigerated display cabinet is operating in a store/supermarket environment, there is always an exchange of heat and moisture of the refrigerated display cabinets with the store environment.. Open-type display cabinets are seriously affected by the amount of moisture in the supermarket whereas the susceptibility of glass-door display cases to moisture is highly dependent on the frequency of usage, i.e. high usage of glass-door display cabinets can result in substantial amount of moisture transfer to the air coils. Thus, in developing mathematical models for supermarket refrigeration systems, it is important to understand the interactions of the store environment, which has varying relative humidity and temperature, with the display cabinets.

Whenever a moist air passes continuously over the cold surface of a heat exchanger having a temperature below the dew-point temperature of the moist air, the water vapor in the air will condense on the heat exchanger surface. If the surface temperature is greater than the water freezing temperature but less than the dew-point temperature of the moist air, the condensed water vapor continuously drains along the heat exchanger surface. However, if the surface temperature is below both the water freezing temperature and the dew-point temperature of the moist air, the transferred water vapor may either condense and then freeze, or desublimates (vapor-to-ice) on the cold surface. As a result, frost forms on the surfaces of air coils, thereby resulting in the reduction of heat transfer rate and blockage of the air passage.

Frost formation phenomenon consists of three stages according to Iragorri et al [23] and Tao et al [24]. The first stage is called drop-wise condensation, during which the condensing droplets in a sub-cooling state form on the cold surfaces and all of the coalescent droplets turn into ice particles after a critical time ( $t_c$ ) is reached. The second stage is the solidification and tip-growth

of frost. This process continues until a transitional time ( $t_r$ ) is reached. The last stage is the densification and bulk-growth of frost. During this stage, the frost shows homogeneous and porous characteristics. A literature review on several frost experiments conducted on flat surfaces with temperature ranging from  $(-15^{\circ}\text{C})$  to  $(-40^{\circ}\text{C})$  showed that frost density and frost thermal conductivity decreased with a decrease in temperature as reported by Getu and Bansal, [25]. Frost growth on air coils decreases the capacity of the air coils that are rated at either normal or dry air conditions. Therefore, in order to operate, for instance, a supermarket refrigeration system under a required condition, different defrosting mechanisms must be devised. Precise prediction and control of defrosting periods and duration requires an in-depth understanding of the frost formation process, the operating conditions of the refrigeration system and its interaction with ambient conditions.

Many researchers have used different experimental techniques to develop correlations, especially empirical ones, for calculating properties of a frost layer growing on a cold flat surface. The frost properties such as frost density, frost thickness and frost thermal conductivity are expressed in terms of the surface type, position, surface temperature, frost/air interface temperature, air temperature, air velocity, and air humidity ratio. Mao et al [26] determined the frost local density by collecting frost over a period of time, measuring the frost thickness, and removing and weighing the frosted aluminum disks (32 mm diameter by 0.5 mm thick). The frost thickness was measured following Besant et al [27], where an apparatus was used consisting of a helium-neon laser beam light source, a light attenuating filter, and a precision light meter. Mao et al [28] then developed a correlation for frost density as a function of time, distance from the leading edge, cold plate temperature ratio, humidity ratio, and Reynolds number. Lee and Ro [29] used CCD camera mounted with stepper motors to measure frost thickness. The frost mass per unit area was calculated by dividing the frost mass by its area and the frost density was determined by dividing the frost mass by its volume. The final mass of the frost layer was also measured by scraping the frost off the surfaces of the plates. They also developed a correlation for frost density based on the same independent variables that were used by Mao et al [28].

A correlation for frost thermal conductivity can be formulated based on Fourier equation, which includes measurements of heat flux, frost thickness and a temperature difference across the frost. The heat flux may be measured using a heat flux-meter or determined based on energy balance. The surface temperature of the frost can be measured with an infrared thermometer or thermocouples by direct contact or extrapolation of the temperature distribution in the frost layer according to the methods proposed by Lee and Ro [29, 30]. Thomas et al [31] employed a technique where a set of aluminum fins were inserted in a cold base plate ( $-35^{\circ}\text{C}$  to  $-40^{\circ}\text{C}$ ) so that the fins could be removed at the end of a test and the height and the mass of the frost could be measured. They used a method similar to Besant et al [27] to measure the frost thickness even if the test set-up was different. They measured the frost mass in such a way that each fin was pulled out and wrapped with a plastic wrap and weighed.

Researchers have also evaluated the performance of heat exchangers, having different geometrical configurations, under frosted conditions. Ogawa et al [32] conducted a series of tests on finned-tube heat exchangers and found out that staging (wide fin spacing) and partial cut of fins were effective in decreasing air pressure drop (attributable to frosting) and increasing the rate of heat transfer. Kondepudi et al [33] reported the effects of different fin configurations, namely flat fin, wavy fin and louver fin, on the performance of finned-tube heat exchangers. They concluded that for the same frontal area and fin and tube spacing, the louvered fin type had the greatest frost accumulation, followed by the wavy and flat fin types. Similarly, Yan et al [34] compared the performance of finned-tube heat exchangers with three different fin types (flat plate fins, one-sided louver fins and redirection louver fins) under frosted conditions. They found that the amount of frost formation was the largest for the heat exchanger with redirection louver fins as compared to the heat exchangers with other types of fins under the same operating conditions.

An attempt was also made by Liu et al [35] to minimize the deposition of frost on a cold copper flat plate surface using anti-frosting paint. They claimed that if coating were applied on metal surfaces, the frost layer thickness could be reduced by about 40% as compared to uncoated surfaces. Though the thickness of the coating considered during their investigation was 0.3 mm,

the main material (powder-like substance) which was mixed with varnish at an unknown ratio was not included in their paper, nor was the effect of the paint on the rate of heat transfer.

There are also some studies which considered integral and differential equations for modeling of frost thickness and density on flat plates and heat exchangers. Yang [36] presented a frost growth model based on the diffusion equation from Lee et al [37] and Sahin [38]. However, initial values for frost thickness and density must be assumed for such equations. In Yang's [36] model,  $2 \times 10^{-5}$  m and  $30 \text{ kg/m}^3$  were taken for frost thickness and density as initial values, respectively. Tso et al [39] also modeled the frost characteristics based on the same philosophy. Some researchers such as Tao and Besant [40], Ismail and Salinas [41] and Chen et al [42] have developed one-dimensional transient frost formation models based upon the local volume averaging technique. Chen et al [42] have estimated an initial frost thickness of  $1 \times 10^{-4}$  m and an ice volume fraction of 30%. Therefore, these frost models (which are not empirical frost property correlations) are highly dependent on the initial conditions of the frost characteristics.

Most of the aforementioned researchers considered one-dimensional frost growth characterization using simple geometries such as horizontal and vertical cold flat surfaces for developing frost correlations. This is because empirical formulation of two- or three-dimensional frost properties such as frost density and thermal conductivity is time consuming, very expensive, and complex in nature, and involves lots of errors if performed on real heat exchangers. For instance, Chen et al [42, 43] reported a three-dimensional (x-, y- and z-positions) representation of frost distribution on a cold flat surface by using a special frost thickness measuring instrument with frost thickness uncertainty as high as 95%. A three-dimensional representation of frost distribution on air-coils is difficult to achieve due to the limitation of instrumentation. Hence, it is imperative to simplify frost characteristics by averaging frost thickness formed on a heat exchanger and assuming uniform frost density and thermal conductivity on cold air-coil surfaces.



In general, a lot of effort has been devoted to understand and develop fundamental correlations for frost properties based either on flat plates or round tubes rather than on a real heat exchanger. The current research, therefore, introduces unique frost property correlations in Chapter 4, which were developed based on a lab-scale flat-finned-tube heat exchanger (combination of flat plates and round tubes). A multi-linear regression analysis was employed on air inlet temperature and humidity ratio, frost-coil interface temperature, refrigerant inlet temperature, Reynolds and Fourier numbers, in order to develop mathematical expressions for frost thickness, density, thermal conductivity and air pressure drop across a frosted air-coil. The newly developed correlations will hopefully be useful to reasonably predict and control defrost periods and duration for medium-temperature (discharge air temperature  $-2^{\circ}\text{C}$ ) applications. They could also be incorporated in generic supermarket numerical models, such as developed by Getu and Bansal [10, 11] and the newly developed robust numerical model for medium-temperature secondary coolant refrigeration systems under the current project.

## **2.5. Secondary coolant systems**

The demand for secondary coolant (see Figure 1.3) refrigeration technology has grown in the last decade to tackle several problems encountered by supermarket owners, which are small profit margin, high energy cost, high refrigerant charge and environmental issues [44]. Direct/Multiplex refrigeration system (see Figure 1.1) is the most commonly employed configuration in supermarkets for providing refrigeration to display cabinets [10]. It consists of a rack (multiple compressors), air-cooled rooftop condenser and evaporators in the display cabinets [8]. The installation of long piping system, fittings and joints also cause huge refrigerant losses. Around 30% to 50% of the charge may be lost each year [45], resulting in higher costs. The refrigerant loss in turn results in high TEWI (total equivalent warming impact) necessitating the need for a secondary coolant system to fill this gap.

In addition to the reduction of leakage rates of the primary refrigerant, secondary coolant refrigeration systems effectively eliminate the long lengths of interconnecting piping through which the primary refrigerant flows. It also eliminates the need to use environmentally damaging

refrigerants. A secondary coolant refrigeration system can potentially reduce the refrigerant charge by up to 80% as compared with direct expansion refrigeration systems [46]. The circulation of refrigerated secondary coolant from an intermediate heat exchanger through the air-coils in the display cabinets has an advantage since the primary refrigerant will not be in contact with customers or employees of the store due to leakage. This refrigeration system, however, needs certain improvements such as higher effectiveness of the intermediate heat exchangers and display cabinet air coils for better heat transfer and minimized frictional losses.

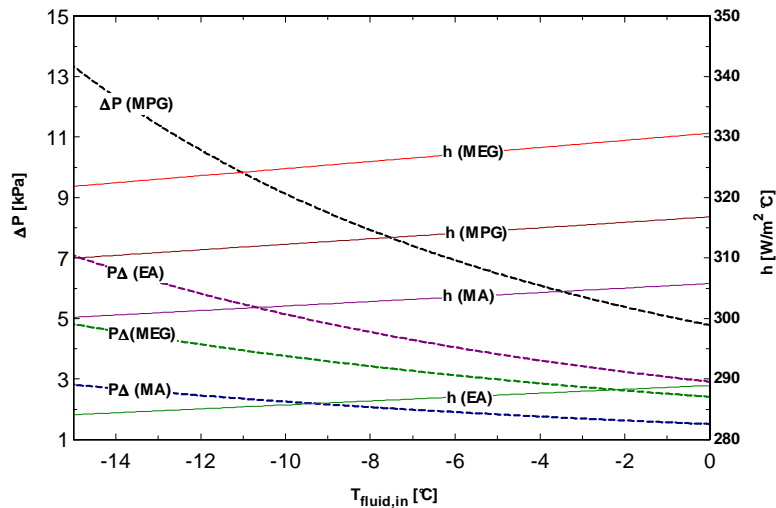
### **2.5.1. Selection of primary refrigerants**

A primary refrigerant is a phase changing fluid as it passes through different components of the primary loop which thermally couples the secondary coolant through the intermediate heat exchanger. Primary refrigerants could be CFCs, HCFCs, hydrocarbons (HCs), HFCs, ammonia (R717) and carbon dioxide (R744). However, CFCs and HCFCs are environmentally damaging refrigerants which have ozone depletion and global warming potentials, respectively. The promising refrigerants to be used in the primary loop of a secondary coolant system are the natural refrigerants such as HCs, R717 and R744. The problems of these refrigerants, especially, HCs and R717 are their - 1) flammability; 2) toxicity; 3) compatibility with materials of construction and oil [6]. Hence, primary refrigerants could be selected based on environmental, compatibility including thermophysical and transport issues. This thesis, however, has considered the use of R22 as a primary refrigerant solely for the purpose of validating the newly developed secondary coolant system model so that the validated model can be used to simulate any primary refrigerant.

### **2.5.2. Selection of secondary coolants**

A secondary coolant is a liquid which is used to thermally couple the primary refrigerant through the intermediate heat exchanger without changing its phase. The coolant can be divided into two categories, aqueous and non-aqueous solutions [6]. The aqueous solutions include ethylene and propylene glycol/water, ethyl alcohol/water, methyl alcohol/water, ammonia/water, chloride and

potassium salt solutions. The non-aqueous coolants include diethylbenzene mixtures, hydrocarbon mixtures, hydrofluoroether and polydimethylsiloxan. An appropriate selection of a secondary coolant includes several factors such as: - 1) toxicity; 2) thermophysical and transport properties; 3) compatibility with materials of construction and primary refrigerant; and 4) cost.



**Freezing temperature:** MPG = -20.8°C; MEG = -23.9°C; MA = -38.5°C; EA = -29.3°C.

**Concentration by mass:** 40% for all secondary refrigerants.

**Heat exchanger geometry and fluid velocity:**  $v_{ave} = 0.95$  m/s;  $A_{channel} = 1.813 \times 10^{-4}$  m<sup>2</sup>;  $L = 0.524$  m

Figure 2.2 Variation of pressure drop and heat transfer coefficient against inlet temperatures of various types of secondary coolants.

This section compares four types of secondary coolants such as monopropylene glycol/water (MPG), monoethylene glycol/water (MEG), methyl alcohol/water (MA) and ethylene alcohol/water (EA) mixtures based on their heat transfer coefficient and pressure drop in the intermediate heat exchanger. Figure 2-2 shows variation of the heat transfer coefficient and pressure drop as a function of the inlet temperature of the secondary coolant, whereas Figure 2.3 shows variation of secondary coolant pump power consumption as a function of the inlet temperature of the coolant. The freezing temperatures of the coolants were calculated following the library routines of EES [9].

The heat transfer coefficients, pressure drops and pumping power requirements of the secondary coolants in Figures 2.2 and 2.3 were calculated according to the following general equations so that the flow regimes could be selected based on Reynolds number.

The heat transfer coefficient was calculated by:

$$h = Nu_D \cdot \frac{k_{fluid}}{D_h} \quad 2-1$$

whereas the Nusselt number ( $Nu_D$ ) and the friction factor ( $f$ ) were determined following the correlations obtained from [47].

For  $Re_D \leq 3000$ ;

$$f = \frac{64}{Re_D} \quad 2-2$$

$$Nu_D = 3.66 + 0.0668 \cdot \left( \frac{D_h}{L} \right) \cdot Re_D \cdot \left( \frac{Pr_D}{1 + 0.41 \cdot ((D_h / L) \cdot Re_D \cdot Pr_D)^{2/3}} \right) \quad 2-3$$

However, the flow conditions, as give in Figure 2.2, correspond to turbulent flow where the corresponding correlations are used as given in Equations 2-4 and 2-5 below.

For  $3000 < Re_D < 10^6$ ;

$$f = 0.184 \cdot Re_D^{-1/5} \quad 2-4$$

$$Nu_D = 0.023 \cdot Re_D^{0.8} \cdot Pr_D^{1/3} \quad 2-5$$

The pressure drop was calculated by:

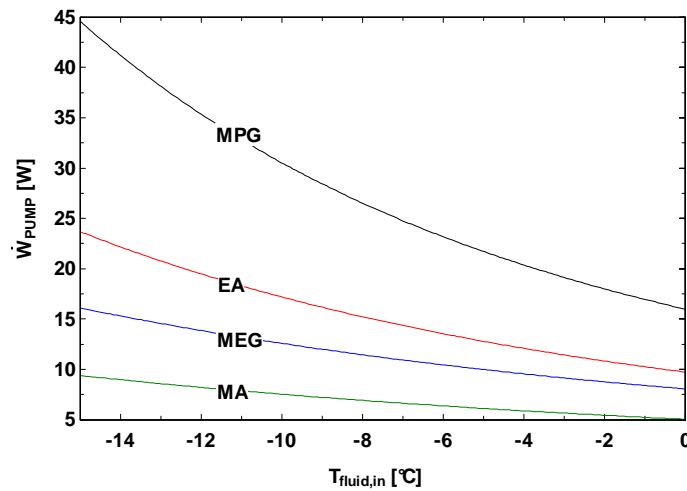
$$\Delta P = f \cdot \frac{L}{D_h} \cdot \frac{v_{avg}^2}{2} \cdot \rho_{fluid} \quad 2-6$$

The pump power was calculated from:

$$\dot{W}_{PUMP} = \dot{V} \cdot \Delta P$$

2-7

The maximum freezing temperature considered for the four secondary coolants was  $-20.8^{\circ}\text{C}$ , whereas the minimum was  $-38.5^{\circ}\text{C}$  at the same concentration (40% by mass). However, comparison of coolants could also be made by assigning different concentration for each coolant while fixing the same freezing temperature for all of them (e.g.  $-20.8^{\circ}\text{C}$ ). The cross-sectional area ( $A_{\text{channel}}$ ) and the length of a single channel ( $L$ ) in the intermediate heat exchanger were  $1.813 \times 10^{-4} \text{ m}^2$  and  $0.524 \text{ m}$ , respectively. The average velocity ( $v_{\text{ave}}$ ) in the heat exchanger was  $0.95 \text{ m/s}$ .



**Freezing temperature:** MPG =  $-20.8^{\circ}\text{C}$ ; EG =  $-23.9^{\circ}\text{C}$ ; MA =  $-38.5^{\circ}\text{C}$ ; EA =  $-29.3^{\circ}\text{C}$ .

**Concentration by mass:** 40% for all secondary refrigerants.

**Heat exchanger geometry and fluid velocity:**  $v_{\text{ave}} = 0.95 \text{ m/s}$ ;  $A_{\text{channel}} = 1.813 \times 10^{-4} \text{ m}^2$ ;  $L = 0.524 \text{ m}$

Figure 2.3 Variation of pump power consumption against inlet temperatures of various secondary coolants.

Generally, it can be observed from Figure 2.2 that the heat transfer coefficient increases, whereas the pressure drop decreases with an increase in fluid inlet temperature of the coolants. Monethylene glycol/water mixture (MEG) has the highest heat transfer coefficient while monopropylene glycol/water (MPG) and methyl alcohol/water mixtures (MA) have the highest

and the lowest pressure drops, respectively. However, MPG has better heat transfer coefficient than EA and MA. All in all, the above analysis indicates that there is always a tradeoff between heat transfer coefficient and pressure drop for specific operating conditions of a secondary coolant refrigeration system, i.e. higher heat transfer coefficient results in higher heat transfer, whereas higher pressure drop results in higher pumping power. Hence, monopropylene glycol/water (MPG) and monoethylene glycol/water mixtures (MEG) were selected for the current research based on safety, heat transfer coefficients, pumping power requirements and cost of the coolants.

Even though secondary coolant refrigeration systems have been in use in Sweden for around ten years, which is encouraging for the supermarket industry, there is limited research available in the open literature related to experimental and numerical studies of such systems. Kazachki [44] compared, experimentally, a traditional direct expansion refrigeration system with a secondary coolant refrigeration system and estimated that the annual energy consumption of the secondary coolant refrigeration system was lower than traditional direct expansion refrigeration system by 6.6 to 8.2% for lower condensing temperatures and degree of subcooling of the primary refrigerants. Inlow and Groll [48] presented a computer model for a secondary coolant refrigeration system employing ammonia as a primary refrigerant and carbon dioxide as a volatile secondary coolant in the secondary coolant circuit of the system. They reported that a trade-off between increased heat gains and pressure drops in the vapor and liquid lines existed. McDowell et al ([49] also presented a computer model of ammonia with a secondary coolant refrigeration system. They evaluated secondary coolants such as propylene glycol, ethylene glycol, mineral oil, ethanol, propane and a silicone-based heat transfer fluids revealing that the use of ammonia with propylene glycol as a secondary coolant would have a performance 4% at  $(-6^{\circ}\text{C})$  to 10% at  $(-29^{\circ}\text{C})$  lower than the performance of R22 with propylene glycol secondary coolant systems. Additionally, they revealed that the highest performance occurred when the exponent of the ratio of condensing pressure to evaporating pressure was between 0.5 and 0.6. They also predicted that the highest overall system performance occurred when the ratio of pump power to compressor power was between 0.01 and 0.03. Horton [46] presented complete secondary coolant system numerical models for both medium- and low-temperature applications

which included all component models except plate heat exchangers. The author also reported a higher coefficient of performance (COP) of secondary coolant systems, around 15% over traditional direct expansion refrigeration systems.

However, all of the aforementioned experimental and numerical studies on secondary coolant systems available in the open literature did not tackle frosting issues on the air-coils. Secondary coolant air-coils both for medium- and low-temperature application tend to be susceptible to frost formation due to fluid characteristics that often leads to deterioration of air-coil capacities. Hence, the effectiveness of the air-coils has been undermined. The other major issue lacking in the existing secondary coolant numerical models is the plate heat exchanger models. Plate heat exchangers are very suitable to thermally couple the primary and the secondary coolant. These plate heat exchangers are also suitable for condensing and subcooling of the primary refrigerant, which are vital to enhance the performance of the secondary coolant systems.

Therefore, notwithstanding several researchers reported that the secondary coolant refrigeration systems could perform better than traditional direct expansion refrigeration systems, the conclusion could not be convincing in the absence of an appropriate secondary coolant system model. A secondary coolant system model should include not only distribution lines, compressors, and coolant pumps but also individual independent models for frosted coils and plate heat exchangers since these components are the main contributors of the overall coefficient of performance (COP) of the system. This was the main motivation behind the current study on the secondary coolant refrigeration systems. Thus, the current medium-temperature secondary coolant model, which is extensively described in Chapter 5, adopted the most appropriate heat transfer, mass transfer and pressure drop correlations obtained from the open literature. The system components such as air-coil, plate heat exchangers, distribution lines, coolant pump and compressor were modeled independently so that a refrigeration engineer could evaluate the design parameters of each component for better component design and selection based on various secondary coolant and refrigerant for medium-temperature applications. In addition, the air-coil model incorporated the newly developed frost correlations for medium-temperature applications. Each component model in turn could be assembled to form a complete overall

secondary coolant refrigeration system model to enable a refrigeration engineer to evaluate the coefficient of performance (COP) of the system in total for additional improvements.

Additionally, the fundamentals of the test setup for the secondary coolant system including the instrumentation for data collection have been presented in Chapter 6. The collected experimental results have been used to validate the numerical models for system components leading to the validation of the overall system model. Finally, the application of the developed models has been discussed in Chapter 7.



## CHAPTER 3.

# Thermodynamic Analyses of an R744-R717 Cascade Refrigeration Systems

---

### 3.1. Introduction

The following sections discuss the thermodynamic analyses of cascade refrigeration systems in general and a carbon dioxide-ammonia (R744-R717) cascade refrigeration system in particular (as an example) to optimize the evaporating temperature of R717 and mass flow ratio, which can give the maximum COP of the system. A multilinear regression analysis was employed to develop mathematical expressions for maximum COP, optimum evaporating and condensing temperatures of the R717-cycle, and an optimum mass flow ratio in terms of sub-cooling, superheating, evaporating temperature, condensing temperature and temperature difference in cascade condenser of the system.

### 3.2. Thermodynamic analysis of a cascade system

The thermodynamic analysis of the two-stage cascade refrigeration system (see Figure 2.1) was performed based on the following general assumptions.

- i. Adiabatic compression with an isentropic efficiency of 0.78 for both high- and low-temperature compressors.
- ii. The change in isentropic efficiency as a function of the change in the pressure ratios (for the temperature range considered in the analysis) is negligible.
- iii. Negligible pressure and heat losses/gains in the pipe networks or system components.
- iv. Isenthalpic expansion of refrigerants in expansion valves.
- v. Negligible changes in kinetic and potential energy.

Table 3.1 Calculation of thermodynamic state points of R744-R717 cascade system using EES [9].

LOW-TEMPERATURE CIRCUIT			
Evaporator outlet	Compressor outlet	Condenser outlet	Expansion valve outlet
$P_1 = f(R1\$, T = T_E, x = 1)$	$P_2 = f(R1\$, T = T_{CAS,C}, x = 1)$	$P_3 = P_2$	$P_4 = P_1$
$T_1 = T_E + \Delta T_{sup}$	$T_2 = f(R1\$, P = P_2, h = h_2)$	$T_3 = T_{CAS,C} - \Delta T_{sub}$	$T_4 = T_E$
$h_1 = f(R1\$, T = T_1, P = P_1)$	$h_{s2} = f(R1\$, P = P_2, s = s_1)$	$h_3 = f(R1\$, P = P_3, T = T_3)$	$h_4 = h_3$
$s_1 = f(R1\$, T = T_1, P = P_1)$	$h_2 = (h_{s2} - h_1)/\eta_{isen} + h_1$		
HIGH-TEMPERATURE CIRCUIT			
$P_{1*} = f(R2\$, T = T_{CAS,E}, x = 1)$	$P_{2*} = f(R2\$, T = T_C, x = 1)$	$P_{3*} = P_{2*}$	$P_{4*} = P_{1*}$
$T_{1*} = T_{CASE} + \Delta T_{sup}$	$T_{2*} = f(R2\$, P = P_{2*}, h = h_{2*})$	$T_{3*} = T_C - \Delta T_{sub}$	$T_{4*} = T_{CAS,E}$
$h_{1*} = f(R2\$, T = T_{1*}, P = P_{1*})$	$h_{s2*} = f(R2\$, P = P_{2*}, s = s_{1*})$	$h_{3*} = f(R2\$, P = P_{3*}, T = T_{3*})$	$h_{4*} = h_{3*}$
$s_{1*} = f(R2\$, T = T_{1*}, P = P_{1*})$	$h_{2*} = (h_{s2*} - h_{1*})/\eta_{isen} + h_{1*}$		

The thermophysical properties of the refrigerants specified in this paper were calculated using a software package called an Engineering Equation Solver (EES) [9], which has built-in property functions of many refrigerants. In EES Software, the first argument of all built-in thermophysical property functions is the name of the substance. This argument is a string which may be provided as a string constant (e.g. R1\$ and R2\$) or a string variable. Many of the thermodynamic functions can take alternate sets of arguments. For example, the enthalpy function for steam can be accessed with temperature and pressure as arguments. In general, any valid set of arguments can be supplied for thermodynamic functions. If the values of enthalpy or entropy are known, but temperature or pressure is unknown, temperature or pressure functions can be used to calculate their respective values. The reference specific enthalpy and entropy were 200 kJ/kg and 1 kJ/kg K (according to IIR), respectively for all refrigerants. In view of the schematic and state points of Figure 2.1, the following sequence of equations was applied for the analysis.

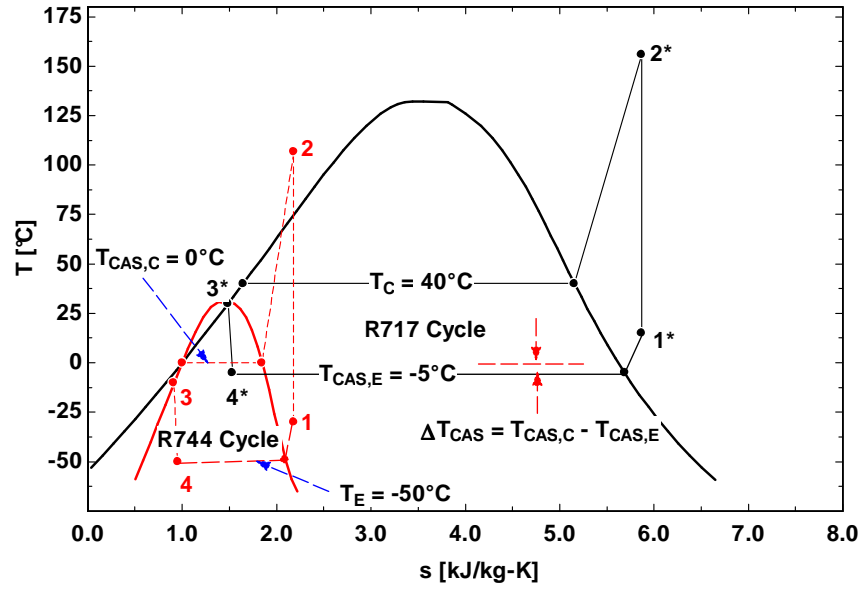


Figure 3.1 Carbon dioxide and Ammonia cycles on T-s property plots.

The capacity of the evaporator is defined by:

$$\dot{Q}_E = \dot{m}_L \times (h_1 - h_4) \quad 3-1$$

Compressor power consumption for high-temperature circuit is given by:

$$\dot{W}_H = \dot{m}_H \times (h_{2*} - h_{1*}) \quad 3-2$$

Where  $h_{2*}$  is calculated as a function of  $h_{s2*}$  (enthalpy calculated as a function of the compressor inlet entropy) and isentropic efficiency ( $\eta_{isen}$ ), as explicitly described in Table 3.1.

Whereas for low-temperature circuit it is given by:

$$\dot{W}_L = \dot{m}_L \cdot (h_2 - h_1) \quad 3-3$$

Where  $h_2$  is calculated as a function of  $h_{s2}$  (enthalpy calculated as a function of the compressor inlet entropy) and isentropic efficiency ( $\eta_{isen}$ ), as explicitly described in Table 3.1.

The rate of heat transfer in the cascade heat exchanger is determined from:

$$\dot{Q}_{CAS} = \dot{m}_L \cdot (h_2 - h_3) = \dot{m}_H \cdot (h_{1*} - h_{4*}) \quad 3-4$$

The mass flow ratio can be derived from Equation (3-4):

$$\dot{m}_H / \dot{m}_L = \frac{h_2 - h_3}{h_{1*} - h_{4*}} \quad 3-5$$

The rate of heat rejection by the air-cooled condenser is given by:

$$\dot{Q}_H = \dot{m}_H \cdot (h_{2*} - h_{3*}) \quad 3-6$$

The overall COP of the system is determined by:

$$COP = \frac{\dot{Q}_E}{\dot{W}_H + \dot{W}_L} \quad 3-7$$

The COP can also be defined solely as a function of specific enthalpies by substituting Equations 3-1 through 3-5 in Equation 3-7.

$$COP = \frac{(h_{1*} - h_{4*}) \cdot (h_1 - h_4)}{(h_{2*} - h_{1*}) \cdot (h_2 - h_3) + (h_{1*} - h_{4*}) \cdot (h_2 - h_1)} \quad 3-8$$

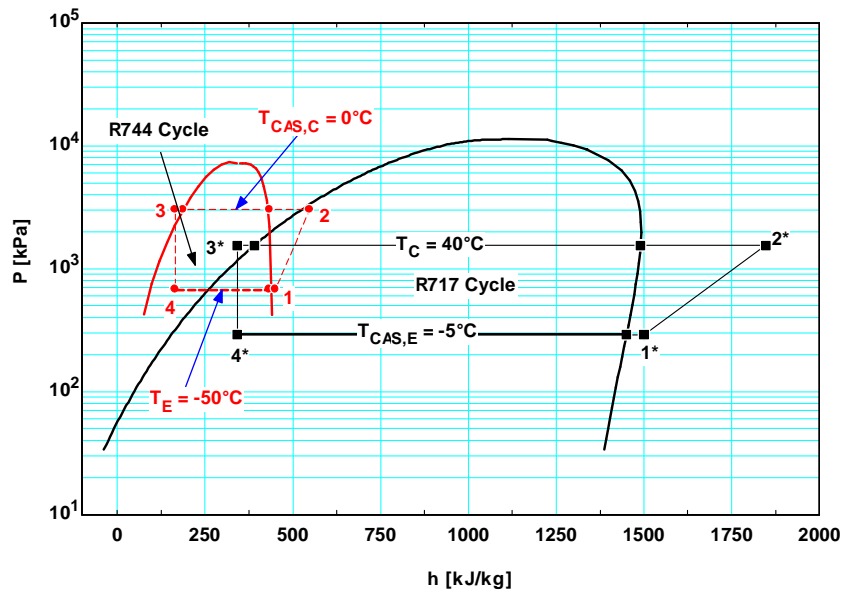


Figure 3.2 Carbon dioxide and Ammonia cycles on P-h property plots.

The calculation of the thermodynamic state points and properties such as pressures, temperatures, specific enthalpies and entropies of the carbon dioxide-ammonia (R744-R717) cascade system are given in Table 3-1, where R1\$ and R2\$ stand for the low-temperature (R744) and high-temperature (R717) refrigerants, respectively. Besides, the equations in Table 3-1 are generic and can be used for any other high- or low-stage refrigerants. The corresponding states points in saturated, superheated and subcooled regimes of the system are plotted in T-s and P-h diagrams in Figures 3.1 and 3.2, respectively, for constant operating conditions. Based on the above calculation scheme, the optimum evaporating temperature of R744 ( $T_{CAS,E,OPT}$ ), optimum mass flow ratio  $(\dot{m}_H \setminus \dot{m}_L)_{OPT}$  and the associated maximum overall COP ( $COP_{MAX}$ ) of the carbon dioxide-ammonia (R744-R717) cascade system were parametrically analysed as a function of subcooling, superheating, evaporating temperature, condensing temperature and temperature difference in the cascade condenser of the system.

### 3.3. High-temperature circuit refrigerant selection

Comparison of system performance and mass flow requirements was investigated for the high-temperature circuit of a two-stage cascade system for an appropriate refrigerant selection. Figures 3.3 and 3.4 depict variation of system COP for R717, R1270, R290 and R404A in the high-temperature circuit with R744 in the low-temperature circuit. The only difference between the two figures is the amount of degree of subcooling and superheat in the system. The evaporating temperature ( $T_{CAS,E}$ ) in the cascade heat exchanger was varied while keeping the other operating parameters such as, condensing temperature ( $T_C$ ), evaporating temperature ( $T_E$ ), temperature difference in cascade condenser, degree of subcooling and superheat constant. As can be seen from both figures, the maximum COP ( $COP_{MAX}$ ) of the system for the same given conditions is highest for ethanol and lowest for R404A. Zero degree of superheat (see Figure 3.5) has little effect on R1270 and R290, whereas it has higher effect on R717 and R404A. But, zero degree of subcooling has great impact on all of the high-temperature refrigerants. In general, degree of superheat alone reduces the overall performance of cascade systems, while degree of subcooling enhances the system performance. The overall performance of R717 is higher than R404A but lower than the other high-temperature circuit refrigerants.

The ratio of mass flow of the refrigerants in the high-temperature circuit to that of R744 in the low-temperature circuit was also compared in Figure 3.7. The use of R404A in the high-temperature circuit requires the highest mass flow ratio ranging from 2.7 to 3.1, whereas using R717 requires the lowest mass flow ratio (from 0.33 to 0.34) due to its high latent heat of vaporization. R1270 and R290 have very small differences both in terms of overall system COP and mass flow ratios. The performance of R290 and R1270 is higher than R717. This is purely because R290 and R1270 need lower vapor compression work than R717 for higher degree of subcooling and superheat.

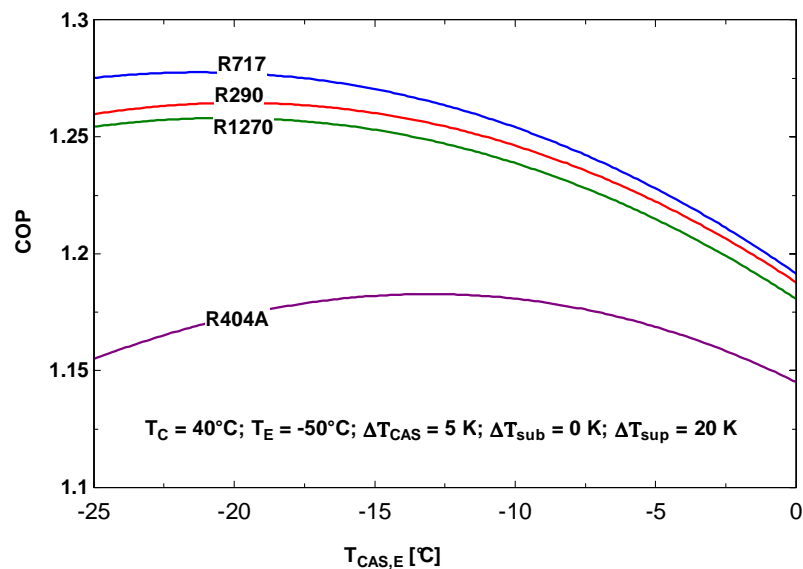


Figure 3.3 Variation of system performance for a subcooling of 0 K and superheat of 20 K in both circuits.

All in all, R717 still becomes the best choice to be used in the high-temperature circuit of a cascade refrigeration system. Hence, the remaining portion of this paper deals with the thermodynamic analysis of carbon dioxide-ammonia (R744-R717) cascade refrigeration systems.

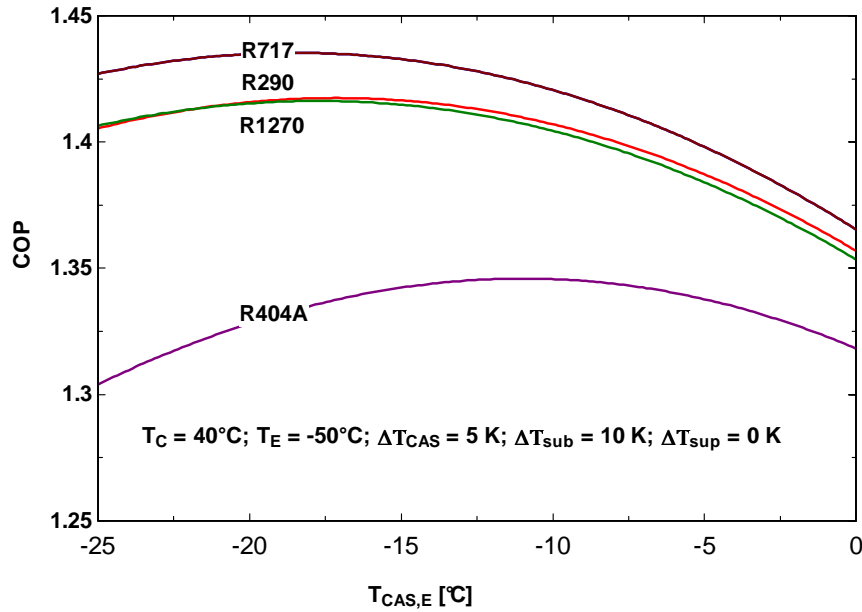


Figure 3.4 Variation of system performance for subcooling of 10 K and superheat of 0 K in both circuits.

### 3.4. Results and discussion of the analysis

#### 3.4.1. Effect of degree of subcooling and superheat

The effect of having different and the same degree of subcooling and superheat in both cycles of the carbon dioxide-ammonia (R744-R717) cascade system were separately and jointly analyzed keeping the other operating parameters constant. These parameters include condensing temperature of R717 ( $T_C = 40^{\circ}C$ ), evaporating temperature of R744 ( $T_E = -50^{\circ}C$ ), temperature difference in cascade condenser ( $\Delta T_{CAS} = 5$  K), evaporating temperature of R717 ( $T_{CAS,E} = -5^{\circ}C$ ) in the cascade condenser and isentropic efficiency of compressors (assuming the same isentropic efficiency in both cycles, i.e.  $\eta_{isen} = 0.78$ ).

##### 3.4.1.1. Effect of degree of subcooling

- i. **Subcooling in R744 cycle:** Degree of subcooling in this cycle was varied from 0 K to 10 K (see Figure 3.8) while keeping degree of subcooling and superheat in R717 cycle at 0 K. It

was observed that the COP of the system increased by higher amount (from 1.28 to 1.37) than in the case of R717 cycle (i.e. 1.28 to 1.31).

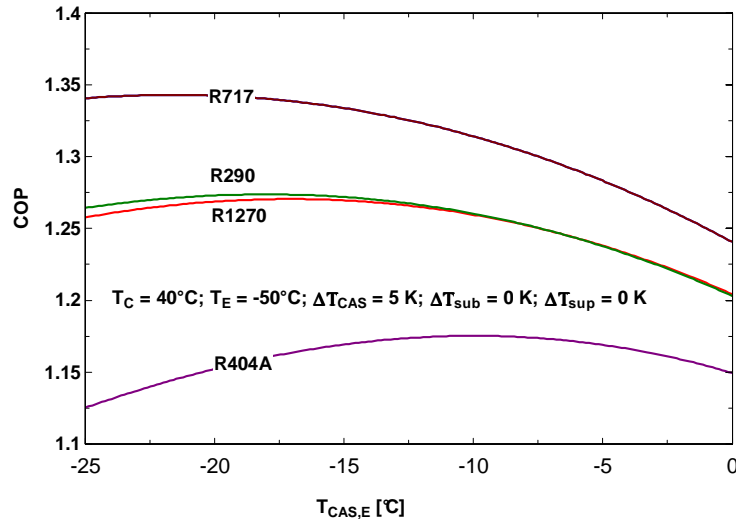


Figure 3.5 Variation of system performance for a subcooling of 0 K and superheat of 0 K in both circuits.

- ii. **Degree of subcooling in R717:** Degree of subcooling in the R717 was varied from 0 K to 10 K (see Figure 3.8) while holding the degree of subcooling and superheat in R744 at 0 K. The COP of the system increased but at much smaller amount (i.e. 1.28 to 1.31) than recorded for subcooling in both cycles (1.28 to 1.4) and in R744 cycle (1.28 to 1.37).
- iii. **Effect of the same degree of subcooling in R744 and R717 cycles:** Degree of subcooling in both cycles was varied simultaneously from 0 K to 10 K (see Figure 3.8) while holding the superheat at 0 K. This resulted in an increase in higher system COP, higher than the reference COP (1.28) by up to 9% for the specified operating conditions. Subsequently, the maximum COP of the system ( $COP_{MAX}$ ) for carbon dioxide-ammonia (R717-R744) cascade system with variation in R717 evaporating temperature ( $T_{CAS,E} = -25^{\circ}C$  to  $0^{\circ}C$ ) and degree of subcooling in both cycles is illustrated in Figure 3.9. The general trend is that the  $COP_{MAX}$  of each graph increases as the degree of subcooling increases, i.e. the  $COP_{MAX}$  rises from a value of 1.34 at  $\Delta T_{sub} = 0$  K by 3.4% and 6.9% at  $\Delta T_{sub} = 5$  K and  $\Delta T_{sub} = 10$  K, respectively. At the same time, the ratio of R717 mass flow to that of R744 increases



with a decrease in R717 evaporating temperature ( $T_{CAS,E}$ ), as shown in Figure 3.10. However, an increase in subcooling shifts the mass ratio graph upwards proportionally.

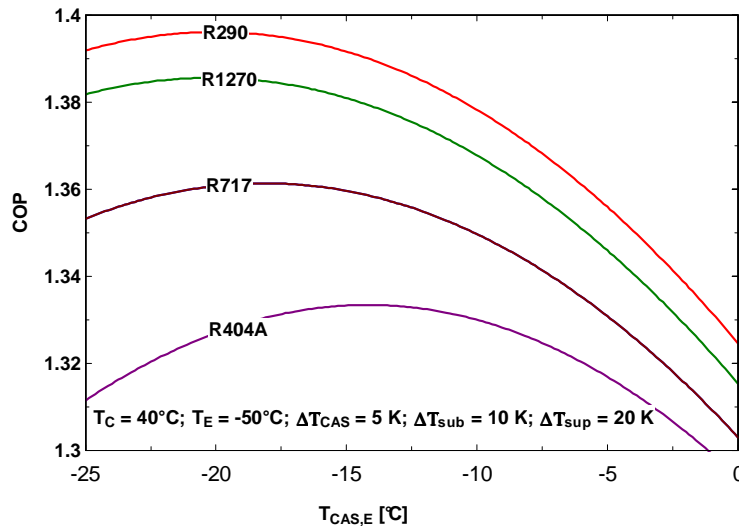


Figure 3.6 Variation of system performance for a subcooling of 10 K and superheat of 20 K in both circuits.

### 3.4.1.2. Effect of degree of superheat

- i. **Degree of superheat in R744 cycle:** Degree of superheat in R744 cycle was varied from 0 K to 20 K (see Figure 3.8) by keeping the degree of subcooling and superheat in R717 cycle at 0 K. This resulted in a decrease in COP of the system at lower amount than in the case of superheating in both cycles.
- ii. **Degree of superheat in R717 cycle:** Degree of superheat in R717 cycle was varied from 0 K to 20 K (see Figure 3.8) by keeping the degree of subcooling and superheat in R744 cycle at 0 K. It decreased COP of the system but showed negligible difference with the effect of degree of superheat in R744 cycle.
- iii. **Effect of the same degree of superheat in R744 and R717 cycles:** Degree of superheat in both cycles was varied from 0 K to 20 K (see Figure 3.8) fixing the degree of subcooling in both cycles at 0 K. Hence, it was evident from Figure 3.8 that superheat in both cycles reduced the overall COP of the cycle more dominantly than superheat in the individual cycles, i.e. it reduced the reference COP (1.28) by about 4.7%. On the other hand, Figure

3.11 depicts the change in the maximum COP of the system ( $COP_{MAX}$ ) at different values of superheat as the evaporating temperature in the cascade condenser ( $T_{CAS,E}$ ) is varied between  $(-25^{\circ}\text{C}$  to  $0^{\circ}\text{C}$ ). Superheat has the opposite effect of subcooling on  $COP_{MAX}$ , i.e  $COP_{MAX}$  shifts downward proportionally with an increase in superheat. It decreased from a value of 1.34 at  $\Delta T_{sup} = 0$  K by 2.6% and 4.9% at  $\Delta T_{sup} = 10$  K and  $\Delta T_{sup} = 20$  K, respectively. Nevertheless, superheat has similar effect on mass flow ratio as degree of subcooling (see Figure 3.12). The mass flow ratio increases with increasing degree of superheat.

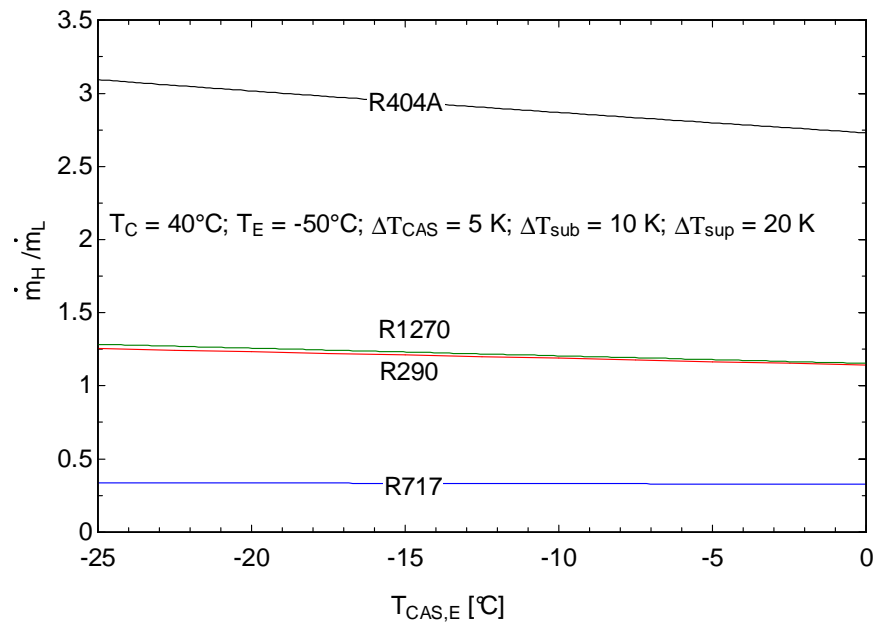


Figure 3.7 The ratio of high-temperature to low-temperature mass flow rates.

Generally, for specific operating conditions and the same isentropic efficiency of compressors in both cycles, Figure 3.8 shows that the  $COP_{MAX}$  of cascade systems lies in the region confined by the graphs of subcooling (in both cycles) in the upper bounds and superheating (in both cycles) in the lower bounds for any of such systems. Therefore, the same degree of subcooling and superheating in both cycles gives an average COP of the cascade refrigeration systems.

### 3.4.2. Effect of condensing, evaporating and differential temperatures

Figure 3.13 depicts the variation of COP for change in condensing ( $T_C$ ), evaporating in the low-temperature circuit ( $T_E$ ), cascade evaporating ( $T_{CAS,E}$ ) and difference in cascade condenser ( $\Delta T_{CAS}$ ) temperatures. Condensing temperature was first varied from  $20^0\text{C}$  to  $50^0\text{C}$ , while the other temperatures such as evaporating temperature ( $T_E = -50^0\text{C}$ ), temperature difference ( $\Delta T_{CAS} = 5\text{ K}$ ) in cascade condenser, cascade evaporating temperature ( $T_{CAS,E} = -5^0\text{C}$ ) in cascade condenser, subcooling ( $\Delta T_{sub} = 10\text{ K}$ ) and superheat ( $\Delta T_{sup} = 20\text{ K}$ ) were held constant. Then, the evaporating temperature was varied from  $(-) 25^0\text{C}$  to  $(-) 55^0\text{C}$  by keeping condensing temperature ( $T_C = 40^0\text{C}$ ), temperature difference in cascade condenser ( $\Delta T_{CAS} = 5\text{ K}$ ), cascade evaporating temperature ( $T_{CAS,E} = -5^0\text{C}$ ) in cascade condenser, subcooling ( $\Delta T_{sub} = 10\text{ K}$ ) and superheat ( $\Delta T_{sup} = 20\text{ K}$ ) constant.

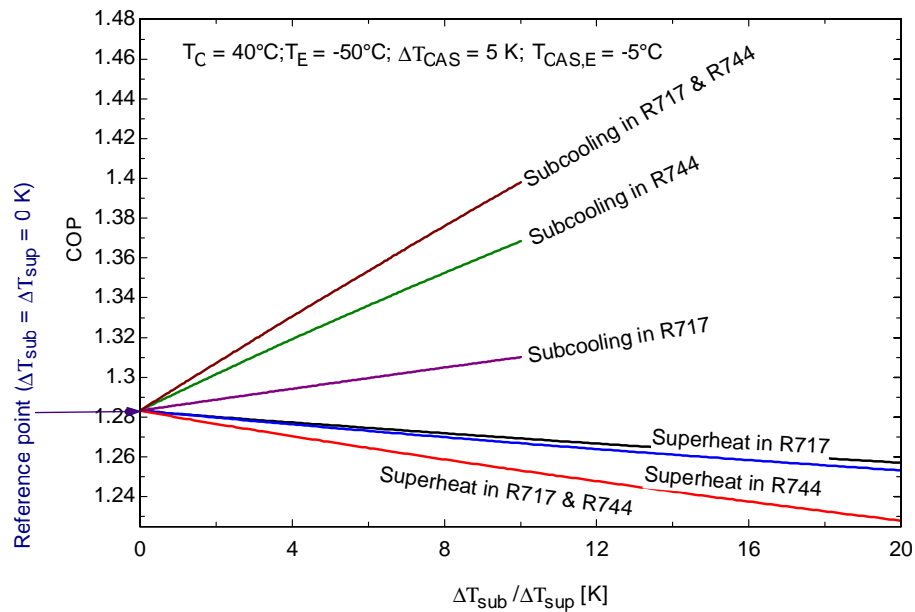


Figure 3.8 Effect of superheating and subcooling on system and individual cycles.

Next, the temperature difference in cascade condenser was varied from  $0^0\text{C}$  to  $10^0\text{C}$  by holding condensing ( $T_C = 40^0\text{C}$ ), evaporating ( $T_E = -50^0\text{C}$ ), cascade evaporating temperature ( $T_{CAS,E} = -5^0\text{C}$ ) in cascade condenser, subcooling ( $\Delta T_{sub} = 10\text{ K}$ ) and superheat ( $\Delta T_{sup} = 20\text{ K}$ ) constant. Lastly, the cascade evaporating temperature ( $T_{CAS,E}$ ) was varied between  $-25^0\text{C}$  and  $0^0\text{C}$  by

fixing condensing ( $T_C = 40^\circ\text{C}$ ), evaporating ( $T_E = -50^\circ\text{C}$ ), temperature difference in cascade condenser ( $\Delta T_{\text{CAS}} = 5 \text{ K}$ ), degree of subcooling ( $\Delta T_{\text{sub}} = 10 \text{ K}$ ) and superheat ( $\Delta T_{\text{sup}} = 20 \text{ K}$ ) constant. As expected a rise in condensing temperature and temperature difference in cascade condenser resulted in a decrease in COP, whereas the increase in evaporating temperature resulted in much higher performance of the system. However, the cascade evaporating temperature ( $T_{\text{CAS,E}}$ ) graph showed that there was an optimum temperature at which the COP of the system was maximum.

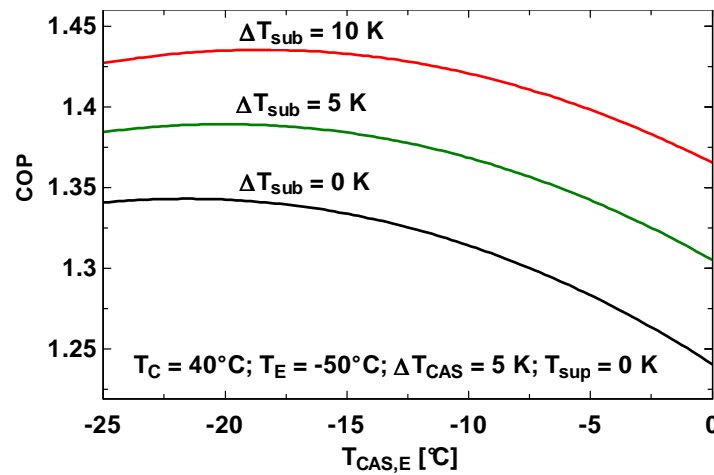


Figure 3.9 System performance curve for R744-R717 with variation in R717 evaporating temperature and degree of subcooling on both cycles.

The same temperature values were also used to analyze the variation of the mass flow ratio of R717 to that of R744 (see Figure 3.14). The mass ratio increased with rise in condensing temperature. However, it decreased with an increase in evaporating temperature of R744 ( $T_E$ ), cascade evaporating temperature ( $T_{\text{CAS,E}}$ ) and temperature difference in cascade condenser ( $\Delta T_{\text{CAS}}$ ) of the system. It is worth mentioning here that an increase in temperature difference in cascade condenser does not always decrease mass flow ratio, since it generally depends on the operating conditions of the cascade system.

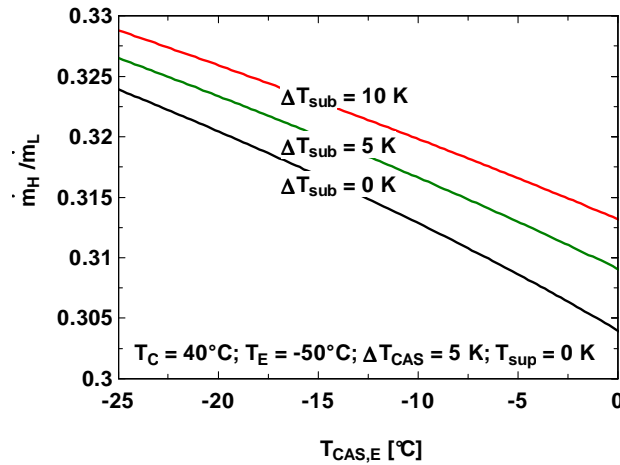


Figure 3.10 Variation of R744-R717 mass ratios with change in R717 evaporating temperature and degree of subcooling in both R744 and R717 cycles.

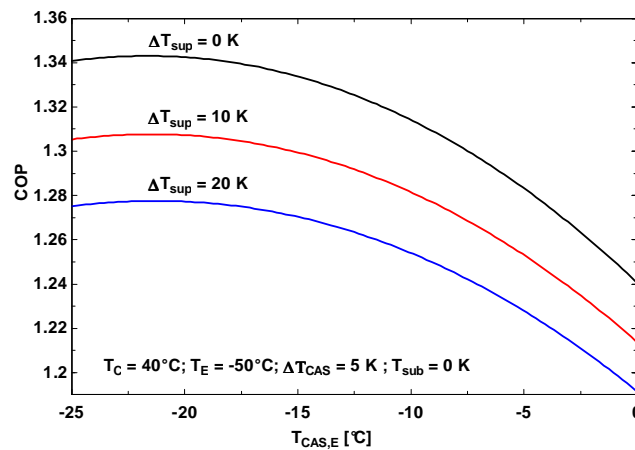


Figure 3.11 Variation of R744-R717 system COP with change in R717 evaporating temperature and degree of superheat in both R744 and R717 cycles.

### 3.4.3. Effect of isentropic efficiencies of compressors

The variation isentropic efficiencies in both cycles (see Figure 3.15 and 3.16) on a carbon dioxide-ammonia (R744-R717) cascade system was studied keeping the other operating parameters constant. However, different degrees of subcooling and superheat for individual and overall system cycles were considered for the following three conditions.

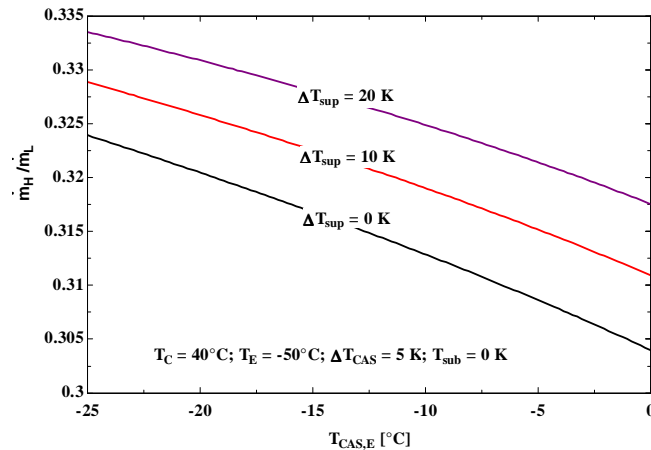


Figure 3.12 Variation of R744-R717 mass ratios with respect to change in superheat.

- i. **Varying isentropic efficiency in R744:** To study the effect of various isentropic efficiency in R744 cycle the constant parameters were the cascade condensing temperature of R717 ( $T_{CAS,C} = -10^0C$ ), evaporating temperature R744 ( $T_E = -50^0C$ ), subcooling ( $\Delta T_{sub} = 10$  K), superheat ( $\Delta T_{sup} = 20$  K) and isentropic efficiency of R717 ( $\eta_{NH3} = 0.8$ ). This scenario shows that for the given operating parameters, an increase in isentropic efficiency of R744 ( $\eta_{CO2} = 0.5$  to  $1.0$ ) results in an increase in system COP from 1.05 to 1.57, which is about 50%.

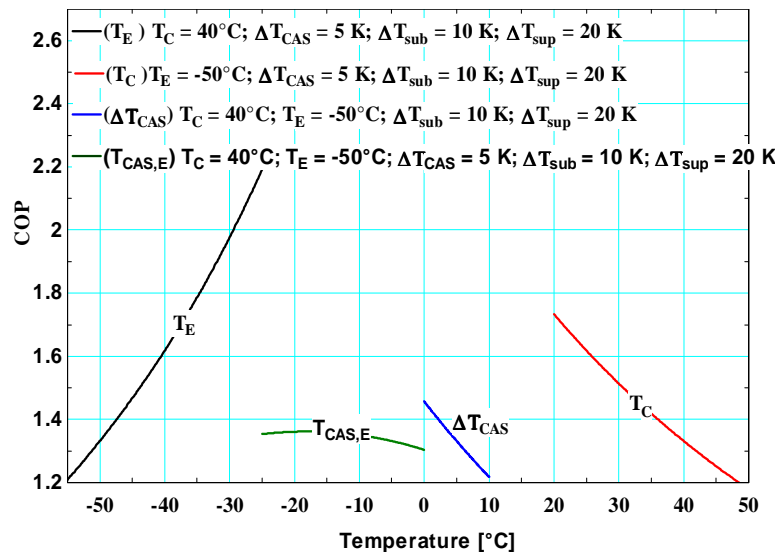


Figure 3.13 Effect of condensing, evaporating and differential temperatures on system performance.

- ii. **Varying isentropic efficiency in R717:** Similarly, the effect of isentropic efficiency in R717 cycle was also studied by taking condensing temperature of R717 ( $T_C = 40^\circ\text{C}$ ), cascade evaporating temperature of R717 ( $T_{\text{CAS,E}} = -15^\circ\text{C}$ ), subcooling ( $\Delta T_{\text{sub}} = 5 \text{ K}$ ), superheat ( $\Delta T_{\text{sup}} = 15 \text{ K}$ ) and isentropic efficiency of R744 ( $\eta_{\text{CO}_2} = 0.8$ ). An increase in isentropic efficiency of R717 ( $\eta_{\text{NH}_3} = 0.5$  to  $1.0$ ) also results in an increase in system COP from 1.0 to 1.57 (about 50%). However, its difference with the case in (i) is very negligible. This leads to a conclusion that considering the same isentropic efficiency for both cycle compressors is reasonable and simplifies the calculation of system COP.

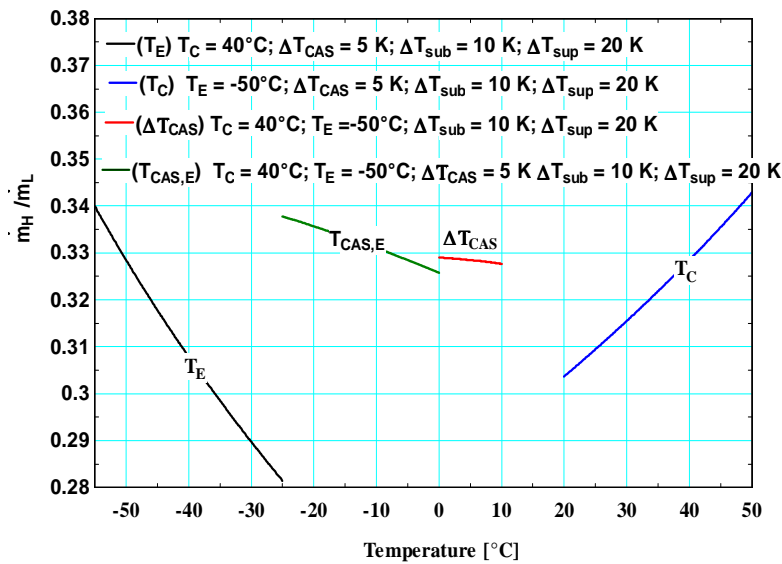


Figure 3.14 Effect of condensing, evaporating and differential temperatures on mass ratio.

- iii. **The same isentropic efficiency in R717 and R744:** The evaporating temperature of R744 ( $T_E = -50^\circ\text{C}$ ), condensing temperature of R717 ( $T_C = 40^\circ\text{C}$ ), temperature difference in cascade condenser ( $\Delta T_{\text{CAS}} = 5 \text{ K}$ ), and degree of subcooling ( $\Delta T_{\text{sub}} = 10 \text{ K}$ ) and superheat ( $\Delta T_{\text{sup}} = 20 \text{ K}$ ) in both circuits were held constant while the cascade evaporating temperature ( $T_{\text{CAS,E}}$ ) was varied between  $0^\circ\text{C}$  and  $(-25)^\circ\text{C}$  in order to investigate the effect of isentropic efficiencies of the compressors. Figure 3.16 showed that there was a linear relationship between isentropic efficiency ( $\eta_{\text{isen}}$ ) of carbon dioxide-ammonia (R744-R717) cascade compressors and the overall COP of the system. The maximum COP from 1.2 at an isentropic efficiency of 70% increased to 1.4 and 1.6 for isentropic efficiencies of 80% and

90%, respectively. The optimum cascade evaporating temperature also increased almost linearly from (–) 18.6°C at an isentropic efficiency of 70% to (–) 18.0°C and (–) 17.6°C for isentropic efficiencies of 80% and 90%, respectively.

#### 3.4.4. Multilinear regression analysis

So far the effects of various temperatures on the performance of the carbon dioxide-ammonia (R744-R717) cascade system have been observed. It is therefore imperative to develop mathematical equations as a guide for setting optimum thermodynamic design parameters at which maximum COP at a given capacity are achieved. With multilinear regression method, the optimum evaporating temperature of R717 ( $T_{CAS,E,OPT}$ ), the optimum mass flow ratio of R717 to that of R744 ( $(\dot{m}_H / \dot{m}_L)_{OPT}$ ) and the maximum coefficient of performance ( $COP_{MAX}$ ) of the cascade system were regressed as a function of the input data such as subcooling ( $\Delta T_{sub}$ ), superheating ( $\Delta T_{sup}$ ), evaporating ( $T_E$ ), condensing ( $T_C$ ), difference in cascade heat exchanger temperatures ( $\Delta T_{CAS}$ ) and a fixed value of 0.78 for isentropic efficiency of compressors in both circuits. The development of the regressed equations included the calculation of 2673 data sets, which were later reduced to 243 since one optimum value for  $COP_{MAX}$  was calculated based on 11 cascade evaporating temperature data points.

The resulted optimum cascade evaporating temperature, the maximum COP and the optimum mass ratio ( $(\dot{m}_H / \dot{m}_L)_{OPT}$ ) of R717 to R744 are respectively given by:

$$T_{CAS,E,OPT} = a_0 + a_1 \cdot \Delta T_{sup} + a_2 \cdot T_C + a_3 \cdot T_E + a_4 \cdot \Delta T_{CAS} + a_5 \cdot \Delta T_{sub} \quad 3-9$$

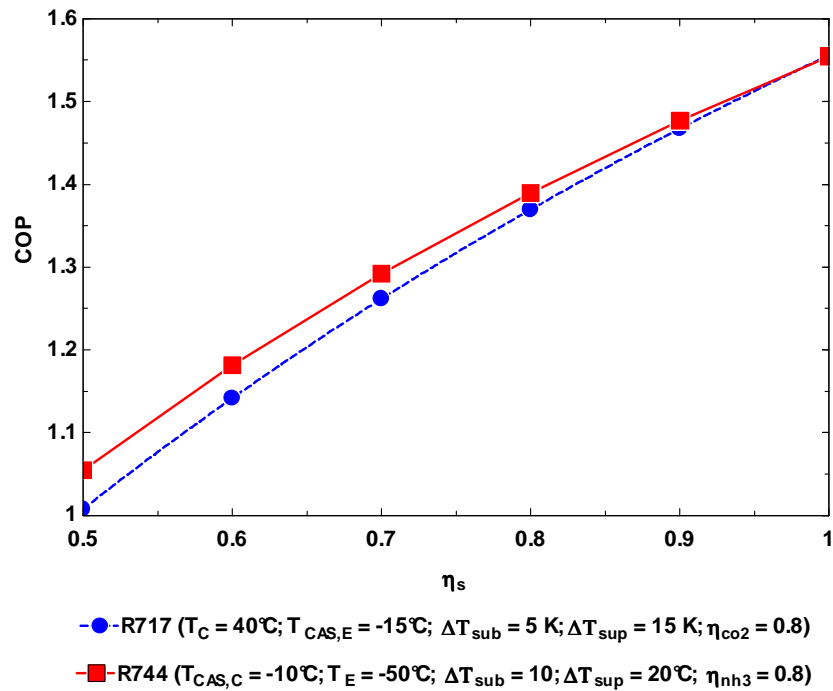
$$COP_{MAX} = a_0 + a_1 \cdot \Delta T_{sup} + a_2 \cdot T_C + a_3 \cdot T_E + a_4 \cdot \Delta T_{CAS} + a_5 \cdot \Delta T_{sub} \quad 3-10$$

$$(\dot{m}_H / \dot{m}_L)_{OPT} = a_0 + a_1 \cdot \Delta T_{sup} + a_2 \cdot T_C + a_3 \cdot T_E + a_4 \cdot \Delta T_{CAS} + a_5 \cdot \Delta T_{sub} \quad 3-11$$



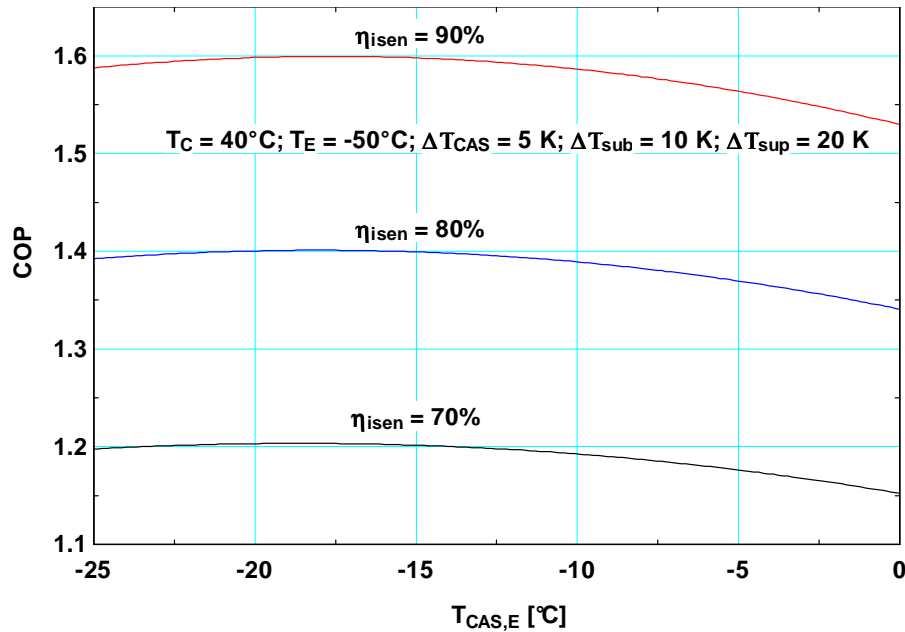
By adding the cascade temperature difference ( $\Delta T_{CAS}$ ) to Equation 3-9, the optimum cascade condensing temperature can be given by Equation 3-12. The values of all the coefficients ( $a_{[0..5]}$ ) in Equation 3-12 are the same as in Equation 3-9.

$$T_{CAS,C,OPT} = a_0 + a_1 \cdot \Delta T_{sup} + a_2 \cdot T_C + a_3 \cdot T_E + (a_4 + 1) \cdot \Delta T_{CAS} + a_5 \cdot \Delta T_{sub} \quad 3-12$$



### 3.15 Effect of having different isentropic efficiencies in the compressors of both cycles.

The linear regression coefficients ( $a_{[0..5]}$ ) of Equation 3-9 through 3-12 are given in Table 3-2 along with other statistical indicators such as standard error, root mean square error (rms), and correlation coefficient ( $R^2$ ). The coefficients have been given in four significant decimal digits since having less number of decimal digits affects especially the values of  $COP_{MAX}$  and the optimum mass flow ratio  $(\dot{m}_H \setminus \dot{m}_L)_{OPT}$ .



3.16 Effect of isentropic efficiency with change in R717 evaporating temperature assuming the same isentropic efficiency in the compressors of both cycles.

Equations 3-9 through 3-12 could be modified to account for any change in isentropic efficiency of both compressors (ammonia and carbon dioxide compressors). This can be done based on the explanation given in Section 3.4.3 (ii) and the graphs depicted in Figure 3.16. In other words, for any change in isentropic efficiency between 70% and 90%, and for any change in the thermodynamic variables, the change in  $COP_{MAX}$  will be linear and can be obtained by interpolation between these graphs. Similarly, the optimum cascade evaporating temperature ( $T_{CAS,E,OPT}$ ) also increases linearly with an incremental of  $0.6^\circ\text{C}$  for every 10% increase in isentropic efficiency of both compressors. The same is true for the optimum cascade condensing temperature ( $T_{CAS,C,OPT}$ ) since it is calculated by adding the cascade temperature difference ( $\Delta T_{CAS}$ ) to the optimum cascade evaporating temperature ( $T_{CAS,E,OPT}$ ). The optimum mass flow ratio (following any change in the isentropic efficiency and the thermodynamic variables) will then be calculated using Equation 3-5 based on the modified optimum cascade evaporating and condensing temperatures.

The statistical terms employed for the regression analyses are defined in the following sequence of equations. The standard error ( $a\_stderr_{[0..5]}$ ) is the standard error of the curve fit parameters defined as the square root of the estimated variance of the parameter. The smaller the standard error the more precise is the estimator. The root mean square error is defined as:

$$rms = \sqrt{\frac{1}{n} \cdot \sum_{i=1}^n (y_i - \hat{y}_i)^2} \quad 3-13$$

where  $n$  is the number of data points (243), and  $\hat{y}_i$  is the  $i^{\text{th}}$  estimated value of  $y_i$  (i.e.,  $T_{\text{CAS,E,OPT}}$ ,  $\text{COP}_{\text{MAX}}$ ,  $(\dot{m}_H / \dot{m}_L)_{\text{OPT}}$ , and  $T_{\text{CAS,C,OPT}}$ ) from Equation 3-9 through 3-12.  $R^2$  can be interpreted as the proportion of the total variation in  $y_{[1..n]}$  that is accounted for by the predictor variable  $x_{[1..n]}$  (i.e.,  $\Delta T_{\text{sup}}$ ,  $T_C$ ,  $T_E$ ,  $\Delta T_{\text{CAS}}$ , and  $\Delta T_{\text{sub}}$ ) and it is given by:

$$R^2 = \frac{\sum_{i=1}^n (\hat{y}_i - \bar{y})^2}{\sum_{i=1}^n (y_i - \bar{y})^2} \cdot 100\% \quad 3-14$$

Table 3.2 Statistical information for Equations 3-9 through 3-12.

Linear regression coefficients for $T_{\text{CAS,E,OPT}}$			Linear regression coefficients for $\text{COP}_{\text{MAX}}$		Linear regression coefficients for $(\dot{m}_H / \dot{m}_L)_{\text{OPT}}$	
	Value	standard error	Value	standard error	Value	standard error
$a_0$	-7.0992	0.18328	3.9207	0.03774	0.1610	0.00063
$a_1$	0.0215	0.00508	-0.0034	0.00105	0.0005	0.00002
$a_2$	0.2662	0.00254	-0.0235	0.00053	0.0013	0.00000
$a_3$	0.4602	0.00254	0.0298	0.00052	-0.0022	0.00000
$a_4$	-0.4264	0.01269	-0.0299	0.00261	0.0001	0.00004
$a_5$	0.2945	0.00846	0.0106	0.00174	0.0004	0.00003
Number of points (n) = 243			Number of points (n) = 243		Number of points (n) = 243	
rms = 0.32298			rms = 0.06651		rms = 0.001107	
$R^2 = 99.48\%$			$R^2 = 95.76\%$		$R^2 = 99.92\%$	

The usefulness of the above unique equations (Equation 3-9 through 3-12) is that for any given design and operating parameters such as refrigeration capacity, isentropic efficiency and various temperatures, these equations enable a design engineer to determine the ideal maximum COP and mass flow requirements of carbon dioxide-ammonia (R744-R717) cascade refrigeration system.

### 3.5. Economic benefits of the new thermodynamic correlations

There are lots of economic benefits in using cascade refrigeration systems for supermarket applications apart from the negative aspect of the initial installation cost being higher than the traditional direct expansion systems [14]. The economic benefits of cascade systems are the use of natural refrigerants, less refrigerant charge, reduced environmental impact and life cycle costs. In addition to the above well understood benefits, the newly developed thermodynamic correlations could potentially lead to energy savings by a significant amount due to increased efficiency.

In order to understand the economic benefits of the new correlations, for example, consider a supermarket display cabinet line-up having a load of 100 kW, charged with R717 and R744, operating at  $T_C = 40^0\text{C}$ ,  $T_E = -50^0\text{C}$ ,  $\Delta T_{CAS} = 5\text{ K}$ ,  $T_{CAS,E} = -5^0\text{C}$ ,  $\Delta T_{sub} = 10^0\text{C}$ ,  $\Delta T_{sup} = 20^0\text{C}$ , and isentropic efficiency of compressors in both cycles being 0.78. Hence, the power consumption of the system using the above inputs from using non-optimum values will be 75 kW. However, using the thermodynamic correlations developed in this research (e.g. Equation 3-9), the optimum evaporating temperature of R717 can be calculated to be  $-18.2^0\text{C}$  (by taking the same inputs such as  $T_C = 40^0\text{C}$ ,  $T_E = -50^0\text{C}$ ,  $\Delta T_{CAS} = 5\text{ K}$ ,  $\Delta T_{sub} = 10^0\text{C}$ ,  $\Delta T_{sup} = 20^0\text{C}$  and assuming the isentropic efficiency of the compressors in both cycles to be 0.78). Just by operating the system at this optimum temperature ( $-18.2^0\text{C}$ ) rather than at  $T_{CAS,E} = -5^0\text{C}$ , a reduced power consumption of 73 kW will be achieved, leading to energy saving of 2 kW (i.e.  $75-73 = 2\text{ kW}$ ). In other words, the energy saving from a single supermarket will be around 17520kWh/year. This illustrates the economic benefit of the new thermodynamic correlations.

In conclusion, the thermodynamic analysis of the cascade refrigeration system, operating at (-) 50<sup>0</sup>C (evaporating) and 40<sup>0</sup>C (condensing) temperatures resulted in the introduction of four new empirical correlations which could be vital for the optimization of thermodynamic parameters of carbon dioxide-ammonia (R744-R717) cascade refrigeration system before implementing any test setup or prototype systems. The new thermodynamic correlations are expected bring about energy savings if used to calculate the optimum operating points of the system. However, a separate study is warranted to conceptualize and evaluate all the related matters such as social, environmental and economic benefits of the cascade supermarket refrigeration systems. Additionally, the calculation steps developed are generic in nature and can also be used to conduct thermodynamic analyses for other refrigerants. The analyses were carried out independent of the development of frost characteristics correlations and a second secondary coolant studies discussed in the chapters that follow.

## CHAPTER 4.

# New Frost Property Correlations

### 4.1. Introduction

This chapter presents unique frost property correlations which were developed based on a lab-scale flat-finned-tube heat exchanger (combination of flat plates and round tubes). A multi-linear regression analysis was employed on air inlet temperature and humidity ratio, frost-coil interface temperature, refrigerant inlet temperature, Reynolds and Fourier numbers, in order to develop mathematical expressions for frost thickness, density, thermal conductivity and air pressure drop across a frosted air-coil. The newly developed correlations will hopefully be useful to reasonably predict and control defrost periods and duration for medium-temperature ( $-10^{\circ}\text{C}$ ) applications. They could also be incorporated in generic supermarket numerical models, such as developed by Getu and Bansal [10, 11].

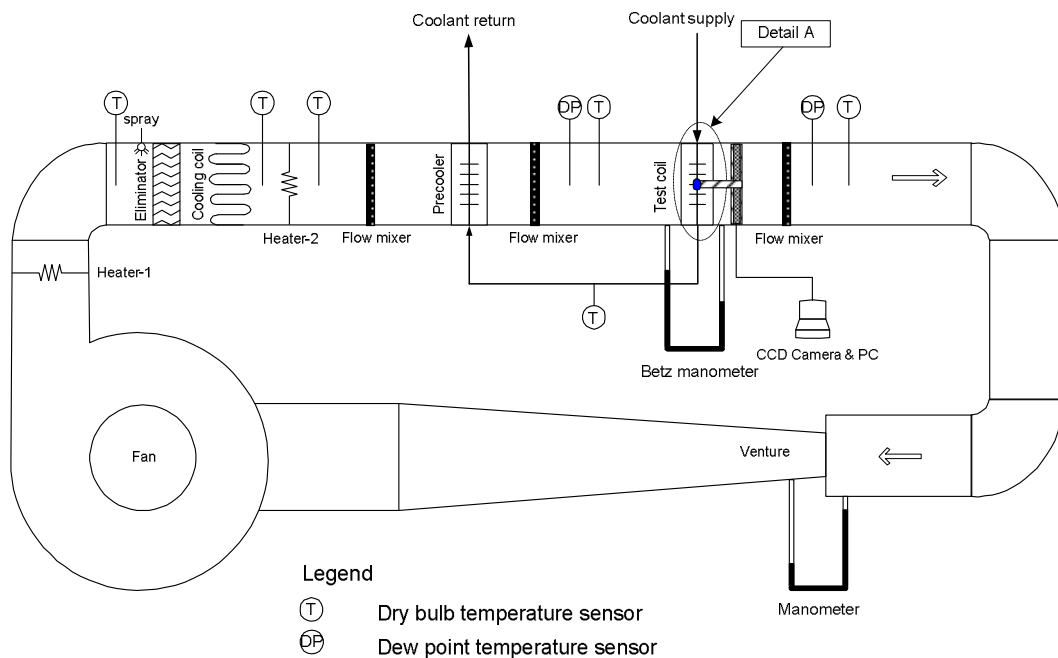


Figure 4.1 Experimental test rig.

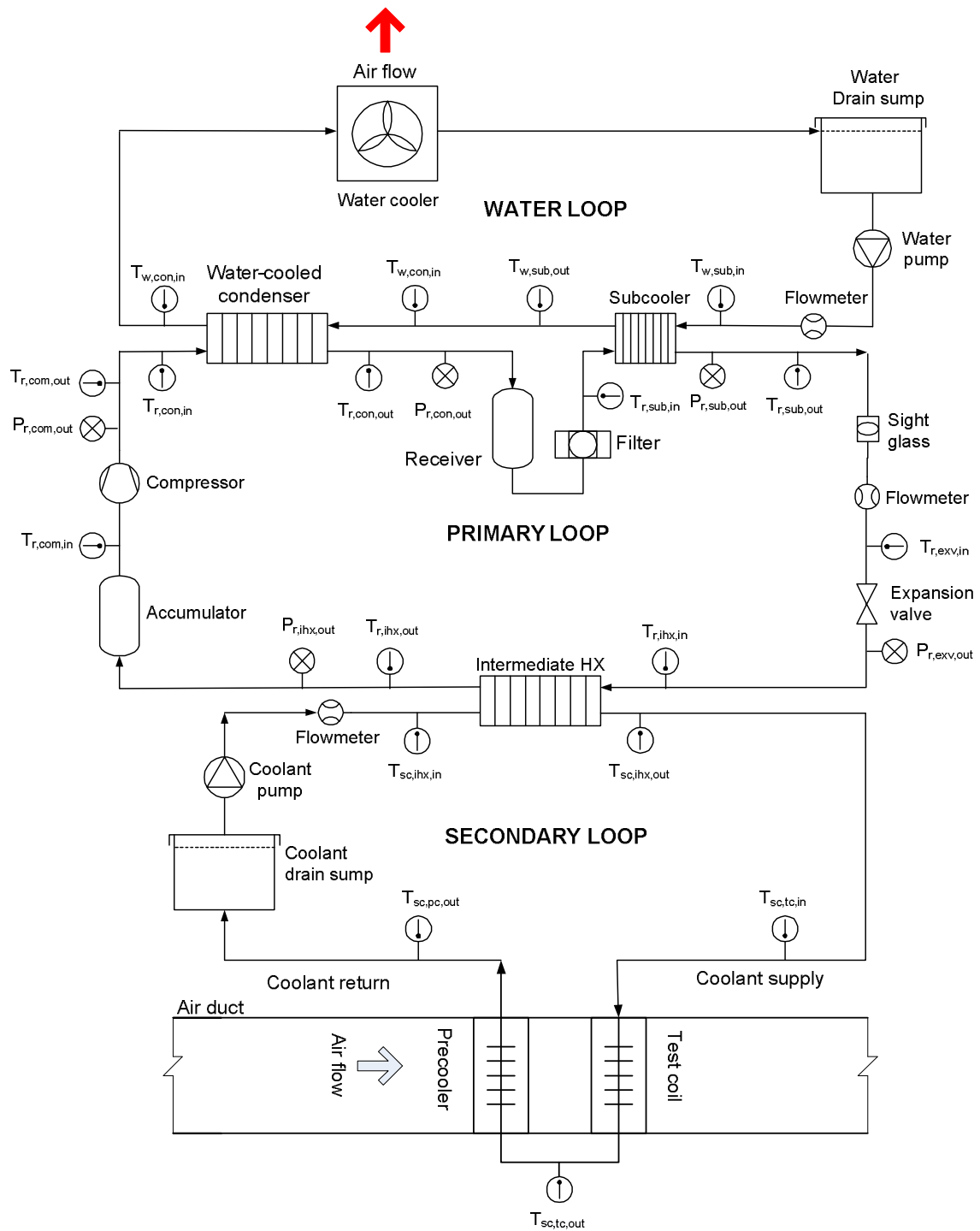


Figure 4.2 Layout of secondary coolant system model and instrumentation.

## 4.2. Test rig setup and measurements

Lab-scale experiments on frost characteristics were carried out using a modified existing air-conditioning test rig shown in Figure 4.1. The air-conditioning unit was coupled with an existing heat pump constructed by Purkayastha and Bansal [50] and Bansal and Purkayastha [51]. The heat pump was converted into a secondary coolant system (see Figure 4.2) to supply a chilled coolant (Mono-propylene and Mono-ethylene glycol/water mixtures with a concentration of 52% and 42% by weight, respectively) to a newly designed and built flat-finned-tube heat exchanger (test coil) whose configuration is shown in Figure 4.3. The secondary coolant system test rig in Figure 4.2 has been extensively discussed in Chapter 6 (Validation of Secondary Coolant Refrigeration System Numerical Model) along with the details of the instrumentation since this section mainly focuses on the test coil.

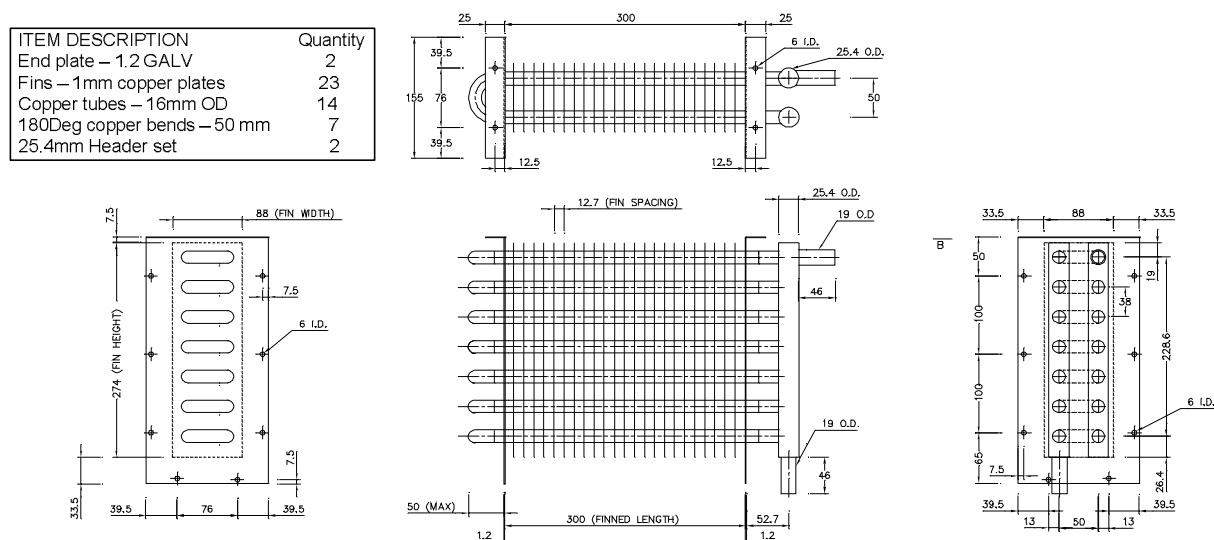


Figure 4.3 Detail A: Test coil design for frost experiment.

Air was circulated in a closed loop in the air-conditioning test rig (see Figure 4.1), which was insulated with a 25 mm thick Thermobreak insulation ( $k=0.032\text{W/m K}$ ). The duct was mounted with a flow nozzle in order to measure the flow rate of the air. The average frost-coil interface



temperature ranged from  $(-)\ 12.8^{\circ}\text{C}$  to  $(-)\ 2.6^{\circ}\text{C}$  whereas the average dry bulb temperature of the circulated air at the leading edges of the heat exchanger fins ranged from  $(-)\ 4.5^{\circ}\text{C}$  to  $4.9^{\circ}\text{C}$ . The average air velocity was varied between 1.8 and 2.5 m/s. The temperature and humidity ratio of the incoming air were regulated by the air conditioning unit which consisted of heaters, a spray, a cooling coil and a pre-cooler. The dew-point temperatures of the air both at the inlet and exit of the test coil were measured using a Precision Dew-point Meter (Optidew Vision 2-Stage Sensor), whereas the dry bulb temperatures at the inlet and exit of the test coil were measured using an RTD and T-type thermocouple, respectively. However, the exit dew-point temperature was periodically measured; whereas the inlet dew-point temperature was measured at an interval of 5 seconds. The air pressure drop across the test coil was measured using Betz manometer with an interval of 30 minutes until the end of the experiment to take the last frost thickness into account.

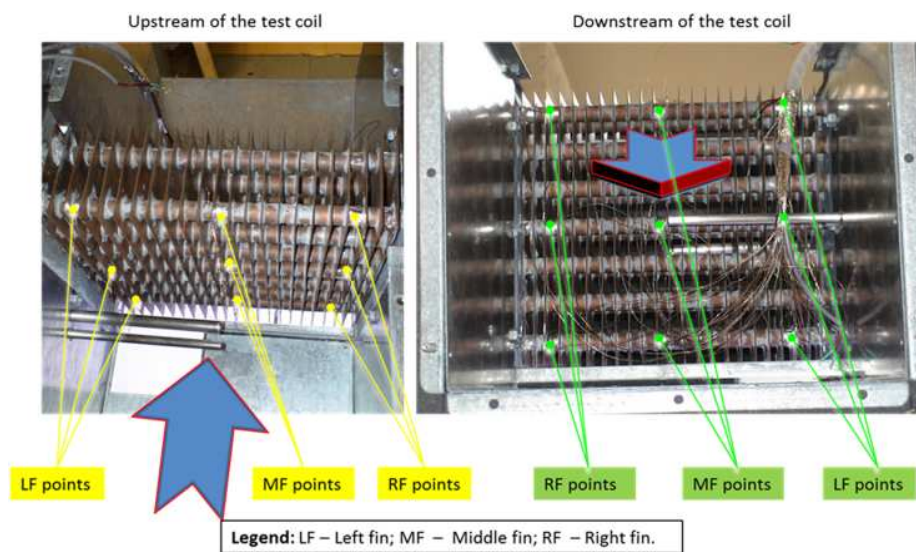


Figure 4.4 Positions of temperature sensors on the test coil fins and tubes.

The average frost thickness and the average frost-coil interface temperatures were measured with a Marlin F-145C2 CCD Camera mounted with Schneider Cinegon 1.4/12 lens and T-type thermocouples respectively. The movement of the CCD Camera was manually controlled and a bank of fluorescent bulbs was used for illumination. Once the position of the camera was fixed

perpendicular to the 76 mm-deep edge of one of the fins under consideration, photos of the frost growth at the third fin from the very left, middle fin and the third fin from the very right of the heat exchanger were logged at an interval of 10 seconds (see Figure 4.4). Eighteen T-type thermocouples were attached securely to three (left, middle and right) of the test coil fins using annealed aluminum foil (Venture Tape) and a heat sink approximately 6 mm away from the edges. The same number of T-type thermocouples was applied on the heat exchanger tubes using the same method by the vicinity of the instrumented fins (see Figure 4.5). Finally, the measurements of all frost-coil interface temperatures were done when the sensors were fully embedded into the frost except at the very beginning of the frost growth period. The time interval for all temperature measurements, except for test coil air exit dew-point temperature, was 5 seconds.

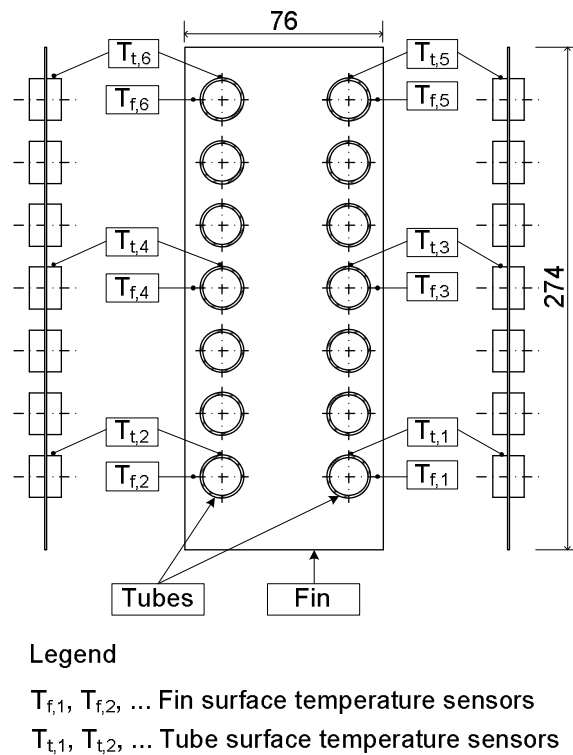


Figure 4.5 Layout of temperature sensors on a single fin-tube arrangement.

The images of the frost, which were taken by the CCD Camera mounted on the top of a double-glazed view window above the test coil (see Figure 4.6), were analyzed using a Vision Builder

AI Software by National Instruments [52] and PCI-8254R, IEEE 1394 Interface Board with configurable I/O. Frost images were calibrated in the following way. The arm of the camera (which holds the camera) was adjusted to be perpendicular to the stand (which holds the arm of the camera). The stand was in turn kept perpendicular to the rails mounted on the air duct (see Figure 4.6). The camera was adjusted to focus on the fin under interest. The camera was then adjusted to be perpendicular to the image. Using simple calibration technique, a pixel coordinate was transformed to a real-world coordinate through scaling in the x (horizontal) and y (vertical directions). All the frost images taken using this particular calibrated camera configuration were then processed for frost thickness measurements as shown in Figure 4.7.

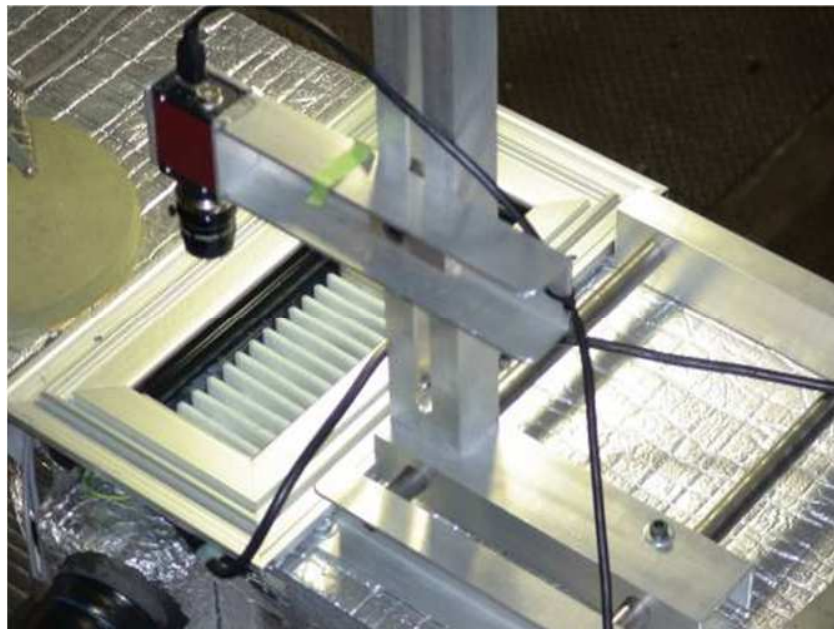


Figure 4.6 Configuration of CCD Camera and the frosted test coil.

The frost thickness on both sides of a fin was measured by searching the edges of the frost along the shorter side of the fin in y-direction based on pixel intensities (see arrows pointing in y-direction in Figure 4.7). Similarly, the frost thickness on the test coil tubes was measured by edge searching technique in the x-direction along the diameter of the tubes perpendicular to the CCD Camera (see arrows pointing in x-direction in Figure 4.7). Finally, the fin thickness and

diameter of the tubes were deducted from the arithmetic mean of frost thicknesses measured along the fin depth and tube diameter, respectively (see the calculation steps in Table 4.1).

The test conditions of the frost consisted of two parts, namely transient and steady state parts (see Figure 4.8). The transient part which lasted from about 20 to 50 minutes comprised of dry, wet and frosted coil, whereas the steady state part consisted of purely frosted surface. The test rig shown on Figure 4.1 was formed by two independent rigs. Namely, the air conditioning test rig (which regulates the inlet air conditions) and the secondary coolant loop (which regulates the surface temperature of the test coil). Because the two test rigs should be run simultaneously to reach steady state conditions at the same time, it was not possible to avoid the dry and wet conditions and directly go to the frost conditions (i.e. without passing through dry and wet conditions). Besides, the test coil geometry and the mounted sensors on the coil surface could not allow wrapping of the coil to separate the surface from dry and wet conditions. These are as such the challenging issues and constraints of the experiment. However, the steady state measurements were nearly constant except for small variations given in Table 4.4. These variations are common in experiments. Hence, it was necessary to average the measurements taken under the steady state conditions in order to account for these variations. Additionally, it is worth mentioning that the main purpose of the current study was to develop representative correlations for real heat exchangers based on the entire frosted test coil surface and the average measurements collected from it. The test coil was not as such designed to conduct local frost characteristics. This is because, the test coil has many surfaces (flat + round) and a single surface has many local points, which make the study of local characteristics very complicated. Hence, to simplify the complex nature of the experiment, the current study focused on the average frost characteristics on the entire test coil.

Furthermore, by taking the resolution of the camera, alignment of the camera, lens distortion and roughness of frosting surface into account, the estimated uncertainty of the frost thickness for the steady state phase was calculated to be  $\pm 0.3$  mm, whereas it was  $\pm 0.4$  mm for the transient state.

The total frost mass was measured in such a way that at the end of each test, the frost from the entire test coil was melted by passing a warm air through the coil and it was collected in a bucket and weighed using a digital balance (Model: SPI SW BB35/A) with an estimated uncertainty of  $\pm 5\text{g}$ . Frost mass during the steady state period was calculated using mass balance equation  $(\sum \dot{m}_a (\Delta \omega \cdot \Delta \tau))$  (indirectly measured). However, to check the validity of the mass balance equation, the melted frost for the entire test period was compared with the calculated frost mass for the entire test period so that the mass balance equation could be used for steady state frost mass measurement.

The transient and the steady state conditions were distinctly separated using the trend of the entire measurement data. In other words, it was possible to separate the two conditions by identifying where the measurement data exactly started to be nearly uniform. Generally speaking, the two conditions (transient and steady state) were separated after the experiments; but not while doing the experiments.

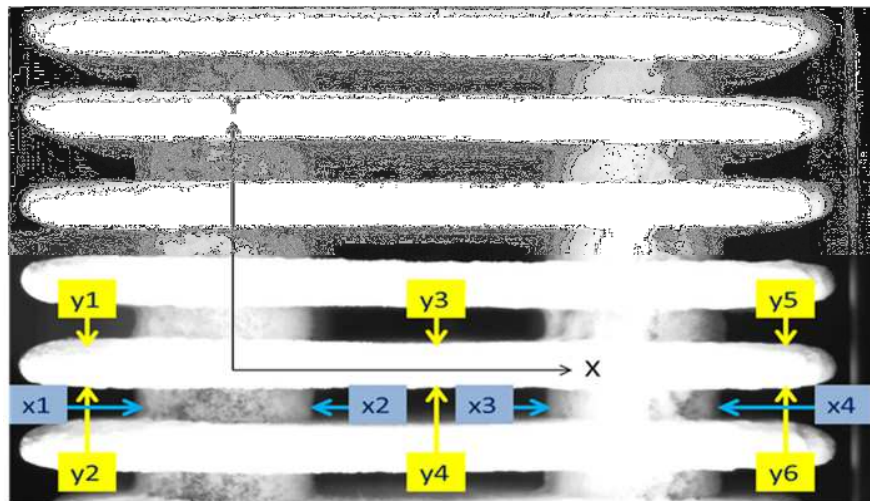


Figure 4.7 Frost thickness measurements.

When the measured frost mass (for transient + steady state) was compared with the calculated frost mass (for transient + steady state) using Equation 4-1 below, it resulted in a discrepancy of (-) 12% to 39% as shown in Figure 4.9.

Table 4.1 Equations used during frost measurements in the steady state part of the test.

Frost characteristics	Test coil surface	Equations
Frost thickness [mm]	Fin	$t_{fst,tube} = \frac{(y_1 - y_2) + (y_3 - y_4) + (y_5 - y_6) - 3 \cdot t_{fin}}{3}$
	Tube	$t_{fst,fin} = \frac{(x_2 - x_1) + (x_4 - x_3) - 2 \cdot D_{o,tube}}{2}$
Frost mass concentration [kg/m <sup>2</sup> ]	Fin & Tube	$m_{fst,con} = \frac{\sum \dot{m}_a \cdot (\omega_{in} - \omega_{out}) \cdot \Delta \tau}{A_o}$
Frost density [kg/m <sup>3</sup> ]	Fin & Tube	$\frac{2000 \cdot m_{fst,con}}{t_{fst,fin} + t_{fst,tube}}$
Heat flux [W/m <sup>2</sup> ]	Fin & Tube	$q_{fst} = \frac{\dot{m}_a \cdot (h_{a,in} - h_{a,out})}{A_o}$
Frost conductivity [W/m °C]	Fin & Tube	$k_{fst} = \frac{q_{fst} \cdot (t_{fst,fin} + t_{fst,tube})}{2000 \cdot \Delta T}$

$$DISCREPANCY = \frac{m_{fst,meas,total} - \sum \dot{m}_a (\Delta \omega \cdot \Delta \tau)}{m_{fst,meas,total}} \cdot 100 \quad 4-1$$

There are a couple of reasons for the discrepancy to be above zero. The first reason is attributable to inaccuracies of the instruments used to measure air mass flow rate, dry bulb temperature, dew point temperature and so forth. It is to be noted that the estimated uncertainty of the total melted frost mass was only  $\pm 5$  g (when weighed) as compared to the uncertainty of the calculated frost mass ( $\pm 29\%$ ). Although all instruments were carefully calibrated, the inaccuracies could not be improved beyond the precision. The second reason is that during transient state (due to instability of water flow rate from the sprayer) of the experiment unmixed water in the air stream could be carried over and drained along the air coil surface into melted frost collection system whose amount depends on the duration of the transient state and the stability of water supply to the sprayer. Besides, the value of discrepancy under zero may not only come from the inaccuracies of the instruments but also come from evaporation, disperse, or residual water. In general, the

uncertainty of frost mass could be reasonably high due to limitations of the instruments, carryover and residual water.

The frost mass measurement errors were considered in the uncertainty analysis presented in the following Section. However, only the calculated frost mass in the steady state phase (which was obtained by mass balance equation) was used for the development of frost correlations. The average frost mass concentration in the steady state phase was calculated by dividing the frost mass in the steady state phase with the total frosted surface area of the heat exchanger.

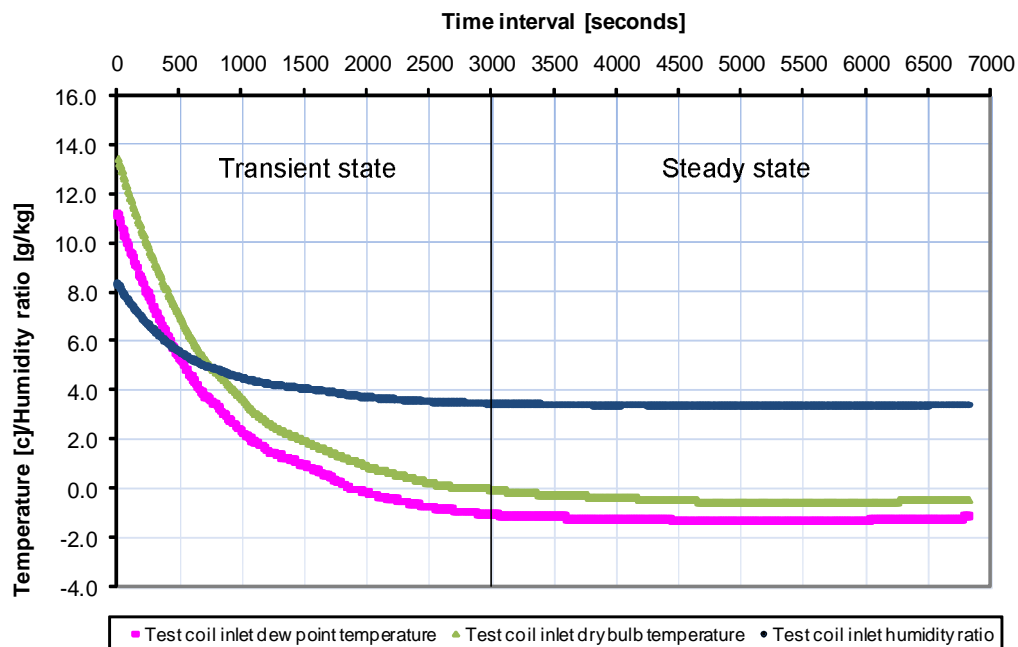


Figure 4.8 Transient and steady state parts of the frost test conditions.

The average frost density was calculated by dividing the mass concentration with the measured frost thickness; and its uncertainty was calculated using an uncertainty of  $\pm 29\%$  of frost mass concentration and  $\pm 0.3$  mm of frost thickness resulting in an uncertainty of  $\pm 31\%$  in frost density. The average heat flux from the surface of the test coil to the air was computed using the product of the air mass flow rate and the difference in thermodynamic state points at both the

inlet and outlet of the test coil thereby dividing the result by the total surface area of the heat exchanger ( $q_{fst} = \dot{m}_a \cdot (h_{a,in} - h_{a,out}) / A_o$ ). The heat flux had an estimated uncertainty ranging from  $\pm 1.8\%$  to  $\pm 3\%$ . The thermal conductivity of the frost was computed by dividing the product of the heat flux and frost thickness by the temperature difference across the frost.

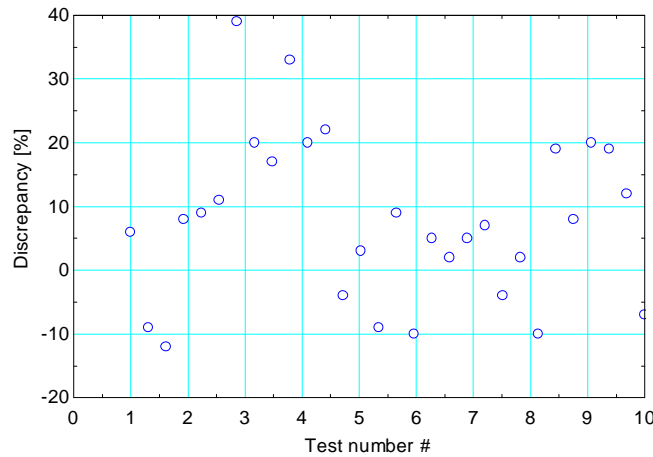


Figure 4.9 Discrepancy between measured and calculated total frost masses.

$$\left( DISCREPANCY = \frac{m_{fst,meas,total} - \sum \dot{m}_a (\Delta \omega \cdot \Delta \tau)}{m_{fst,meas,total}} \cdot 100 \right)$$

The frost surface temperatures were measured by direct contact (i.e. manually passing two thermocouples through specially made holes on the side of the air duct) at the end of each test run. The two thermocouples, at the inlet and outlet of the test coil, were kept inside the duct to achieve the same temperature with the air stream flowing over the air coil. Additionally, these thermocouples were placed at multiple points, in rotation, on the surface of the frost to reduce errors. It was the average of those multiple measurements which was considered as the surface temperature of the frost. This measured average frost surface temperature was then approximated using ( $T_{fst,surface} = ((T_{a,in} + T_{a,out}) / 2 + T_{interface,avg}) / 2$ ) as this could be easily available for refrigeration engineers without complicated frost surface temperature measurements. It is to be noted that the approximated frost surface temperature was used to develop a correlation only for frost thermal conductivity. It doesn't as such affect the results of the other frost correlations, such as frost



density, frost thickness and air pressure drop. The estimated uncertainty for the approximated frost temperature was also taken to be as high as  $\pm 1^{\circ}\text{C}$ . The comparison between the measured and the approximated frost surface temperatures could be observed from Table 4.2 below.

Table 4.2 Comparison of manually measured and approximated frost surface temperatures.

Test #	Run#	Manually measured frost surface temperature [C]	Approximated frost surface temperature[C]	Test #	Run#	Manually measured frost surface temperature [C]	Approximated frost surface temperature[C]
1	1	-6.0	-5.4	6	1	0.7	0.9
	2	-5.6	-5.4		2	0.8	0.9
	3	-5.4	-5.4		3	0.7	0.9
2	1	-4.4	-3.9	7	1	-5.5	-4.8
	2	-4.0	-3.9		2	-4.9	-4.8
	3	-4.5	-3.9		3	-5.4	-4.8
3	1	-4.5	-3.9	8	1	-6.1	-6.1
	2	-4.0	-3.9		2	-6.1	-6.1
	3	-3.9	-3.9		3	-6.6	-6.1
4	1	-9.9	-9.0	9	1	-7.0	-6.8
	2	-9.3	-9.0		2	-7.2	-6.8
	3	-9.6	-9.0		3	-7.0	-6.8
5	1	-8.3	-7.7	10	1	-5.2	-5.2
	2	-7.8	-7.7		2	-5.9	-5.2
	3	-8.1	-7.7		3	-5.8	-5.2

The equations for calculating useful frost characteristics are given in Table 4.1. All of the calibrated T-type thermocouples had uncertainty of  $\pm 0.1^{\circ}\text{C}$  resulting in an estimated uncertainty of  $\pm 27\%$  in the calculated frost thermal conductivity.

### 4.3. Uncertainty analysis

All uncertainty calculations for this experiment were performed following EES [9] and Holman and Gajda [53]. The approach is based on a careful specification of the uncertainties in various

primary experimental measurements. The result  $R$  (calculated quantity) is a given function of the independent variables (measured quantities)  $x_1, x_2, x_3 \dots x_n$ . Therefore,

$$R = R(x_1, x_2, x_3, \dots x_n) \quad 4-2$$

Let  $w_R$  be the uncertainty in the result; and  $w_1, w_2, w_3 \dots w_n$  be the uncertainties in the independent variables, and then  $w_R$  can be given by:

$$w_R = \left[ \left( \frac{\partial R}{\partial x_1} w_1 \right)^2 + \left( \frac{\partial R}{\partial x_2} w_2 \right)^2 + \left( \frac{\partial R}{\partial x_3} w_3 \right)^2 + \dots + \left( \frac{\partial R}{\partial x_n} w_n \right)^2 \right]^{1/2} \quad 4-3$$

For regression analysis, it is to be expected that the set of measurements ( $y_{[i..n]}$ ) in the response variables  $Y_{[i..n]}$  (i.e., frost thickness, frost density, frost thermal conductivity and test coil pressure drop) and the set of measurements ( $x_{[i..n]}$ ) in the predictor variables  $X_{[i..k]}$  (i.e., air inlet temperature, frost coil interface temperature, coolant inlet temperature, humidity ratio, Reynolds number, and Fourier number) may have different experimental uncertainties. Hence, the uncertainties in  $y_{[i..n]}$  and  $x_{[i..n]}$  can be estimated by the standard deviations of the mean values of  $y_{[i..n]}$  and  $x_{[i..n]}$  as follows:

$$\sigma_m = \frac{\sigma}{\sqrt{n}} \quad 4-4$$

where  $\sigma_m$  is the standard deviation of the mean value of  $y_{[i..n]}$  or  $x_{[i..n]}$ ;  $\sigma$  is the standard deviation of the set of measurements of a response variable  $y_{[i..n]}$  or a predictor variable  $x_{[i..n]}$ ; and  $n$  is the number of measurements in the set. Chances for deviations from mean value of a normal-distribution curve and better estimates of uncertainties using Chauvenet's criterion can be found from reference [53]. All of the uncertainties in the primary and calculated quantities for the current study are given in Table 4.3.

Table 4.3 Results of uncertainty analysis.

Uncertainty in primary measurements		Uncertainty in calculated quantities	
Variable	Uncertainty	Variable	Uncertainty
Air inlet dry bulb temperature	$\pm 0.1^{\circ}\text{C}$	Frost mass during steady state [g]	$\pm 30\%$
Air inlet dew-point temperature	$\pm 0.2^{\circ}\text{C}$	Frost mass concentration [ $\text{kg}/\text{m}^2$ ]	$\pm 30\%$
Air outlet dry bulb temperature	$\pm 0.1^{\circ}\text{C}$	Frost density [ $\text{kg}/\text{m}^3$ ]	$\pm 31\%$
Air inlet humidity ratio	$\pm 1.7\%$	Heat flux [ $\text{W}/\text{m}^2$ ]	$\pm 1.8\%$ to $\pm 3\%$
Frost-coil interface temperature	$\pm 0.1^{\circ}\text{C}$	Frost thermal conductivity [ $\text{W}/\text{m}^{\circ}\text{C}$ ]	$\pm 27\%$
Test coil coolant inlet temperature	$\pm 0.1^{\circ}\text{C}$	Frontal air velocity	$\pm 0.04$ to $\pm 0.06$ m/s
Frost thickness	$\pm 0.3$ mm	Reynolds number [-]	$\pm 29\%$
Air mass flow rate [ $\text{kg}/\text{min}$ ]	$\pm 1.6\%$ to $\pm 3\%$	Fourier number [-]	$\pm 0.9$
Test coil pressure drop	$\pm 2$ Pa		

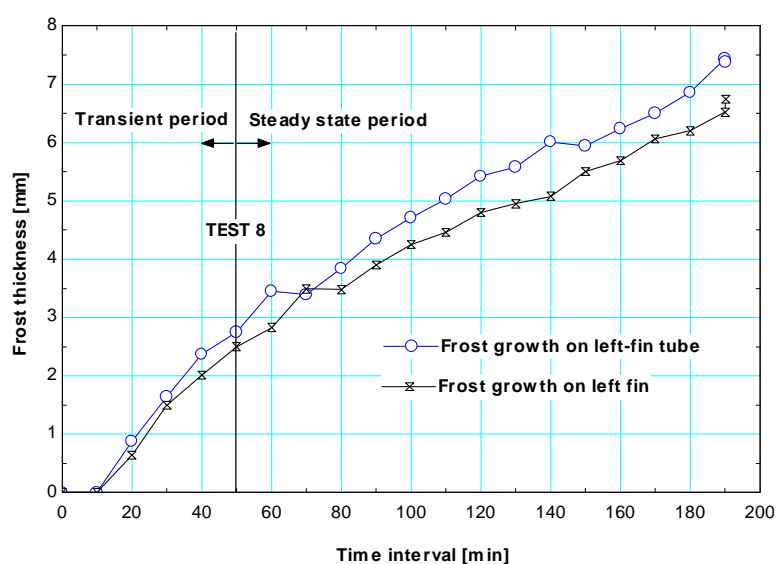


Figure 4.10 Test 8: Frost growth on fins and tubes on the left side of the test coil.

#### 4.4. Test conditions and results

A total of 26 tests were conducted during the entire experiment, out of which only 10 were selected based on the stability and repeatability of the steady state conditions of the experiments. The conditions and results of these selected tests were analyzed and discussed in the following sections.

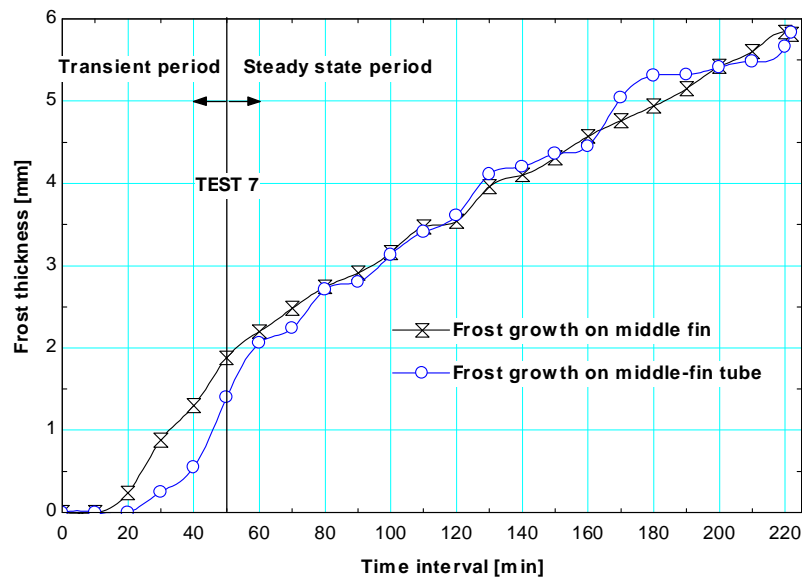


Figure 4.11 Test 7: Frost growth on fins and tubes in the middle of the test coil.

##### 4.4.1. Test conditions

The test coil was constructed in such a way that the fins were soldered to the tubes in order to minimize the surface temperature difference between the fins and the tubes of the test coil. It is to be noted that refrigeration heat exchangers are different from the test coil. Traditionally, cooling coils with aluminum fins on expanded copper tubes are used in display cabinets [54]. The energy use and cost for a system are normally influenced by the selection of cooling coil design. However, the newly developed frost correlations consider the average surface temperature of the test coil. The average surface temperature is a representative surface temperature of the top frost surface exposed to the air stream, whereas the frost-coil interface

temperature (to be discussed later) is the temperature between the coil surface and the bottom of the frost surface measured by embedding the sensor into the frost. Hence, if the average surface temperature of a refrigeration air-coil with the same geometry is within the operating range of the current study, the new correlations can be applicable. The variations of the experimental parameters, during the steady state condition periods, such as air dry bulb and dew point temperatures, air inlet humidity ratio, frost-coil interface temperature, coolant inlet temperature, air mass flowrates and Reynolds number were carefully observed and entered in Table 4.4 along with the range of measurements.

Table 4.4 Steady state experimental conditions.

Experimental parameters	Measurement range	Maximum variations
Air inlet dry bulb temperature [ $^{\circ}\text{C}$ ]	-4.5 to 4.9	$\pm 0.8^{\circ}\text{C}$
Air inlet dew-point temperature [ $^{\circ}\text{C}$ ]	-4.7 to 4.6	$\pm 0.6^{\circ}\text{C}$
Air outlet dry bulb temperature [ $^{\circ}\text{C}$ ]	-5.8 to 3.7	$\pm 0.7^{\circ}\text{C}$
Air inlet humidity ratio [ $\text{g/kg}_{\text{DA}}$ ]	2.5 to 5.3	$\pm 0.18 \text{ g/kg}_{\text{DA}}$
Frost-coil interface temperature [ $^{\circ}\text{C}$ ]	-12.8 to -2.6	$\pm 1.1^{\circ}\text{C}$
Test coil coolant inlet temperature [ $^{\circ}\text{C}$ ]	-19.0 to -10.4	$\pm 1.1^{\circ}\text{C}$
Air mass flow rate [ $\text{kg/min}$ ]	12.58 to 17.08	$\pm 0.3$
Reynolds number [dimensionless]	1781 to 2380	$\pm 530$
Fourier number [dimensionless]	213 to 1547	n/a
Test span [minutes]	34 to 237	n/a

#### 4.4.2. Test results

The measured and calculated parameters of the experiment during the steady state conditions of the tests are given in Table 4.5, 4.6 and 4.7, respectively. The frost thickness growth on the surface of the test coil with time for the entire test periods of three tests of measurements are depicted in Figures 4.10 through 4.12. All of the graphs in these figures have a couple of common features. Firstly, the graphs are not linear. Besides, the frost thickness does not sometimes change with time between two consecutive measurement points. These conditions might be due to the densification of the frost. In other words, the sublimation of the water vapor

in the incoming air contributes to an increase in the frost density rather than an increase in the frost thickness. Secondly, for the first 10 or 20 minutes during the transient state, the frost thickness could not be measured due to the coil being either dry or wet.

Frost thickness and distribution on the surface of a heat exchanger depends on several factors, such as the geometry of the heat exchanger surface, air inlet and frost-coil interface conditions. Figure 4.10 depicts graphs of frost thickness on fins and tubes on the left side of the test coil for Test number 8. The difference between the frost-fin and the frost-tube interface temperatures was about  $0.5^{\circ}\text{C}$ . During the transient state, which lasted for 50 minutes, the frost thickness on the fin was much less than that on the tubes. The difference between the two frost thicknesses (between tube and fin frost thicknesses) ranged from 0 to 0.5 mm. In the steady state part, beyond the 50 minutes duration of the test, the frost thickness on the fin was even much less than that on the tube, the difference between the two ranging from 0 to 1 mm.

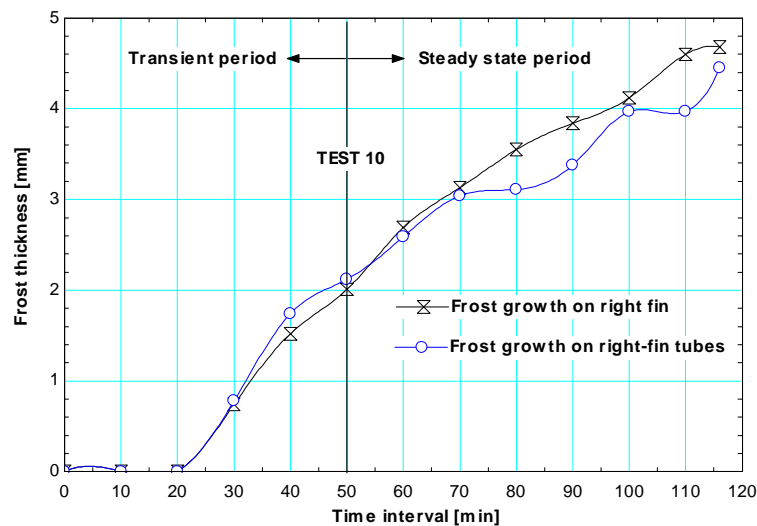


Figure 4.12 Test 10: Frost growth on fins and tubes on the right side of the test coil.

Figure 4.11 shows graphs of frost thickness on fins and tubes in the middle of the test coil for Test number 7. The difference between the frost-fin and the frost-tube interface temperatures was

about 0.9°C. During the transient state, which lasted for 50 minutes, the frost thickness on the fin was higher than the frost thickness on the tubes; the difference between the two ranging from 0.2 to 0.75 mm. In the steady state part (beyond the 50 minute duration of the test), the frost thickness on the fin with respect to that of the tube had a mixed trend. In other words, it was a little bit higher or equal or lower than that on the tubes.

Table 4.5 Measured air conditions during the steady state parts of the tests.

Test #		Duration under steady state	Average air inlet dry bulb temp	Average air inlet dew point temp	Average air outlet dry bulb temp	Average air inlet humidity ratio	Average frost-coil interface temp	Average air mass flow rate
		[s]	[°C]	[°C]	[°C]	[g/kg]	[°C]	[kg/min]
1	1	10910	-0.8	-0.9	-1.9	3.5	-9.4	12.58
	2	8090	-0.8	-0.9	-1.9	3.5	-9.4	12.58
	3	6290	-0.8	-0.9	-1.9	3.5	-9.4	12.58
2	1	7180	-0.2	-0.3	-1.1	3.7	-7.1	16.73
	2	5380	-0.2	-0.3	-1.1	3.7	-7.1	16.73
	3	3580	-0.2	-0.3	-1.1	3.7	-7.1	16.73
3	1	7495	0.1	-0.1	-0.6	3.7	-7.5	15.62
	2	3895	0.1	-0.1	-0.6	3.7	-7.5	15.62
	3	2095	0.1	-0.1	-0.6	3.7	-7.5	15.62
4	1	6365	-4.5	-4.7	-5.8	2.5	-12.8	15.45
	2	4565	-4.5	-4.7	-5.8	2.5	-12.8	15.45
	3	2765	-4.5	-4.7	-5.8	2.5	-12.8	15.45
5	1	11370	-2.5	-2.6	-4.0	3.0	-12.2	13.67
	2	7770	-2.5	-2.6	-4.0	3.0	-12.2	13.67
	3	4170	-2.5	-2.6	-4.0	3.0	-12.2	13.67
6	1	14205	4.9	4.6	3.7	5.3	-2.6	17.08
	2	8805	4.9	4.6	3.7	5.3	-2.6	17.08
	3	5205	4.9	4.6	3.7	5.3	-2.6	17.08
7	1	9685	-0.4	-1.5	-1.6	3.3	-8.6	16.61
	2	6085	-0.4	-1.5	-1.6	3.3	-8.6	16.61
	3	2485	-0.4	-1.5	-1.6	3.3	-8.6	16.61
8	1	7830	-1.7	-2.1	-2.8	3.2	-9.9	16.55
	2	4230	-1.7	-2.1	-2.8	3.2	-9.9	16.55
	3	2430	-1.7	-2.1	-2.8	3.2	-9.9	16.55
9	1	4035	-2.9	-3.7	-4.3	2.8	-9.9	13.77
	2	3135	-2.9	-3.7	-4.3	2.8	-9.9	13.77
	3	2235	-2.9	-3.7	-4.3	2.8	-9.9	13.77
10	1	3840	-1.0	-1.3	-2.2	3.4	-8.8	14.10
	2	2940	-1.0	-1.3	-2.2	3.4	-8.8	14.10
	3	2040	-1.0	-1.3	-2.2	3.4	-8.8	14.10

Figure 4.12 shows graphs of frost thickness on fins and tubes on the right side of the test coil for Test number 10. The difference between the frost-fin and the frost-tube interface temperatures was about  $0.5^{\circ}\text{C}$ . During the transient state, which lasted for 50 minutes, the frost thickness on the fin was less than that on the tubes; the difference between the two ranging from 0 to 0.25 mm. In the steady state part (beyond the 50 minute duration of the test) the frost thickness on the fin became higher than that on the tubes by as much as 0.5 mm.

The test results shown in Figure 4.10 and 4.12 had the same interface temperature difference between frost-fin and the frost-tube interfaces, which was about  $0.5^{\circ}\text{C}$ . But, the fins had different locations on the test coil (left and right). As a result, the fin frost thicknesses were higher than that on the tube in the transient state of the test period in both figures (Figure 4.10 & 4.12). However, the fin frost thicknesses in the steady state parts of the same figures showed opposite trends. In other words, the fin frost thickness in Figure 4.10 was lower than that of the tubes, whereas in Figure 12 it was higher than that of tubes.

When Figure 4.10 and 4.12 were compared with Figure 4.11, the difference between frost-fin and the frost-tube interface temperatures in Figure 4.11 was higher than that of Figure 4.10 and 4.12 by about  $0.4^{\circ}\text{C}$ . However, the frost thickness on the fin was greater than or equal to or less than that on the tubes where the location of the fin was in the middle of the test coil. Therefore, the frost thickness on the fin could be either greater than or equal or lower than the frost thickness on the tubes depending on the fin position for frost-fin and frost-tube interface temperature difference ranging from  $0.5^{\circ}\text{C}$  to  $0.9^{\circ}\text{C}$ . The possible reasons for these scenarios could be – 1) geometry of the surfaces (i.e. flat and round); 2) the position of the fins and tubes; and 3) air flow pattern on the test coil, which have likely played major roles in the distribution of frost on the entire heat transfer surface area of the test coil. In other words, the aforementioned three scenarios were much more influential than the difference between frost-fin and frost-tube interface temperatures ( $0.5^{\circ}\text{C}$  to  $0.9^{\circ}\text{C}$ ), which as such require further study. It is worth mentioning here that the maximum difference between the frost thickness of the tubes and the fins was about 1 mm for the above interface temperature differences ( $0.5^{\circ}\text{C}$  to  $0.9^{\circ}\text{C}$ ).



Table 4.6 Measured frost and inlet coolant conditions during the steady state parts of the tests.

		Duration under steady state	Average Test coil coolant inlet temperature	Frost thickness at the end of each test	Frost mass during the steady state period	Frost mass during the entire test period (transient +steady state)	Average test coil pressure drop at the end of each test
Test #		[s]	[C]	[mm]	[g]	[g]	[Pa]
1	1	10910	-16.9	7.4	632.0	858.0	204.0
	2	8090	-16.9	5.4	452.0	576.0	65.0
	3	6290	-16.9	4.5	348.0	465.0	39.0
2	1	7180	-14.8	5.6	411.0	720.0	176.0
	2	5380	-14.8	5.2	338.0	612.0	111.0
	3	3580	-14.8	4.2	229.0	502.0	51.0
3	1	7495	-13.8	5.8	301.0	772.0	188.0
	2	3895	-13.8	4.2	154.0	404.0	120.0
	3	2095	-13.8	3.2	81.0	301.0	59.0
4	1	6365	-19.0	4.9	370.0	942.0	88.0
	2	4565	-19.0	4.2	265.0	659.0	64.0
	3	2765	-19.0	3.1	161.0	538.0	47.0
5	1	11370	-17.9	8.4	831.0	1006.0	299.0
	2	7770	-17.9	6.4	568.0	811.0	206.0
	3	4170	-17.9	4.8	305.0	479.0	116.0
6	1	14205	-10.4	8.5	1348.0	2070.0	141.0
	2	8805	-10.4	7.1	916.0	1210.0	86.0
	3	5205	-10.4	5.4	542.0	1012.0	69.0
7	1	9685	-16.1	5.8	649.0	938.0	174.0
	2	6085	-16.1	4.5	408.0	713.0	141.0
	3	2485	-16.1	3.1	167.0	470.0	84.0
8	1	7830	-16.2	7.1	565.0	826.0	180.0
	2	4230	-16.2	5.2	308.0	611.0	133.0
	3	2430	-16.2	4.5	179.0	423.0	67.0
9	1	4035	-16.6	3.1	189.0	404.0	27.0
	2	3135	-16.6	2.8	147.0	312.0	26.0
	3	2235	-16.6	2.4	105.0	307.0	24.0
10	1	3840	-15.1	4.6	205.0	454.0	57.0
	2	2940	-15.1	4.0	157.0	359.0	39.0
	3	2040	-15.1	3.5	109.0	251.0	18.0

In the current study, it is to be emphasized that the average frost-coil interface temperature (the arithmetic mean of frost-fin and frost-tube interface temperatures) was used to formulate frost property correlations for the entire coil surface for the sake of simplicity and reducing the frost thickness difference between the frosted tubes and fins of the air-coil. Thus, the frost characteristics such as frost thickness, frost density, frost thermal conductivity and air pressure

drop across the frosted coils were formulated to represent just the average values on the entire air-coil surface, irrespective of specific position on the coil.

#### 4.5. Multilinear regression analysis for frost correlations

A multilinear regression method was employed following Getu and Bansal [55] in order to regress the frost thickness, frost density, thermal conductivity and air pressure drop across a frosted test coil as a function of the input data such as test coil air inlet temperature ( $T_{a,in}$ ), frost-coil interface temperature ( $T_{interface}$ ), inlet air humidity ratio ( $\omega_{in}$ ), test coil coolant inlet temperature ( $T_{coolant,in}$ ), Reynolds number ( $Re_{D,h}$ ), and Fourier number ( $Fo$ ), which were given in Table 4.5 through 4.7. The hydraulic diameter was calculated following the philosophy presented by Wich et al [56]. The calculation steps are given by Equations 4.5 through 4.13.

The total number of tubes in the heat exchanger is given by;

$$N_{total} = N_T \cdot N_V \quad 4-5$$

Effective flow length of the air along the heat exchanger parallel to air flow direction is given by;

$$L_{flow} = N_T \cdot W_T \quad 4-6$$

Fin heat transfer area is given by;

$$A_{fin} = 2 \cdot L_{hx} \cdot F_p \cdot N_{total} \cdot \left( S_T \cdot W_T - \pi \cdot \frac{D_o^2}{4} \right) \quad 4-7$$

whereas, the total exposed tube surface area of the heat exchanger is given by;

$$A_{tube} = N_{total} \cdot \pi \cdot D_o \cdot L_{hx} \cdot (1 - F_p \cdot \delta_{fin}) \quad 4-8$$

Minimum frontal air flow area of the heat exchanger is determined by;

$$A_{min} = L_{hx} \cdot N_v \cdot (S_T - D_o) \cdot (1 - F_p \cdot \delta_{fin}) \quad 4-9$$

whereas, the heat exchanger frontal area is determined by;

$$A_{fr} = L_{hx} \cdot S_T \cdot N_v \quad 4-10$$

The ratio of minimum flow area to the heat exchanger frontal area is given by;

$$\sigma = \frac{A_{min}}{A_{fr}} \quad 4-11$$

Total heat transfer area could be obtained by adding equations 4-7 and 4-8;

$$A_o = A_{fin} + A_{tube} \quad 4-12$$

Finally, the hydraulic diameter of the heat exchanger is obtained by;

$$D_h = 4 \cdot \sigma \cdot L_{flow} \cdot \frac{A_{fr}}{A_o} \quad 4-13$$

The Reynolds and Fourier numbers were determined by Equations 4-14 and 4-15 respectively. It is worth mentioning that the Reynolds number takes the fin depth of the test coil (76 mm) into account, i.e. Equations 4-16 through 4-19 implicitly consider the spatial distribution of frost along the air flow direction. Furthermore, it is important to note that Fourier number contains the time parameter ( $\tau$ ) which is useful to calculate the time span between defrosting processes.

$$Re_{D,h} = \frac{v_a \cdot \rho_{a,in} \cdot D_h}{\mu_{a,in}} \quad 4-14$$

$$Fo = \frac{k_{a,in} \cdot \tau}{\rho_{a,in} \cdot cp_{a,in} \cdot D_h^2} \quad 4-15$$

Table 4.7 Calculated parameters during the steady state parts of the tests (for the same duration as in Tables 4.4 and 4.5).

		Frontal air velocity	Average Reynolds number	Average Fourier number	Frost mass concentration	Frost density	Heat flux	Frost thermal conductivity
Test #		[m/s]	[-]	[-]	[kg/m <sup>2</sup> ]	[kg/m <sup>3</sup> ]	[W/m <sup>2</sup> ]	[W/m <sup>0</sup> C]
1	1	1.8	1781	1129	0.4885	66	369	0.6358
	2	1.8	1781	837	0.3494	65	369	0.4640
	3	1.8	1781	651	0.2690	60	369	0.3867
2	1	2.4	2365	749	0.3177	57	274	0.4454
	2	2.4	2365	561	0.2613	50	274	0.4136
	3	2.4	2365	373	0.1770	42	274	0.3341
3	1	2.3	2206	783	0.2327	40	269	0.4106
	2	2.3	2206	407	0.1190	28	269	0.2973
	3	2.3	2206	219	0.0626	20	269	0.2265
4	1	2.2	2210	645	0.2860	58	388	0.4581
	2	2.2	2210	462	0.2048	49	388	0.3927
	3	2.2	2210	280	0.1244	40	388	0.2898
5	1	2.0	1944	1171	0.6423	76	409	0.7082
	2	2.0	1944	800	0.4390	69	409	0.5396
	3	2.0	1944	429	0.2358	49	409	0.4047
6	1	2.5	2380	1547	1.0419	123	557	1.2615
	2	2.5	2380	959	0.7080	100	557	1.0537
	3	2.5	2380	567	0.4189	78	557	0.8014
7	1	2.4	2349	1014	0.5016	86	492	0.6965
	2	2.4	2349	637	0.3154	70	492	0.5404
	3	2.4	2349	260	0.1291	42	492	0.3723
8	1	2.4	2349	816	0.4367	62	493	0.8540
	2	2.4	2349	441	0.2381	46	493	0.6255
	3	2.4	2349	253	0.1384	31	493	0.5413
9	1	2.0	1961	414	0.1461	47	340	0.3012
	2	2.0	1961	322	0.1136	41	340	0.2721
	3	2.0	1961	230	0.0812	34	340	0.2332
10	1	2.0	1997	402	0.1585	34	315	0.3720
	2	2.0	1997	307	0.1214	30	315	0.3235
	3	2.0	1997	213	0.0843	24	315	0.2830

The development of the regressed equations (Equations 4-16 to 4-19) included the calculation of tens of thousands of data points, which were later reduced to thirty data sets. These polynomial forms of frost characteristic correlations were developed based on universally acceptable methods following design of experiments (DOE) [57] and regression analysis [58]. The changes of the independent variables were carefully observed by changing the dependent variables in the

designed experiment. The statistically sound polynomial forms of frost correlations were formulated by integrating simple and powerful statistical methods into the experimental design methodology. Hence, the resulted frost properties such frost thickness, density and thermal conductivity including the pressure drop across the frosted test coil are respectively given by:

$$t_{fst} = a_0 + a_1 \cdot \omega_{in} + a_2 \cdot \omega_{in}^2 + a_3 \cdot \tilde{T} + a_4 \cdot \tilde{T}^2 + a_5 \cdot Re_{D,h} + a_6 \cdot Re_{D,h}^2 + a_7 \cdot Fo + a_8 \cdot Fo^2 \quad [mm] \quad 4-16$$

$$\rho_{fst} = a_0 + a_1 \cdot \omega_{in} + a_2 \cdot \omega_{in}^2 + a_3 \cdot \tilde{T} + a_4 \cdot \tilde{T}^2 + a_5 \cdot Re_{D,h} + a_6 \cdot Re_{D,h}^2 + a_7 \cdot Fo + a_8 \cdot Fo^2 \quad [kg \ m^{-3}] \quad 4-17$$

$$k_{fst} = a_0 + a_1 \cdot \omega_{in} + a_2 \cdot \omega_{in}^2 + a_3 \cdot \tilde{T} + a_4 \cdot \tilde{T}^2 + a_5 \cdot Re_{D,h} + a_6 \cdot Re_{D,h}^2 + a_7 \cdot Fo + a_8 \cdot Fo^2 \quad [W \ m^{-1} K^{-1}] \quad 4-18$$

$$\Delta P_{COIL} = a_0 + a_1 \cdot \omega_{in} + a_2 \cdot \omega_{in}^2 + a_3 \cdot \tilde{T} + a_4 \cdot \tilde{T}^2 + a_5 \cdot Re_{D,h} + a_6 \cdot Re_{D,h}^2 + a_7 \cdot Fo + a_8 \cdot Fo^2 \quad [Pa] \quad 4-19$$

Ratio of the temperature difference represented in Equations 4-16 through 4-19 is given by:

$$\tilde{T} = \frac{T_{coolant,in} - T_{interface}}{T_{a,in} - T_{interface}} \quad 4-20$$

The linear regression coefficients ( $a_{[0...8]}$ ) of Equations 4-16 through 4-19 are given in Tables 4.8 and 4.9 along with other statistical indicators such as standard error, bias error, root mean square error (rms), and correlation coefficient ( $R^2$ ). Each term is defined in the following sequence of equations.

The standard errors ( $a\_stderr_{[0...8]}$ ) are the standard errors of the curve fit parameters ( $a_{[0...8]}$ ) defined as the square root of the estimated variance of the parameter. The smaller the standard error the more precise is the estimator.

Bias error is defined as:

$$bias = \frac{1}{n} \times \sum_{i=1}^n (y_i - \hat{y}_i) \quad 4-21$$

The root mean square error is defined as:

$$rms = \sqrt{\frac{1}{n} \times \sum_{i=1}^n (y_i - \hat{y}_i)^2} \quad 4-22$$

where n is the number of data points (30), and  $y_i$  is the  $i^{\text{th}}$  value of the response variable  $Y_{[i..n]}$  (i.e.,  $t_{fst}$ ,  $\rho_{fst}$ ,  $k_{fst}$  and  $\Delta P_{COIL}$ ) and  $\hat{y}_i$  is the fitted value.

Table 4.8 Statistical information for frost thickness and density.

Regression coefficients for frost thickness [t <sub>fst</sub> , mm]			Regression coefficients for frost density [ρ <sub>fst</sub> , kg/m <sup>3</sup> ]	
	Value	std error	Value	std error
a <sub>0</sub>	2.0799E+01	1.5376E+01	9.2315E+02	2.3824E+02
a <sub>1</sub>	1.9985E+00	8.7347E-01	-8.4801E+01	1.3534E+01
a <sub>2</sub>	-1.9233E-01	1.0969E-01	1.1187E+01	1.6996E+00
a <sub>3</sub>	1.7929E+01	4.9892E+00	9.0734E+01	7.7305E+01
a <sub>4</sub>	8.2178E+00	2.8823E+00	5.2563E+01	4.4660E+01
a <sub>5</sub>	-1.4254E-02	1.3622E-02	-6.8862E-01	2.1107E-01
a <sub>6</sub>	3.6405E-06	3.2482E-06	1.6558E-04	5.0329E-05
a <sub>7</sub>	4.6575E-03	9.3764E-04	5.5788E-02	1.4528E-02
a <sub>8</sub>	-5.8322E-07	5.8600E-07	-6.2902E-06	9.0797E-06
Number of points (n) = 30			Number of points (n) = 30	
bias = -8.0231E-19			bias = 1.2554E-16	
rms = 3.9064E-01			rms = 6.0527E+00	
R <sup>2</sup> = 94.24%			R <sup>2</sup> = 93.35%	
Operating range of the independent variables in the correlations				
2.5 ≤ ω <sub>in</sub> ≤ 5.3		-1.1 ≤ $\tilde{r}$ ≤ -0.6		1780 ≤ Re <sub>D,h</sub> ≤ 2380
213 ≤ Fo ≤ 1547				

R<sup>2</sup> in Equation 4-23 can be interpreted as the proportion of the total variation in the response variable  $Y_{[i..n]}$  that is accounted for by the set of predictor variables  $X_{[1..n]}$  (i.e.,  $\tilde{T}$ ,  $\omega_{in}$ ,  $Re_{D,h}$ , and  $Fo$ ), and it is given by:

$$R^2 = \left( 1 - \frac{\sum_{i=1}^{i=n} (y_i - \hat{y}_i)^2}{\sum_{i=1}^{i=n} (y_i - \bar{y})^2} \right) \times 100 \quad 4-23$$

Here,  $\bar{y}$  represents the mean of  $y_{[i..n]}$  value of the response variable  $Y_{[i..n]}$ .

The usefulness of the above unique equations (Equation 4-16 through 4-19) is that a refrigeration engineer can easily estimate the time interval between defrost cycles based on the Fourier number (since it contains the time for frost build up) and the frost thickness between the fins of an air-coil. Refrigeration engineers can also estimate air pressure drop across frost air-coils based on the heat exchanger geometry, the inlet variables of the air, coolant and surface conditions of the heat exchangers. Besides, the heat and time span required for defrosting frosted heat exchangers can be estimated using Equations 4-24 and 4-25, respectively;

Table 4.9 Statistical information for frost thermal conductivity and air coil pressure drop.

Regression coefficients for frost thermal conductivity [k <sub>fst</sub> , W/mK]			Regression coefficients for test coil pressure drop [ΔP <sub>COIL</sub> , Pa]	
	Value	std error	Value	std error
a <sub>0</sub>	9.8829E+00	2.6442E+00	-1.4972E+03	9.9669E+02
a <sub>1</sub>	-5.3277E-01	1.5021E-01	2.6245E+02	5.6620E+01
a <sub>2</sub>	8.2130E-02	1.8864E-02	-3.5387E+01	7.1105E+00
a <sub>3</sub>	-8.4582E-02	8.5802E-01	1.0690E+03	3.2341E+02
a <sub>4</sub>	-3.7020E-01	4.9569E-01	5.3007E+02	1.8684E+02
a <sub>5</sub>	-8.5823E-03	2.3427E-03	1.3485E+00	8.8302E-01
a <sub>6</sub>	2.1275E-06	5.5860E-07	-2.9527E-04	2.1055E-04
a <sub>7</sub>	1.8370E-04	1.6125E-04	2.5887E-01	6.0780E-02
a <sub>8</sub>	1.3039E-07	1.0078E-07	-5.4207E-05	3.7986E-05
Number of points (n) = 30			Number of points (n) = 30	
bias = 2.4828E-18			bias = -5.4482E-16	
rms = 6.7179E-02			rms = 2.5322E+01	
R <sup>2</sup> = 92.74%			R <sup>2</sup> = 86.86%	
Operating range of the independent variables in the correlations				
2.5 ≤ ω <sub>in</sub> ≤ 5.3		-1.1 ≤ $\tilde{\tau}$ ≤ -0.6		1780 ≤ Re <sub>D,h</sub> ≤ 2380      213 ≤ Fo ≤ 1547

$$Q = \rho_{fst} \cdot t_{fst} \cdot A_o \cdot [(h_o - h_{ice}) + h_{hf}] \quad 4-24$$

$$\tau_{defrost} = \frac{Q}{W_{elec}} \quad 4-25$$

Where;  $h_o$  = Enthalpy of melted frost (water) leaving the heat exchanger at 4°C (from measurement),  $h_{ice}$  = Enthalpy of ice at  $[(T_{a,in} + T_{a,out})/2 + T_{interface}]/2$ ,  $h_{hf}$  = Enthalpy of fusion of

the frost and  $W_{elec}$  = the electric power input to the defrosting elements mounted on the heat exchangers.

#### 4.6. Comparison of measured and correlation predicted frost characteristics

The measured frost density, thermal conductivity, thickness and air pressured drop across the frost test coil were compared with those correlation predicted as shown in Figure 4.13 and 4.14. The predicted frost density deviated by  $\pm 25\%$  (see Figure 4.13 (a)) from the measured frost density. Similarly, the predicted frost thermal conductivity deviated by  $\pm 26\%$  (see Figure 4.13 (b)) from the measured frost thermal conductivity.

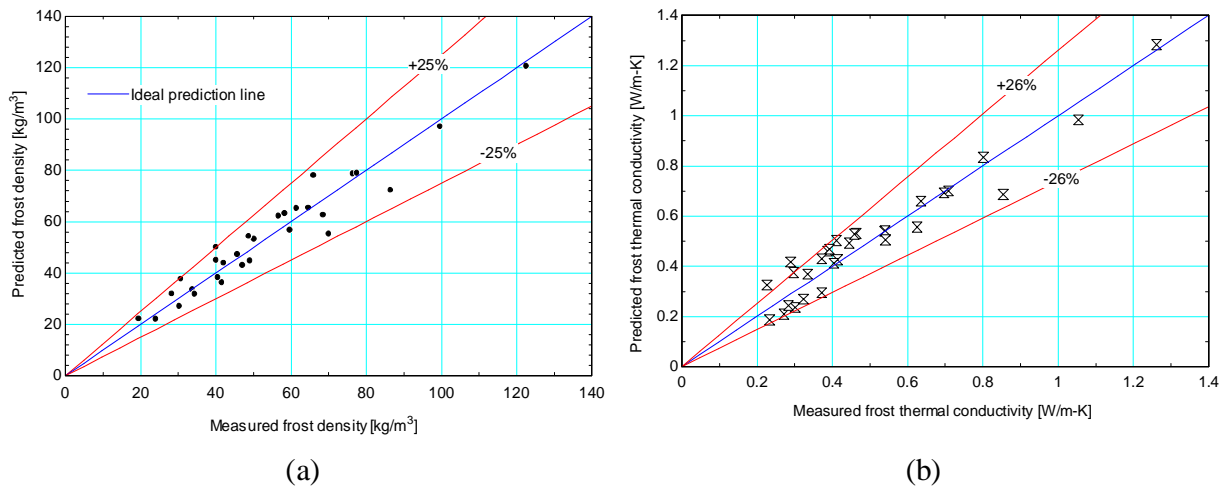


Figure 4.13 Comparison of measured and correlation predicted a) frost density; and b) frost thermal conductivity.

The predicted frost thickness shows a good agreement with the measured frost thickness as shown in Figure 4.14 (a), having a deviation of  $\pm 11\%$  from the measured frost thickness. However, the predicted air pressure drop across the frost test coil deviated by as much as  $\pm 60\%$  from the measured pressure drop as shown in Figure 4.14 (b).



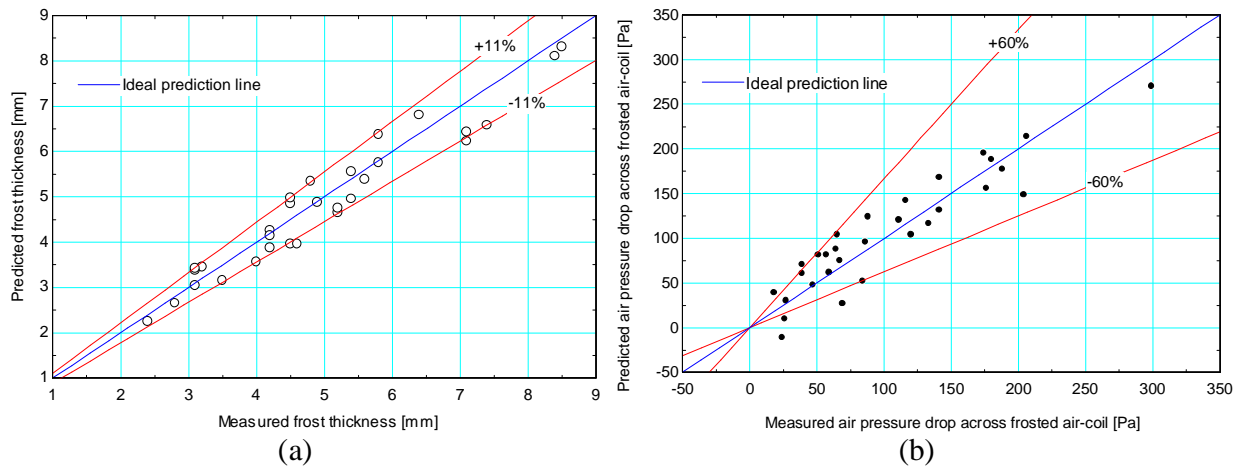


Figure 4.14 Comparison of measured and correlation predicted a) frost thickness; and b) frosted coil air pressure drop.

Deviations of correlation predicted frost characteristics from measured ones depend on several factors, such as the type of functions (e.g. polynomial, exponential or power function), the number of data sets and the number of sensors with different measurement uncertainties used for frost experiment. However, the new frost correlations could also be applied on air-coils having different geometry taking these deviations into consideration. It is also suggested that the correlations need to be used for the same geometry in the current form until such time that they are fully validated on other geometries.

To conclude, four new empirical frost property correlations were developed on a lab-scale flat-finned-tube heat exchanger. These new correlations can reasonably predict frost properties on actual heat exchangers. The experimental results showed that the frost thickness on the fin could be either greater than or equal or lower than the frost thickness on the tubes depending on the fin position for frost-fin and frost-tube interface temperature difference ranging from  $0.5^{\circ}\text{C}$  to  $0.9^{\circ}\text{C}$ . The possible reasons for this were the geometry of surfaces, the position of fins and tubes, and air flow pattern on the test coil. These factors could have played significant role in the distribution of frost on the entire heat transfer surface area of the test coil than the difference between the frost-fin and the frost-tube interface temperature. In general, the newly developed frost property correlations, which were formulated based on the average frost-coil interface

temperature (the arithmetic mean of frost-fin and frost-tube interface temperatures), could be useful for refrigeration engineers to easily estimate the time interval between defrost cycles, the heat input and time span required for defrosting frosted heat exchangers. Energy savings can potentially be achieved in the refrigeration industry if the frost correlations are gainfully applied within the experimental operation regimes during the design phase and the operation of the refrigeration systems.

Additionally, the fundamentals of the experimental techniques have been developed for frost property studies by which any interested researchers can conduct further frost experiments in the future. These new frost property correlations have also been applied on the air-coil numerical model developed for a secondary coolant refrigeration system, discussed in Chapter 5, for medium-temperature applications.

## CHAPTER 5.

# Development of Numerical Model for Secondary Coolant Systems

---

### 5.1. Introduction

In-situ experimental investigation of secondary coolant refrigeration systems in a supermarket store is normally a good way of identifying energy consuming parameters of such systems in order to improve system performance and achieve energy savings. However, conducting actual experiments in supermarket stores is very expensive, time consuming and has inconvenient interference with customers and operation personnel in the establishments. Besides, placement of measurement sensors in display cabinets may result in fatal errors in the bulk data collection process due to the fact that the sensors are normally moved or damaged by customers and supermarket personnel. Thus, a validated complete numerical model of a secondary coolant system is an important tool to predict system performance with a reasonable degree of accuracy for supermarket applications thereby eliminating unnecessary waste of time and resources in supermarket stores.

The numerical model for medium-temperature secondary coolant systems in the current project incorporates air-coil frost property correlations developed for this purpose. Hence, this tool is very useful for the supermarket industry to identify which fluid-component interaction of the system needs improvement. This chapter, in general, presents methodology and approach applied on the development of numerical models for various components of the system. All component models such as air-coil, plate heat exchangers, distribution lines, pumps and compressors and expansion device of the medium-temperature secondary coolant systems will then be linked, as shown in the form of flowchart in Figure 5.1, to form a complete system model. The component models are however discussed in the order different from the one shown in Figure 5.1 for the sake of convenience. After the completion of the overall numerical system model, validation will

be carried out using reliable data collected from a lab-scale test-rig located in the thermodynamics laboratory, the University of Auckland, New Zealand.

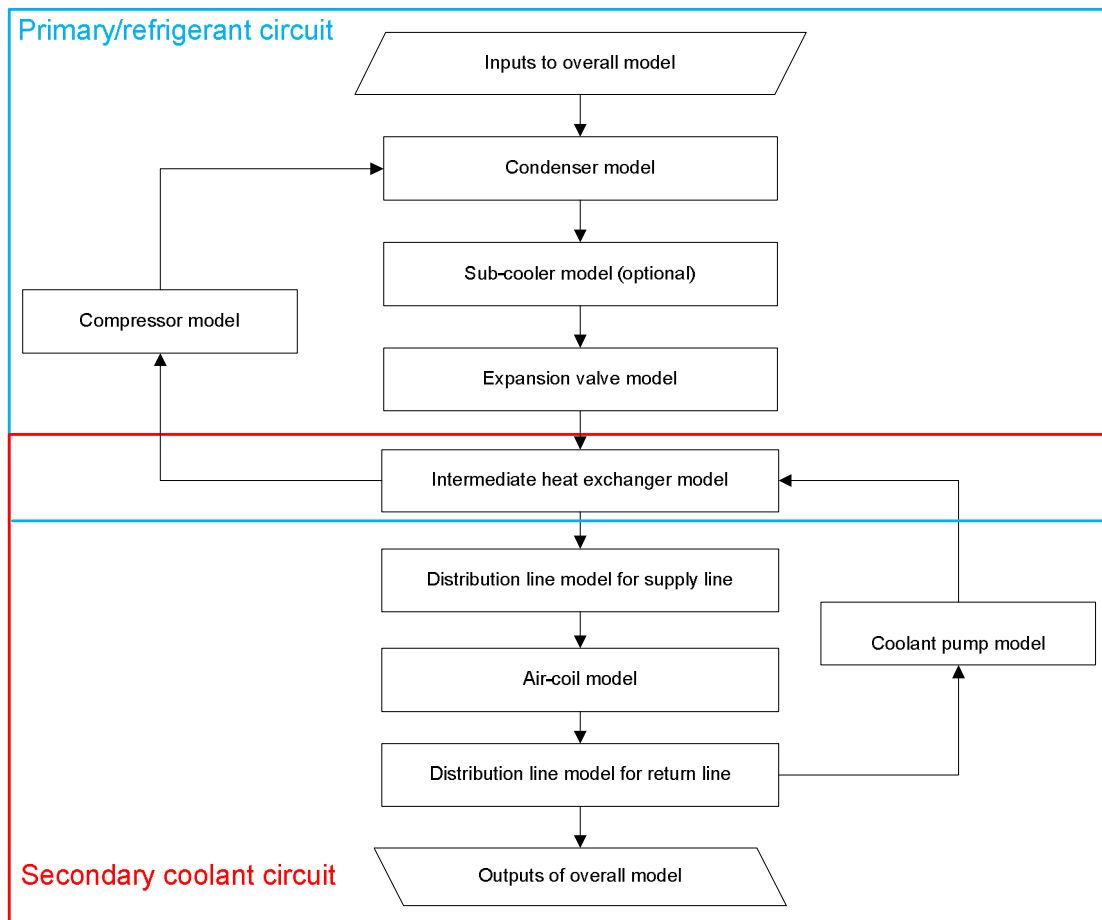


Figure 5.1 Flowchart of medium-temperature secondary coolant refrigeration system model.

## 5.2. Air-coil model

In this project air-coil is the term used to describe a heat exchanger for cooling an incoming air stream using chilled secondary coolants, whereas an evaporator is defined as a heat exchanger used to cool an incoming air stream using an evaporating refrigerant. Hence, keeping these

terms in mind, the following Sub-sections sequentially describe the modeling techniques applied on air-coils (flat-finned-tube heat exchangers) to predict their performance.

### 5.2.1. General assumptions

The following assumptions were used in the calculation procedures of the numerical model to predict the performance of air-coils for medium-temperature secondary coolant refrigeration systems.

- Steady state operation.
- Negligible kinetic and potential energy changes.
- Constant heat transfer coefficients over a heat exchanger element.
- Negligible fouling resistances.
- Negligible heat loss/gain from the surrounding.
- Same number of tubes in each circuit, each with the same fraction of the total mass flow rate. Also constant mass flux of air,  $G_{\max}$  across the air-coil.
- The air-coil is completely frosted.
- Frosting and condensation cannot simultaneously occur on the air-coil surface.

### 5.2.2. Sequence of calculation

The air-coil model divides the average row of the coil into n-number of equal elements (see Figure 5.2) depending on the size of the air-coil, simulation time required and accuracy of the model outputs. The model was written in a software package called Engineering Equation Solver [9], which has built-in properties of many refrigerants and readily available library routines.

### 5.2.3. Inputs

Different types of air-coil inputs (independent variables) are required in order to predict the outputs (dependent variables) of the air-coil numerical model. For instance, geometric

parameters (e.g. tube diameter, fin pitch, tube length, etc); heat exchanger construction material and circuiting information such as number of tubes, rows and so forth should be given as described in the following Sub-Sections. Besides, air-side and coolant-side inlet conditions including mass flowrates should be given for both fluids.

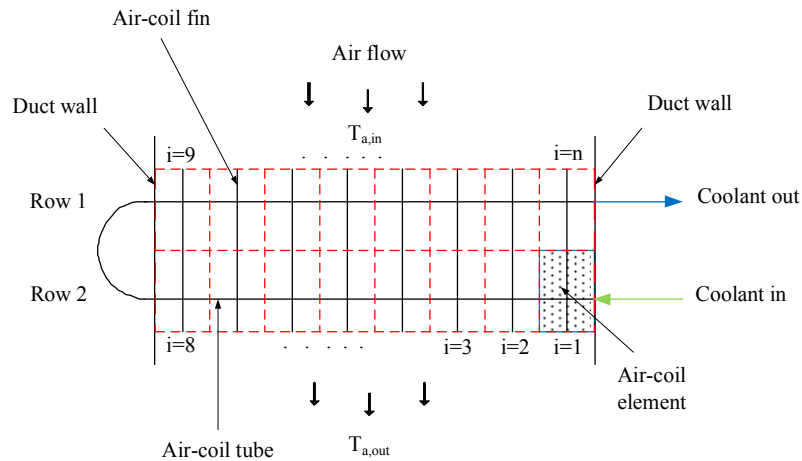


Figure 5.2 Air-coil divided into n-number of elements.

### 5.2.3.1. Air-coil geometrical inputs

• Fin thickness	$\delta_{fin}$
• Coolant tube wall thickness	$\delta_{tube}$
• Coolant tube inner diameter	$D_i = D_o - 2 \times \delta_{tube}$
• Coolant tube outer diameter	$D_o$
• Fin pitch	$F_p$
• Length of the heat exchanger	$L_{hx}$
• Total length of a coolant tube in a circuit	$L_{total}$
• Ratio of total coolant tube length to inner diameter	$L_{overD}$
• Number of circuit in the heat exchanger	$N_{circuit}$
• Number of tubes in the air flow direction	$N_T$
• Number of tubes counted vertically	$N_V$

• Number of elements in a circuit	$n$
• Number of tube passes in a circuit	pass
• Coolant tube inner radius	$r_i$
• Coolant tube outer radius	$r_o$
• Coolant tube roughness	relRough
• Vertical distance between tubes (centre-to-centre)	$S_T$
• Horizontal distance between tubes (centre-to-centre)	$W_T$
• Construction material of fin and tube	Copper

#### 5.2.3.2. Air- and coolant-side inputs

• Air inlet dry bulb temperature	$T_{a,in}$
• Air inlet dew point temperature	$DP_{a,in}$
• Air humidity ratio	$\omega_{a,in}$
• Air mass flowrate	$\dot{m}_a$
• Air inlet pressure	$P_{a,in}$
• Air-coil-frost interface temperature	$T_{interface}$
• Secondary coolant type	SC\$
• Coolant concentration by weight (%)	Concentration
• Coolant inlet temperature for the first element	$T_{sc,in}$
• Coolant mass flowrate	$\dot{m}_{sc}$
• Time span required before defrosting starts	$\tau$
• Electric power input to defrosting elements	$W_{elec}$

#### 5.2.4. Outputs

The outputs (dependent variables) of the air-coil numerical model such as air outlet conditions, frost thermal conductivity, frost density, frost thickness, air-side pressure drop, secondary

coolant outlet conditions, coolant-side total pressure drop, overall heat transfer coefficient, heat exchanger effectiveness and rate of heat transfer are described in detail below.

#### 5.2.4.1. Air- and coolant-side outputs

• Air outlet temperature from an air-coil element	$T_{a,out}[i]$
• Average air exit temperature from the entire air-coil	$T_{a,out,avg}$
• Air outlet dew point temperature from an air-coil element	$DP_{a,out}[i]$
• Average air outlet dew point temperature from the entire air-coil	$DP_{a,out,avg}$
• Air outlet relative humidity from an air-coil element	$RH_{a,out}[i]$
• Average air outlet relative humidity from the entire air-coil	$RH_{a,out,avg}$
• Air outlet humidity ratio from an air-coil element	$\omega_{a,out}[i]$
• Average air outlet humidity ratio from the whole air-coil	$\omega_{a,out,avg}$
• Air-side heat transfer coefficient over an air-coil element	$h_a[i]$
• Air-side latent convective heat transfer coefficient over an air-coil element	$h_{a,lat}[i]$
• Average frost thermal conductivity over the whole air-coil	$k_{fst,avg}$
• Average frost thickness over the whole air-coil	$t_{fst,avg}$
• Average frost density over the whole air-coil	$\rho_{fst,avg}$
• Average air pressure drop over the whole air-coil	$\Delta P_{a,coil,avg}$
• Secondary coolant exit temperature from an air-coil element	$T_{sc,out,i}$
• Secondary coolant exit temperature from the whole air-coil	$T_{sc,out}$
• Coolant-side heat transfer coefficient over an air-coil element	$h_{sc}[i]$
• Fin efficiency in an air-coil element	$\eta_{fin}[i]$
• Overall heat transfer coefficient in an air-coil element	$U[i]$
• Average overall heat transfer coefficient over the whole air-coil	$U_{avg}$
• Effectiveness of an air-coil element	$\varepsilon[i]$
• Average effectiveness of the whole air-coil	$\varepsilon_{avg}$
• Total secondary coolant pressure drop in the air-coil pipes and manifolds	$\Delta P_{SC}$
• Defrosting heat input the air-coil [J]	$Q$
• Time span for defrosting the air coil [s]	$\tau_{defrost}$



- Heat exchanger capacity

$$\dot{Q}_{a,coil}$$

### 5.2.5. Air-side heat transfer coefficient and pressure drop

The convective heat transfer coefficient on the air-side of the air-coil element is evaluated in terms of a 'j-factor' from Kim et al [59] following Equations 5-4 and 5-6.

Mass flux, as a function of free-flow frontal area and air mass flowrate in a frontal air-coil element per circuit, can be determined by;

$$G_{ma,i} = \frac{\dot{m}_a}{A_{free,flow} \cdot (N_{circuit} \cdot n / pass)} \quad \text{for } i = 1 \text{ to } n \quad 5-1$$

Reynolds number for air-side heat transfer coefficient is determined based on tube outside diameter by;

$$Re_{Da,i} = G_{ma,i} \cdot \frac{D_o}{\mu_{a,in,i}} \quad \text{for } i = 1 \text{ to } n \quad 5-2$$

Prandtl number for the air-side heat transfer coefficient is given by;

$$Pr_i = C_p m a_i \times \frac{m_{a,in,i}}{k_{a,in,i}} \quad \text{for } i = 1 \text{ to } n \quad 5-3$$

Colburn-j factor for a heat exchanger with 3 or more tubes in the air flow direction is determined by;

$$j_{3N,i} = 0.24 \times Re_{Da,i}^{-0.409} \cdot (S_T / W_T)^{0.425} \cdot (S_F / D_o)^{-0.035} \quad \text{for } i = 1 \text{ to } n \quad 5-4$$

The air-side heat transfer coefficient for an air-coil element based on 3 or more tubes in the air flow direction is obtained from;

$$h_{a,i} = j_{3N,i} \cdot G_{ma,i} \cdot \frac{Cpma_{in,i}}{Pr_i^{2/3}} \quad \text{for } i = 1 \text{ to } n \quad 5-5$$

Colburn-j factor for a heat exchanger with less than 3 tubes in the air flow direction is given by;

$$j_{N,i} = j_{3N,i} \cdot 0.931 \cdot \left[ Re_{Da,i}^{-0.162} \cdot (S_T / W_T)^{-0.892} \cdot (S_F / D_o)^{-0.152} \cdot (S_T / D_o)^{1.49} \right]^{(3-N_T)} \quad 5-6$$

The air-side heat transfer coefficient for an air-coil element based on less than 3 tubes in the air flow direction is obtained from;

$$h_{a,i} = j_{N,i} \cdot G_{ma,i} \cdot \frac{Cpma_i}{Pr_i^{2/3}} \quad \text{for } i = 1 \text{ to } n \quad 5-7$$

The latent convective heat transfer coefficient over an air-coil element is determined by;

$$h_{a,lat,i} = h_{a,i} \cdot H_{sg,i} \cdot \frac{C_i}{Le \cdot Cpma_i} \quad \text{for } i = 1 \text{ to } n \quad 5-8$$

Latent heat of sublimation is estimated from a correlation proposed by Ismail and Salinas [41].

$$H_{sg,i} = \left[ -0.04667 \times (1.8 \times T_{a,ave,i} + 32) + 1220.1 \right] \times 2322 \quad \text{for } i = 1 \text{ to } n \quad 5-9$$

The average temperature in an air-coil element described in Equation 5-9 is given by;

$$T_{a,ave,i} = \frac{T_{a,in,i} + T_{sc,in,i}}{2} \quad \text{for } i = 1 \text{ to } n \quad 5-10$$

Variable  $C_i$  in an air-coil element described in Equation 5-8 is given by;

$$C_i = \frac{\omega_{a,in,i} - \omega_{a,out,i}}{\Delta T_i} \quad \text{for } i = 1 \text{ to } n \quad 5-11$$

The temperature difference in an air-coil element described in Equation 5-11 is given by;

$$\Delta T_i = (T_{a,in,i} - T_{a,out,i}) \quad \text{for } i = 1 \text{ to } n \quad 5-12$$

whereas the Lewis number (Le) described in Equation 5-8 is approximated to unity. The air-side heat transfer coefficient for an air-coil element calculated either from Equation 5-5 or 5-7 should be inserted in Equation 5-8 in order to calculate the latent convective heat transfer coefficient.

Air pressure drop across the frosted air-coil is calculated by Equation 4-19.

### 5.2.6. Coolant-side heat transfer coefficient and pressure drop

The average Nusselt numbers and friction factors in a circular pipe for developing or fully-developed flow in the laminar, transitional or turbulent flow regimes are calculated from Nellis and Klein [60] using EES [9] routine.

For a laminar flow in the air-coil circular pipe element (i.e. for  $Re_i < 2300$ ), the average Nusselt number can be calculated, assuming a constant wall heat flux, by;

$$Nusselt_{sc,i} = 4.36 + \frac{\left(0.1156 + \frac{0.08569}{Pr_{sc,i}^{0.4}}\right) \times \left(\frac{Re_{sc,i} \times Pr_{sc,i}}{L_{hx,e} / D_i}\right)}{1 + 0.1158 \times \left(\frac{Re_{sc,i} \times Pr_{sc,i}}{L_{hx,e} / D_i}\right)^{0.6}} \quad \text{for } i = 1 \text{ to } n \quad 5-13$$

whereas, the friction factor is obtained from;

$$f_{sc,i} = \frac{4}{Re_{sc,i}} \times \left[ \frac{3.44}{\sqrt{\left(\frac{L_{hx,e}}{D_i}\right)}} + \frac{\frac{1.25}{4 \times \left(\frac{L_{hx,e}}{D_i}\right)} + 16 - \sqrt{\left(\frac{L_{hx,e}}{D_i}\right)}}{1 + 0.00021 \times \left(\frac{L_{hx,e}}{D_i}\right)^{-2}} \cdot \sqrt{\left(\frac{L_{hx,e}}{D_i}\right)} \right] \quad \text{for } i = 1 \text{ to } n \quad 5-14$$

The dimensionless parameters such as Reynolds and Prandtl numbers in the circular pipe are calculated by Equations 5-16 and 5-17, respectively.

$$Re_{sc,i} = \frac{G_{m,sc,i} \cdot D_i}{\mu_{c,in,i}} \quad \text{for } i = 1 \text{ to } n \quad 5-15$$

$$Pr_{sc,i} = Cp_{sc,in,i} \cdot \frac{\mu_{sc,in,i}}{k_{sc,in,i}} \quad \text{for } i = 1 \text{ to } n \quad 5-16$$

For a turbulent and transitional flow in the air-coil circular pipe element (i.e. for  $Re_i > 2300$ ), the friction factor and the average Nusselt number are calculated by the following sequence of equations.

The friction factor is calculated based on Petukhov [61], which accounts for developing flow.

$$\text{for } i = 1 \text{ to } n$$

$$f_{sc,i} = \left[ -2 \cdot \log \left( 2 \cdot \frac{relRough}{7.4} - 5.02 \cdot \frac{\log \left( \frac{2 \cdot Relrough}{7.4} + \frac{13}{Re_{sc,i}} \right)}{Re_{sc,i}} \right) \right]^{-2} \cdot \left( 1 + \left( \frac{1}{L_{hx,e}/D_i} \right)^{0.7} \right) \quad 5-17$$

The Nusselt number is calculated based on Gnielinski [62], which accounts for developing flow.

for  $i = 1$  to  $n$

$$Nusselt_{sc,i} = \frac{\left( (0.79 \times \ln(Re_{sc,i}) - 1.64)^{-2} / 8 \right) \times (Re_{sc,i} - 1000) \times Pr_{sc,i}}{1 + 12.7 \times \sqrt{\left( (0.79 \times \ln(Re_{sc,i}) - 1.64)^{-2} / 8 \right) \times (Pr_{sc,i}^{2/3} - 1)}} \times \left( 1 + \left( \frac{L}{L_{hx,e} / D_i} \right)^{0.7} \right) \quad 5-18$$

The average heat transfer coefficient of the secondary coolant (for laminar or turbulent flow) in an air-coil pipe element is calculated by;

$$h_{sc,i} = Nusselt_i \cdot \frac{k_{c,ini}}{D_i} \quad \text{for } i = 1 \text{ to } n \quad 5-19$$

The coolant pressure drop in an air-coil pipe element is given by;

$$\Delta P_{sc,i} = f_{sc,i} \cdot \rho_{sc,ini} \cdot \frac{L_{hx,e}}{D_i} \cdot \frac{v_{sc,i}^2}{2} \quad \text{for } i = 1 \text{ to } n \quad 5-20$$

The total coolant pressure drop in an air-coil due to a contraction loss at entry, expansion loss at exit, plus a 180° turn-around if there is more than one tube-side pass, will be given following reference [63] by;

$$\Delta P_h = K_h \cdot \left( \rho_{sc,ini} \cdot \frac{v_{sc,i}^2}{2} \right) \cdot pass \quad 5-21$$

Where  $K_h = 0.9$  for one tube-side pass; and  $K_h = 1.6$  for two or more passes including U-tubes.

The total pressure drop in the air-coil circuit or the entire air-coil is given by;

$$\Delta P_{sc,coil,total} = \left( \sum_{i=1}^n \Delta P_{sc,i} \quad \text{for } i = 1 \text{ to } n \right) + \Delta P_h \quad 5-22$$

The index  $i$  represents the  $i^{th}$  element, whereas  $n$  represents the total number of elements in an air-coil circuit.

**5.2.7. Effectiveness-NTU method for air-coil analysis**

Whenever only the inlet conditions of both air and secondary coolant fluids in the air-coil are known, we need to use effectiveness-NTU method to figure out the exit conditions of the fluids. Nevertheless, the exit conditions are computed iteratively and are very time consuming, especially, if the air-coil is subdivided into a large number of elements. Thus, the number of elements in the heat exchanger should be reasonably determined based on the degree of accuracy and variable change required in the calculated values. Otherwise, a lot of time will be wasted unnecessarily during simulation process.

The first step in the effectiveness-NTU method is to calculate overall heat exchanger efficiency, if the air-coil is a finned-tube heat exchanger type. Hence, the overall efficiency is determined by;

$$\eta_o = 1 - \frac{A_{fin}}{A_{total}}(1 - \phi_f) \quad 5-23$$

whereas the fin efficiency ( $\phi_f$ ) described in Equation 5-23 for circular fins with insulated tips may be calculated analytically by;

$$\phi_f = \left( \frac{2 \times r_l}{m \times (r_2^2 - r_l^2)} \right) \times \frac{K_l \times (m \times r_l) \times I_l \times (m \times r_2) - I_l \times (m \times r_l) \times K_l \times (m \times r_2)}{K_o \times (m \times r_l) \times I_l \times (m \times r_2) + I_o \times (m \times r_l) \times K_l \times (m \times r_2)} \quad 5-24$$

If the fin of the heat exchanger is not of circular type its outside radius can be approximated by;

$$r_2 = \frac{S_T + W_T}{4} \quad 5-25$$

whereas,  $r_l$  is equal to the air-coil pipe outer radius ( $D_o/2$ ).

For dry coil, the parameter  $m$  described in Equation 5-24 excludes the latent heat transfer coefficient ( $h_{lat}$ ) whereas for frosted coil it takes the form;

$$m = \left[ \frac{2 \times (h_a + h_{lat})}{k_{fin} \times t_{fin}} \right]^{(1/2)} \quad 5-26$$

$I_0$  and  $K_0$  are the modified zero-order Bessel functions of the first and second kinds, respectively whereas  $I_1$  and  $K_1$  are the modified first-order Bessel functions of the first and second kinds, respectively.

#### 5.2.7.1. Heat exchanger effectiveness

Heat exchanger effectiveness is defined as the ratio of the actual rate of heat transfer to the maximum possible rate of heat transfer in a heat exchanger. Hence, the effectiveness of a given heat exchanger element can be given by;

$$\epsilon_i = \frac{\dot{Q}_{act,i}}{\dot{Q}_{max,i}} \quad \text{for } i = 1 \text{ to } n \quad 5-27$$

The maximum possible rate of heat transfer in the air-coil element is determined by;

$$\dot{Q}_{max,i} = C_{min,i} \cdot (T_{a,in,i} - T_{sc,in,i}) \quad \text{for } i = 1 \text{ to } n \quad 5-28$$

The actual rate of heat transfer in the air-coil element is obtained from;

$$\dot{Q}_{act,i} = \epsilon_i \cdot C_{min,i} \cdot (T_{a,in,i} - T_{sc,in,i}) \quad \text{for } i = 1 \text{ to } n \quad 5-29$$

The actual rate of heat transfer on the air-side of the air-coil element is calculated by;

$$\dot{Q}_{act,i} = \dot{m}_{a,i} \cdot C_{pma_i} \cdot (T_{a,in,i} - T_{a,out,i}) \quad \text{for } i = 1 \text{ to } n \quad 5-30$$

The actual rate of heat transfer on the air-side is equated to the rate of heat transfer on the secondary coolant-side as;

$$\dot{m}_{sc,i} \cdot Cp_{sc,i} \cdot (T_{sc,out,i} - T_{sc,in,i}) = \dot{m}_{a,i} \cdot Cp_{ma,i} \cdot (T_{a,in,i} - T_{a,out,i}) \quad \text{for } i = 1 \text{ to } n \quad 5-31$$

The air-coil effectiveness-NTU relationship is computed based on the correlations for cross flow, which considers the secondary coolant and the air as unmixed fluids. Hence, the effectiveness of a given air-coil element is given by;

$$\epsilon_i = 1 - \exp\left(\left(\frac{NTU_i^{0.22}}{C_i}\right) \cdot \left(\exp(-C_i \cdot NTU_i^{0.78}) - 1\right)\right) \quad \text{for } i = 1 \text{ to } n \quad 5-32$$

The number of heat transfer units ( $NTU$ ), which is dimensionless, for an air-coil element is given by;

$$NTU_i = \frac{UA_i}{C_{min,i}} \quad \text{for } i = 1 \text{ to } n \quad 5-33$$

The product of the overall heat transfer coefficient and area of an air-coil element can be obtained from;

$$\text{for } i = 1 \text{ to } n$$

$$UA_i = \frac{1}{\frac{1}{(h_{a,i} + h_{a,lat,i}) \cdot (A_{o,e} \cdot \eta_{o,i})} + \frac{\ln(r_o / r_i)}{2 \cdot \pi \cdot L_{hx,e} \cdot k_{tube,i}} + \frac{t_{fst,i}}{k_{fst,i} \cdot 1000 \cdot A_{o,e} \cdot \eta_{o,i}} + \frac{1}{(h_{i,i} \cdot A_{i,e})}} \quad 5-34$$

The fouling resistances of the fluids and the contact resistance between the fins and the tubes of the air-coil have been neglected in Equation 5-34, since the overall heat transfer coefficient is predominantly influenced by the heat transfer coefficients of the fluids and the thermal conductivities of the tube and frost of the air-coil. It is also worth mentioning that the overall elemental efficiency ( $\eta_{o,i}$ ) described in Equations 5-34 should be calculated based on the



operating conditions of the air-coil element, since the parameter  $m$  described Equations 5-24 and 5-26 may be different for each element, whereas the fin radii ( $r_1$  and  $r_2$ ) remain the same.

The frost thickness ( $t_{fst}$ ) and thermal conductivity ( $k_{fst}$ ) described in Equation 5-34 are obtained from Equations 4-16 and 4-18, respectively.

The overall heat transfer coefficient in an air-coil element is determined by;

$$U_i = \frac{UA_i}{A_{o,e}} \quad \text{for } i = 1 \text{ to } n \quad 5-35$$

The heat capacity rates for both air and secondary coolant as a function of the inlet conditions are given respectively by the following equations.

$$C_{a,i} = Cp_{a,i} \cdot \dot{m}_{a,i} \quad \text{for } i = 1 \text{ to } n \quad 5-36$$

$$C_{sc,i} = Cp_{sc,i} \cdot \dot{m}_{sc,i} \quad \text{for } i = 1 \text{ to } n \quad 5-37$$

The minimum heat capacity rate over an air-coil element will be;

$$C_{min,i} = \min(C_{a,i}, C_{sc,i}) \quad \text{for } i = 1 \text{ to } n \quad 5-38$$

The elemental air mass flowrate over a given air-coil element is given by;

$$\dot{m}_{a,i} = \frac{\dot{m}_a}{N_{circuit} \times (n / pass)} \quad \text{for } i = 1 \text{ to } n \quad 5-39$$

whereas, secondary coolant mass flowrate in a given air-coil element is given by;

$$\dot{m}_{sc,i} = \frac{\dot{m}_{sc}}{N_{circuit}} \quad \text{for } i = 1 \text{ to } n \quad 5-40$$

The calculations of geometrical parameters of the air-coil element are given in the following sequence of equations.

The air-coil element length perpendicular to air flow direction is given by;

$$L_{hx,e} = \frac{L_{hx}}{(n / pass)} \quad \text{for } i = 1 \text{ to } n \quad 5-41$$

The bare tube outside surface area of the air-coil element is given by;

$$A_{tube,e} = \frac{A_{tube}}{N_{circuit} \cdot n} \quad \text{for } i = 1 \text{ to } n \quad 5-42$$

Tube internal surface area of the air-coil element is given by;

$$A_{i,e} = \frac{A_i}{N_{circuit} \cdot n} \quad \text{for } i = 1 \text{ to } n \quad 5-43$$

Fin surface area of the air-coil element is given by;

$$A_{fin,e} = \frac{A_{fin}}{N_{circuit} \cdot n} \quad \text{for } i = 1 \text{ to } n \quad 5-44$$

Total outside surface area of the air-coil element is given by;

$$A_{o,e} = \frac{A_o}{N_{circuit} \cdot n} \quad \text{for } i = 1 \text{ to } n \quad 5-45$$

Geometrical parameters of the entire air-coil (without being divided into elements) can be calculated in the following sequence of equations.

The total number of tubes in the air-coil is given by;

$$N_{total} = N_T \cdot N_V \quad 5-46$$

Effective flow length of the air-coil along the air flow direction is given by;

$$L_{flow} = N_T \cdot W_T \quad 5-47$$

The frontal area of the air-coil is;

$$A_{fr} = L_{hx} \cdot S_T \cdot N_V \quad 5-48$$

The fin heat transfer area is;

$$A_{fin} = 2 \cdot L_{hx} \cdot F_p \cdot N_{total} \cdot \left( S_T \cdot W_T - \pi \cdot \frac{D_o^2}{4} \right) \quad 5-49$$

The bare tube surface area is;

$$A_{tube} = N_{total} \cdot \pi \cdot D_o \cdot L_{hx} \cdot (1 - F_p \cdot \delta_{fin}) \quad 5-50$$

The minimum flow area is;

$$A_{min} = L_{hx} \cdot N_V \cdot (S_T - D_o) \cdot (1 - F_p \cdot \delta_{fin}) \quad 5-51$$

The free-flow frontal area is;

$$A_{free,flow} = A_{fr} - N_V \cdot D_o \cdot L_{hx} \cdot (1 - F_p \cdot \delta_{fin}) - L_{hx} \cdot (N_V \cdot S_T) \cdot F_p \cdot \delta_{fin} \quad 5-52$$

The total outside air-coil area;

$$A_o = A_{fin} + A_{tube} \quad 5-53$$

The total tube internal surface area is;

$$A_i = N_{total} \cdot \pi \cdot D_i \cdot L_{hx} \quad 5-54$$

The fin spacing is;

$$S_F = I / F_p \quad 5-55$$

The ratio of minimum air-coil face area to the frontal area is;

$$\sigma = A_{min} / A_{fr} \quad 5-56$$

Air outlet temperature from an air-coil element can be readily available from;

$$T_{a,out,i} = T_{a,in,i} - \epsilon_i \cdot C_{min,i} \cdot \frac{T_{a,in,i} - T_{sc,in,i}}{(\dot{m}_a \cdot Cp_{ma_i})} \quad \text{for } i = 1 \text{ to } n \quad 5-57$$

whereas, the secondary coolant outlet temperature from an air-coil element is obtained from;

$$T_{sc,out,i} = \epsilon_i \cdot C_{min,i} \cdot \frac{T_{a,in,i} - T_{sc,in,i}}{\dot{m}_c \cdot Cp_{sc,i}} + T_{sc,in,i} \quad \text{for } i = 1 \text{ to } n \quad 5-58$$

The other air outlet properties such as humidity ratio ( $\omega$ ) and dew point temperature (DP) from an air-coil element are calculated as a function of the outlet air temperature, relative humidity ( $RH = 1$ ) and air inlet pressure using built-in property functions from EES [9]. Hence, the air outlet humidity ratio is given by;

$$\omega_{a,out,i} = f(T = T_{a,out,i}, R = RH_{a,out,i}, P = P_{a,in,i}) \quad \text{for } i = 1 \text{ to } n \quad 5-59$$

whereas, the air outlet dew point temperature is obtained from;

$$DP_{a,out,i} = f \left( T = T_{a,out,i}, R = RH_{a,out,i}, P = P_{a,in,i} \right) \quad \text{for } i = 1 \text{ to } n \quad 5-60$$

The average air inlet temperature, which is an input, for all air-coil elements (see Figure 5.1) in the first row of an air-coil circuit will have the same value; whereas the average air temperature leaving the first row of the air-coil circuit, which is considered to be the inlet temperature of all elements in the second row of the air-coil circuit is calculated by;

$$T_{a,out,avg,row1} = \frac{\sum_{i=(n/2+1)}^n (T_{a,out,i})}{n - (n/2 + 1)} \quad 5-61$$

Therefore, the air inlet temperature for each element in the second row of an air-coil circuit is given by;

$$T_{a,in,i} = T_{a,out,avg,row1} \quad \text{for } i = 1 \text{ to } n/2 \quad 5-62$$

The average outlet temperature from the second row of the air-coil circuit (the entire air-coil) is given by;

$$T_{a,out,avg,row2} = \frac{\sum_{i=1}^{n/2} (T_{a,out,i})}{n/2} \quad 5-63$$

The average dew point temperature leaving the first row of the air-coil circuit, which is considered to be the inlet dew point temperature of all elements in the second row of an air-coil circuit, is calculated by;

$$DP_{a,out,avg,row1} = \frac{\sum_{i=(n/2+1)}^n (DP_{a,out,i})}{n - (n/2 + 1)} \quad 5-64$$

The inlet dew point temperature for each element in the second row of an air-coil circuit is given by;

$$DP_{a,in,i} = DP_{a,out,avg,row1} \quad \text{for } i = 1 \text{ to } n/2 \quad 5-65$$

The average outlet dew point temperature from the second row of the air-coil circuit (the entire air-coil) is given by;

$$DP_{a,out,avg,row2} = \frac{\sum_{i=1}^{n/2} (DP_{a,out,i})}{n/2} \quad 5-66$$

The average humidity ratio leaving the first row of the air-coil circuit, which is considered to be the inlet humidity ratio of all elements in the second row of an air-coil circuit, is calculated by;

$$\omega_{a,out,avg,row1} = \frac{\sum_{i=(n/2+1)}^n (\omega_{a,out,i})}{n - (n/2 + 1)} \quad 5-67$$

The inlet humidity ratio for each element in the second row of an air-coil circuit is given by;

$$\omega_{a,in,i} = \omega_{a,out,avg,row1} \quad \text{for } i = 1 \text{ to } n/2 \quad 5-68$$

The average outlet dew point temperature from the second row of the air-coil circuit (the entire air-coil) is given by;

$$\omega_{a,out,avg,row2} = \frac{\sum_{i=1}^{n/2} (\omega_{a,out,i})}{n/2} \quad 5-69$$

Given the inlet temperature of the secondary coolant of the air coil circuit, the inlet temperature of the consecutive neighboring elements of an air-coil is computed in the following manner;

$$T_{sc,in,i+1} = T_{c,out,i} \quad \text{for } i = 1 \text{ to } n-1 \quad 5-70$$

Finally, the average overall heat transfer coefficient, effectiveness and the total rate of heat transfer of the air-coil are respectively calculated using Equations 5-71 through 5-73. Additionally, the general air-coil simulation flowchart has been given in Figure 5.3

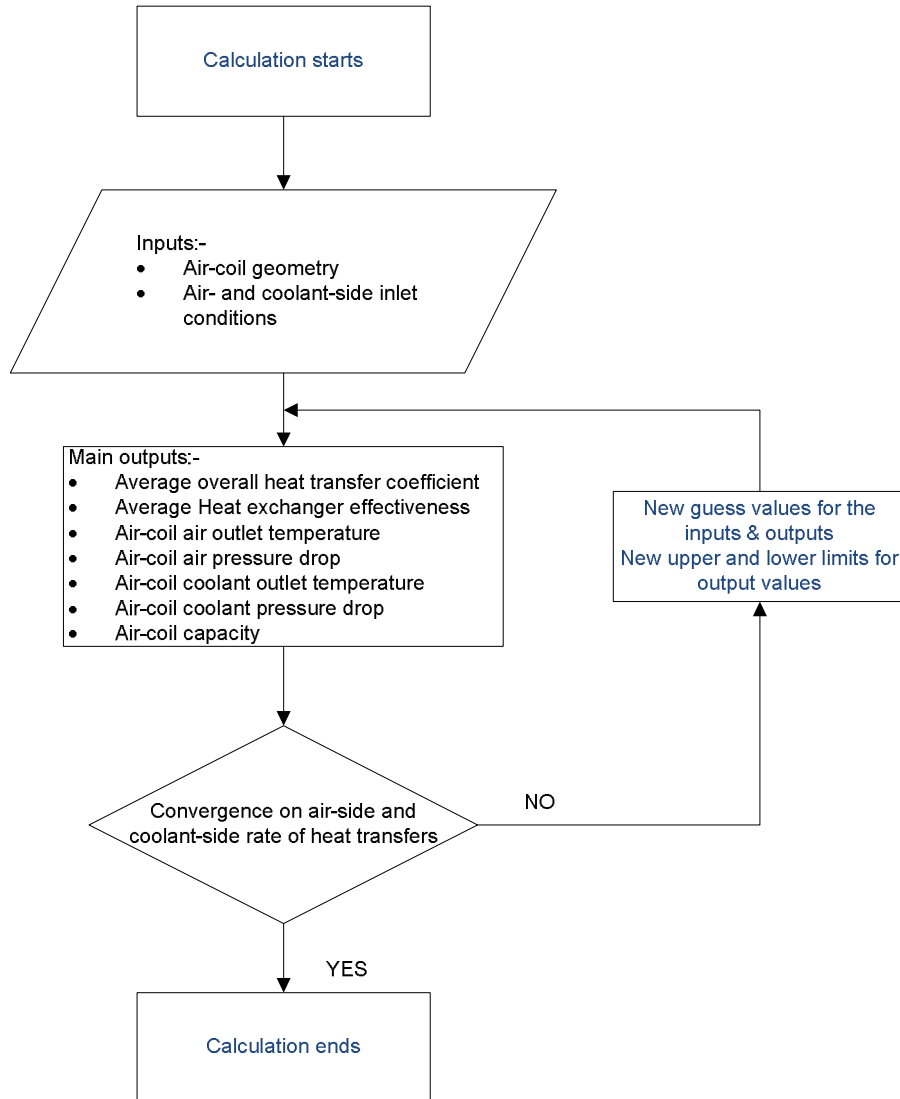


Figure 5.3 Air-coil simulation flowchart to predict frosted air-coil performance for medium-temperature secondary coolant applications.

$$U_{avg} = \frac{\sum_{i=1}^n U_i}{n} \quad 5-71$$

$$\epsilon_{avg} = \frac{\sum_{i=1}^n \epsilon_i}{n} \quad 5-72$$

$$\dot{Q}_{total} = \sum_{j=1}^m \sum_{i=1}^n \dot{Q}_{act,i}$$

5-73

Where the indices (i) and (j) represent the  $i^{th}$  element and the  $j^{th}$  circuit of the air-coil, respectively. The variable (n) represents the total number of elements in a single air-coil circuit, whereas (m) represents the total number of circuits in the air-coil.

### 5.3. Plate heat exchanger models

Conventional plate heat exchangers consist of a stack of thin corrugated plates assembled together using metal frames, bolts and gaskets for sealing. These types of plate heat exchangers were mostly used for single-phase flow applications. However, they were later in use for two-phase heat transfer in evaporators and condensers for chillers and heat pump applications [64, 65]. However, the requirements of high-pressure, high-temperature, compactness and efficiency led to the development of brazed plate heat exchangers. Unlike the conventional plate heat exchangers, the brazed plate heat exchangers are formed by vacuum brazing (i.e. without the involvement of gaskets, tightening bolts and frames) the stainless steel (AISI 316) plates, which are in contact the fluids, with pure copper material.

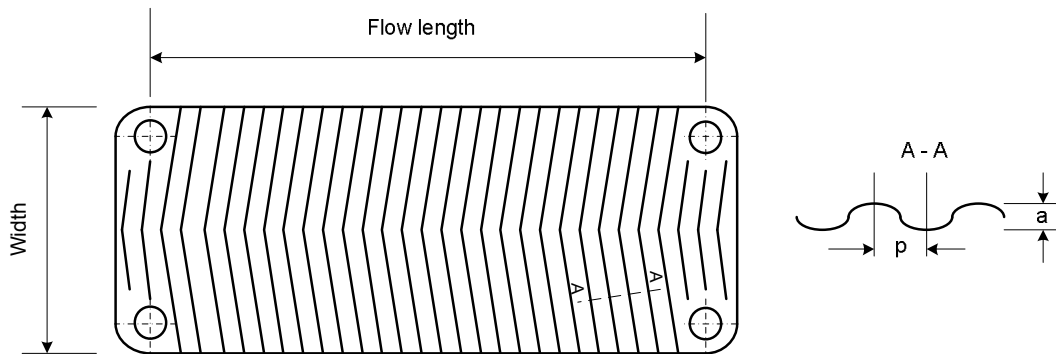


Figure 5.4 A typical brazed plate heat exchanger plate.

All of the plate heat exchangers such as sub-cooler, condenser and intermediate heat exchanger for the present secondary coolant system (see Figure 4.2), which are numerically modeled under



this Section, have herringbone pattern (see Figure 5.4), i.e. the corrugations are pressed to the same depth as the plate spacing. The chevron angle is reversed on adjacent plates in such a way that when the plates are clamped together the corrugations cross one another to provide numerous contact points. The herringbone type, hence, has greater strength than the washboard type, which is capable of withstanding higher pressures with smaller plate thickness [66].

### **5.3.1. General assumptions**

The following assumptions were used in the calculation procedures of the numerical model to predict the performance of plate heat exchanger for medium-temperature secondary coolant refrigeration systems.

- Negligible heat loss to the surroundings.
- Negligible kinetic and potential energy changes.
- Constant fluid properties and heat transfer coefficients over a heat exchanger element.
- Negligible fouling resistance.
- Fully developed conditions for the fluids.

### **5.3.2. Sub-cooler model**

The sub-cooler is treated as a single-phase plate heat exchanger and its model divides the plate heat exchanger into n-number of equal elements perpendicular to flow direction (see Figure 5.5) depending on the size of the heat exchanger, simulation time required and accuracy of the model outputs. The model was written in a software package called Engineering Equation Solver [9].

#### **5.3.2.1. Inputs**

Different types of plate heat exchanger inputs (independent variables) are required in order to predict the outputs (dependent variables) of the sub-cooler numerical model. Geometric parameters, such as number of channels, gap between channels, and so forth should be given as

described in the following Sub-Sections. Besides, the construction material of the heat exchanger plates, water-side and refrigerant-side inlet conditions including mass flowrates should be given for both fluids.

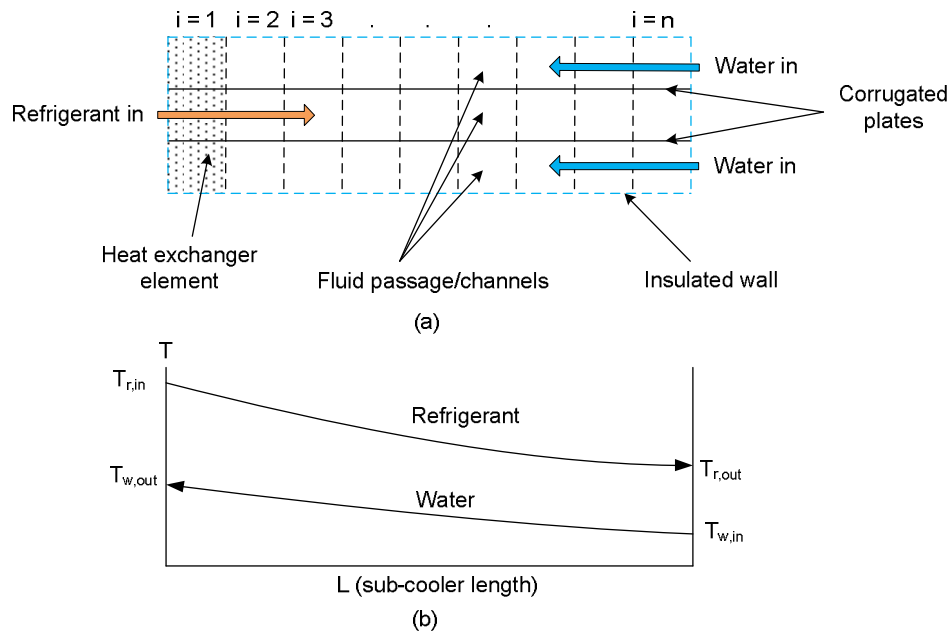


Figure 5.5 Sub-cooler (a) divided into  $n$ -number of elements with equal size; and (b) temperature distribution for a counterflow arrangement.

#### 5.3.2.1.1. Sub-cooler geometrical inputs

- Plate thickness  $\delta_{sub,plate}$
- Effective flow length of the fluid in the heat exchanger in flow direction  $L_{sub,flow}$
- Diagonal flow length between two ports of the heat exchanger  $L_{sub,flow,d}$
- Effective width of the heat exchanger  $W$
- Mean plate gap or amplitude  $a$
- Number of plates of the sub-cooler  $N_{sub,plates}$
- Number of refrigerant ports  $N_{r,p}$
- Number of water ports  $N_{w,p}$
- Number of channels on the water-side  $N_{channel,w}$

- Number of channels on the refrigerant-side  $N_{\text{channel},r}$
- Number of elements the heat exchanger is divided into  $n$
- Port inner diameter  $D_{\text{port},i}$
- Heat transfer area of a single plate on both sides  $A_{\text{plate}}$
- Port cross-sectional area  $A_{\text{port}}$
- Channel cross-sectional area  $A_s$
- Total heat transfer area of the heat exchanger  $A_{\text{total}}$
- Number of flow pass in the sub-cooler  $\text{pass}$
- Hydraulic diameter  $D_e$

#### 5.3.2.1.2. Refrigerant- and water-side inputs

- Water inlet temperature  $T_{w,in}$
- Ambient pressure  $P_{\text{atm}}$
- Mass flowrate of water  $\dot{m}_w$
- Refrigerant inlet temperature  $T_{r,in}$
- Refrigerant inlet pressure  $P_{a,in}$
- Mass flowrate of refrigerant  $\dot{m}_r$
- Refrigerant type  $R\$$

#### 5.3.2.2. Outputs

The outputs (dependent variables) of the sub-cooler numerical model, such as outlet conditions of the two fluids (water and refrigerant), pressure drops of both water and refrigerant, overall heat transfer coefficient, heat exchanger effectiveness and rate of heat transfer are described in detail below.

##### 5.3.2.2.1 Water- and refrigerant-side outputs

- Water outlet temperature from a heat exchanger element  $T_{w,out,i}$

• Water exit temperature from the whole heat exchanger	$T_{w,out}$
• Water-side heat transfer coefficient over a heat exchanger element	$h_{w,i}$
• Total water pressure drop in the heat exchanger	$\Delta P_{w,total}$
• Refrigerant exit temperature from a heat exchanger element	$T_{r,out,i}$
• Refrigerant exit temperature from the whole heat exchanger	$T_{r,out}$
• Refrigerant-side heat transfer coefficient over a heat exchanger element	$h_{r,i}$
• Overall heat transfer coefficient in a heat exchanger element	$U_{sub,i}$
• Average overall heat transfer coefficient over the heat exchanger	$U_{sub,avg}$
• Effectiveness of a heat exchanger element	$\epsilon_{sub,i}$
• Average effectiveness of the whole heat exchanger	$\epsilon_{sub,avg}$
• Total refrigerant pressure drop in the heat exchanger	$\Delta P_{r,total}$
• Heat exchanger capacity	$\dot{Q}_{sub}$

### 5.3.2.2.2 Water- and refrigerant-side heat transfer coefficients

The convective heat transfer coefficients on the water- and refrigerant-side of the heat exchanger element are calculated using general Nusselt number correlations for both laminar and turbulent flow regimes presented by Bounapane and Troupe [67] and Marriott [68], respectively.

A general Nusselt number ( $Nusselt_D$ ) correlation for turbulent flow was calculated from [68].

$$\text{for } i = 1 \text{ to } n$$

$$Nusselt_{D,turbulent,i} = 0.37 \cdot Re_{D,i}^{0.668} \cdot Pr_i^{0.333} \cdot (\mu_{b,i} / \mu_{w,i})^{0.15} \quad 5-74$$

The heat transfer coefficient for turbulent flow is calculated by;

$$h_{turbulent,i} = Nusselt_{D,turbulent,i} \cdot \frac{k_{fluid,i}}{D_e} \quad \text{for } i = 1 \text{ to } n \quad 5-75$$

whereas the friction factor ( $f$ ) for a typical plate was determined following the correlations obtained from [66].

$$f_{turbulent,i} = \frac{2.5}{Re_{D,i}^{0.3}} \text{ for } i = 1 \text{ to } n \quad 5-76$$

Buonopane and Troupe [67] presented generalized relationships for a number of geometries for laminar flow using the following equation from [68];

$$\text{for } i = 1 \text{ to } n$$
$$Nusselt_{D,laminar,i} = 3.15 \cdot \left( Re_{D,i} \cdot Pr_i \cdot D_e / L_{sub,flow,d,i} \right)^{0.333} \cdot (\mu_{b,i} / \mu_{w,i})^{0.14} \quad 5-77$$

The heat transfer coefficient for laminar flow is calculated by;

$$h_{laminar,i} = Nusselt_{D,i} \cdot \frac{k_{fluid,i}}{D_e} \text{ for } i = 1 \text{ to } n \quad 5-78$$

Depending on the geometry of the plate heat exchanger, replace  $D_h$  by  $D_e$  and  $L_{sub,flow,d}$  is the effective plate length (diagonal length between two ports).

For a typical plate, the friction factor ( $f$ ) for laminar flow is given by [66];

$$f_{laminar} = \frac{2.5}{Re_{D,i}^{0.3}} \text{ for } i = 1 \text{ to } n \quad 5-79$$

Where the Reynolds number ( $Re_D$ ) used in the above set of equations is based on equivalent diameter ( $D_e$ ), which is given by;

$$D_e = \frac{4 \cdot W \cdot a}{2 \cdot (W + a)} = 2 \cdot a \quad 5-80$$

Where  $a$  is the mean plate gap/amplitude and  $W$  is the effective plate width (gasket to gasket). As can be seen from Equation 5-80,  $a$  is very small compared to  $W$ .

### 5.3.2.2.3 Water- and refrigerant-side pressure drops

The pressure drop in a plate heat exchanger consists of several pressure components. Empirically, pressure drop associated with the inlet and outlet manifolds and ports ( $\Delta P_p$ ) of the heat exchanger is approximately 1.5 times the inlet velocity head per pass as given below [66].

$$\Delta P_p = 1.5 \cdot \left( \rho_{fluid,in} \cdot \frac{u_m^2}{2} \right) \cdot N_{sub,p} \quad 5-81$$

Where ( $N_{sub,p}$ ) is the number of fluid ports and ( $u_m$ ) is the mean velocity through the ports given by;

$$u_m = \frac{\dot{m}_{fluid}}{\rho_{fluid} \cdot A_{port}} \quad 5-82$$

Pressure drop associated within the plate passages is given by the sum of the friction effect and momentum effect by;

$$\Delta P_{e,i} = \underbrace{\frac{4 \cdot f_{e,i} \cdot L_{sub,flow,d,i} \cdot G_{fluid}^2}{2 \cdot D_e} \cdot \left( \frac{1}{\rho_{e,fluid,i}} \right)_m}_{friction\ effect} + \underbrace{G_{fluid}^2 \cdot \left( \frac{1}{\rho_{e,fluid,in,i}} - \frac{1}{\rho_{e,fluid,out,i}} \right)}_{momentum\ effect} \quad 5-83$$

Where,

$$\left( \frac{1}{\rho_{e,fluid,i}} \right)_m = \frac{1}{2} \cdot \left( \frac{1}{\rho_{e,fluid,in,i}} + \frac{1}{\rho_{e,fluid,out,i}} \right) \quad for\ i = 1\ to\ n \quad 5-84$$

And where ( $G_{fluid}$ ) is the elemental mass velocity and ( $L_{sub,flow,d,i}$ ) is the elemental flow passage length, which is equal to the distance (diagonal) between the centre of the inlet and outlet ports divided by the number of elements. For liquids the momentum effect is assumed to be negligible.

The mass velocity is given by;

$$G_{fluid} = \frac{\dot{m}_{fluid}}{A_s \cdot N_{channel}} \quad 5-85$$

Where  $N_{channel}$  is the number of channels and  $A_s$  is channel cross sectional area of any one of the fluids flowing in the heat exchanger. The channel cross sectional area can be calculated by;

$$A_s = W \cdot a \quad 5-86$$

The sub-cooler diagonal element length is given by;

$$L_{sub,flow,d,i} = \frac{L_{sub,flow,d}}{(n / pass)} \quad for \ i = 1 \ to \ n \quad 5-87$$

The pressure drop due to the elevation difference between the inlet and outlet ports is given by;

$$\Delta P_g = \pm (\rho_{fluid})_m \cdot g \cdot L \quad 5-88$$

Where plus (+) sign in Equation 5-88 shows vertical upward flow, the minus (–) sign indicates vertical downward flow, whereas  $g$  is gravitational acceleration.

The total pressure drop on one side of the sub-cooler (plate exchanger) is the sum of all of the above pressure drops and is given by;

$$\Delta P_{sub,total} = \sum_{i=1}^n (P_{e,i}) + \Delta P_p + \Delta P_g \quad 5-89$$

The pump power requirement of the sub-cooler (plate heat exchanger) can be calculated from;

$$\dot{W}_{PUMP,SUB} = \dot{V}_{sub,water} \cdot \Delta P_{sub,total} \quad 5-90$$

#### 5.3.2.2.4 Effectiveness-NTU method for sub-cooler

Whenever only the inlet conditions of two fluids in the sub-cooler are known, we need to use effectiveness-NTU method to figure out the exit conditions of the fluids. Nevertheless, the exit conditions are computed iteratively and are very time consuming, especially, if the plate heat exchangers are subdivided into a large number of elements. Thus, the number of elements in a sub-cooler should be reasonably determined based on the degree of accuracy and variable change required in the calculated values. Besides, elemental analysis in compact heat exchangers, especially with liquids, may not be necessary since the change in the output values are negligible to affect the local heat transfer coefficients of the fluids.

#### 5.3.2.2.5 Heat exchanger effectiveness

The effectiveness of a given sub-cooler element can be given by;

$$\epsilon_i = \frac{\dot{Q}_{act,i}}{\dot{Q}_{max,i}} \quad \text{for } i = 1 \text{ to } n \quad 5-91$$

The maximum possible rate of heat transfer in the sub-cooler element is determined by;

$$\dot{Q}_{max,i} = C_{min,i} \cdot (T_{r,in,i} - T_{w,in,i}) \quad \text{for } i = 1 \text{ to } n \quad 5-92$$

The actual rate of heat transfer in the sub-cooler element is obtained from;

$$\dot{Q}_{act,i} = \epsilon_i \cdot C_{min,i} \cdot (T_{r,in,i} - T_{w,in,i}) \quad \text{for } i = 1 \text{ to } n \quad 5-93$$

The actual rate of heat transfer on the refrigerant-side of the sub-cooler element is calculated by;

$$\dot{Q}_{act,i} = \dot{m}_r \cdot C_{p,r,i} \cdot (T_{r,in,i} - T_{r,out,i}) \quad \text{for } i = 1 \text{ to } n \quad 5-94$$



The actual rate of heat transfer on the water-side is equated to the rate of heat transfer on the water-side as;

$$\dot{m}_w \cdot C_{p_{w,i}} \cdot (T_{w,out,i} - T_{w,in,i}) = \dot{m}_r \cdot C_{p_{r,i}} \cdot (T_{r,in,i} - T_{r,out,i}) \quad \text{for } i = 1 \text{ to } n \quad 5-95$$

The sub-cooler effectiveness-NTU relationship is computed based on the correlations for counterflow arrangement. Hence, the effectiveness of a given sub-cooler element is given by;

$$\epsilon_{sub,i} = \frac{1 - \exp(-(1 - C_i) \cdot NTU_i)}{1 - C_i \cdot \exp(-(1 - C_i) \cdot NTU_i)} \quad \text{for } i = 1 \text{ to } n \quad 5-96$$

The number of heat transfer units ( $NTU$ ), which is dimensionless, for a sub-cooler element is given by;

$$NTU_i = \frac{UA_{sub,i}}{C_{min,i}} \quad \text{for } i = 1 \text{ to } n \quad 5-97$$

The product of the overall heat transfer coefficient and area of a sub-cooler element can be obtained from;

$$UA_{sub,i} = \frac{A_{sub,i}}{\frac{1}{h_{r,i}} + \frac{t_{plate}}{k_{plate}} + \frac{1}{h_{w,i}}} \quad \text{for } i = 1 \text{ to } n \quad 5-98$$

Where  $A_{sub,i}$  is a sub-cooler elemental heat transfer area which is given by;

$$A_{sub,i} = \frac{2 \times (W + a) \cdot L_{sub,flow}}{n} \quad 5-99$$

The variable  $n$  in Equation 5-99 is the number of elements the sub-cooler is divided into.

The overall heat transfer coefficient in a sub-cooler element is determined by;

$$U_{sub,i} = \frac{UA_{sub,i}}{A_{sub,e}} \quad \text{for } i = 1 \text{ to } n \quad 5-100$$

The heat capacity rates for both refrigerant and water as a function of the inlet conditions are given respectively by the following equations.

$$C_{r,i} = Cp_{r,i} \cdot \dot{m}_r \quad \text{for } i = 1 \text{ to } n \quad 5-101$$

$$C_{w,i} = Cp_{w,i} \cdot \dot{m}_w \quad \text{for } i = 1 \text{ to } n \quad 5-102$$

The minimum heat capacity rate over a sub-cooler element will be;

$$C_{min,i} = \min(C_{r,i}, C_{w,i}) \quad \text{for } i = 1 \text{ to } n \quad 5-103$$

The elemental refrigerant and water mass flowrates over a given sub-cooler element are the same as the total mass flowrates for each fluid, since the sub-cooler is divided along its width as shown in Figure 5.5.

Refrigerant outlet temperature from a sub-cooler element can be readily available from;

$$T_{r,out,i} = T_{r,in,i} - \epsilon_{sub,i} \cdot C_{min,i} \cdot \frac{T_{r,in,i} - T_{w,in,i}}{(\dot{m}_r \cdot Cp_{r,i})} \quad \text{for } i = 1 \text{ to } n \quad 5-104$$

whereas, the water outlet temperature from a sub-cooler element is obtained from;

$$T_{w,out,i} = T_{w,in,i} + \epsilon_{sub,i} \cdot C_{min,i} \cdot \frac{T_{r,in,i} - T_{w,in,i}}{\dot{m}_w \cdot Cp_{w,i}} \quad \text{for } i = 1 \text{ to } n \quad 5-105$$

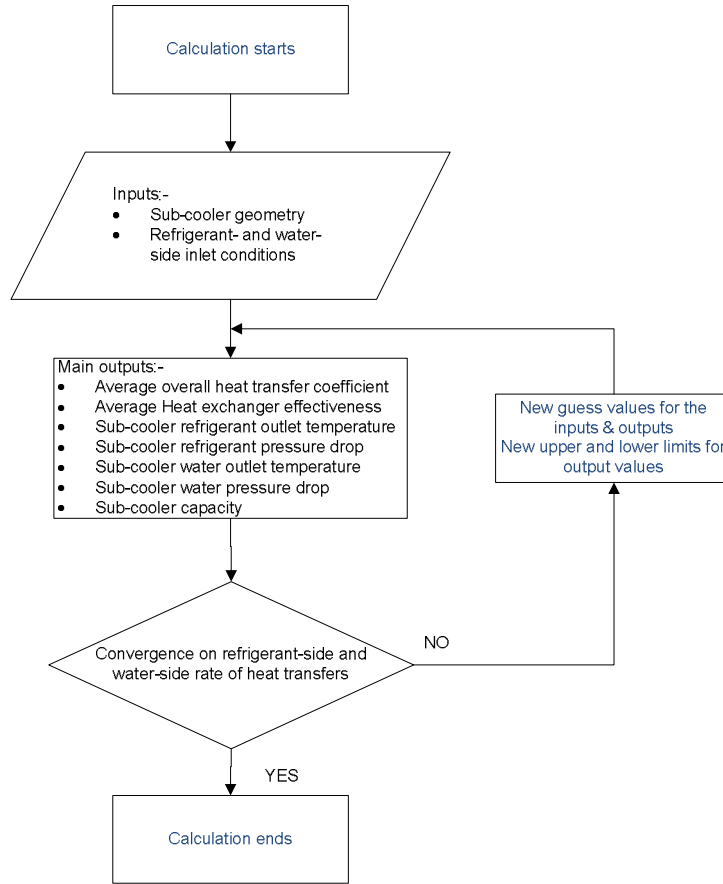


Figure 5.6 Sub-cooler simulation flowchart to predict sub-cooler performance for medium-temperature secondary coolant applications.

The average overall heat transfer coefficient, effectiveness and the total rate of heat transfer of the sub-cooler are respectively calculated using Equations 5-106 through 5-108.

$$U_{sub,avg} = \frac{\sum_{i=1}^n U_i}{n} \quad 5-106$$

$$\epsilon_{sub,avg} = \frac{\sum_{i=1}^n \epsilon_{sub,i}}{n} \quad 5-107$$

$$\dot{Q}_{sub,total} = \sum_{i=1}^n \dot{Q}_{act,i}$$

5-108

Where the index (i) represents the  $i^{th}$  element of the sub-cooler and variable (n) represents the total number of elements in a sub-cooler.

The general sub-cooler simulation flowchart in Figure 5.6 could be used as a guide for applying the sub-cooler model.

### 5.3.3. Intermediate heat exchanger model

The intermediate heat exchanger is treated as a two-phase heat exchanger on the refrigerant-side, whereas it is treated as single-phase plate heat exchanger on the coolant-side. The model divides the plate heat exchanger into two-phase and superheated regimes as can be seen from Figure 5.7. The model was written in a software package called Engineering Equation Solver [9].

#### 5.3.3.1. Inputs

Different types of plate heat exchanger inputs (independent variables) are required in order to predict the outputs (dependent variables) of the intermediate heat exchanger model. Geometric parameters, such as number of channels, gap between channels, and so forth should be given as described in the following Sub-Sections. Besides, the construction material of the heat exchanger plates, water-side and refrigerant-side inlet conditions including mass flowrates should be given for both fluids.

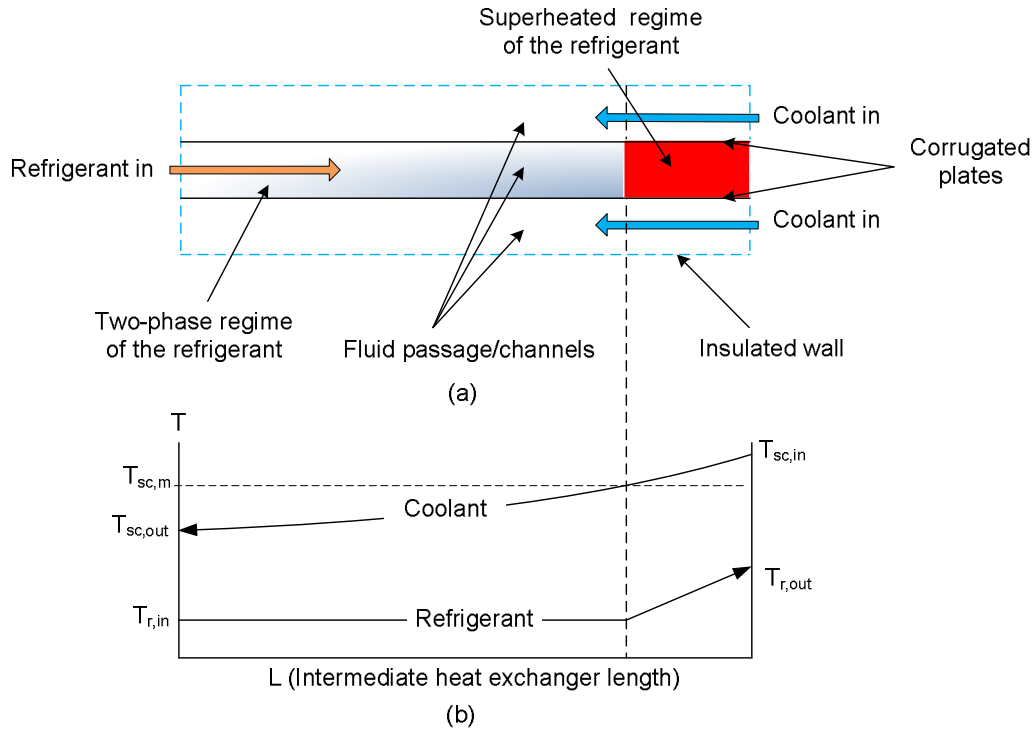


Figure 5.7 Intermediate heat exchanger a) divided into two-phase and superheated regimes; b) temperature distribution for a counterflow arrangement.

#### 5.3.3.1.1. Intermediate heat exchanger geometrical inputs

- Effective flow length of the fluid in the heat exchanger  $L_{ihx,flow}$
- Effective width of the heat exchanger  $W$
- Mean plate gap or amplitude  $a$
- Number of plates of the heat exchanger  $N_{ihx,plates}$
- Number of refrigerant ports  $N_{r,p}$
- Number of secondary coolant ports  $N_{sc,p}$
- Number of channels on the coolant-side  $N_{channel,sc}$
- Number of channels on the refrigerant-side  $N_{channel,r}$
- Number of elements the heat exchanger is divided into  $n$
- Port inner diameter  $D_{port,i}$
- Heat transfer area of a single plate on both sides  $A_{plate}$

- Port cross-sectional area  $A_{\text{port}}$
- Channel cross-sectional area  $A_s$
- Total heat transfer area of the heat exchanger  $A_{\text{total}}$
- Number of flow pass in the heat exchanger  $\text{pass}$
- Plate thickness  $t_{\text{plate}}$
- Plate construction material

#### 5.3.3.1.2. Refrigerant- and coolant-side inputs

- Coolant inlet temperature  $T_{\text{sc,in}}$
- Ambient pressure  $P_{\text{atm}}$
- Mass flowrate of coolant  $\dot{m}_{\text{sc}}$
- Refrigerant saturation temperature  $T_{\text{r,sat}}$
- Refrigerant degree of superheat  $\Delta T_{\text{r,sup}}$
- Refrigerant inlet pressure  $P_{\text{a,in}}$
- Mass flowrate of refrigerant  $\dot{m}_{\text{r}}$
- Coolant type  $\text{SC\$}$
- Refrigerant type  $\text{R\$}$

#### 5.3.3.2. Outputs

The outputs (dependent variables) of the intermediate heat exchanger model, such as outlet conditions of the two fluids (coolant and refrigerant), pressure drops of both coolant and refrigerant, overall heat transfer coefficient, heat exchanger effectiveness and rate of heat transfer are described in detail below.

##### 5.3.3.2.1. Coolant- and refrigerant-side outputs

- Coolant outlet temperature from a heat exchanger regime  $T_{\text{sc,m}}$
- Coolant exit temperature from the whole heat exchanger  $T_{\text{sc,out}}$

• Total coolant pressure drop in the heat exchanger	$\Delta P_{sc,total}$
• Refrigerant exit temperature from a heat exchanger	$T_{r,out}$
• Average overall heat transfer coefficient over the heat exchanger	$U_{ihx,avg}$
• Average refrigerant heat transfer coefficient over the heat exchanger	$h_{ihx,r}$
• Average coolant heat transfer coefficient over the heat exchanger	$h_{ihx,sc}$
• Average effectiveness of the whole heat exchanger	$\epsilon_{ihx,avg}$
• Total refrigerant pressure drop in the heat exchanger	$\Delta P_{r,total}$
• Heat exchanger capacity	$\dot{Q}_{ihx}$

### 5.3.3.3. Coolant- and refrigerant-side heat transfer coefficients in the heat exchanger

There is limited research in the calculation of convective heat transfer coefficients in the two-phase regime of refrigerant in brazed plate heat exchangers. Hence, the average heat transfer coefficient of the refrigerant (for both single- and two-phase flow) will be derived from the average overall heat transfer coefficient of the heat exchanger to be calculated following Equation 5-109.

The overall heat transfer coefficient in the intermediate heat exchanger is not a known parameter but a calculated parameter obtained based on Equations 5-109 through 5-118 according to references [65, 69, 70].

$$U_{ihx,avg} = \frac{\dot{Q}_{total}}{A_{total} \cdot \Delta T_{ln}} \quad 5-109$$

The total rate of heat transfer in the heat exchanger is calculated by;

$$\dot{Q}_{total} = \dot{Q}_{tp} + \dot{Q}_{sup} \quad 5-110$$

Whereas, the rate of heat transfers in the two-phase and single-phase regimes of the heat exchanger are respectively calculated by;

$$\dot{Q}_{tp} = \dot{m}_r \cdot (h_{r,tp,out} - h_{r,in}) \quad 5-111$$

$$\dot{Q}_{sup} = \dot{m}_r \cdot (h_{r,out} - h_{r,tp,out}) \quad 5-112$$

The overall logarithmic temperature difference of the heat exchanger is calculated by;

$$\Delta T_{ln} = \frac{\dot{Q}_{total}}{\frac{\dot{Q}_{tp}}{\Delta T_{ln,tp}} + \frac{\dot{Q}_{sup}}{\Delta T_{ln,sup}}} \quad 5-113$$

Whereas, the logarithmic temperature differences in the two-phase and single-phase regimes of the heat exchanger are respectively calculated by;

$$\Delta T_{ln,tp} = \frac{T_{sc,m} - T_{sc,out}}{\ln \left( \frac{T_{sc,m} - T_{r,sat}}{T_{sc,out} - T_{r,sat}} \right)} \quad 5-114$$

$$\Delta T_{ln,sup} = \frac{(T_{sc,in} - T_{r,out}) - (T_{sc,m} - T_{r,sat})}{\ln \left( \frac{T_{sc,in} - T_{r,out}}{T_{sc,m} - T_{r,sat}} \right)} \quad 5-115$$

The secondary coolant temperature at the boundary of the two-phase and single-phase refrigerant regimes is calculated by;

$$T_{sc,m} = T_{sc,in} - \frac{\dot{Q}_{sup}}{\dot{m}_{sc} \cdot C_{p_{sc}}} \quad 5-116$$

The total heat transfer area of the intermediate heat exchanger is determined by;

$$A_{total} = L_{ihx,flow} \cdot W \cdot (N_{ihx,plates} - 2) \quad 5-117$$



Finally, the refrigerant-side heat transfer coefficient of the intermediate heat exchanger is derived from;

$$h_{ihx,r} = \left[ \frac{I}{U_{ihx,avg}} - \left( \frac{t_{plate}}{k_{plate}} + \frac{I}{h_{ihx,sc}} \right) \right]^{-1} \quad 5-118$$

Whereas, the coolant-side heat transfer coefficient ( $h_{ihx,sc}$ ) is calculated using Equations 5-75 and 5-78 for turbulent and laminar flow, respectively.

#### **5.3.3.4. Coolant- and refrigerant-side pressure drops**

Coolant-side and single-phase refrigerant pressure drops in the intermediate heat exchanger including the pump power requirements are calculated following Equations 5-81 through 5-90.

However, the total pressure drop of the two-phase refrigerant in the heat exchanger is determined using the following sequence of equations.

The pressure drop in inlet and outlet of refrigerant port per pass is obtained from;

$$\Delta P_{r,p} = 1.5 \cdot \left( \frac{\rho_{r,m} \cdot u_{r,m}^2}{2} \right) \cdot N_{sc,p} \quad 5-119$$

The friction pressure drop associated within the plate passages for two-phase flow is given based on [65] by;

$$\Delta P_{r,f} = 1.425 \cdot \left( \frac{G_r^2}{2 \cdot \rho_{r,m}} \right) \quad 5-120$$

Where, the mean density of the refrigerant is calculated from;

$$\rho_{r,m} = \left( \frac{x_m}{\rho_g} + \frac{1-x_m}{\rho_f} \right)^{-1} \quad 5-121$$

Where the calculation of the mass velocity of the refrigerant ( $G_r$ ) and the heat exchanger port mean velocity ( $u_m$ ) follows Equations 5-82 and 5-85, respectively.

The momentum refrigerant pressure drop within the plates is calculated by;

$$\Delta P_{r,m} = G_r^2 \cdot (v_g - v_f) \cdot \text{abs}(\Delta x) \quad 5-122$$

The mean refrigerant quality described in Equation 5-121 is given by;

$$x_m = \frac{x_{in} + x_{out}}{2} \quad 5-123$$

Where ( $\Delta x$ ) described in Equation 5-122 is the change in quality of the refrigerant between the inlet and outlet of the heat exchanger. The pressure drop due to the elevation difference between the inlet and outlet ports is given as described in Equation 5-88.

The total pressure drop on the refrigerant-side of the plate exchanger is the sum of all of the above pressure drops and is given by;

$$\Delta P_{ihx,total} = P_{r,p} + \Delta P_{r,f} + P_{r,m} + \Delta P_{r,g} \quad 5-124$$

#### **5.3.3.5. Effectiveness-NTU method for the intermediate heat exchanger**

Whenever only the inlet conditions of two fluids in a heat exchanger are known, we need to use effectiveness-NTU method to figure out the exit conditions of the fluids. However, in the case of the intermediate heat exchanger the inlet and exit conditions are known thereby eliminating the necessity of effectiveness-NTU method. Therefore, the effectiveness of the heat exchanger is calculated to only evaluate the performance of the intermediate heat exchanger.

**5.3.3.5.1. Heat exchanger effectiveness**

The effectiveness of the intermediate heat exchanger was assumed to be equal to the effectiveness of the two-phase area of the heat exchanger as given by 5-125, since the superheated area of the heat exchanger was negligible.

$$\epsilon_{ihx} = \epsilon_{tp} \quad 5-125$$

However, the effectiveness both in the superheated regime ( $\epsilon_{sup}$ ) and two-phase regime ( $\epsilon_{tp}$ ) could be respectively given by;

$$\epsilon_{sup} = \frac{\dot{Q}_{sup}}{C_{sup,min} \cdot (T_{sc,m} - T_{r,out})} \quad 5-126$$

$$\epsilon_{tp} = \frac{\dot{Q}_{tp}}{C_{tp,min} \cdot (T_{sc,out} - T_{r,in})} \quad 5-127$$

The minimum heat capacity rates for both single ( $C_{sup,min}$ ) and two-phase ( $C_{tp,min}$ ) regimes in the intermediate heat exchanger can be calculated from Equations 5-128 and 5-129, respectively.

$$C_{sup,min} = \min(Cp_{r,in} \cdot \dot{m}_r, Cp_{sc,in} \cdot \dot{m}_{sc}) \quad 5-128$$

$$C_{tp,min} = \min(Cp_{r,tp,in} \cdot \dot{m}_r, Cp_{sc,m} \cdot \dot{m}_{sc}) \quad 5-129$$

The secondary coolant heat capacity rate ( $Cp_{sc,m} \cdot \dot{m}_{sc}$ ) will be taken as the minimum value in the two-phase regime, since the specific heat capacity of the refrigerant in two-phase regime is infinity.

Secondary coolant outlet temperature from an intermediate heat exchanger can simply be calculated from;

$$T_{sc,out} = T_{sc,in} - \frac{\dot{Q}_{tp} + \dot{Q}_{sup}}{\dot{m}_{sc} \cdot C_{p_{sc}}} \quad 5-130$$

The general simulation flowchart of the intermediate heat exchanger is shown in Figure 5.8.

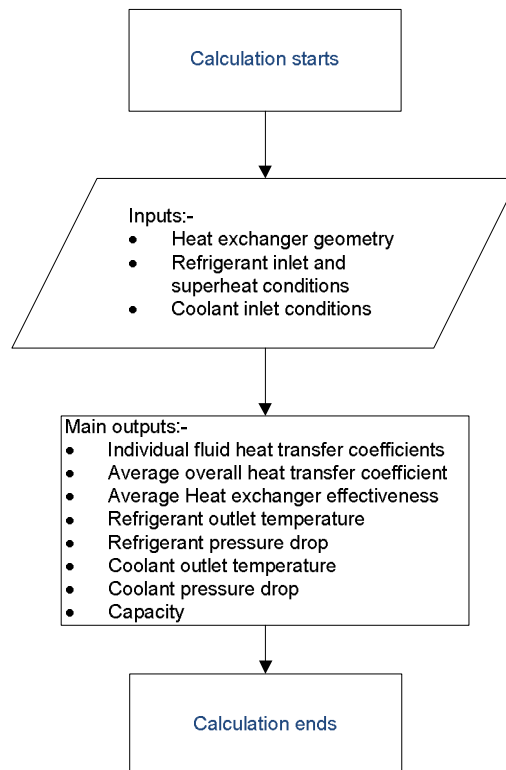


Figure 5.8 Intermediate heat exchanger simulation flowchart to predict its performance for medium-temperature secondary coolant applications.

### 5.3.4. Condenser model

The condenser is treated as a two-phase flow on the refrigerant-side, whereas it is a single-phase flow plate heat exchanger on the water-side. The model does not take any sub-cooling into account. However, it considers desuperheating since it is assumed that the temperature of the

refrigerant and the superheated vapor does not directly condense on entry due to a desuperheating area at the inlet of the condenser. Unlike desuperheating, it is assumed that there is no sub-cooling area at the outlet of the condenser leading to only saturated liquid on exit. The condenser model can be seen from Figure 5.9. The model was written in a software package called Engineering Equation Solver [9].

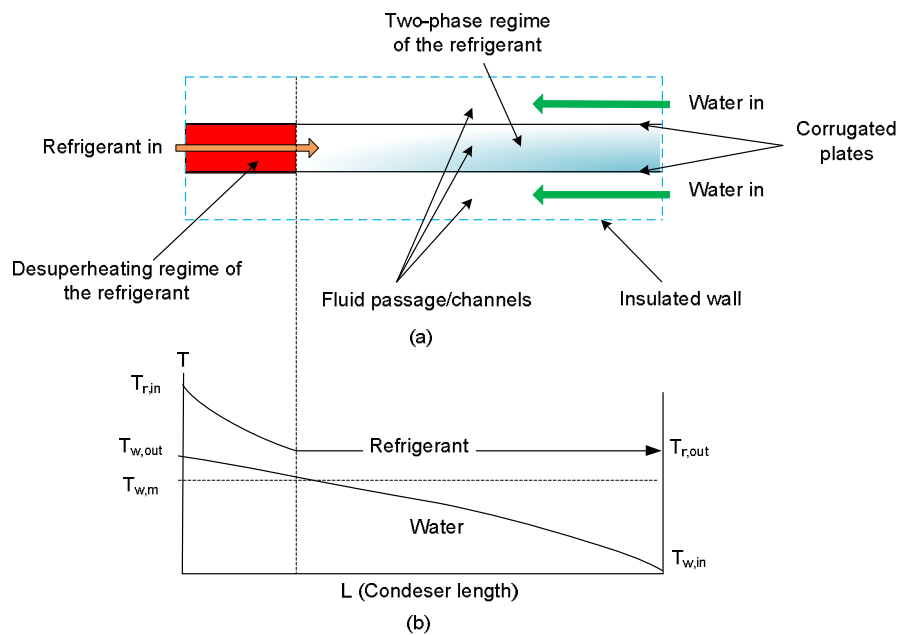


Figure 5.9 Condenser model a) divided into two-phase and superheated regimes; b) temperature distribution for a counterflow arrangement.

#### 5.3.4.1. Inputs

Different types of plate heat exchanger inputs (independent variables) are required in order to predict the outputs (dependent variables) of the condenser model. Geometric parameters, such as number of channels, gap between channels, and so forth should be given as described in the following Sub-Sections. Besides, the construction material of the heat exchanger plates, water- and refrigerant-side inlet conditions including mass flowrates should be given for both fluids.

##### 5.3.4.1.1. Condenser geometrical inputs

- Effective flow length of the fluid in the heat exchanger  $L_{con,flow}$

• Effective width of the heat exchanger	$W$
• Mean plate gap or amplitude	$a$
• Number of plates of the heat exchanger	$N_{\text{con,plates}}$
• Number of refrigerant ports	$N_{r,p}$
• Number of water ports	$N_{\text{water,p}}$
• Number of channels on the water-side	$N_{\text{channel,w}}$
• Number of channels on the refrigerant-side	$N_{\text{channel,r}}$
• Number of elements the heat exchanger is divided into	$n$
• Port inner diameter	$D_{\text{port,i}}$
• Heat transfer area of a single plate on both sides	$A_{\text{plate}}$
• Port cross-sectional area	$A_{\text{port}}$
• Channel cross-sectional area	$A_s$
• Total heat transfer area of the heat exchanger	$A_{\text{total}}$
• Number of flow pass in the heat exchanger	$\text{pass}$
• Plate thickness	
• Plate construction material	

#### 5.3.4.1.2. Refrigerant- and water-side inputs

• Water inlet temperature	$T_{w,\text{in}}$
• Ambient pressure	$P_{\text{atm}}$
• Mass flowrate of water	$\dot{m}_w$
• Refrigerant inlet temperature	$T_{r,\text{in}}$
• Refrigerant saturation temperature	$T_{r,\text{sat}}$
• Refrigerant inlet pressure	$P_{a,\text{in}}$
• Mass flowrate of refrigerant	$\dot{m}_r$
• Refrigerant type	$R\$$

### 5.3.4.2. Outputs

The outputs (dependent variables) of the condenser model, such as outlet conditions of the two fluids (water and refrigerant), pressure drops of both water and refrigerant, overall heat transfer coefficient, heat exchanger effectiveness and rate of heat transfer are described in detail below.

#### 5.3.4.2.1 Water- and refrigerant-side outputs

• Water exit temperature from the heat exchanger	$T_{w,out}$
• Total water pressure drop in the heat exchanger	$\Delta P_{w,total}$
• Refrigerant exit temperature from the heat exchanger	$T_{r,out}$
• Average overall heat transfer coefficient over the heat exchanger	$U_{con,avg}$
• Average water heat transfer coefficient over the heat exchanger	$h_{con,w}$
• Average refrigerant heat transfer coefficient over the heat exchanger	$h_{con,r}$
• Average effectiveness of the heat exchanger	$\epsilon_{con,avg}$
• Total refrigerant pressure drop in the heat exchanger	$\Delta P_{r,total}$
• Heat exchanger capacity	$\dot{Q}_{con}$

#### 5.3.4.3. Water- and refrigerant-side heat transfer coefficients in the condenser

The condenser is assumed to have a desuperheating (as discussed in Section 5.3.4) but not sub-cooling regime. Hence, the refrigerant-side heat transfer coefficient is calculated from the overall heat transfer coefficient of the heat exchanger in a similar fashion to that of the intermediate heat exchanger.

The overall heat transfer coefficient in the condenser is calculated by;

$$U_{con,avg} = \frac{\dot{Q}_{total}}{A_{total} \cdot \Delta T_{ln}} \quad 5-131$$

The total rate of heat transfer in the heat exchanger is;

$$\dot{Q}_{total} = \dot{Q}_{tp} + \dot{Q}_{desup} \quad 5-132$$

Whereas, the rate of heat transfers in the two-phase and single-phase regimes of the heat exchanger are respectively given by;

$$\dot{Q}_{tp} = \dot{m}_r \cdot (h_{r,out} - h_{r,tp,in}) \quad 5-133$$

$$\dot{Q}_{desup} = \dot{m}_r \cdot (h_{r,in} - h_{r,tp,in}) \quad 5-134$$

The overall logarithmic temperature difference of the heat exchanger is calculated by;

$$\Delta T_{ln} = \frac{\dot{Q}_{total}}{\frac{\dot{Q}_{tp}}{\Delta T_{ln,tp}} + \frac{\dot{Q}_{desup}}{\Delta T_{ln,desup}}} \quad 5-135$$

Whereas the logarithmic temperature differences in the two-phase and single-phase regimes of the heat exchanger are respectively calculated by;

$$\Delta T_{ln,tp} = \frac{T_{w,out} - T_{w,in}}{\ln \left( \frac{T_{r,sat} - T_{w,out}}{T_{r,sat} - T_{w,in}} \right)} \quad 5-136$$

$$\Delta T_{ln,desup} = \frac{(T_{r,in} - T_{w,out}) - (T_{r,sat} - T_{w,m})}{\ln \left( \frac{T_{r,in} - T_{w,out}}{T_{r,sat} - T_{w,m}} \right)} \quad 5-137$$

The water temperature at the boundary of the two-phase and single-phase refrigerant regimes is calculated by;



$$T_{w,m} = T_{w,in} + \frac{\dot{Q}_{tp}}{\dot{m}_w \cdot Cp_w} \quad 5-138$$

The total heat transfer area of the condenser is determined by;

$$A_{total} = L_{con,flow} \cdot W \cdot (N_{cond,plates} - 2) \quad 5-139$$

The heat transfer coefficient of the refrigerant is then determined from;

$$h_{con,r} = \left[ \frac{1}{U_{con,avg}} - \left( \frac{t_{plate}}{k_{plate}} + \frac{1}{h_{con,w}} \right) \right]^{-1} \quad 5-140$$

Whereas, the water-side heat transfer coefficient ( $h_{con,w}$ ) is calculated using Equations 5-75 and 5-78 for turbulent and laminar flow, respectively.

#### **5.3.4.4. Water- and refrigerant-side pressure drops**

Water-side drop in the condenser including the pump power requirements are calculated following Equations 5-81 through 5-90. The total pressure drop of the two-phase refrigerant in the heat exchanger is determined using the following Equations 5-119 through 5-124. However the friction pressure drop associated within the plate passages for two-phase flow is slightly different from that of the intermediate heat exchanger, which is given by Equation 5-140 following [64].

$$\Delta P_{r,f} = 1.835 \cdot \left( \frac{G_r^2}{2 \cdot \rho_{r,m}} \right) \quad 5-141$$

Similarly, the total pressure drop on the refrigerant-side of condenser is given by;

$$\Delta P_{con,total} = P_{r,p} + \Delta P_{r,f} + P_{r,m} + \Delta P_{r,g}$$

5-142

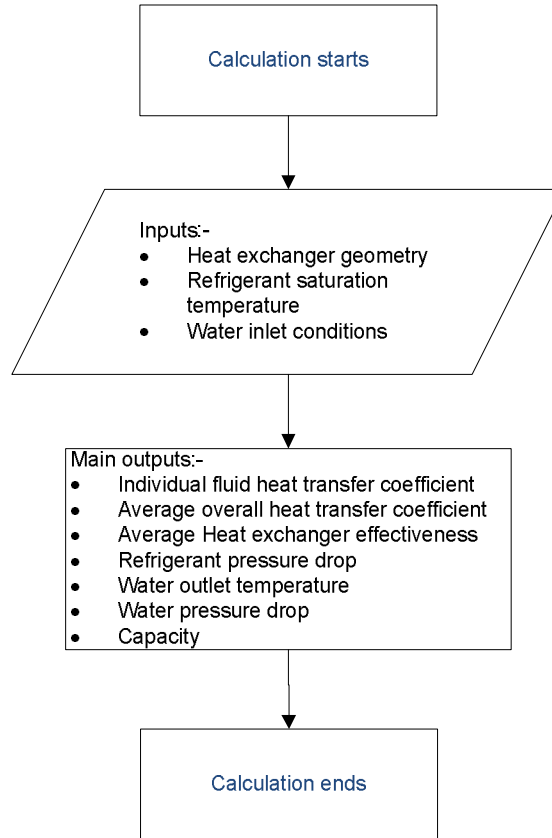


Figure 5.10 Condenser simulation flowchart to predict its performance for medium-temperature secondary coolant applications.

#### 5.3.4.5. Effectiveness-NTU method for the condenser

Whenever only the inlet conditions of two fluids in a heat exchanger are known, we need to use effectiveness-NTU method to figure out the exit conditions of the fluids. However, the saturation temperature of the refrigerant in the condenser is known (i.e. inlet and exit temperatures of the refrigerant are known) thereby eliminating the necessity of effectiveness-NTU method. Therefore, the effectiveness is calculated to only evaluate the performance of the condenser.

**5.3.4.5.1. Heat exchanger effectiveness**

The effectiveness of the condenser was assumed to be equal to the effectiveness of the two-phase area of the heat exchanger as given by 5-143, assuming negligible desuperheated area.

$$\epsilon_{cond} = \epsilon_{tp} \quad 5-143$$

However, the effectiveness both in the desuperheated regime ( $\epsilon_{desup}$ ) and two-phase regime ( $\epsilon_{tp}$ ) of the condenser are respectively given by;

$$\epsilon_{desup} = \frac{\dot{Q}_{desup}}{C_{desup,min} \cdot (T_{r,in} - T_{w,m})} \quad 5-144$$

$$\epsilon_{tp} = \frac{\dot{Q}_{tp}}{C_{tp,min} \cdot (T_{r,tp,in} - T_{w,in})} \quad 5-145$$

The minimum heat capacity rates for both single ( $C_{desup,min}$ ) and two-phase ( $C_{tp,min}$ ) regimes in the condenser can be calculated from Equations 5-146 and 5-147, respectively.

$$C_{desup,min} = \min(Cp_{r,in} \cdot \dot{m}_r, Cp_{w,m} \cdot \dot{m}_w) \quad 5-146$$

$$C_{tp,min} = \min(Cp_{r,tp,in} \cdot \dot{m}_r, Cp_{w,in} \cdot \dot{m}_w) \quad 5-147$$

The water heat capacity rate will be taken as the minimum value in the two-phase regime, since the specific heat capacity of the refrigerant in two-phase regime is infinity.

Water outlet temperature from the condenser can be obtained from;

$$T_{w,out} = T_{w,in} + \frac{\dot{Q}_{desup} + \dot{Q}_{tp}}{\dot{m}_w \cdot Cp_w} \quad 5-148$$

The general simulation flowchart of the condenser has been shown in Figure 5.10 for more clarity.

#### 5.4. Distribution line model

In a secondary coolant system, a coolant circuit is thermally coupled with a refrigerant circuit in an intermediate heat exchanger. These fluids (coolant and refrigerant) are in turn circulated to various components of the secondary coolant refrigeration system via connecting pipe networks. Secondary coolant circuit consists of longer distribution lines as compared to refrigerant lines, especially, in supermarket establishments. This is because, the secondary coolant distribution lines stretch from plant room to display cabinets, whereas the refrigerant lines are confined to the plant room. Thus, the pressure drop and heat transfer of the secondary coolants need to be taken into account, whereas the values of the same variables are assumed to be negligible in the refrigerant distribution lines in the plant room. The distribution line model could be depicted schematically as shown in Figure 5.11.

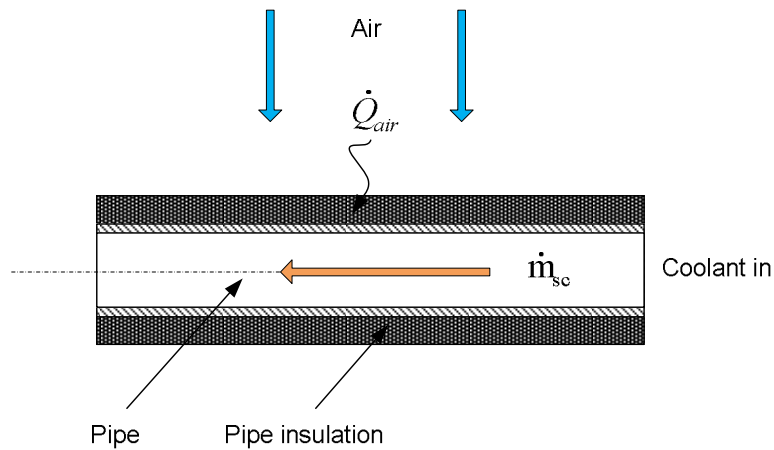


Figure 5.11 Secondary coolant distribution line model.

### 5.4.1. General assumptions

The following assumptions were used in the calculation procedures of the distribution line model for medium-temperature secondary coolant refrigeration systems.

- Steady state condition.
- Negligible kinetic and potential energy changes.
- Constant fluid properties and heat transfer coefficients over an element.
- For free convection, the heat transfer coefficient of the air is  $10 \text{ W m}^{-2} \text{ K}^{-1}$ .
- Negligible fouling resistance.

### 5.4.2. Inputs

Geometric parameters of the coolant pipe and insulation such as diameter, length, thickness and so forth should be given as described in the following Sub-Sections. Besides, the construction materials of the pipe and insulation, the surrounding air conditions and coolant mass flowrate should be given.

#### 5.4.2.1. Distribution line geometrical inputs

- |   |               |
|---|---------------|
| • Flow length of the secondary coolant pipe | $L_{sc,line}$ |
| • Outer diameter of coolant pipe            | $D_{pipe,o}$  |
| • Outer diameter of pipe insulation         | $D_{insul,o}$ |
| • Coolant pipe thickness                    | $t_{pipe}$    |
| • Coolant pipe insulation thickness         | $t_{insul}$   |
| • Coolant pipe roughness                    | relRough      |
| • Number of distribution line elements      | n             |

#### 5.4.2.2. Coolant- and air-side inputs

- |                             |             |
|-----------------------------|-------------|
| • Coolant inlet temperature | $T_{sc,in}$ |
|-----------------------------|-------------|

- Ambient temperature  $T_{atm}$
- Ambient pressure  $P_{atm}$
- Mass flowrate of coolant  $\dot{m}_{sc}$
- Coolant type SC\$

### 5.4.3. Outputs

The outputs of the distribution line model such as secondary coolant outlet temperature, pressure drop and rate of heat transfer are described below.

#### 5.4.3.1. Coolant- and air-side outputs

- Secondary coolant exit temperature  $T_{sc,line,out}$
- Pressure drop in the distribution line  $\Delta P_{sc,line}$
- Rate of heat transfer from/to distribution line  $\dot{Q}_{line}$

### 5.4.4. Coolant-side heat transfer coefficient and pressure drop

The friction factors in a circular pipe for developing or fully-developed flow in the laminar, transitional or turbulent flow regimes are calculated from Nellis and Klein [60] using EES [9] routine. The Reynolds and Prandtl numbers for the distribution line are calculated by Equations 5-15 and 5-16, respectively. For a laminar flow in the distribution pipe element (i.e. for  $Re_i < 2300$ ), the friction factor is calculated by Equation 5-14, whereas for turbulent and transitional flow in the circular pipe element (i.e. for  $Re_i > 2300$ ) the friction factor is calculated by Equation 5-17. The average heat transfer coefficient of the secondary coolant (for laminar or turbulent flow) in the distribution pipe element is calculated by Equation 5-19.

The coolant pressure drop in a distribution pipe element is given by;

$$\Delta P_{sc,line,i} = f_{sc,line,i} \cdot \rho_{sc,line,in,i} \cdot \frac{L_{sc,line}}{D_{line,i}} \cdot \frac{v_{sc,line,i}^2}{2} \quad \text{for } i = 1 \text{ to } n \quad 5-149$$

The total pressure drop in valve and fittings of the distribution line is obtained from;

$$\Delta P_{valves,fittings} = K_{valves,fittings} \cdot \left( \rho_{sc,line} \cdot \frac{v_{sc,line}^2}{2} \right) \quad 5-150$$

where  $K_{valves,fittings}$  (loss coefficient) is obtained from Tables 1 through 5, Chapter 35 of ASHRAE Handbook [71].

The total pressure drop in the secondary coolant distribution line is given by;

$$\Delta P_{sc,line,total} = \left( \sum_{i=1}^n \Delta P_{sc,line,i} \quad \text{for } i = 1 \text{ to } n \right) + \Delta P_{valves,fittings} \quad 5-151$$

The index  $i$  represents the  $i^{th}$  element, whereas  $n$  represents the total number of elements in a distribution line of a secondary coolant system.

#### 5.4.5. Heat transfer and coolant outlet temperature of distribution line

The essential design parameters of the distribution line of a secondary coolant system are heat and pressure losses. The pressure loss determines the selection of the coolant pump, whereas the heat loss determines the selection of distribution line insulation. The following sequence of equations is used to determine the aforementioned design parameters.

Heat loss or gain of the coolant in a distribution line element is determined by;

$$\text{for } I = 1 \text{ to } n$$

$$\dot{Q}_{line,e,I} = \dot{m}_{sc} \cdot C_{p,sc,in,I} \cdot (T_{sc,line,in,I+1} - T_{sc,line,in,I}) \quad 5-152$$

The temperature of coolant leaving a distribution line element is given by;

for  $I = 1$  to  $n$

$$T_{sc,line,in,I+1} = UA_{line,e} \cdot \left( \frac{T_{a,\infty} - T_{sc,line,in,I}}{\dot{m}_{sc} \cdot Cp_{sc,in,I}} \right) + T_{sc,line,in,I} \quad 5-153$$

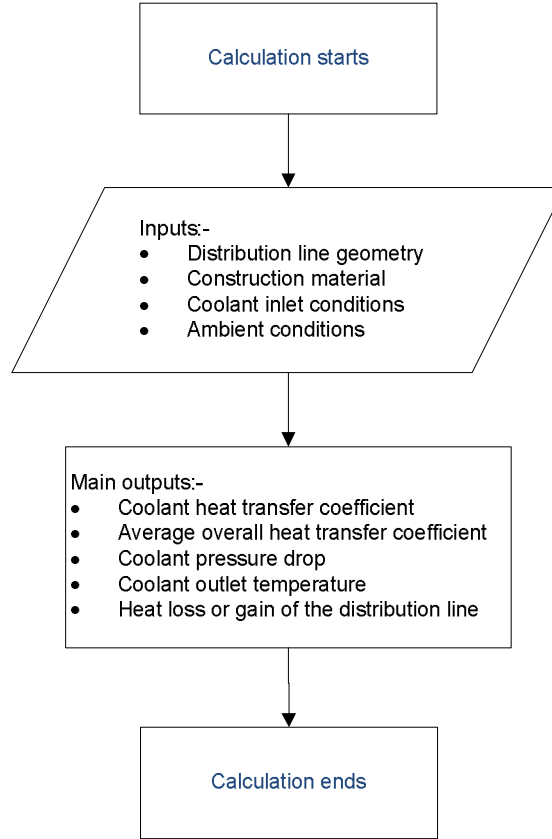


Figure 5.12 Distribution line simulation flow chart to predict its outlet conditions for medium-temperature secondary coolant applications.

Whereas the UA value of the distribution line element is obtained from;

for  $I = 1$  to  $n$

$$UA_{line,e} = \left[ \frac{1}{h_{sc,line,I} \cdot A_{line,i,e}} + \frac{\ln(r_{pip,o} / r_{pipe,i})}{2 \cdot \pi \cdot k_{pipe,I} \cdot L_{line,e}} + \frac{\ln(r_{insul,o} / r_{insul,i})}{2 \cdot \pi \cdot k_{insul} \cdot L_{line,e}} + \frac{1}{(h_{a,line} \cdot A_{line,o,e})} \right]^{-1} \quad 5-154$$



The total heat loss or gain of the coolant in the supply or return distribution line of the secondary coolant refrigeration system is given by;

$$\dot{Q}_{air} = \dot{Q}_{line,total} = \sum_{l=1}^n \dot{Q}_{line,e,l} \quad 5-155$$

The general simulation steps of the distribution line could be simplified using the flowchart shown in Figure 5.12.

### 5.5. Secondary coolant pump model

Secondary coolant pump model has been schematically depicted in Figure 5.13. The secondary coolant pump power requirement is an important element in the design and selection process of secondary coolant refrigeration systems. This is due to the fact that the coefficient of performance (COP) of the system mainly depends on the power consumptions of the pump and the compressors of the refrigeration systems. Thus, the total system pressure drop of the secondary coolants should be taken into account in order to predict pump power requirements.

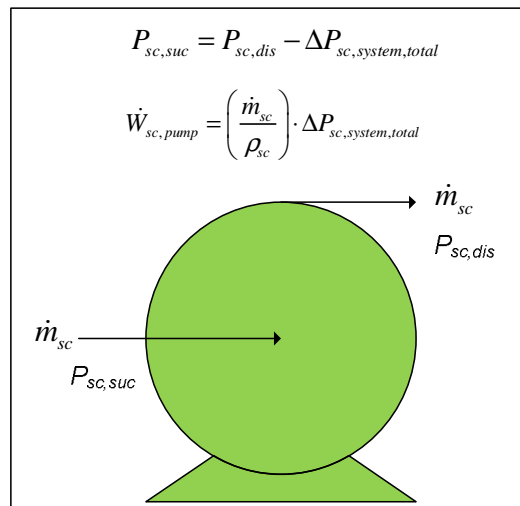


Figure 5.13 Secondary coolant pump model.

Assuming incompressible fluid and steady state conditions, the theoretical power to circulate coolant in a secondary coolant refrigeration system can be calculated by;

$$\dot{W}_{sc,pump} = \left( \frac{\dot{m}_{sc}}{\rho_{sc}} \right) \cdot \Delta P_{sc,system,total} \quad 5-156$$

where the total system pressure drop is the sum of all pressure drops in the secondary coolant circuit, which is given by;

$$\Delta P_{sc,system,total} = \Delta P_{sc,coil,total} + \Delta P_{thx,total} + \Delta P_{sc,line,total} \quad 5-157$$

The pump efficiency is calculated by the ratio of the output power to the input power as;

$$\eta_{pump} = \frac{\dot{W}_{sc,pump,total}}{\dot{W}_{sc,pump,elec}} \cdot 100 \quad 5-158$$

The pump power input ( $\dot{W}_{sc,pump,elec}$ ) required to operate the pump can be determined by direct measurement or from the manufacturers' Pump Performance Curve. The curve is obtained through test of an actual pump running under standard conditions to produce the required flow and pressure.

## 5.6. Compressor model

Semi-hermetic reciprocating compressors may be modeled based on a philosophy presented by Popovic and Shapiro [72], if the performance data of the compressors is known. This model normally requires inputs such as refrigerant inlet state, outlet refrigerant pressure, clearance volume, polytropic exponent for specific refrigerants and motor speed to calculate refrigerant mass flow rate, refrigerant outlet state and compressor power consumption based on volumetric efficiency as extensively described in [73]. However, if the aforementioned information is lacking, the compressor power consumption may be estimated from the manufacturers' compressor performance data based on refrigerant type, capacity and refrigerant mass flowrate.

The outlet temperature of the compressor could then be calculated using the first law of thermodynamics by balancing the heat transfer across the compressor. The compressor model could be depicted using Figure 5.14.

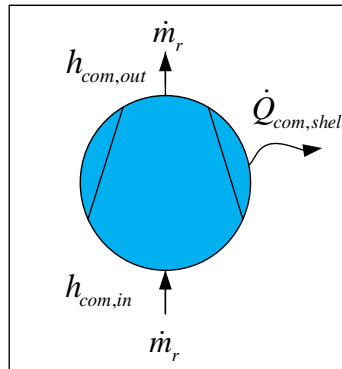


Figure 5.14 Compressor model for secondary coolant refrigeration system.

### 5.6.1. General assumptions

The following assumptions have been incorporated into the compressor model.

- The modeled compressor cycle is an approximation of the real compressor cycle.
- Steady state operation.
- The compressor shell heat transfer rate is a constant fraction of the electrical power input to the compressor.

### 5.6.2. Compressor model inputs and outputs

The following input parameters are needed for the present compressor model:

- Refrigerant inlet temperature and pressure.
- Compressor outlet pressure.

- Refrigerant type.
- Refrigerant mass flowrate.
- Compressor power from manufacturers' performance data based on refrigerant type, heat exchanger capacity, evaporating and condensing temperatures.

The output values of the compressor model will be the compressor outlet enthalpy and temperature as shown in Figure 5.14.

Thus, the compressor under the current study (ZR462-TFD-230 Copeland Scroll type) is modeled based on heat balance across the compressor. The outlet enthalpy is given by;

$$h_{com,out} = \frac{\dot{W}_{com} - \dot{Q}_{com,shell}}{\dot{m}_r} + h_{com,in} \quad 5-159$$

where the compressor shell heat transfer rate  $(\dot{Q}_{com,shell})$  is calculated from;

$$\dot{Q}_{com,shell} = \alpha \cdot \dot{W}_{com} \quad 5-160$$

The fraction of the compressor power  $(\alpha)$  was assumed to be 3% as per Ge and Tassou [74].

Finally, the outlet temperature of the compressor is determined as a function of refrigerant type, compressor outlet pressure and enthalpy using EES [9] thermodynamic function given by Equation 5-161.

$$T_{com,dis} = f(R\$ , P_{com,out} , h_{com,out}) \quad 5-161$$

### 5.7. Expansion valve model

Throttling of liquid refrigerant is accomplished in an expansion device as shown in Figure 5.15. This device can be either thermostatic or electronic expansion valve. Modeling of the expansion valve (Flica TMVX) under the current study is achieved by assuming the throttling process as isenthalpic (i.e. the pressure drop across the expansion valve is isenthalpic). The inputs of the model are pressure and enthalpy of the refrigerant at the inlet of the device, whereas the outputs are enthalpy, pressure and quality of the refrigerant at the outlet of the device.

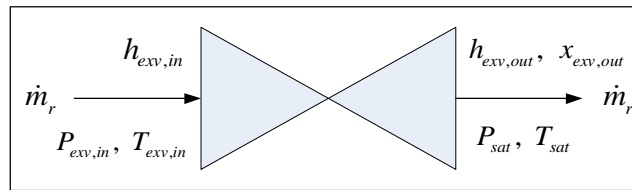


Figure 5.15 Thermostatic expansion valve model.

The expansion valve refrigerant outlet enthalpy is assumed to be equal to the inlet enthalpy.

$$h_{exv,out} = h_{exv,in} \quad 5-162$$

The quality of the refrigerant at the outlet of the expansion valve can be calculated from;

$$x_{exv,out} = \frac{h_{exv,out} - h_f}{h_g - h_f} \quad 5-163$$

Where  $h_f$  and  $h_g$  are respectively the enthalpy of saturated liquid and vapor of refrigerant in the evaporator or intermediate heat exchanger at a given saturation temperature ( $T_{sat}$ ).

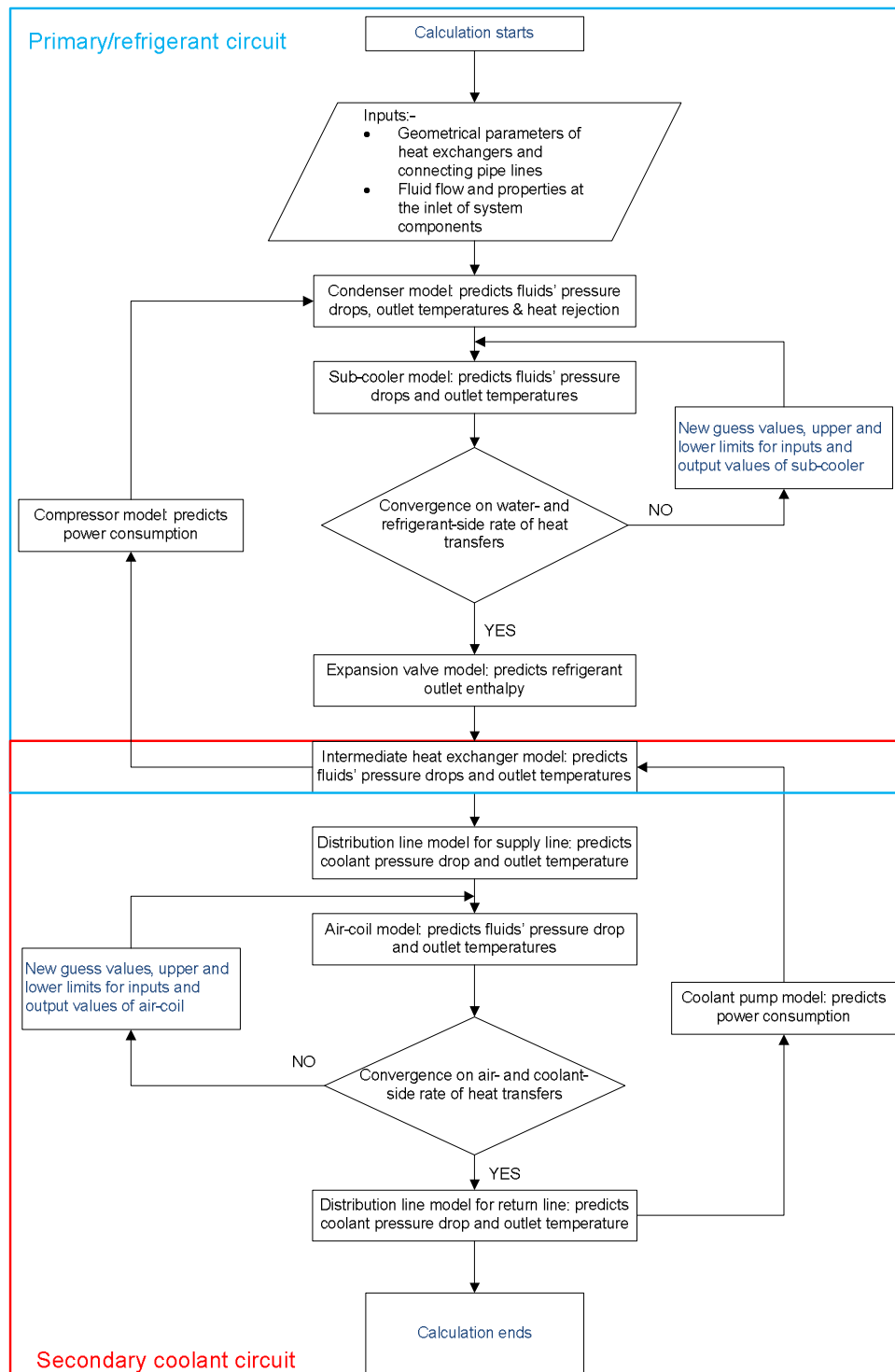


Figure 5.16 Secondary coolant system model simulation flowchart.

### **5.8. Overall secondary coolant refrigeration system model**

The overall secondary coolant refrigeration system is nothing but linking all the component models which have been extensively discussed previously. In other words, some of the outputs of one component are taken as inputs to the other forming the coolant and the refrigerant loops of the overall secondary coolant system as discussed below.

#### ***Coolant loop***

- The test coil coolant outlet temperature was taken as the inlet temperature of the coolant return line.
- The return line coolant outlet temperature was taken as the inlet temperature of the intermediate heat exchanger.
- The return line coolant outlet temperature was also taken as the inlet/outlet temperature of the coolant pump.
- The coolant outlet temperature, which is the inlet temperature of the supply line, from the intermediate heat exchanger was then calculated to complete the coolant loop of the overall system model.

#### ***Refrigerant loop***

- The evaporating temperature and degree of superheat of the refrigerant, which are inputs to the intermediate heat exchanger, were taken to calculate the outlet temperature of the refrigerant.
- The outlet temperature of the refrigerant from the intermediate heat exchanger was taken as inlet temperature of the compressor.
- The outlet temperature of the compressor was taken as the inlet temperature of the condenser.
- The condensing temperature, which is input to the condenser, and the water inlet temperature of the condenser were taken to determine the outlet temperature of the water from the condenser.

- The outlet temperature of the refrigerant from the condenser was taken as inlet temperature of the sub-cooler.
- The outlet temperature of the sub-cooler (sub-cooler was considered as integral part of the condenser since it was not validated) was taken as the inlet temperature of the expansion valve to complete the refrigerant loop of the overall system model.

The overall simulation model is as shown in the form of a flowchart in Figure 5.16. There are two iteration loops in the overall secondary coolant system model. The first iteration loop is that of the refrigerant circuit which determines the sub-cooler outlet temperature and pressure thereby calculating the enthalpy of the refrigerant entering expansion valve (or the enthalpy of the refrigerant entering the intermediate heat exchanger). The first iteration loop should converge on the rate heat transfers both on the refrigerant- and water-side of the sub-cooler. The second iteration loop is attributable to the secondary coolant circuit. This iteration loop determines the outlet temperatures of both the secondary coolant and the air stream across the air-coil. The second iteration loop should converge on the rate heat transfers both on the secondary coolant- and air-side of the air coil. However, the inclusion of the sub-cooler model is optional (i.e. it could be omitted if required) leading to having only one iteration loop.

Once the convergence is achieved in the sub-cooler and air-coil, all other calculations are conducted in an orderly manner for the remaining components of the system such as thermostatic expansion valve, intermediate heat exchanger, compressor, condenser, secondary coolant pump, and connecting pipe lines of the secondary coolant system. The outputs of all system component models could then be linked in series via coolant and the refrigerant connecting lines of the secondary coolant refrigeration system, in an orderly manner, resulting in the calculation of the coefficient of performance (COP) of the system as given by Equation 5-164 below.

$$COP = \frac{\dot{Q}_{aircoil,total}}{\dot{W}_{com} + \dot{W}_{sc,pump,elect}} \quad 5-164$$



Table 5.1 Calculation of thermodynamic state points of secondary coolant system using EES [9].

REFRIGERANT/WATER		
	Inlet	Outlet
Two-phase regime enthalpy	$h_{in} = h(\text{Fluid}, T = T_{sat}, x = 0)$	$h_{out} = h(\text{Fluid}, T = T_{sat}, x = 1)$
Single-phase enthalpy	$h_{in} = h(\text{Fluid}, T = T_{in}, P = P_{in})$	$h_{out} = h(\text{Fluid}, T = T_{out}, P = P_{out})$
Single-phase specific heat capacity	$Cp_{in} = Cp(\text{Fluid}, T = T_{in}, P = P_{in})$	$Cp_{out} = Cp(\text{Fluid}, T = T_{out}, P = P_{out})$
Single-phase thermal conductivity	$k_{in} = k(\text{Fluid}, T = T_{in}, P = P_{in})$	$k_{out} = k(\text{Fluid}, T = T_{out}, P = P_{out})$
Single-phase dynamic viscosity	$\mu_{in} = Visc(\text{Fluid}, T = T_{in}, P = P_{in})$	$\mu_{out} = Visc(\text{Fluid}, T = T_{out}, P = P_{out})$
Single-phase density	$\rho_{in} = \rho(\text{Fluid}, T = T_{in}, P = P_{in})$	$\rho_{out} = \rho(\text{Fluid}, T = T_{out}, P = P_{out})$
SECONDARY COOLANT		
	Inlet	Outlet
Specific heat capacity	$Cp_{in} = Cp(SC, Con, T_{in})$	$Cp_{out} = Cp(SC, Con, T_{out})$
Thermal conductivity	$k_{in} = k(SC, Con, T_{in})$	$k_{out} = k(SC, Con, T_{out})$
Dynamic viscosity	$\mu_{in} = Visc(SC, Con, T_{in})$	$\mu_{out} = Visc(SC, Con, T_{out})$
Density	$\rho_{in} = \rho(SC, Con, T_{in})$	$\rho_{out} = \rho(SC, Con, T_{out})$
AIR		
	Inlet	Outlet
Enthalpy	$h_{in} = h(\text{AirH2O}, T = T_{in}, P = P_{in}, D = DP_{in})$	$h_{out} = h(\text{AirH2O}, T = T_{out}, P = P_{out}, D = DP_{out})$
Specific heat capacity	$Cp_{in} = Cp(\text{AirH2O}, T = T_{in}, P = P_{in}, D = DP_{in})$	$Cp_{out} = Cp(\text{AirH2O}, T = T_{out}, P = P_{out}, D = DP_{out})$
Thermal conductivity	$k_{in} = k(\text{AirH2O}, T = T_{in}, P = P_{in}, D = DP_{in})$	$k_{out} = k(\text{AirH2O}, T = T_{out}, P = P_{out}, D = DP_{out})$
Dynamic viscosity	$\mu_{in} = Visc(\text{AirH2O}, T = T_{in}, P = P_{in}, D = DP_{in})$	$\mu_{out} = Visc(\text{AirH2O}, T = T_{out}, P = P_{out}, D = DP_{out})$
Humidity ratio	$\omega_{in} = \omega(\text{AirH2O}, T = T_{in}, P = P_{in}, D = DP_{in})$	$\omega_{out} = \omega(\text{AirH2O}, T = T_{out}, P = P_{out}, R = RH_{out})$
Density	$\rho_{in} = \rho(\text{AirH2O}, T = T_{in}, P = P_{in}, D = DP_{in})$	$\rho_{out} = \rho(\text{AirH2O}, T = T_{out}, P = P_{out}, D = DP_{out})$

The thermophysical properties of the fluids specified for the secondary coolant system were calculated using a software package called an Engineering Equation Solver (EES) [9], which has built-in property functions of many refrigerants. The first argument of all built-in thermophysical

property functions is the name of the substance. This argument is a string which may be provided as a string constant (e.g. Fluid\$ and SC\$) or a string variable. Many of the thermodynamic functions can take alternate sets of arguments. For example, the enthalpy function for refrigerant can be accessed with temperature and pressure as arguments. All in all, any valid set of arguments can be supplied for thermodynamic functions. If the values of enthalpy or entropy are known, but temperature or pressure is unknown, temperature or pressure functions can be used to calculate their respective values. Table 5.1 summarizes the thermodynamic functions used for the secondary coolant systems.

To summarize, numerical models for secondary coolant system components have been developed thereby forming a complete numerical model of a secondary coolant refrigeration system. These models have been validated using data collected from a lab-scale test rig which is extensively discussed in Chapter 6. The validated models could be used for sizing, rating and selection of components for a medium-temperature secondary coolant supermarket refrigeration system.

## CHAPTER 6.

# Validation of Secondary Coolant Refrigeration System Numerical Model

---

### 6.1. Introduction

Measurements were collected using a lab-scale secondary coolant system test rig, which was modified by coupling the existing air-conditioning system (see Figure 4.1) with an existing heat pump (see Figure 4.2) constructed by Purkayastha and Bansal [50] and Bansal and Purkayastha [51]. The heat pump was converted into a secondary coolant system to supply a chilled coolant (e.g. Mono-ethylene and Mono-propylene glycol/water mixtures with different concentrations by weight) to a newly designed and built flat-finned-tube heat exchanger (test coil). The main aim of the measurements was to obtain all the necessary data from different components of the system, i.e. air-coil, secondary coolant pipe lines, secondary coolant pump, intermediate heat exchanger, compressor, water-cooled condenser, sub-cooler and an expansion device. These data were then used to validate the numerical model developed to investigate the performance of the secondary coolant refrigeration systems.

### 6.2. Test rig details

The schematic of the general test setup for the secondary coolant system is shown in Figure 4.2. It consists of three loops such as the water-loop, the primary-loop and the secondary-loop (secondary coolant loop). The water-loop is comprised of air-cooled water cooler (NQAC400, finned-tube-type), drain sump (for regulating water pressure), water circulating pump (PEDROLLO PKM70/1), sub-cooler (B8 SWEP Plate-type heat exchanger) and water-cooled condenser (B25 SWEP Plate-type heat exchanger) through which the water-loop is thermally coupled with the primary-loop. The primary loop is constructed of accumulator (Virginia VA54-7SRD), compressor (ZR462TFD Copeland Scroll type), receiver, filter (Castel 4016/3), expansion valve (Flica TMVX), and an intermediate heat exchanger (B25 SWEP Plate-type) to

thermally couple the secondary-loop of the system. The secondary-loop consists of a secondary coolant circulating pump (DAB KPS 30/16 M), drain sump (to regulate pressure) an air-coil.

The primary refrigerant carries the heat absorbed from secondary coolant via the thermally coupled intermediate heat exchanger and rejects it in the water-cooled condenser. Finally, the heat load absorbed by the water is removed through the air-cooled water cooler to the surrounding. By controlling the air and water flow rates in the water cooler, the condensing temperature of the primary refrigerant (R22) can be regulated. The mass flow rate of the primary refrigerant (R22) can also be controlled through a standby manually operated expansion valve in order to determine the evaporating and the outlet temperature of the secondary coolant. Detailed schedule of components of the secondary coolant system can be obtained from Tables A.1 through A.4 in Appendix A.

### **6.3. Instrumentation**

The positions of the measurement sensors for the secondary coolant system are depicted in Figure 4.2. All the temperature sensors but three are RTDs (Resistance Temperature Detectors). The three temperature sensors are K-type and T-type thermocouples which were used for measuring sub-cooler refrigerant outlet temperature, and test-coil inlet and outlet temperatures respectively. Five pressure transmitters were installed at different locations along the primary loop pipeline. Four of the pressure transmitters were Danfoss type AKS 33. But, one transmitter (for measuring the outlet pressure of the compressor) was from WIKA (Model no. 891.13.500). Schedules of temperature and pressure sensors of the secondary coolant system can be obtained from Tables B.1 through B.3 in Appendix B.

The primary loop refrigerant mass flowrate was measured using a microprocessor-based mass flow rate transmitter combined with a micro-motion flow sensor. The mass flowrate of the secondary loop coolant was measured using a flow transducer (RS stock No. 257-133), whereas

the mass flowrate of water for cooling the refrigerant was measured using a Fischer and Porter rotameter (Model No. 10A3567XA).

The power consumption of the compressor was measured using Fluke 434 (3-Phase Power Quality Analyzer) which records all measurement values in a 3-Phase system. The power consumptions of the water pump and the secondary coolant pump were measured using LEM HEME-Analyst 2000P, which is a clip-on measuring instrument. A detailed schedule of flow and power measuring instruments for the secondary coolant system can be obtained from Table B.4 in Appendix B.

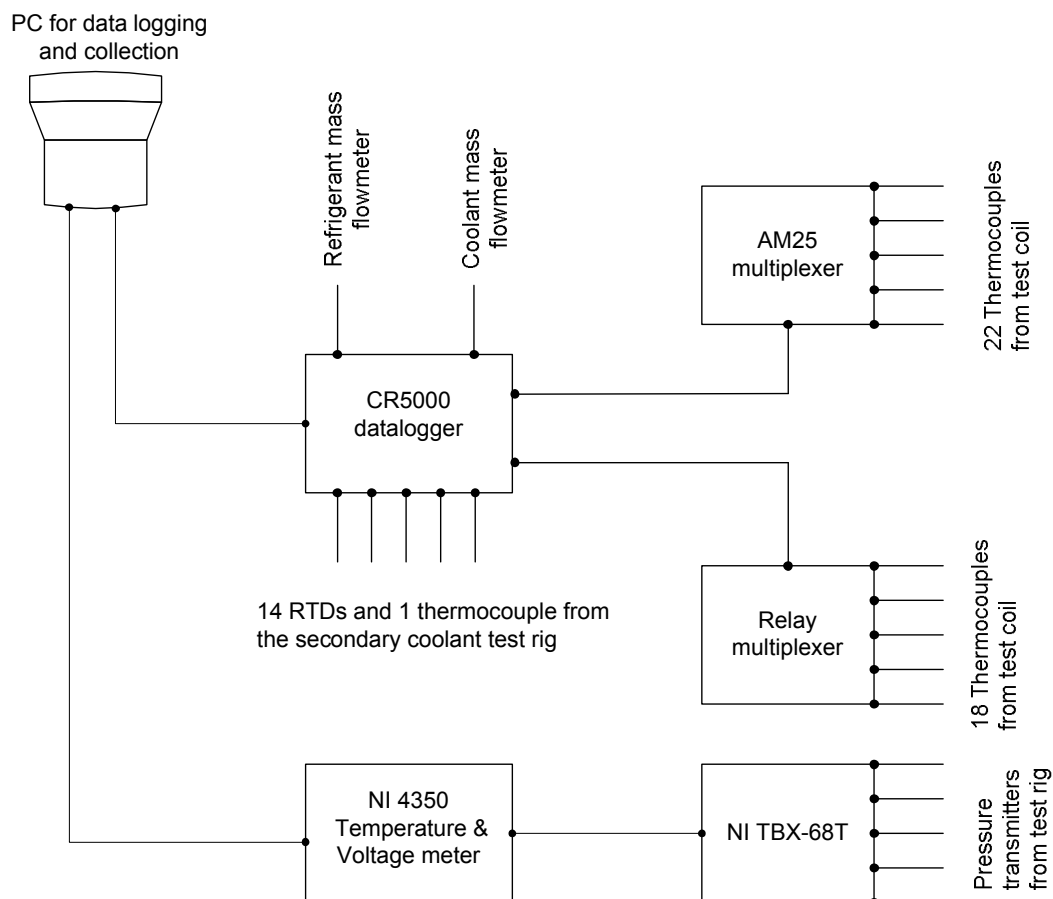


Figure 6.1 Layout of temperature, pressure and mass flowrate data logging system.

### 6.3.1. Data logging

Measurement data collection of the secondary coolant system test rig consisted of two independent data logging systems. The first data logging system (see Figure 6.1) comprised of a PC connected to CR5000 data logger and NI 4350 temperature and voltmeter. The CR5000 data logger was connected to refrigerant and coolant mass flowmeters; 14 RTDs and 1 thermocouple; AM25 and Relay multiplexers. AM25 multiplexer was connected to 22 thermocouples mounted on the test coil to measure fin surface, coolant inlet and outlet temperatures. The Relay multiplex was connected to 18 thermocouples mounted on the tubes of the test coil to measure tube surface temperatures at various locations. The NI 4350 device was connected to a 68-pin DIN-rail mountable terminal block with screw terminals, which was in turn connected to five pressure transmitters to measure pressure from the primary refrigerant of the secondary coolant system. A computer program called Labview was used to log and collect pressure measurement data at an interval of 2.5 seconds.

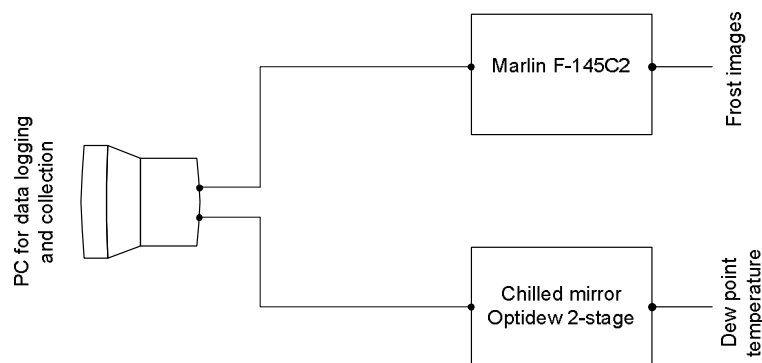


Figure 6.2 Layout of frost image and dew point measurement data logging system.

The second data logging system (see Figure 6.2) comprised of a separate PC connected to an Optidew 2-stage chilled mirror and Marlin F-145C2 CCD camera mounted with Schneider 1.4/12 lens. This data logging system was used to measure dew point temperatures of the air stream across the test coil and frost thickness forming on the surface of the test coil using the

chilled mirror and the CCD Camera, respectively. The dew point temperatures and frost images (for frost thickness calculation) were logged with an interval of 5 and 10 seconds respectively.

The bulk data collected using the above two data logging systems were then transferred to a laptop every day for analysis. The average of the measurement values was used to represent the average value for a single test run.

### **6.3.2. Calibration of measurement sensors**

The calibration of measurement sensors is an essential element in the experimental procedure. In this procedure, the sensors were checked against standard instruments having well known accuracy. Calibration normally minimizes errors and improves accuracy of measurement sensors since the standard instruments are more accurate than the sensors to be calibrated. The following Sections discuss the methods of calibration applied on temperature, pressure and flowmeter sensors.

#### ***6.3.2.1. Calibration of temperature sensors***

The thermocouples for the current research were selected based on accuracy, application and cost. K-type (chromel-alumel) thermocouples could be applied satisfactorily for temperatures ranging from (-) 18<sup>0</sup>C to (+) 1370<sup>0</sup>C. These thermocouples have an accuracy of around  $\pm 0.7^{\circ}\text{C}$ , whereas T-type (copper-constantan) thermocouples are recommended for operating temperatures ranging from (-) 180<sup>0</sup>C to (+) 260<sup>0</sup>C with an accuracy of  $\pm 0.5^{\circ}\text{C}$  [53]. RTDs were chosen mainly based on their accuracy. RTD consists of a resistive element, which is exposed a medium to be measured.

The thermocouples were calibrated in two stages. Low-temperature thermocouples (measurement temperatures ranging from -40<sup>0</sup>C to 0<sup>0</sup>C) were calibrated using dry-ice and

ethanol mixture in a small bath whereas high-temperature ones (measurement temperatures ranging from 0<sup>0</sup>C to 100<sup>0</sup>C) were calibrated using ice and water mixture in a water-tank under controlled heat input. Similarly, RTDs were calibrated in two stages. The first stage consisted of calibration of low-temperature RTDs, whereas the second one consisted of calibration of high-temperature RTDs. The dry-ice/ethanol and ice and water mixtures were continuously stirred in the bath/tank to have uniform temperature distribution throughout the calibration period of all temperature sensors.

All temperature sensors were calibrated against a standard thermometer (Ebro TFX 430 digital with type TPX 230 Pt 100 probe) having a resolution of 0.02<sup>0</sup>C and an estimated uncertainty of  $\pm 0.03^0\text{C}$ . The polynomial expressions of the true temperatures as a function of the indicated temperatures of the calibrated temperature sensors are given in Tables B.1 through B.3 in Appendix B.

#### ***6.3.2.2. Calibration of pressure transmitters***

The pressure transmitters were calibrated using the Budenberg Dead Weigh Tester for the range of pressures the sensors were intended to measure. The operating pressure of two of the Danfoss pressure transmitters ranged from -1 to 12 bar gauge, whereas the operating pressure for the other two Danfoss pressure transmitters ranged from 0 to 20 bar gauge. The operating pressure of the WIKA pressure transmitter ranged from 0 to 50 bar gauge. The Dead Weigh Tester comprises of oil-filled cylinders and calibrated weights. The device works on the principle that oil under pressure in the cylindrical column supports weights applied according to the pressure value required. The calibration equations of the pressure transmitters are described in Table B.3, Appendix B.

#### ***6.3.2.3. Calibration of mass flowmeters***

The Micro Motion mass flowmeter, which was used to measure refrigerant mass flowrate, consisted of flow rate transmitter (Model No. RFT9712) and a micro-motion flow sensor (Model



No. DS025S119SS). It was calibrated by directly weighing the amount of water in a bucket and recording the time elapsed for the quantity of water to flow through the flowmeter. The same calibration method was applied in order to calibrate the secondary coolant flow sensor (RS stock No. 257-133) and the Fischer and Porter rotameter (Model No. 10A3567XA). However, the secondary coolant flow sensor was calibrated using mono-propylene and mono-ethylene glycol/water mixtures at  $(-) 10^{\circ}\text{C}$  for better accuracy since these fluids were to be measured approximately at the specified temperature. The polynomial expressions of the true mass flowrates as a function of the indicated mass flowrates of the calibrated flowmeters can be obtained from Table B.4 in Appendix B.

#### **6.4. Uncertainty analysis and test results of the secondary coolant system**

The uncertainty analyses for the measurements taken from the secondary coolant system were conducted following Equations 4-2 through 4-4, which were applied on frost measurements. Regarding the test results, a total of 26 tests were conducted during the entire experiment, out of which only 10 were selected based on the stability and repeatability of the steady state conditions of the experiments. The experimental results and uncertainties of the measured and calculated quantities of these selected tests were analyzed and discussed in the following sections.

##### **6.4.1. Uncertainty analysis**

All of the uncertainties in the primary and calculated quantities for the secondary coolant system are given in Table 6.1. The highest uncertainties ( $\pm 112\%$ ) were observed in the measurements of refrigerant pressure drops in the intermediate heat exchanger due to low pressure drop values combined with high inaccuracies of the pressure transmitters. Hence, the refrigerant pressure drop measurements in the intermediate heat exchanger have been discarded. The pressure drops in the sub-cooler were low, but higher than the pressure drops in the intermediate heat exchanger, resulting in uncertainty of  $\pm 24\%$ . This measurement uncertainty of pressure drops in the sub-cooler was not within acceptable limit, since the calculated pressure drops could be much lower than the uncertainty ( $\pm 24\%$ ). Refrigerant pressure drops in the water-cooled condenser could not be measured, since the discharge temperature of the compressor for all of the tests

conducted was out of the operating range of the pressure sensor (i.e. the operating temperature of the sensor is between  $-20^{\circ}\text{C}$  and  $80^{\circ}\text{C}$  according to the manufacturer's data sheet).

Table 6.1 Results of uncertainty analysis.

Uncertainty in primary measurements		Uncertainty in calculated quantities	
Variable	Uncertainty	Variable	Uncertainty
All thermocouple temperatures	$\pm 0.1^{\circ}\text{C}$	Mono-propylene-side rate of heat transfer in intermediate exchanger [W]	$\pm 9\%$
All RTD temperatures	$\pm 0.06^{\circ}\text{C}$	Mono-ethylene-side rate of heat transfer in intermediate exchanger [W]	$\pm 6\%$
All pressure measurements	$\pm 1\%$	Refrigerant-side rate of heat transfer in plate heat exchangers [W]	$\pm 5\%$
Mono-propylene mass flowrate [kg/min]	$\pm 9\%$	Water-side rate of heat transfer in condenser [W]	$\pm 3\%$
Mono-ethylene mass flowrate [kg/min]	$\pm 6\%$	Water-side rate of heat transfer in subcooler [W]	$\pm 30\%$ to $\pm 120\%$
Refrigerant mass flowrate [kg/min]	$\pm 4.8\%$	Air-side rate of heat transfer in test coil [W]	$\pm 11\%$
Water mass flowrate [kg/min]	$\pm 0.6\%$	Mono-propylene-side rate of heat transfer in test coil [W]	$\pm 15\%$
Air mass flowrate [kg/min]	$\pm 1.6\%$ to $3\%$	Mono-ethylene-side rate of heat transfer in test coil [W]	$\pm 19\%$
Air inlet pressure [kPa]	$\pm 0.9\%$	Mono-propylene-side rate of heat transfer in precooler [W]	$\pm 7\%$
Test coil air pressure drop	$\pm 2\text{Pa}$	Mono-ethylene-side rate of heat transfer in precooler [W]	$\pm 8\%$
Intermediate heat exchanger refrigerant pressure drop	$\pm 112\%$	COP	$\pm 8\%$
Subcooler refrigerant pressure drop	$\pm 24\%$		

It is also important to notice uncertainties in the calculated quantities. The uncertainty in the air-side rate of heat transfer ( $\pm 11\%$ ) across the test coil was less than the uncertainties in the coolant-side rate of heat transfers ( $\pm 15\%$  to  $\pm 19\%$ ), since the air mass flowrate uncertainty ( $\pm 1.6\%$  to  $\pm 3\%$ ) was less than the coolant mass flowrate uncertainties ( $\pm 6\%$  to  $\pm 9\%$ ). Furthermore, the uncertainty in the refrigerant-side rate of heat transfer ( $\pm 5\%$ ) within the plate heat exchangers was less than the uncertainties in the coolant-side rate of heat transfers ( $\pm 6\%$  to  $\pm 9\%$ ), since the

refrigerant mass flowrate uncertainty ( $\pm 4.8\%$ ) was less than the coolant mass flowrate uncertainties. It is also important to note that the uncertainty in coolant-side rate of heat transfer ( $\pm 15\%$  to  $\pm 19\%$ ) across the test coil was higher than the uncertainties in the coolant-side rate of heat transfers ( $\pm 6\%$  to  $\pm 9\%$ ) within the plate heat exchangers due to the fact that the temperatures in the test coil were measured with uncertainty of  $\pm 0.1^\circ\text{C}$ , whereas the temperatures in the plate heat exchangers were measured with uncertainty of  $\pm 0.06^\circ\text{C}$ .

It is worth observing the uncertainties in the water-side rate of heat transfers both in the condenser and subcooler. The difference between the inlet and outlet water temperatures (e.g.  $3^\circ\text{C}$  to  $5^\circ\text{C}$ ) in the condenser is much higher than the measurement uncertainties of the temperatures ( $\pm 0.06^\circ\text{C}$ ) leading to  $\pm 3\%$  uncertainty in the calculated water-side rate of heat transfer. However, the difference between the inlet and outlet water temperatures (e.g.  $0.06^\circ\text{C}$  to  $0.28^\circ\text{C}$ ) in the subcooler was virtually identical to the measurement uncertainties of the temperatures ( $\pm 0.06^\circ\text{C}$ ) resulting in  $\pm 30\%$  to  $\pm 120\%$  uncertainty of the calculated water-side rate of heat transfer in the subcooler. Hence, water-side rate of heat transfer in the subcooler was assumed invalid under the current study.

Finally, the combination of uncertainties in the primary measurements and the calculated quantities has given rise to an uncertainty of  $\pm 8\%$  in the overall coefficient of performance (COP) of the secondary coolant system.

## **6.5. Test results of the secondary coolant system**

The test results for the secondary coolant system using mono-propylene glycol/water (MPG) mixture have been presented in Tables C.1 through C.6 in Appendix C. The test results for mono-ethylene glycol/water (MEG) mixture have been given in Tables D.1 through D.6 in Appendix D. Test numbers 1 to 3 and 9 to 10 represent experimental results of the system with MPG, whereas test numbers ranging from 4 to 8 represent experimental results of the secondary coolant system with MEG. Furthermore, the variations of the experimental parameters under

steady state condition such temperature, pressure, mass flowrate, heat transfer and energy consumption of the secondary coolant system were carefully analyzed, reduced and entered in the tables along with the range of measurements. However, refrigerant pressure measurements at the outlet of the compressor (the inlet of condenser) for both MPG and MEG tests could not be achieved due to the fact that discharge temperature of the compressor for all of the tests was out of the operating range of the pressure sensor (operating temperature  $-20^{\circ}\text{C}$  to  $80^{\circ}\text{C}$ ). Hence, the compressor discharge pressure was assumed to be equal to the saturation pressure at the condensing temperature. Additionally, the last three pressure measurements (TEST# 6 to 8) at the outlet of the intermediate heat exchanger were omitted because of high error in the readings.

#### **6.5.1. Variation of rate of heat transfers in heat exchanger between two fluids**

Variations in rate of heat transfers between two fluids (e.g. refrigerant-coolant, refrigerant-water, and air-coolant) across the test coil and within plate heat exchangers were calculated and presented in Figures 6.3 through 6.5. These variations arose as a result of inaccuracies in the measurement sensors, fluid characteristics, heat gain or loss of the heat exchangers from or to the surrounding and the combination of the above.

The variations in rates of heat transfer between two fluids in the heat exchangers were calculated using the following sequence of equations.

Variation (discrepancy) between refrigerant- and coolant-side rates of heat transfers is given by;

$$Discrepancy = \frac{\dot{Q}_r - \dot{Q}_{sc}}{\dot{Q}_r} \quad 6-1$$

Discrepancy between refrigerant- and water-side rates of heat transfers is given by;

$$Discrepancy = \frac{\dot{Q}_r - \dot{Q}_{water}}{\dot{Q}_r} \quad 6-2$$

Discrepancy between coolant- and air-side rates of heat transfers is given by;

$$Discrepancy = \frac{\dot{Q}_{sc} - \dot{Q}_{air}}{\dot{Q}_{sc}} \quad 6-3$$

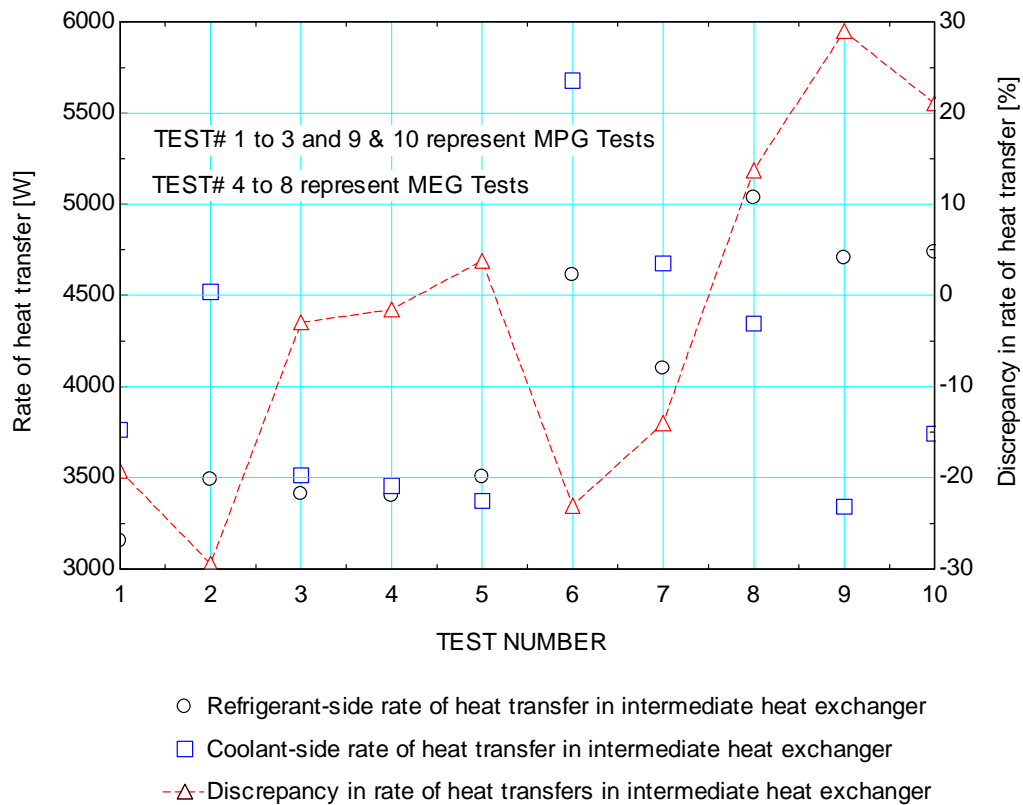


Figure 6.3 Variation of rate of heat transfer on the refrigerant- and coolant-sides in the intermediate heat exchanger.

Rate of heat transfer variations in the sub-cooler were not calculated due to unacceptable uncertainty in the calculated water-side rate of heat transfer as explained in Section 6.4.1.

Rate of heat transfer variation between refrigerant and coolant in the intermediate heat exchange was shown in Figure 6.3 for all tests. The highest discrepancy was observed for MPG tests, which ranged from (-) 29% to (+) 29%, whereas for MEG tests the discrepancy ranged from (-) 23% to (+) 14%.

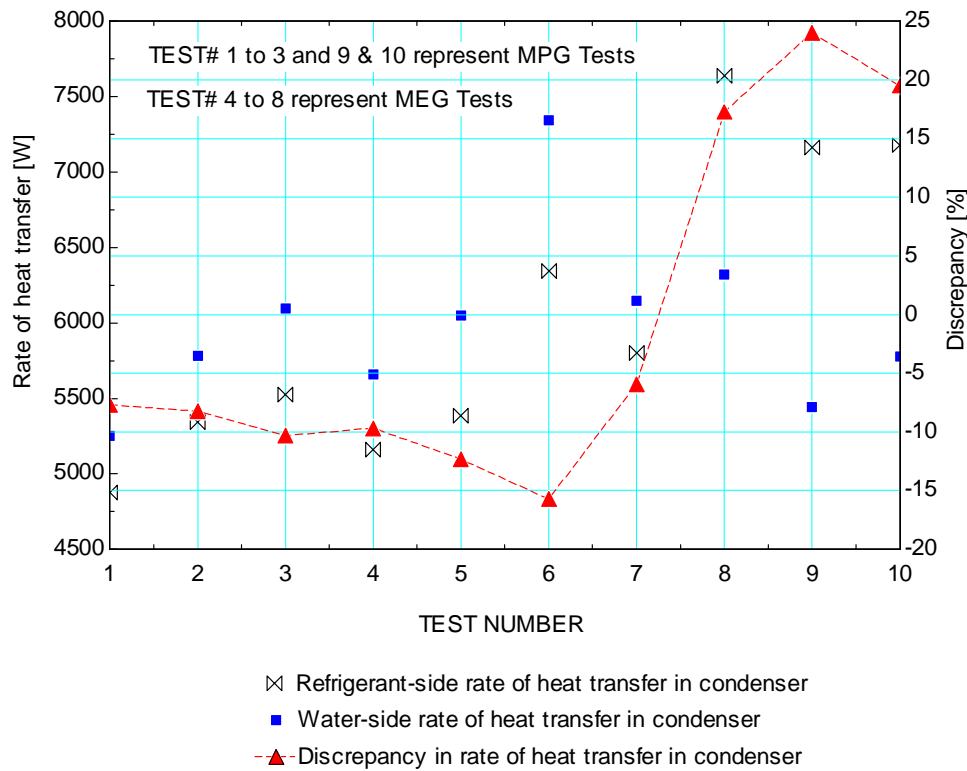


Figure 6.4 Variation of rate of heat transfer on the refrigerant- and water-sides in the condenser.

Rate of heat transfer variation between refrigerant and cooling water in the condenser was shown in Figure 6.4 for all tests. The highest discrepancy was also observed for MPG tests which ranged from (-) 10% to (+) 24%, whereas for MEG tests the discrepancy ranged from (-) 16% to (+) 17%.

Similarly, the rate of heat transfer variation between air and coolant in the test coil was shown in Figure 6.5 for all tests. Here again, the highest discrepancy was observed for MPG tests which

ranged from (-) 5% to (+) 45%, whereas for MEG tests the discrepancy ranged from (-) 37% to (+) 33%.

All in all, the aforementioned variations in rate of heat transfers depend upon inaccuracies in the measurement sensors, heat gain/loss of the heat exchangers from/to the surrounding, especially, fluid characteristics, and the combination of these conditions. Furthermore, the discrepancies were very useful to demonstrate the limitations of the experiment conducted on the secondary coolant system. Hence, the measurements of the air-coil (test coil) and plate heat exchangers, except for the sub-cooler, can be used to validate the numerical models of the secondary coolant system. Besides, the pressure drops in all plate heat exchangers could not be validated because of the reasons explicitly described in Sections 6.4.1 through 6.5.1.

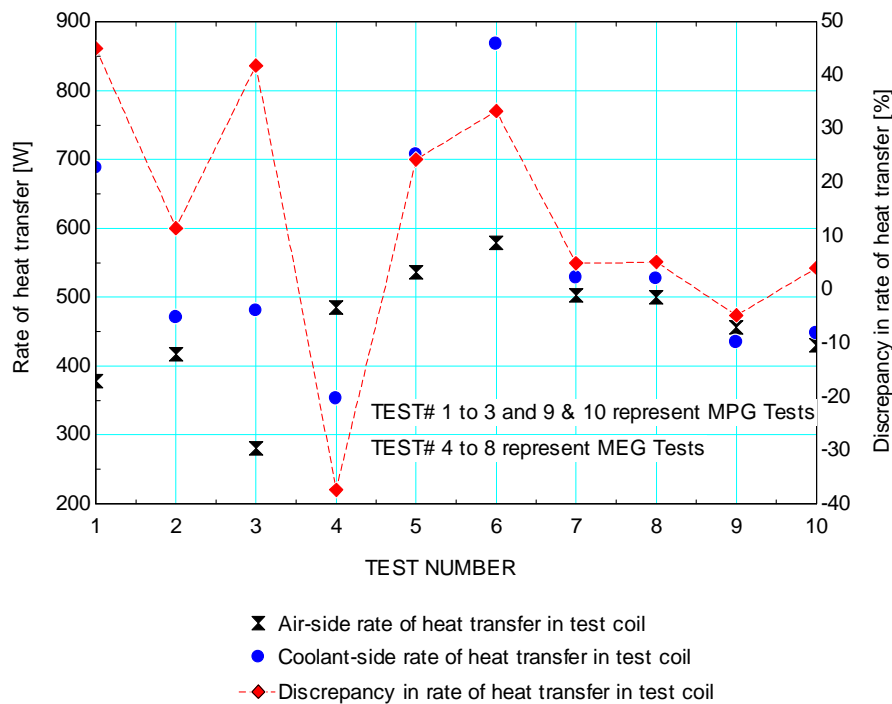


Figure 6.5 Variation of rate of heat transfer on the air- and coolant-sides in the test coil.

### 6.5.2. Coefficient of performance of the secondary coolant system

Coefficient of performance (COP) of the secondary coolant system under the current study was evaluated using the most influential measured quantities of the system such as condensing and evaporating temperatures, coolant type, coolant mass flowrate, coolant test coil inlet temperature, refrigerant mass flowrate, frontal air velocity and air inlet temperature. System COP against the

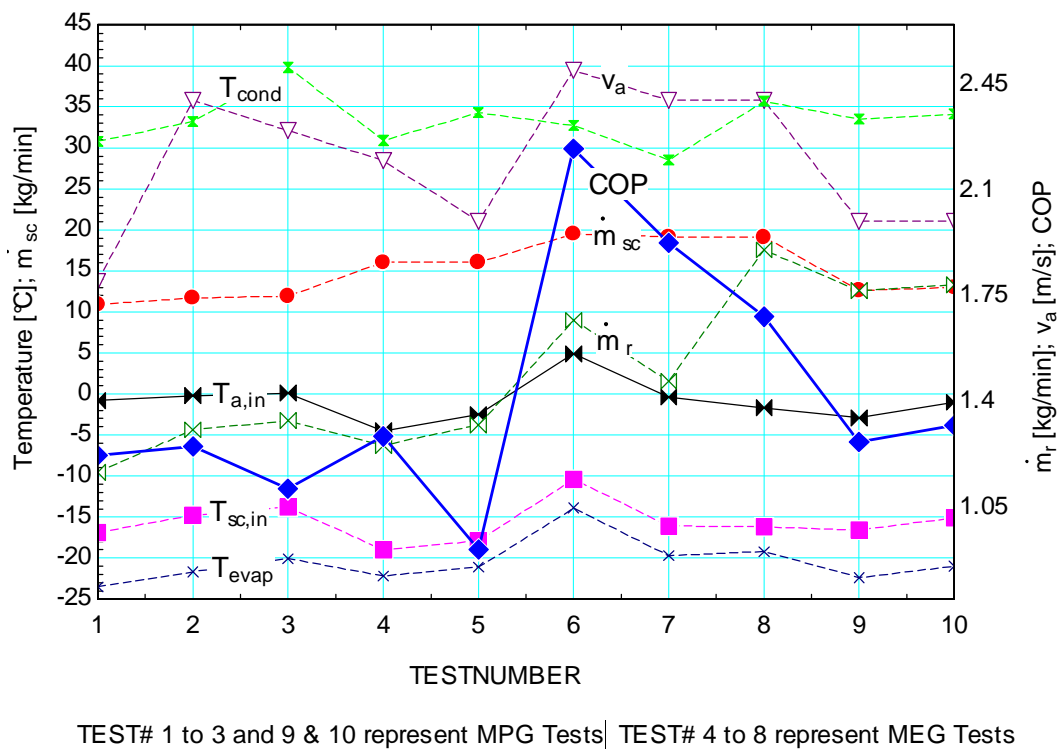


Figure 6.6 Coefficient of performance (COP) of the secondary coolant system for various tests.

aforementioned parameters is depicted in Figure 6.6 for all of the tests (i.e. TEST# 1 to 10) whose data have been given in Tables C.1 through D.6 in Appendix C and D. COP was calculated using compressor power consumption, coolant pump power consumption, test coil capacity and the rate of heat transfer in the pre-cooler. The reason for considering the rate of heat transfer in the pre-cooler was due to the fact that the same coolant passed through both the



test coil and pre-cooler in a closed loop system as shown in Figure 4.2. In fact, the pre-cooler was not part of the experiment, but it was used to cool the air before entering the test coil to achieve the required air temperatures for the test coil. Hence, system COP was computed using Equation 6-4 below.

$$COP = \frac{\dot{Q}_{aircoil,total} + \dot{Q}_{precooler}}{\dot{W}_{com} + \dot{W}_{sc,pump}} \quad 6-4$$

Where  $\dot{Q}_{aircoil,total}$  is the air-side rate of heat transfer in the test coil,  $\dot{Q}_{precooler}$  is coolant-side rate of heat transfer in the pre-cooler; and  $\dot{W}_{com}$  and  $\dot{W}_{sc,pump}$  are compressor and coolant pump power consumptions, respectively.

Table 6.2 COP in descending order as a function of operating parameters of the secondary coolant system.

TEST#	COP	Coolant type	Refrigerant mass flowrate	Coolant mass flowrate	Frontal air velocity	Evaporating temperature	Condensing Temperature	Test coil air inlet temperature	Test coil coolant inlet temperature
			[kg/min]	[kg/min]	m/s	°C	°C	°C	°C
6	<b>2.24</b>	MEG	1.672	19.51	2.5	-13.9	32.7	4.9	-10.4
7	<b>1.93</b>	MEG	1.471	19.16	2.4	-19.7	28.5	-0.4	-16.1
8	<b>1.68</b>	MEG	1.905	19.11	2.4	-19.2	35.7	-1.7	-16.2
10	<b>1.33</b>	MPG	1.790	12.98	2.0	-21.0	34.1	-1.0	-15.1
4	<b>1.29</b>	MEG	1.258	16.05	2.2	-22.2	30.9	-4.5	-19.0
9	<b>1.27</b>	MPG	1.770	12.62	2.0	-22.4	33.5	-2.9	-16.6
2	<b>1.26</b>	MPG	1.310	11.70	2.4	-21.7	33.2	-0.2	-14.8
1	<b>1.22</b>	MPG	1.170	10.89	1.8	-23.5	30.8	-0.8	-16.9
3	<b>1.11</b>	MPG	1.340	11.94	2.3	-20.1	39.8	0.1	-13.8
5	<b>0.91</b>	MEG	1.326	16.07	2.0	-21.1	34.3	-2.5	-17.9

The energy consumptions of the water-loop components (see Figure 4.2) such as water pump and air fan of the water cooler were not considered in the calculation of system COP, since it was assumed that the heat absorbed by the water could be used for heating applications thereby offsetting these energy consumptions. Furthermore, the test coil fan energy consumption was assumed to be negligible since in actual conditions it could be a small amount as compared to the energy consumptions of the compressor and the coolant pump. The energy consumptions of the compressor and the secondary coolant pump are given in Tables C.6 and D.6 in Appendix C and D, respectively. As can be seen from these tables, the secondary coolant pump power consumption varied between 310W and 351W for all the tests. In other words, it was nearly constant. However, the compressor power consumption varied between 2000W and 2450W. Additionally, the other operating parameters given in Table 6.2 were not held constant in order to vary and study the effect of individual parameters, since this exercise is very time consuming and requires a lot of resources. Thus, the maximum and minimum system COPs of the tests were compared solely as guidelines to refrigeration engineers as to which system operating parameters seriously influence system performance. Besides, it should be understood that the main purpose of conducting the experiments on secondary coolant system is only to validate the numerical model developed for the secondary coolant systems by which system performance is evaluated by varying individual operating parameters while holding the other ones constant.

In addition to Figure 6.6, Table 6.2 has been presented to show system COP (in descending order) to clearly understand the influence of the operating parameters of the secondary coolant system. The highest and the lowest COPs (see the blue and red clouds in Table 6.2) among the tests were observed in Test# 6 and 5, respectively. The main reasons for achieving the highest COP could be attributed to a number of factors, including of 1) evaporating temperature ( $-13.9^{\circ}\text{C}$ ) and lower condensing temperature ( $32.7^{\circ}\text{C}$ ), leading to lower compressor power consumption (2225W); and 2) the coolant (MEG) having better thermophysical and transport property for high coolant temperature ( $-10.4^{\circ}\text{C}$ ), leading to higher heat transfer coefficient (see Figure 2.2).

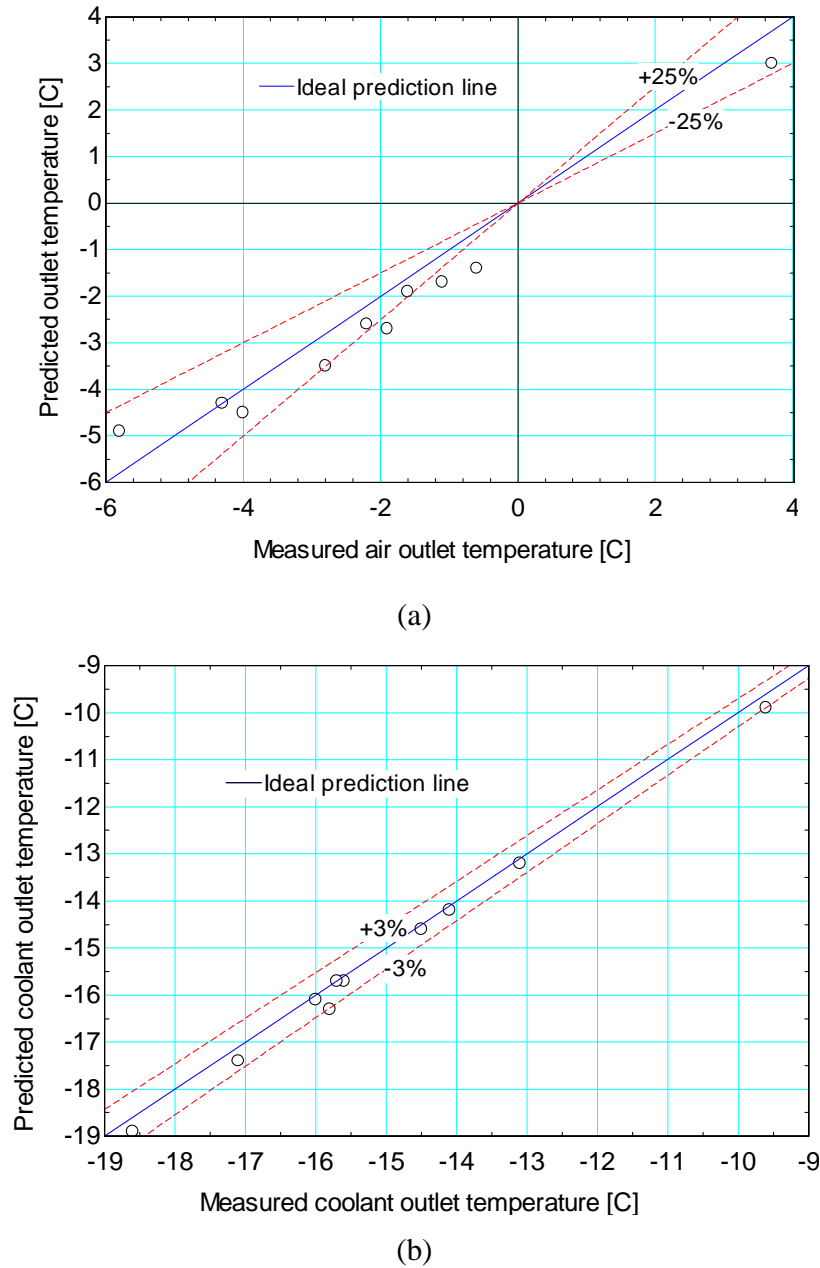


Figure 6.7 Air-coil model prediction of (a) air; and (b) coolant outlet temperatures.

The main reasons for obtaining the lowest COP in Test #5 among the tests conducted could be the combination of 1) Lower evaporating temperature ( $-20.1^{\circ}\text{C}$ ) and highest condensing temperature ( $39.8^{\circ}\text{C}$ ), which led to the highest compressor power consumption (2450W); and 2) The frontal air velocity (2.3m/s) being lower at the air inlet temperature ( $0.1^{\circ}\text{C}$ ) thereby decreasing the capacity of the system (3165W).

It is to be noted that the influence of coolant pump power consumption in the evaluation of system COP described in Figure 6.6 and Table 6.2 was negligible, since the power consumption was roughly held constant. However, coolant type, coolant inlet temperature and mass flowrate have significant impact on pump power consumption as depicted in Figures 2.2 and 2.3. Therefore, validation of the numerical models of the secondary coolant system components is imperative in order to individually investigate the effect of the aforementioned operating parameters on the performance of the system.

## **6.6. Validation of secondary coolant system numerical model**

The main purpose of validating the numerical models of the overall secondary coolant system and its components is to make sure that the deviations of the predicted variables from the measured quantities are within acceptable limits. Hence, the comparison between the model-predicted and the measured values will be presented in the following the subsequent sections.

### **6.6.1. Air coil model validation**

The air coil model validation has been presented in Figures 6.7 and 6.8. The air outlet temperature has been predicted by the air coil model within  $\pm 25\%$  for 70% of the data. The coolant outlet temperature has been predicted within  $\pm 3\%$  for 100% of the data with the highest degree of accuracy, whereas the predicted effectiveness of the air coil deviated from the actual effectiveness by  $\pm 6\%$  for 70% of the data. The main reason for larger deviation of the predicted air outlet temperature by as much as  $\pm 25\%$  from the actual ones is that the heat capacity of the

air is much smaller than the heat capacity of the coolant. In other words, a small change in rate of heat transfer results in larger temperature difference between the inlet and the outlet of the air temperatures, which in turn brings about larger error in the prediction of the air outlet temperature. However, when the coolant-side rate of heat transfer is equated to the air-side rate of heat transfer, the temperature difference between the inlet and the outlet of the coolant will

not be as high as that of the temperature difference in the inlet and the outlet of the air due to higher coolant heat capacity. Hence, the error in the prediction of the coolant outlet temperature was much less than that of the error in the prediction of the air outlet temperature. Additionally, deviation of the predicted air coil effectiveness by  $\pm 6\%$  from the actual one is mainly attributable to UA-value of the air coil. The UA-value is highly influenced by the new frost thermal conductivity as can be seen from Equation 5-34. It is to be noted that the frost thermal conductivity has uncertainty as high as  $\pm 27\%$ .

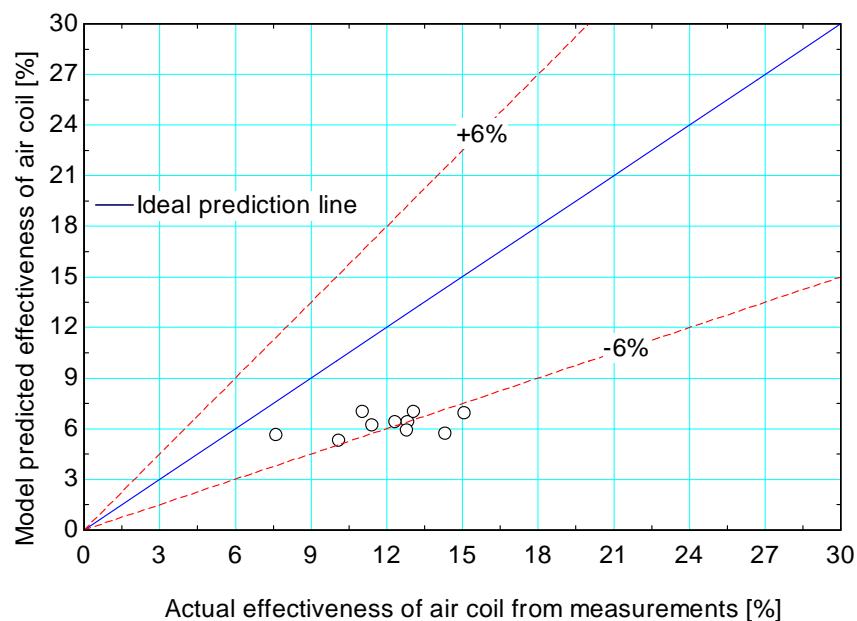


Figure 6.8 Air-coil model prediction of air coil effectiveness.

As discussed in Section 6.5.1, there were also variations (based on measurements) in rate of heat transfers between the coolant- and the air-sides due to inaccuracies in the measurement sensors, heat gain/loss of the heat exchangers from/to the surrounding, especially, fluid characteristics. Hence, the deviation of the model predicted values from the measured ones were anticipated and within acceptable limits considering the limitations in measurements of the air coil (test coil).

### 6.6.2. Intermediate heat exchanger model validation

The predicted coolant outlet temperatures of the intermediate heat exchanger of the secondary coolant system have agreements with the measured coolant outlet temperatures within  $\pm 10\%$  for 90% of the data as shown in Figure 6.9. It is to be noted that, as shown in Figure 6.3, high discrepancy ranging from (-) 29% to (+) 29% in rate of heat transfers between the refrigerant and coolant was observed based on measurements. However, due to the coolant higher heat capacity, the predicted outlet temperature could not deviate very much from the measured coolant outlet temperature resulting in acceptable errors in the intermediate heat exchanger model.

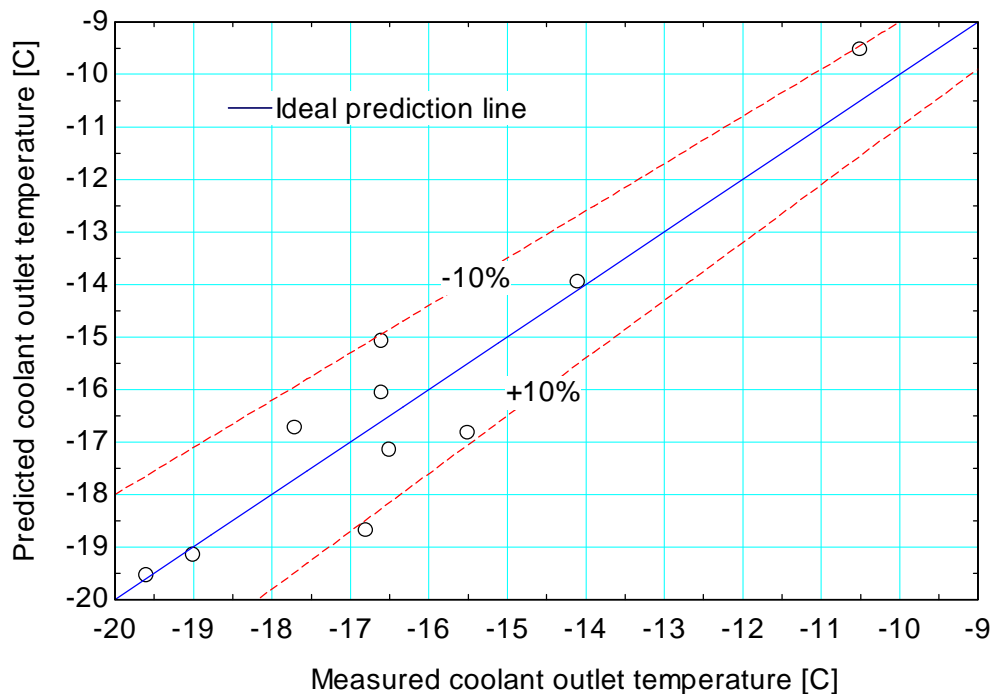


Figure 6.9 Intermediate heat exchanger model prediction of coil coolant outlet temperature.

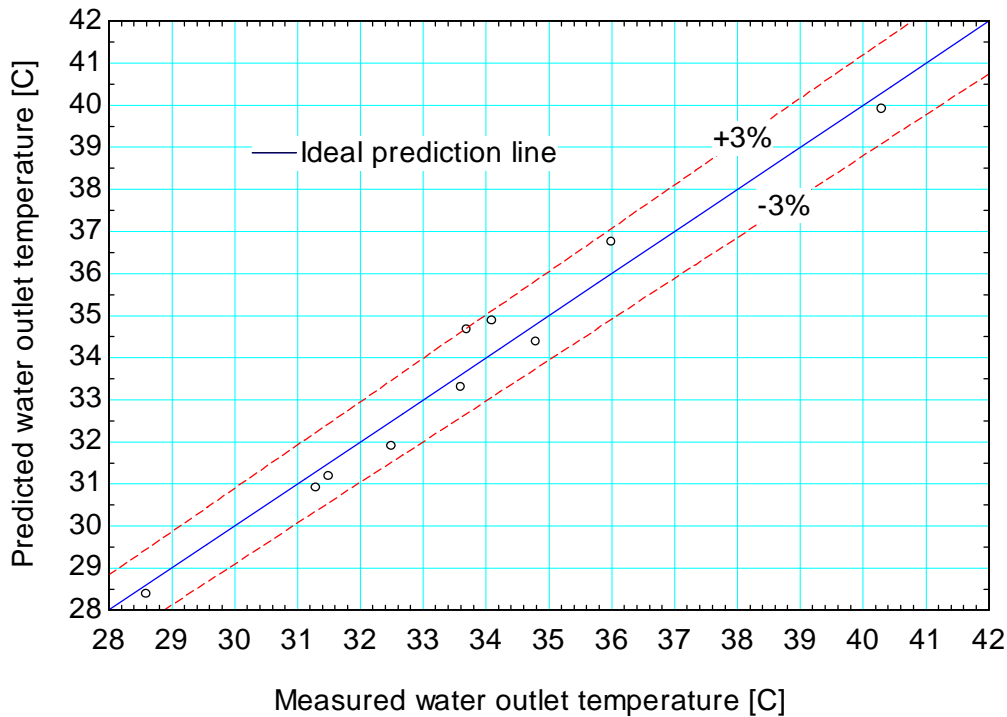


Figure 6.10 Condenser model prediction of cooling water outlet temperature.

### 6.6.3. Condenser model validation

The predicted water outlet temperatures of the condenser in the secondary coolant system have agreements with the measured water outlet temperatures within  $\pm 3\%$  for 100% of the data as shown in Figure 6.10. Here again, as described in Figure 6.4, high discrepancy ranging from (-) 16% to (+) 24% in rate of heat transfers between the refrigerant and the cooling water was recorded based on measurements, which were attributable to inaccuracy of sensors and heat loss/gain to the surrounding. However, due to the water higher heat capacity, the predicted outlet temperature could not deviate very much from the measured coolant outlet temperature resulting in reduced errors in the condenser model.

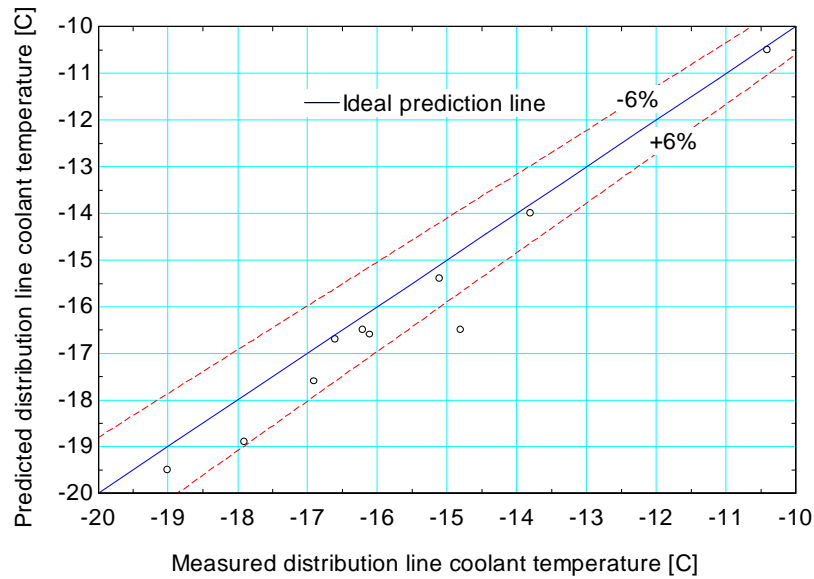


Figure 6.11 Prediction of coolant outlet temperature from supply line of the secondary coolant circuit.

#### 6.6.4. Distribution line model validation

The predicted coolant outlet temperatures of the supply line of the secondary coolant circuit have agreements with the measured coolant outlet temperatures within  $\pm 6\%$  for 90% of the data as shown in Figure 6.11. The main reasons for achieving these good agreements are due to 1) short length of the supply line; and 2) higher coolant heat capacity. The coolant higher heat capacity has resulted in limiting the deviation of the predicted outlet temperatures from the measured coolant outlet temperatures.

The supply line of the secondary coolant circuit is a representative for any part of the pipeline of the circuit. Hence, the validation of the return line applies for the entire distribution line of the secondary coolant refrigeration system.



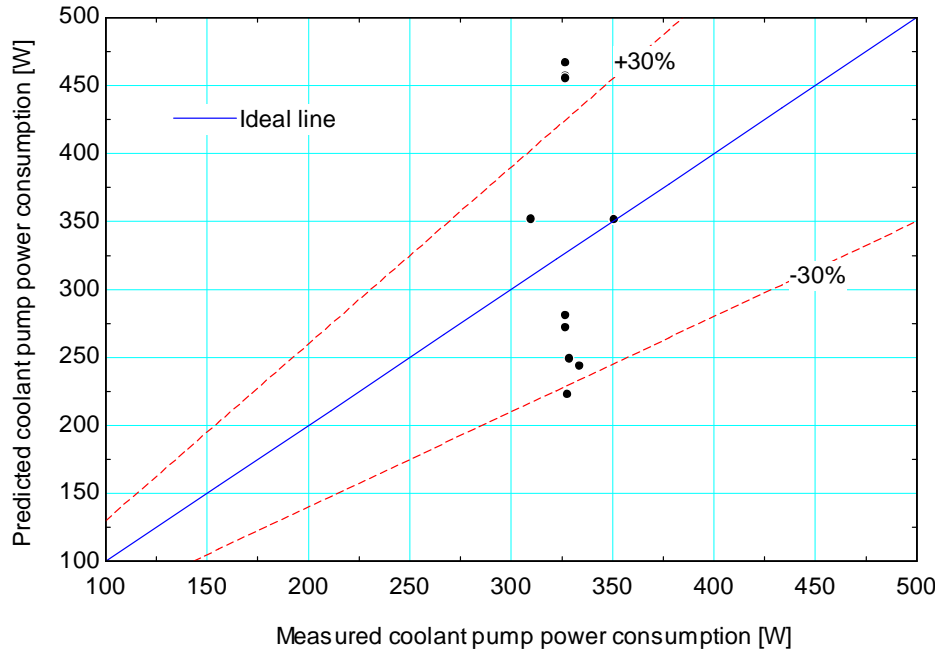


Figure 6.12 Pump model prediction of secondary coolant pump power consumption.

#### 6.6.5. Secondary coolant pump model validation

The predicted coolant pump power consumption deviated from the measured coolant pump power consumption by as much as  $\pm 30\%$  for 70% of the data as shown in Figure 6.12. The reasons for such deviations were mainly due to lack of 1) proper friction coefficients for secondary coolants in plate heat exchangers; and 2) proper secondary coolant pressure loss coefficients for fittings and manifolds in the numerical coolant pump model. It is important to note that there are significant uncertainties in the friction and fittings loss coefficients since these design variables are highly dependent on pipe diameter, surface roughness, the Reynolds number, and the configuration of the coolant loop components as a whole. Additionally, the pump efficiency was assumed to have a representative value of 19% for all tests which could considerably affect the predicted pump power consumption. This pump efficiency was chosen or calculated until the predicted pump power consumption matched the actual one within a reasonable degree of accuracy. It could also be necessary to observe that the contribution of the pump power consumption was about 11% to 15% of the total power (pump + compressor) consumption of the experimental test rig. Thus, the deviation of the predicted pump power

consumption from the actual one does not as such influence the COP of the secondary coolant system considerably.

Hence, future development of proper empirical friction coefficients for plate heat exchangers, fittings and manifolds for various secondary coolants is vital for accurate pressure loss calculations in the secondary coolant refrigeration systems which in turn will enable accurate predictions of coolant pump power consumptions.

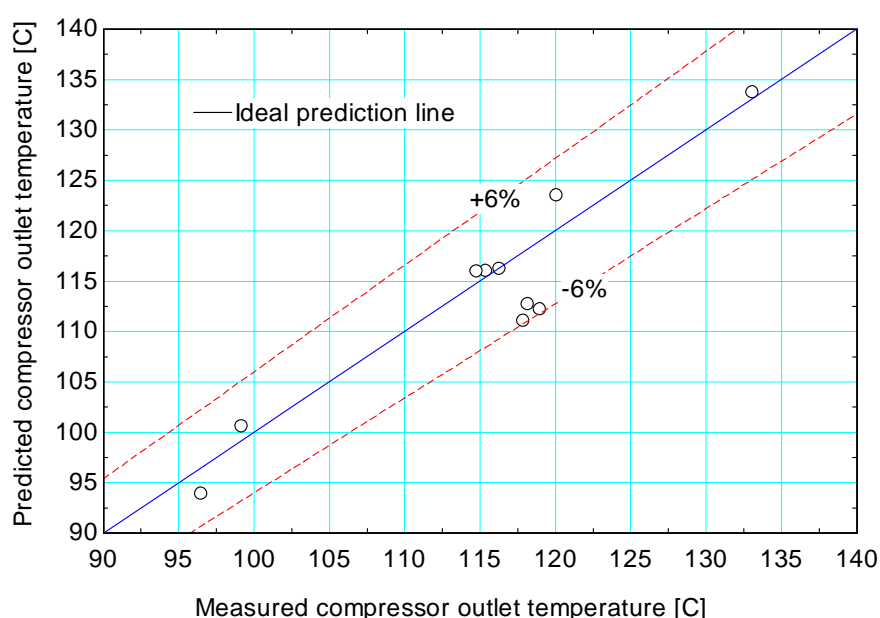


Figure 6.13 Compressor model prediction of compressor outlet temperature.

#### 6.6.6. Compressor model validation

Suppliers normally provide information on compressor power consumption based on heat exchanger (e.g. intermediate heat exchanger) capacity, refrigerant type, evaporating and condensing temperatures. In the current study, the power consumption was directly measured. Compressor measurement data for all tests under the current project can be observed from Tables C.6 and D.6 in Appendix C and D, respectively. However, these measurements were

approximated to the closest Supplier's compressors power consumption data. The approximated power consumptions were then taken as inputs to the compressor model to predict the outlet temperature of the compressor. This is as such part of secondary coolant component selection process.

Based on the aforementioned input data, the predicted compressor outlet temperature had a good agreement with the measured compressor outlet temperature within  $\pm 6\%$  for 100% of the data as shown in Figure 6.13. The reasons for such good agreements were mainly due to good compressor power consumption measurement data.

#### **6.6.7. Validation of sub-cooler and expansion valve models**

Because of high uncertainties in rate of heat transfer ( $\pm 120\%$ ) and pressure drops ( $\pm 24\%$ ) in the sub-cooler, validation of sub-cooler could not be conducted. For instance, the error in the measured refrigerant-side pressure drop ( $\pm 24\%$ ) was much higher than the calculated pressure drops. Hence, the sub-cooler was considered to be an integral part of the condenser. However, the sub-cooler model presented under Section 5.3.2 could be very useful to design a secondary coolant refrigeration system to achieve sub-cooling for enhancing intermediate heat exchanger capacity. Validation of the sub-cooler model could be carried out only when measurements of inlet and outlet refrigerant pressures could be collected via highly precise pressure transmitters. Furthermore, temperature differential of the water flowing in the sub-cooler should be reasonably high (above the resolution of temperature sensor) to enable energy balance calculations.

Regarding validation of expansion valve, the inlet enthalpy was exactly equated to the outlet enthalpy eliminating the necessity of all calculations but the quality of the refrigerant. Quality was not measured, hence could not be validated. However, the exit enthalpy and quality were

taken as inputs to the intermediate heat exchanger model, which was already validated under Section 6.6.2.

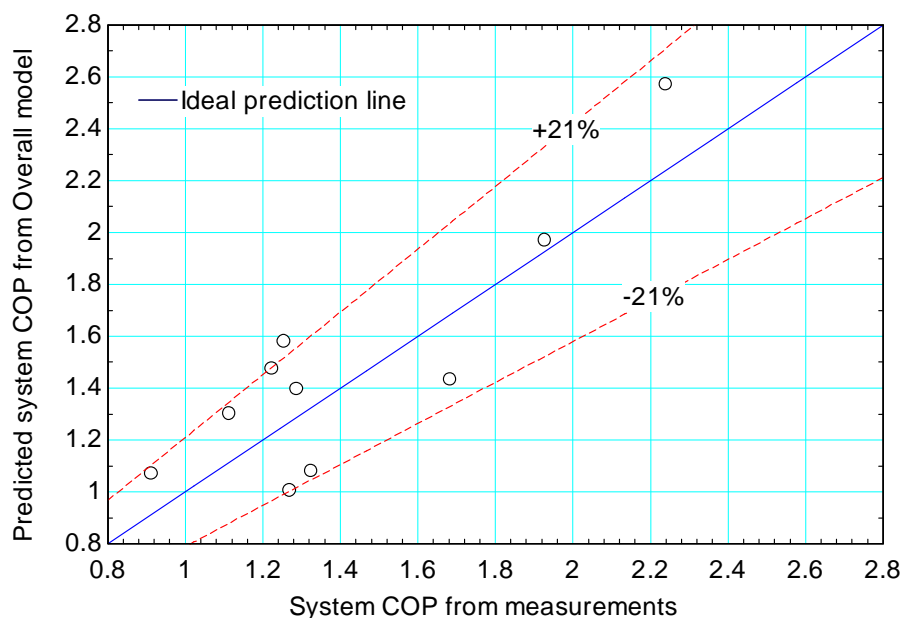


Figure 6.14 Overall system model prediction of secondary coolant system COP.

#### 6.6.8. Validation of overall secondary coolant system model

Validation of the overall secondary coolant refrigeration system was carried out by combining the outputs of the air coil, compressor and secondary coolant pump and computing the coefficient of performance (COP) of the system as given by Equation 5-164. However, it is to be noted that the rate of heat transfer in the pre-cooler was considered in COP calculation since the same coolant passed through both the test coil and pre-cooler in a closed loop system as described in Section 6.5.2.

Generally, the model predicted COP of the system deviated from the system COP obtained using measurements as much as  $\pm 21\%$  for 100% of the data as shown in Figure 6.14. The reasons for such deviations were mainly due to deviations in 1) the prediction of secondary coolant pump

power consumption; and 2) air-coil air outlet temperature and effectiveness. However, these deviations can be greatly improved if deviations in the prediction of, especially, coolant pump power consumption can be reduced through development of proper pressure loss coefficients for plate heat exchangers, fittings and manifolds.

In conclusion, the numerical models of secondary coolant refrigeration system components and the overall refrigeration system have been validated within acceptable accuracy taking all measurement constraints and the challenging task of selecting appropriate heat transfer and pressure loss coefficients into account. Hence, these models are very useful and could be used to design, select and evaluate secondary coolant refrigeration systems. Furthermore, the application of the aforementioned numerical models has been incorporated in Chapter 7 in detail.

## **CHAPTER 7.**

# **Application of Secondary Coolant Model for Supermarket Refrigeration Systems**

---

### **7.1. Introduction**

The main purpose of this chapter is to discuss the use of the current numerical model of the secondary coolant refrigeration systems for medium-temperature applications in supermarkets. However, the chapter does not attempt to make comparisons with any other supermarket refrigeration systems in terms of performance, cost or environmental impact. In other words, the purpose of the chapter is solely to point out that the numerical model could be used as guidelines to design, select system components and evaluate the secondary coolant systems as a whole before making decisions to install them in supermarket stores.

Comparison of different types of supermarket refrigeration systems requires identifying supermarkets with identical display cabinet lineup configuration and loads, which is difficult to achieve. Consequently, the following sections will present simulation of a secondary coolant refrigeration system based on the arrangements and cooling duty or loads of display cabinets of an in-situ direct expansion supermarket refrigeration system operating in Auckland [73]. This approach could be considered as replacing the components of medium-temperature direct expansion refrigeration system with that of medium-temperature secondary coolant refrigeration system by keeping the configuration of the cabinets and the associated distribution lines intact.

### **7.2. Details of supermarket selected for simulation**

Low-temperature cabinets have not been considered for simulation since the numerical model developed in the current study is only for medium-temperature applications. However, they have

been included in the general layout of the selected supermarket, as shown in Figure 7.1, for information purpose only.

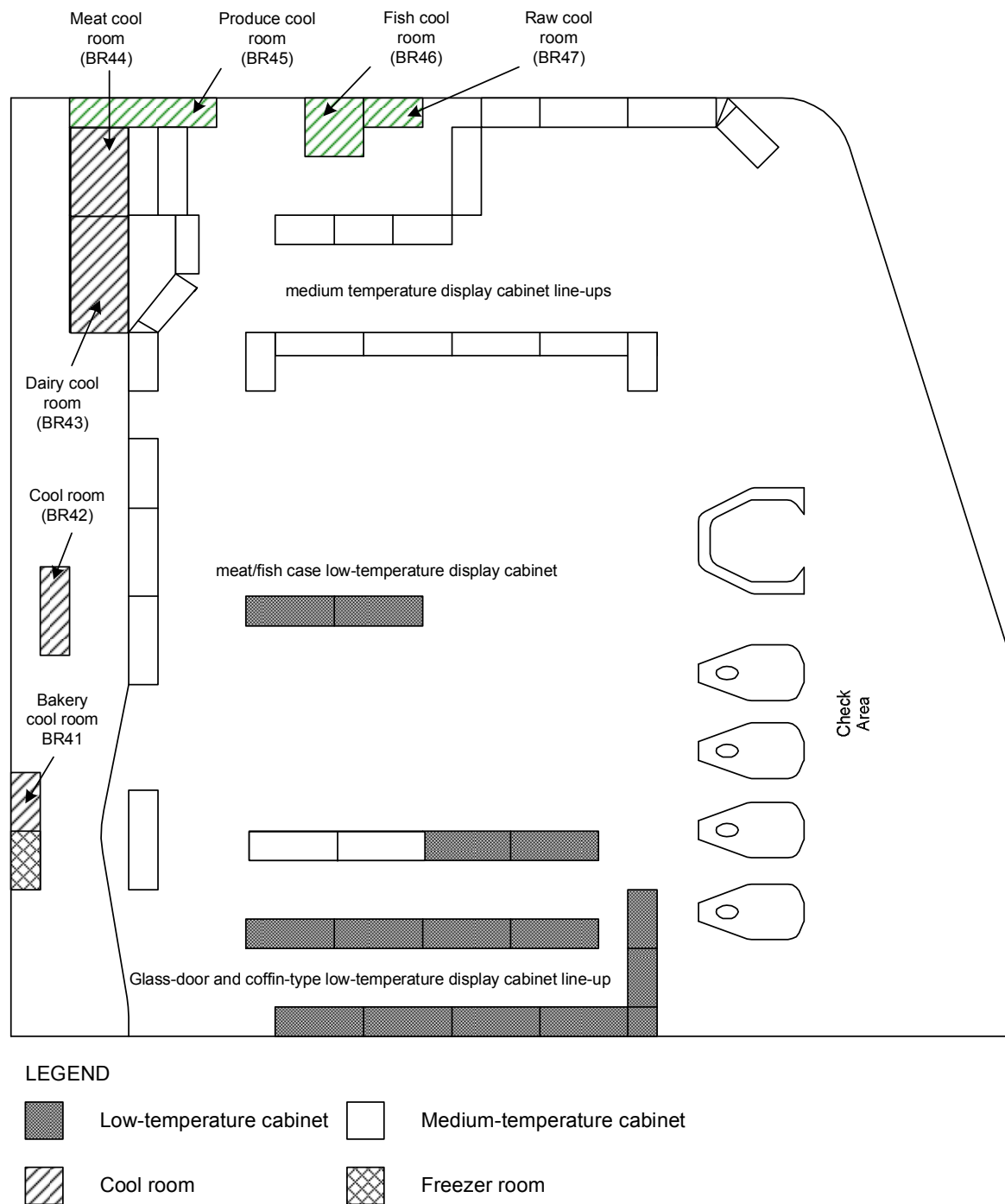


Figure 7.1 Layout of supermarket selected for simulation.

The selected supermarket has 3440 m<sup>2</sup> sales area, and comprises two parallel rack systems along with two air-cooled condensers. These racks provide refrigeration for all display cabinets, cool rooms, freezer rooms, and refrigerated preparation sections of the supermarket. Both the low- and medium-temperature display cabinets use electric defrost mechanism. The simulation of the secondary coolant system, in general, deals with replacing the medium-temperature direct expansion refrigeration system. Thus, the description of the supermarket is confined to this system only.

The medium-temperature refrigeration system consists of six major circuits, namely Circuit A, Circuit B, Circuit C, Circuit D, Circuit E and Cool Room Circuit charged with hydrofluorocarbon refrigerant (R404A). Circuit A feeds refrigerant to produce, lunch/drinks, beer and wine cabinets, whereas Circuit B feeds refrigerant to home meal, deli, dairy, salads, beer, milk and pet food cabinets. Circuit C feeds refrigerant to hang-sell, pizza, sushi, cheese, deli and dairy cabinets. Circuit D feeds refrigerant to cheese and dairy cabinets. Circuit E feeds refrigerant to shell fish, meat and cake cabinets. The Cool Room Circuit feeds refrigerant to fish, raw, produce, meat dairy, deli and bakery cool rooms. Schedule of the medium-temperature cabinets can be obtained from Table E.1 through E.6 in Appendix E.

The aforementioned refrigerant circuits could be operated independently or collectively depending on the requirements of the supermarket display cabinet load conditions. Hence, simulation of the secondary coolant refrigeration system has been conducted based on one of these circuits since the procedure of the simulation is exactly identical for the other circuits as well. Circuit A has been selected for this purpose since all the display cabinets have the same evaporating temperature ( $-8^{\circ}\text{C}$ ).

Similarly, the corresponding secondary coolant circuits could be operated independently or collectively using isolating valves mounted both on the coolant pumps and the display cabinet air-coils as shown in Figure 7.2. The schematic in this figure shows the arrangement of five of



the secondary coolant system circuits and the associated cabinets and cool rooms, which have the same load conditions as the direct expansion refrigeration system chosen for simulation purpose.

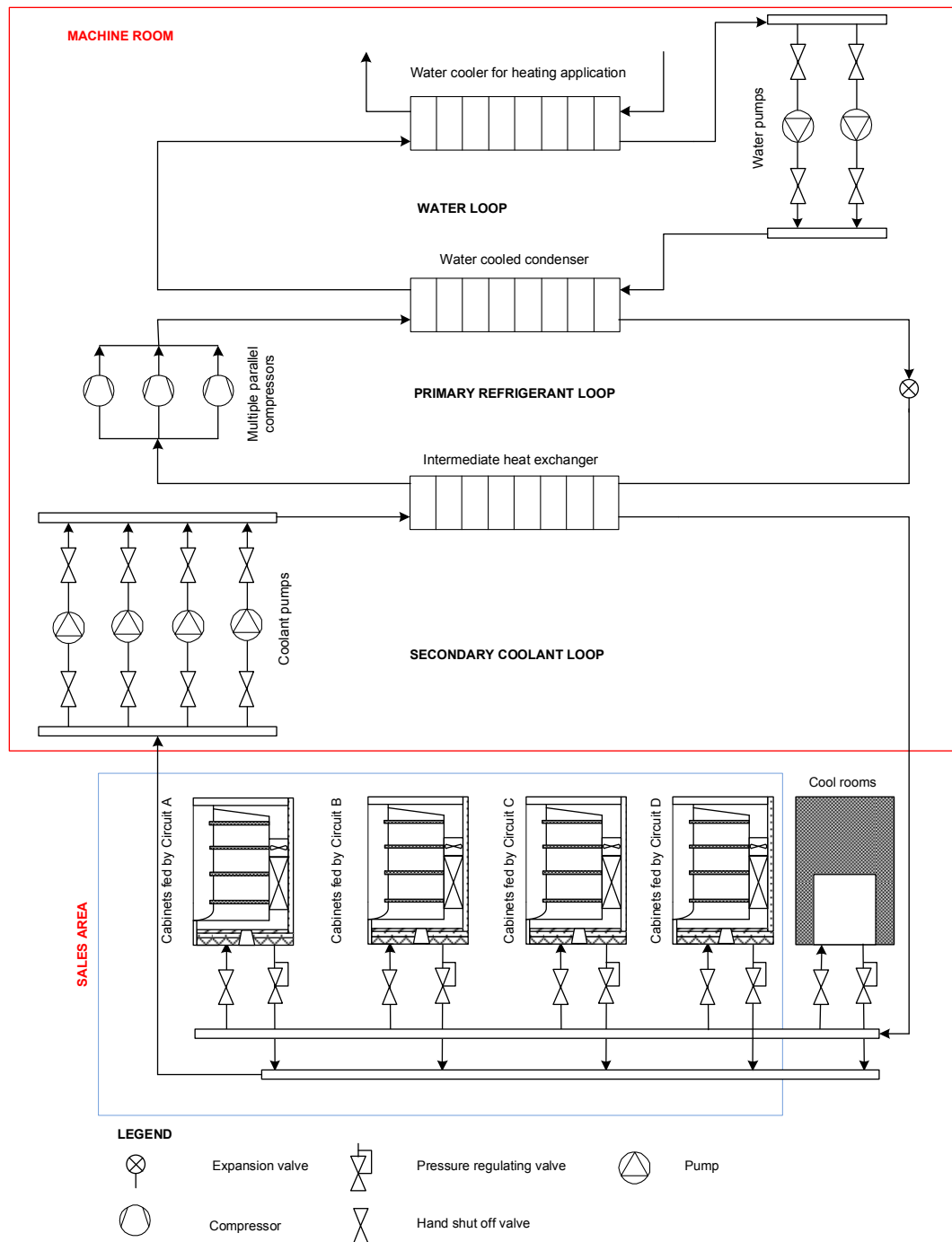


Figure 7.2 Layout of simulated secondary coolant refrigeration system for supermarkets.

The piping layout of Circuit A for direct expansion refrigeration system in the supermarket is shown in Figure 7.3. This circuit feeds refrigerant to three groups of display cabinets. Group1 consists of Produce Cabinets (BR29 and BR30), whereas Group2 consists of Produce Cabinets (BR31 and BR32). Group3 consists of Lunch/Drinks to Go (BR33), Wine (BR35) and Beer (BR36) Cabinets. Each cabinet in each group is installed in parallel. The arrangement of the secondary coolant system in Circuit A was chosen to be exactly identical to that of the direct expansion refrigeration system except for the sizes of the display cabinet air-coils and distribution pipelines. Each cabinet in the secondary coolant system, as previously explained, can be isolated using isolating valves mounted at the inlet and the outlet of the display cabinet air-coil.

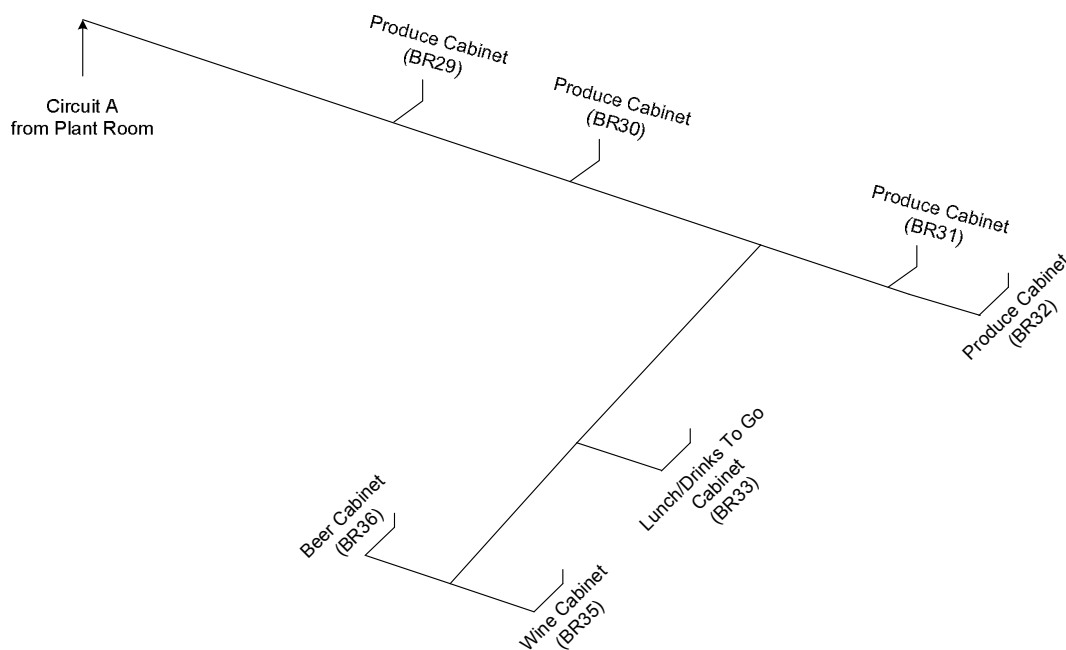


Figure 7.3 Piping layout of Circuit A in the selected supermarket for simulation.

To simplify the simulation procedure of the secondary coolant refrigeration system, selection of systems and components has been carried out in this way. Firstly, among six major circuits, Circuit A has been selected from the model shown in Figure 7.2. Secondly, among three groups

of display cabinets whose piping layout has been shown in Figure 7.3; Group3 has been selected since the cooling loads, air-coil sizes and the operating temperature of the cabinets in Group3 are similar. Finally, the sizing of the display cabinet air-coils has been carried out (as discussed in Section 7.3.1 below) based on the model presented in Figure 7.4. Once the appropriate size of the air-coil has been determined, the right amount of the secondary coolant mass flowrate will be estimated based on the given load of the specific display cabinet in Group3. Additionally, the air-coil size and the mass flowrate for each display cabinet in Group3 have been assumed to remain the same. It is important to note that the procedure of simulating display cabinets in the other groups is exactly identical. In other words, the same simulation procedure can be followed for other circuits, groups of display cabinets and air-coils of the supermarket medium-temperature secondary coolant refrigeration systems.

### **7.3. Simulation of secondary coolant refrigeration system components**

The following sections present step by step simulations of secondary coolant refrigeration system components and the overall system performance for medium-temperature applications in supermarket stores.

#### **7.3.1. Simulation of air-coil for display cabinets**

Simulation of the display cabinet air-coil follows the general assumptions and sequence of calculations described under Section 5.2. Another important assumption here is that the orientation of the air-coil has negligible effect on the performance of the display cabinet as long as the air flow direction is also rotated along with the air-coil. For example, if the air-coil layout in Figure 7.4 is rotated by  $90^0$  to the left or right together with the air flow direction, the rotation of the air-coil will have negligible impact on its performance. Additionally, the general configuration of the display cabinet air-coils is similar to the test coil design presented in Figure 4.3. However, the length, width and number of circuits may be modified depending on the size and load conditions of the display cabinet. The modification of display cabinet air-coil geometry

is done in the way shown in Figure 7.4. In other words, the length of a display cabinet air-coil can be increased in x-direction by increasing the length of the test coil tubes, whereas the width and number of circuits of a display cabinet air-oil can be increased in the y-direction by increasing the number of test coils. In this technique, it is assumed that display cabinet air-coils consist of two or more test coils connected in parallel for a given length. However, these test coils are considered as integral part of a single display cabinet air-coil. For example, if the display cabinet width is increased by two test coils in the y-direction, then the number of circuits and rows of tubes of the display cabinet air-coil will be double of that of the test coil for a given length.

In the display cabinet air-coil assembly illustrated in Figure 7.4, the average air temperature leaving the first test coil ( $T_{a,out,1}$ ) will be considered as the inlet air temperature of the second test coil and the average air temperature leaving the second test coil ( $T_{a,out,2}$ ) will be the inlet air temperature of the third test coil ( $T_{a,out,3}$ ) and so forth. Besides, the secondary coolant inlet temperature to each circuit is assumed to be equal since the coolant is fed to each circuit by a common supply manifold. Similarly, the coolant outlet temperatures from all display cabinet air-coil circuits are averaged to represent the outlet temperature of the coolant from the air-coil since the circuits are connected to a common return manifold.

Unlike other numerical models (in the literature) developed for secondary coolant refrigeration systems, the current model incorporates the consideration of frost characteristics on the air-coils. Hence, during the development of the frost property correlations (see Chapter 4), the secondary coolants used in the test coil were only mono-ethylene glycol (MEG) and mono-propylene glycol (MPG) water mixtures. Type of secondary coolants is believed to influence the property and distribution of frost on air coil surfaces. Therefore, the choice of the secondary coolants for the display cabinet air-coils is between these two coolants (i.e. MEG and MPG), since use of other secondary coolants require extensive experiment and validation of the newly developed frost property correlations on such fluids.

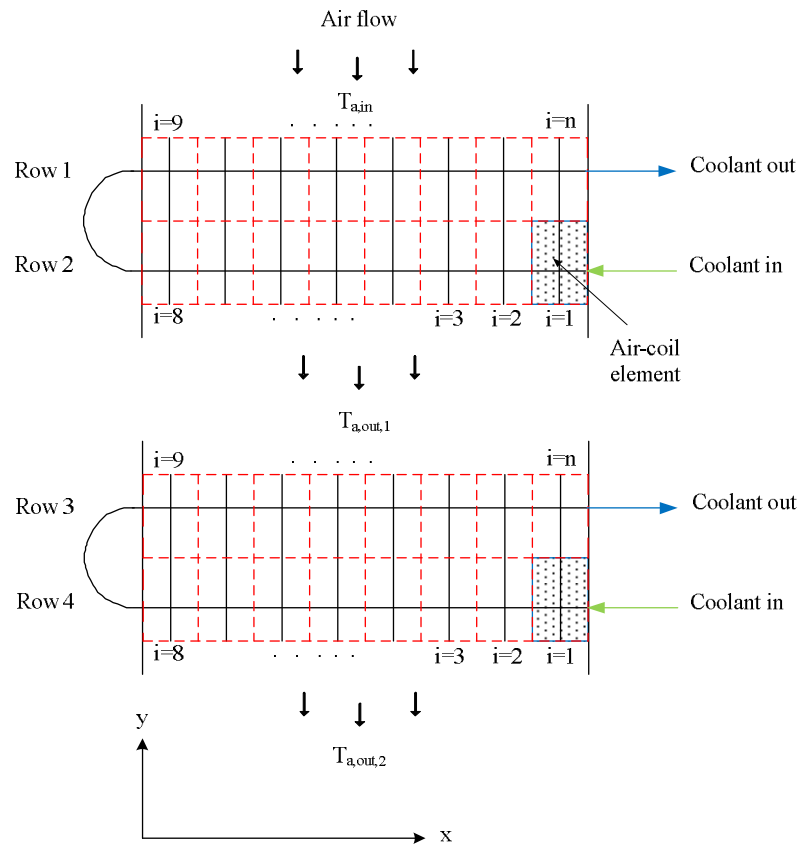


Figure 7.4 Layout of display cabinet air-coil.

Mono-ethylene glycol (MEG) has lower pressure drop and higher heat transfer coefficient (see Figure 2.2) as discussed in Section 2.4.1. Additionally, it has been experimentally demonstrated in Figure 6.6 that medium-temperature secondary coolant refrigeration with MEG has better performance than that with MPG. The only setback with MEG is its toxicity. It may be harmful if swallowed. Consequently, MPG has been selected for simulation as a secondary coolant for display cabinet air-coils since it does not have a serious health risk.

Additionally, MPG has the potential to be combined with Ammonia/ $\text{CO}_2$  cascade refrigeration system [75]. This concept ( $\text{CO}_2$  – Glycol cascade system) involves an open cascade system with  $\text{CO}_2$  as a refrigerant in direct expansion duty for freezing refrigeration loads, and ammonia as the primary refrigerant for high stage duty chilling a secondary coolant which is circulated to the cool rooms and also used as a medium to condense  $\text{CO}_2$ . The first cost of the Ammonia/Glycol

systems also proves to be in line with the first cost of Ammonia/CO<sub>2</sub> brine systems [76], while it has higher life time cost.

### 7.3.2. Inputs and outputs of the simulated display cabinet air-coils

The inputs of a display cabinet air-coil such as geometric parameters and air-side and coolant-side inlet conditions including velocity for both fluids are given in Table 7.1 and 7.2, respectively. The coolant inlet temperature was chosen to be (–) 15.1<sup>0</sup>C, whereas the air inlet temperature was chosen to be (–) 1.0<sup>0</sup>C based on the best coefficient of performance (COP) of the MPG tests as reported in both Figure 6.6 and Table 6.2. Furthermore, the operating conditions of medium-temperature display cabinets are similar to the reported test coil temperatures. Thus, Test # 10 was assumed to represent the operating conditions of the simulated display cabinets since it had the best COP of the secondary coolant system among the MPG Tests which were extensively discussed in Chapter 6. The length and width of the air-coils were estimated using the display cabinet models given in Table E.1 under Appendix E. However, as explained earlier, the other geometric parameters (e.g. tube diameter, fin pitch, fin thickness, heat exchanger construction material, etc.) remain the same as that of the test coil.

The first estimation of the secondary coolant mass flowrate for the display cabinet air-coil is made by limiting the velocity of the coolant to unity ( $v_{sc} = 1 \text{ ms}^{-1}$ ) using Equation 7-1. For energy saving, a simple rule of thumb is to use only half of this velocity [77], since the results in the same reference shows that system performance curves are relatively flat around the optimum value. However, the optimum secondary coolant velocity which should match the display cabinet air-coil loads is normally less than half of unity.

$$\dot{m}_{sc} = \rho_{sc,in} \cdot \left( \frac{\pi \cdot D_i^2}{4} \right) \cdot v_{sc} \quad 7-1$$

Using the first estimation of the coolant velocity, the given display cabinet load is equated to the rate of heat transfer of the secondary coolant in the display cabinet air-coil as shown in Equation

7-2. The velocity is then parametrically adjusted (increased or decreased) until the condition in Equation 7-2 is satisfactorily met.

$$\dot{Q}_{display,load} = \dot{m}_{sc} \cdot C p_{sc,in} \cdot (T_{sc,out} - T_{sc,in}) \quad 7-2$$

Table 7.1 Air-coil geometrical inputs for selected display cabinets (BR33, BR35 and BR36).

Fin thickness [mm]	1	# Circuit in the heat exchanger	14
Tube wall thickness [mm]	1.245	# Tubes in the air flow direction	4
Tube inner diameter [mm]	13.51	# Tubes counted vertically	4
Tube outer diameter [mm]	16	# Tube passes in a circuit	2
Fin pitch [mm]	77	Tube roughness	0
Heat exchanger length [mm]	3750	Vertical distance between tubes (centre-to-centre) [mm]	50
Total tube length in a circuit [mm]	7500	Horizontal distance between tubes (centre-to-centre) [mm]	38
Ratio of total tube length to inner diameter	555	# Air-coils	5
Construction material of fin and tube			Copper

Table 7.2 Air- and coolant-side inputs of the display cabinet air-coils.

Display cabinet load [W]	5900
Air inlet dry bulb temperature [ $^{\circ}\text{C}$ ]	-1.0
Air inlet dew point temperature [ $^{\circ}\text{C}$ ]	-1.3
Air inlet humidity ratio [g/kg]	3.4
Frontal air velocity [ $\text{m s}^{-1}$ ]	2.0
Air inlet pressure [kPa]	101
Air-coil-frost interface temperature [ $^{\circ}\text{C}$ ]	-8.8
Secondary coolant type	MPG
Coolant concentration by weight (%)	52
Coolant inlet temperature [ $^{\circ}\text{C}$ ]	-15.1
Coolant velocity [ $\text{m s}^{-1}$ ]	0.31
Defrost period (time required before defrosting starts) [s]	3840
Electric power input to defrosting elements [W]	1400

Finally, the heat input and time span required for defrosting the frosted display cabinet air-coils are respectively estimated following Equation 4-24 and 4-25 once the correct rate of secondary coolant mass flowrate is determined. All the required outputs of the display cabinet air-coils are entered in Table 7.3 below.

Table 7.3 Outputs of display cabinet air-coils.

Average air exit temperature from the entire air-coil [ $^{\circ}\text{C}$ ]	-3.0
Average air outlet dew point temperature from the entire air-coil [ $^{\circ}\text{C}$ ]	-3.0
Average air outlet relative humidity from the entire air-coil [%]	100
Average air outlet humidity ratio from the whole air-coil [g/kg]	3.0
Average frost thermal conductivity over the whole air-coil [ $\text{W m}^{-1} \text{K}^{-1}$ ]	0.32
Average frost thickness over the whole air-coil [mm]	4.7
Average frost density over the whole air-coil [ $\text{kg m}^{-3}$ ]	36.3
Average air pressure drop over the whole air-coil [Pa]	197
Coolant mass flowrate of a display cabinet air-coil [ $\text{kg s}^{-1}$ ]	0.6592
Secondary coolant exit temperature from the whole air-coil [ $^{\circ}\text{C}$ ]	-12.5
Total coolant pressure drop in the air-coil tubes and manifolds [kPa]	25.0
Average overall heat transfer coefficient of the air-coil [ $\text{W m}^{-2} \text{K}^{-1}$ ]	16.0
Average effectiveness of the display cabinet air-coil [%]	4.1
Defrosting heat input [kJ]	1907
Time span for defrosting an air-coil [s]	1362

### 7.3.3. Simulation of plate heat exchangers

The calculation procedure of the plate heat exchangers such as the intermediate heat exchanger and condenser follows the general assumptions and sequence of heat transfer and pressure drop calculations described under Section 5.3.1 and 5.3.2 through 5.3.4, respectively. However, sub-cooler was not included in the simulation of plate heat exchangers since it was not validated for the reasons given in Section 6.6.7. Before processing with the detailed calculation, the plate heat exchangers are first to be selected from Suppliers data sheet using types of fluid, flow pattern, heat load, and inlet temperatures of single phase fluids, condensing or evaporating temperatures of two phase fluids, mass flowrates, maximum pressure drop and number of passes of the fluids for both sides of the heat exchanger. Based on these inputs, the selected plate heat exchangers are SWEP B400T and SWEP B500T for intermediate heat exchanger and condenser, respectively. The geometrical parameters of the selected intermediate heat exchanger and condenser have been entered in Table 7.4. The fluid-side inputs and the required outputs of these heat exchangers are also given in Table 7.5 and 7.6, respectively.



Table 7.4 Geometrical inputs of intermediate heat exchanger and condenser.

<b>Geometrical parameters</b>	<b>Intermediate Heat Exchanger (SWEP B400T)</b>	<b>Condenser (SWEP B500T)</b>
Effective flow length of fluid in the heat exchanger [mm]	694	979
Effective width of the heat exchanger [mm]	304	304
Mean plate gap or amplitude [mm]	2	2
Number of plates of the heat exchanger	28	28
Number of refrigerant ports	2	2
Number of secondary coolant/water ports	2	2
Number of channels on the coolant-/water-side	14	14
Number of channels on the refrigerant-side	13	13
Port inner diameter [mm]	73	100
Number of flow pass in the heat exchanger	1	1
Plate thickness [mm]	0.933	0.719
Plate construction material	AISI 316	AISI 316

The primary refrigerant selected for the simulation of the secondary coolant system is ammonia, since it is a naturally available refrigerant with good thermophysical properties. The performance of ammonia for high-temperature circuits has been amply discussed in Chapter 3. Besides, the risk associated with toxicity and flammability of ammonia could be reduced since it is confined to the machine room as explained in Section 2.3.

The mass flowrate of the primary refrigerant can be estimated based on the evaporating temperature, the total loads of the display cabinets plus total distribution line heat gain as shown in Equation 7-3 below.

$$\dot{m}_r = \frac{\sum_{i=1}^n \dot{Q}_{display,load} + \dot{Q}_{line,supply,total} + \dot{Q}_{line,return,total}}{(h_g - h_f)} \quad 7-3$$

Where  $(h_g)$  and  $(h_f)$  are the enthalpies for saturated vapor and liquid of the refrigerant at the specified evaporating and condensing temperatures, respectively. The index  $(i)$  represents the  $i^{th}$

display cabinet load, whereas the variable ( $n$ ) represents the total number of similar display cabinets in a group.

The supply ( $\dot{Q}_{line,supply,total}$ ) and return line ( $\dot{Q}_{line,return,total}$ ) total rate of heat losses are determined following Equation 5-155, which has been explicitly explained in Section 5.5.1.

Table 7.5 Inputs of fluid conditions for the intermediate heat exchanger and condenser.

<b>Intermediate Heat Exchanger</b>	
Heat load [W]	33000
Ambient pressure [kPa]	101
Refrigerant saturation/evaporating temperature [ $^{\circ}\text{C}$ ]	-20.0
Refrigerant degree of superheat [K]	5.0
Refrigerant inlet pressure [kPa]	190.1
Refrigerant type	R717
Coolant inlet temperature [ $^{\circ}\text{C}$ ]	-12.4
Mass flowrate of coolant [ $\text{kg s}^{-1}$ ]	3.295
Coolant type	MPG (52%)
<b>Condenser</b>	
Heat load [W]	38000
Water inlet temperature [ $^{\circ}\text{C}$ ]	30
Water exit temperature from the heat exchanger [ $^{\circ}\text{C}$ ]	34
Refrigerant inlet temperature [ $^{\circ}\text{C}$ ]	80
Refrigerant saturation/condensing temperature [ $^{\circ}\text{C}$ ]	35
Refrigerant inlet pressure [kPa]	1351.0

The mass flowrate of water in the condenser is determined by first setting the velocity of the water to unity ( $v_w = 1 \text{ ms}^{-1}$ ) using Equation 7-4 in order to reduce water pressure drop in the condenser. The next thing to do would be parametrically analyzing the pressure drop of the water by decreasing the velocity (below unity) and increasing the number of water-side channels and applying Equation 5-81 through 5-89 until the pressure drop falls below 15 kPa in order to minimize the water pump power consumption.

$$\dot{m}_w = \rho_{w,in} \cdot (v_w \cdot A_s \cdot N_{channel,w}) \quad 7-4$$

Where ( $\rho_{w,in}$ ) is the density of water at the inlet temperature of water, ( $A_s$ ) is channel cross-sectional area and ( $N_{channel,w}$ ) represents the number of channels on the water-side of the condenser.

Table 7.6 Outputs of intermediate heat exchanger and condenser.

<b>Intermediate Heat Exchanger</b>	
Mass flowrate of refrigerant [ $\text{kg s}^{-1}$ ]	0.03005
Refrigerant exit temperature [ $^{\circ}\text{C}$ ]	-15.0
Total refrigerant pressure drop in the heat exchanger [kPa]	0.16
Coolant exit temperature [ $^{\circ}\text{C}$ ]	-15.2
Total coolant pressure drop in the heat exchanger [kPa]	50.0
Average effectiveness of the heat exchanger [%]	61
<b>Condenser</b>	
Mass flowrate of water [ $\text{kg s}^{-1}$ ]	2.271
Refrigerant exit temperature from the heat exchanger [ $^{\circ}\text{C}$ ]	35
Total water pressure drop in the heat exchanger [kPa]	13.0
Average effectiveness of the heat exchanger [%]	90

### 7.3.4. Simulation of secondary coolant distribution line

The calculation procedure of the main and branch distribution lines of the secondary coolant refrigeration system follows the general assumptions and sequence of heat transfer and pressure drop calculations described under Section 5.4.1 and 5.5, respectively. The diameters of the distribution lines can be estimated by using mass flowrates of the coolant and velocity limitations in the pipelines. If the coolant velocity is very high, the pumping power requirement will be very high, since the pressure drop is directly proportional to the square of velocity as given in Equation 5-20. Thus, the diameters of the main distribution line and each branch connected to each display cabinet can be calculated by Equation 7-5 and 7-6, respectively.

$$D_{main,i} = 2 \cdot \sqrt{\frac{\sum_{i=1}^n \dot{m}_{sc}}{\pi \cdot \rho_{sc,in} \cdot v_{sc}}} \quad 7-5$$

Where  $(\dot{m}_{sc})$  is the coolant mass flowrate in each display cabinet air-coil,  $(\rho_{sc,in})$  is the density of the coolant at the inlet of the distribution line, and  $(v_{sc})$  is the coolant velocity in the main distribution line. The index  $(i)$  represents the  $i^{\text{th}}$  coolant mass flowrate in a display cabinet, whereas the variable  $(n)$  represents the total number of similar display cabinets in a group.

Table 7.7 Geometrical inputs and outputs of distribution line.

<b>Geometrical Parameter</b>	<b>Main Distribution Line</b>	<b>Branch Distribution Line</b>
<b>Geometrical Inputs</b>		
Flow length of the coolant pipe [mm] (return + supply lines)	2x64700	2x12000
Construction material of pipe	Copper	Copper
Insulation type	Indaflex	Indaflex
<b>Geometrical Outputs</b>		
Internal diameter of coolant pipe [mm]	99.2	50.42
Outer diameter of coolant pipe [mm]	104.8	53.97
Coolant pipe thickness [mm]	2.794	1.778
Coolant pipe roughness	0	0
Outer diameter of pipe insulation [mm]	155.6	104.8
Coolant pipe insulation thickness [mm]	25	25

Similarly, the diameter of each branch connecting the main distribution line and each air-coil of the display cabinet is given by;

$$D_{branch,i} = 2 \cdot \sqrt{\frac{\dot{m}_{sc}}{\pi \cdot \rho_{sc,in} \cdot v_{sc}}} \quad 7-6$$

Insulation is then selected based on the outer diameters of the main distribution line and the branch pipes. However, the thickness of the insulation (25 mm) has been determined based on the thickness of the insulation used for the experimental test rig (see Table A.3 in Appendix A). The geometrical inputs and outputs of the distribution line and pipe insulation have been given in Table 7.7. The fluid-side inputs and all the necessary outputs have also been given Table 7.8.

Table 7.8 Fluid-side inputs and outputs of distribution line.

<b>Fluid conditions</b>	<b>Main Distribution Line</b>	<b>Branch Distribution Line</b>
<b>Fluid Inputs</b>		
Ambient temperature [ $^{\circ}\text{C}$ ]	20	20
Ambient pressure [kPa]	101	101
Coolant exit temperature [ $^{\circ}\text{C}$ ]	-15.1	-15.1
Mass flowrate of coolant [ $\text{kg s}^{-1}$ ]	3.295	0.6592
Coolant type	MPG (52%)	MPG (52%)
<b>Fluid Outputs</b>		
Coolant inlet temperature [ $^{\circ}\text{C}$ ]	-15.2	-15.1
Pressure drop in the distribution line [kPa] (Supply + Return Lines)	14.0	4.4
Rate of heat gain/loss of distribution line [W] (Supply + Return Lines)	3100	Negligible

### 7.3.5. Simulation of secondary coolant pump

Simulation of the secondary coolant pump is carried out using the calculation methods and assumptions discussed in Section 5.6. The selection of the coolant pump is then conducted by using Spaix Pump Selection Software [78] based on user inputs such as fluid type, minimum inlet pressure, viscosity, operating temperature and volumetric flowrate of the coolant. Using the Pump Selection Software the most suitable pump for the secondary coolant (MPG) was found to be Biral EBZ 45 V/4-108. It is to be reminded that the provision of correct pump inputs will be vital for the pump to operate efficiently and achieve long component life.

The volumetric flowrate of the pump can be determined by Equation 7-7, whereas the total pressure of the system is obtained from Equation 5-157.

$$\dot{V}_{sc} = v_{sc} \cdot \left( \frac{\pi \cdot D_{main,i}^2}{4} \right) \quad 7-7$$

Applying the pump calculation procedure and the selection criteria, the inputs and the outputs of the selected secondary coolant pump were then entered in Table 7.9 below.

Table 7.9 Inputs and outputs of secondary coolant pump.

<b>Pump Inputs</b>	
Operating temperature [ $^{\circ}\text{C}$ ]	-15.1
Minimum inlet pressure [kPa]	10.4
Volumetric flowrate of coolant [ $\text{m}^3 \text{s}^{-1}$ ]	0.00311
Total pump pressure (including inlet pressure) [kPa]	104212
Coolant kinematic viscosity [ $\text{mm}^2 \text{s}^{-1}$ ]	59
Coolant type	MPG (52%)
<b>Pump Outputs</b>	
Pump efficiency [%]	31
Theoretical pump power consumption [W]	324
Actual pump power consumption [W]	1100

Table 7.10 Inputs and outputs of compressor.

<b>Compressor Inputs</b>	
Cooling (evaporating) capacity [W]	33000
Refrigerant inlet temperature [ $^{\circ}\text{C}$ ]	-15.0
Refrigerant inlet pressure [kPa]	190
Refrigerant outlet pressure/condensing pressure [kPa]	1351
Refrigerant mass flowrate [ $\text{kg s}^{-1}$ ]	0.03005
Refrigerant type	R717
<b>Compressor Outputs</b>	
Refrigerant outlet temperature [ $^{\circ}\text{C}$ ]	80
Compressor power consumption [W]	15744
Oil cooler load [W]	10630

### 7.3.6. Simulation of compressor

The general assumptions and calculation procedure of the refrigerant compressor are carried out following Section 5.7.1 and 5.7.2, respectively. The selection of the compressor is conducted using Bitzer Software [79] based on user inputs such as refrigerant type, cooling (evaporating) capacity of the intermediate heat exchanger, mass flowrate, degree of superheat, evaporating and condensing temperatures of the refrigerant. Once the appropriate compressor (in this case it was found to be Model OSNA5351-K) is selected using the aforementioned parameters, the

discharge temperature of the compressor is calculated following Equation 5-161. The inputs and outputs of the compressor are given in Table 7.10.

### 7.3.7. Simulation of expansion valve

The general assumptions and calculation procedure of the thermostatic expansion valve follow Section 5.8. The selection of the expansion valve is conducted based on refrigerant type, rated capacity, evaporating temperature range and pressure drop across the valve. Following the selection of an appropriate thermostatic valve (e.g. Danfoss TEA 20-12 has been selected in this exercise), the outlet enthalpy and quality of the refrigerant are calculated using Equation 5-162 and 5-163, respectively. The inputs and outputs of the expansion valve are given in Table 7.11 below.

Table 7.11 Inputs and outputs of thermostatic expansion valve.

<b>Thermostatic Expansion Valve Inputs</b>	
Rated capacity [W]	33000
Refrigerant mass flowrate [ $\text{kg s}^{-1}$ ]	0.03005
Refrigerant inlet temperature [ $^{\circ}\text{C}$ ]	35
Refrigerant outlet temperature/evaporating temperature [ $^{\circ}\text{C}$ ]	-20
Refrigerant inlet pressure/condensing pressure [kPa]	1351
Refrigerant outlet pressure/evaporating pressure [kPa]	190
Refrigerant inlet enthalpy [ $\text{kJ kg}^{-1}$ ]	
Refrigerant type	R717
<b>Thermostatic Expansion Valve Outputs</b>	
Pressure drop across the valve [kPa]	1161
Refrigerant outlet enthalpy [ $\text{kJ kg}^{-1}$ ]	366
Refrigerant outlet quality	0.19

### 7.3.8. Simulation of overall secondary coolant refrigeration system

As previously discussed in Section 5.9, the overall system model comprises a collection of system components. Hence, some of the outputs of one component are considered as inputs to the next component which is connected to it in series. The coefficient of performance (COP) of the overall system is evaluated using Equation 5-164, which combines all system components.

However, this equation is modified to account for all display cabinet loads and the actual secondary coolant pump power consumption as shown in Equation 7-8 below. The inputs and outputs of this equation can be obtained from Table 7.12.

$$COP = \frac{\sum_{i=1}^n \dot{Q}_{display,load}}{\dot{W}_{com} + \dot{W}_{sc,pump,elec}} \quad 7-8$$

It is worth mentioning once again that the energy consumptions of the water-loop components (see Figure 7.2) were not considered in the calculation of system COP, since it was assumed that the heat absorbed by the water could be used for heating applications thereby offsetting these energy consumptions. This assumption as such has been explained under Section 6.5.2 during the discussion of the experimental results. Some findings from literature [80] also confirm that supermarket medium-temperature secondary coolant refrigeration systems in Canada, which use MPG/water mixtures as a secondary coolant, have heat recovery systems in order to utilize the heat rejection from condensers for heating applications.

Table 7.12 Inputs and outputs of the overall secondary coolant refrigeration system.

Inputs	
Total load of display cabinets [W]	29500
Compressor power consumption [W]	15744
Secondary coolant pump power consumption [W]	1100
Outputs	
System COP	1.75

#### 7.4. Summary of the application of secondary coolant model for supermarkets

The application of the medium-temperature secondary coolant refrigeration system model has been summarized to be used as a guideline to design the system, select system components and evaluate the secondary coolant refrigeration system for supermarkets as listed below.

- Select refrigerant type for the refrigerant circuit.
- Set evaporating and condensing temperatures for the intermediate heat exchanger and condenser, respectively.



- Estimate intermediate heat exchanger capacity based on air coil load.
- Select compressor type based on intermediate heat exchanger capacity, refrigerant type, degree of superheat, evaporating and condensing temperatures of the refrigerant.
- Select expansion valve based on intermediate heat exchanger capacity, refrigerant type, evaporating and condensing temperatures of the refrigerant.
- Select coolant type (e.g. Monopropylene glycol or Monoethylene glycol/water mixture) and its concentration based on the required application (e.g. medium-temperature refrigeration).
- Estimate air-coil load, air and coolant inlet temperatures and flowrates.
- Specify air-coil size and geometry (similar in configuration with the test coil) based on the required air outlet temperature, capacity and reduced coolant pressure drop.
- Calculate sizes and types of connecting lines to achieve reduced heat and pressure losses.
- Select coolant pump based on coolant type, coolant mass flowrate and pressure loss of the coolant in heat exchangers and pipe lines.
- Use secondary coolant component models to calculate air coil outlet conditions and capacity, secondary coolant pressure drops and so forth.
- Combine air-coil capacity, compressor and secondary coolant pump power consumptions to evaluate system performance (COP).
- Repeat the procedure to design another medium-temperature secondary coolant refrigeration system for a supermarket based on different secondary coolant, refrigerant or operating conditions of the store.

In conclusion, the application of the numerical models of secondary coolant refrigeration system components and the overall refrigeration system have been explicitly demonstrated to retrofit an existing medium-temperature direct expansion refrigeration system or completely design a new medium-temperature secondary coolant refrigeration system. A step-by-step system design and component selection was also carried out in this chapter. Particularly, defrost period, defrosting heat input and the time span required to completely defrost the display cabinet air-coils have been accurately determined which can potentially lead to energy savings and prevention of product deterioration. However, only Monopropylene and Monoethylene glycol/water mixtures

should be employed as secondary coolants in these models since the new frost property correlations were developed based on the aforementioned secondary coolants. If other types of secondary coolants are used, the air-coil model results may not be reliable.

### **7.5. Economic benefits of the new secondary coolant system model**

The current computer model of medium-temperature supermarket secondary coolant refrigeration systems can serve to select and simulate system components based on primary refrigerant types, secondary coolant types, simplified piping network and construction material. Appropriate material selection and simplified secondary coolant system design can in turn bring about economic benefits in the supermarket refrigeration industry. For instance, the primary refrigerant loop in Figure 7.2 can be confined to a small plant room resulting in a reduced refrigerant charge due to a reduced length of the primary refrigerant piping network. Oil return pipes to the compressors are also automatically eliminated. Hence, the reduction of refrigerant charge, interconnecting pipes and installation in the primary loop results in cost savings for the industry. Unlike the primary refrigerant loop, the piping material for the secondary coolant loop can be selected to be plastic thereby eliminating the necessity of having copper pipes resulting in additional cost savings.

According to the study carried out by Van [81], the estimated added cost estimates of the supermarket secondary coolant refrigeration systems were up to 40%. However, if the current model is used to design, select components and operate secondary coolant systems properly, there may not be added costs to the systems. Additionally, energy savings can potentially be achieved by determining the right amount of heat necessary to defrost medium-temperature display cabinet air-coils in supermarkets. For example, consider a medium-temperature display cabinet air-coil with a 5.9 kW load operating at an air discharge temperature of (-) 3<sup>0</sup>C and having defrosting heating elements of 0.6 kW capacity. The other inputs and outputs of the display cabinet considered for this example are given in Tables 7.1 through 7.3. The frost thickness calculated using the new frost thickness correlation (see Equation 4-16) will be 4.7 mm. Assume this frost thickness (4.7 mm), based on fin spacing of the air-coil, is the right

amount to initiate defrosting the air-coil. Then, the right amount of heat input required to defrost the air-coil will be 1948 kJ, which is calculated using Equation 4-24. Hence, the time required to defrost the air-coil (see Equation 4-25) will be 54 minutes leading to an energy consumption of 0.54 kWh for defrosting. However, if the heat input to defrost the air-coil is set to be 4000 kJ for the same operating conditions, due to lack of a proper mechanism to determine the right amount of heat, then the energy consumption will be 1.11 kWh resulting in an added energy consumption of 0.57 kWh. The duration of defrosting would also be increased to 111 minutes from 54 minutes, which is a significant increase.

To have a bigger picture of the potential energy savings, consider a supermarket which has 100 display cabinets similar to the one discussed above. The total amount of the additional energy consumed for defrosting the air-coils with 4000 kJ defrost heat input (instead of the correct amount of heat input, 1948 kJ) will be 57 kWh per defrost period. If the number of defrost periods per day is 8, then the total amount of the additional energy consumed will be 456 kWh per day. This is the contribution of the newly developed frost property correlations, which has a significant economic benefit for medium-temperature supermarket secondary coolant refrigeration systems in addition to proper sizing and selection of system components.

Nevertheless, additional research is required to apply the frost correlations to real supermarkets and use the model for component sizing, selection and to make cost estimates based on actual prices of the selected components. This can be done by obtaining quotes of system components and installation work from various suppliers and installation contractors (once the selection of components is completed based on the present secondary coolant model). The recommended research should, of course, eliminate the unnecessary misconception that secondary coolant supermarket refrigeration systems are more expensive than traditional ones, and thereby encourage supermarket owners to adopt secondary coolant supermarket refrigeration systems around the world.

Additionally, many areas of improvements which require further study in secondary coolant refrigeration systems including cost estimates have been extensively discussed in Chapter 8.

## CHAPTER 8.

# Conclusions and Recommendations

---

### 8.1. Conclusions

The following sections discuss about the conclusions of this project on a thermodynamic analysis of a cascade refrigeration system, newly developed frost property correlations, the medium-temperature secondary coolant refrigeration system model and the use of this model for supermarket applications.

#### 8.1.1. Thermodynamic analysis of a cascade refrigeration system

A thermodynamic analysis of a cascade refrigeration system, operating at  $(-) 50^{\circ}\text{C}$  (evaporating) and  $40^{\circ}\text{C}$  (condensing) temperatures was presented in this project. The results of the analysis demonstrated that  $\text{COP}_{\text{MAX}}$  was highest for ethanol followed by R717 and lowest for R404A for the same conditions. The project also revealed that highest mass flow rate of R404A was required as compared to R717 in the high-temperature circuit of the cascade system. Furthermore, the parametric analyses of the optimum cascade evaporating ( $T_{\text{CAS,E,OPT}}$ ) and condensing ( $T_{\text{CAS,C,OPT}}$ ) temperatures, the associated maximum overall COP ( $\text{COP}_{\text{MAX}}$ ) and optimum mass flow ratio  $(\dot{m}_{\text{H}} \setminus \dot{m}_{\text{L}})_{\text{OPT}}$  of the carbon dioxide-ammonia (R744-R717) cascade refrigeration system led to the following conclusions:

- An increase of superheat increased mass flow ratio but reduced COP of the system.
- An increase in sub-cooling increased both COP and mass flow ratio.
- An increase in condensing temperature resulted in a decrease in COP and an increase in refrigerant mass flow ratios. An increase in evaporating temperature increased COP of the system and decreased mass flow ratios. An increase in temperature difference in cascade condenser reduced both COP and mass flow ratios.
- An increase in isentropic efficiency of compressors increased COP linearly.

- Four new empirical correlations have been developed that could be useful to refrigeration engineers for setting optimum thermodynamic parameters of a carbon dioxide-ammonia (R744-R717) cascade system.

### **8.1.2. New frost property correlations for flat-finned tube air coils**

This project introduced four new empirical frost property correlations that were developed on a lab-scale flat-finned-tube heat exchanger. These new correlations could reasonably predict frost properties on actual heat exchangers. The experimental results showed that the frost thickness on the fin could be either greater than or equal or lower than the frost thickness on the tubes depending on the fin position for frost-fin and frost-tube interface temperature difference ranging from  $0.5^{\circ}\text{C}$  to  $0.9^{\circ}\text{C}$ . The possible reasons for this were the geometry of surfaces, the position of fins and tubes, and air flow pattern on the test coil. These factors could have played significant role in the distribution of frost on the entire heat transfer surface area of the test coil than the difference between the frost-fin and the frost-tube interface temperature. In general, the newly developed frost property correlations, which were formulated based on the average frost-coil interface temperature (the arithmetic mean of frost-fin and frost-tube interface temperatures), could be useful for refrigeration engineers to easily estimate the time interval between defrost cycles, the heat input and time span required for defrosting frosted heat exchangers. Energy savings can potentially be achieved in the refrigeration industry if the frost correlations are gainfully applied within the experimental operation regimes during the design phase and the operation of the refrigeration systems.

### **8.1.3. New numerical model for medium-temperature secondary coolant refrigeration system**

A medium-temperature secondary coolant refrigeration system model has been developed to include the most appropriate heat transfer, mass transfer and pressure drop correlations obtained from the open literature. The system components such as air-coil, plate heat exchangers, distribution lines, coolant pump, compressor and a thermostatic expansion valve were modeled

independently so that a refrigeration engineer can evaluate the design parameters of each component for better design and selection of components based on various secondary coolants and refrigerants. It is worth emphasizing here that the fundamental differences between the existing models and the current one are the air-coil model incorporated the newly developed frost correlations for medium-temperature applications. Additionally, complete individual models were developed for plate heat exchangers such as intermediate heat exchanger, condenser and sub-cooler based on their applications. Each component model was in turn linked to form a complete overall secondary coolant refrigeration system model to enable a refrigeration engineer to evaluate the coefficient of performance (COP) of the system in total for further improvements. The model results were validated against the measurements taken from a lab-scale secondary coolant test rig located in the Thermodynamic Laboratory, the University of Auckland, New Zealand.

The predicted results of the component and overall medium-temperature numerical models showed the following agreements with the measurements results: -

- The air outlet temperature has been predicted by the air coil model within  $\pm 25\%$  for 70% of the data. The coolant outlet temperature has been predicted within  $\pm 3\%$  for 100% of the data with the highest degree of accuracy, whereas the predicted effectiveness of the air-coil deviated from the actual effectiveness by  $\pm 6\%$  for 70% of the data.
- The predicted coolant outlet temperatures of the intermediate heat exchanger of the secondary coolant system have agreements with the measured coolant outlet temperatures within  $\pm 10\%$  for 90% of the data.
- The predicted water outlet temperatures of the condenser in the secondary coolant system have agreements with the measured water outlet temperatures within  $\pm 3\%$  for 100% of the data.
- The predicted coolant outlet temperatures of the supply line of the secondary coolant circuit have agreements with the measured coolant outlet temperatures within  $\pm 6\%$  for 90% of the data.

- The predicted coolant pump power consumption has agreement with the measured coolant pump power consumption within  $\pm 30\%$  for 70% of the data.
- The predicted compressor outlet temperature had a good agreement with the measured compressor outlet temperature within  $\pm 6\%$  for 100% of the data.
- The predicted COP of the system has agreement with the system COP obtained using measurements within  $\pm 21\%$  for 100% of the data.

Additionally, the experimental results on the medium-temperature secondary coolant system revealed that the highest discrepancy in rate of heat transfer was observed between R22 and Mono-propylene glycol (MPG), which ranged from (-) 29% to (+) 29%, whereas discrepancy in rate of heat transfer between R22 and Mono-ethylene glycol (MEG) ranged from (-) 23% to (+) 14%. In the condenser, the highest discrepancy in rate of heat transfer between the refrigerant and cooling water was also observed for MPG tests which ranged from (-) 10% to (+) 24%, whereas for MEG tests the discrepancy ranged from (-) 16% to (+) 17%. Similarly, the highest discrepancy in the rate of heat transfer between the air and coolant in the test coil was again observed for MPG tests which ranged from (-) 5% to (+) 45%, whereas for MEG tests the discrepancy ranged from (-) 37% to (+) 33%. In general, the aforementioned discrepancies in rate of heat transfers depend upon inaccuracies in the measurement sensors, heat gain/loss of the heat exchangers from/to the surrounding, especially, fluid characteristics, and the combination of these conditions.

The tests result also showed that the highest system COP was observed for MEG tests. The main reasons for achieving the highest COP could be attributable to the combination of 1) highest evaporating temperature and lower condensing temperature, which led to lower compressor power consumption; 2) coolant type (MEG) having better thermophysical and transport property for higher coolant temperature, which led to higher heat transfer coefficient; and 3) the frontal air velocity being higher at higher air inlet temperature thereby increasing the capacity of the system. Besides, the lowest system COP was obtained in MPG tests, the main reasons being the combination of 1) lower evaporating temperature and highest condensing temperature, which led to the highest compressor power consumption; 2) coolant type (MPG) having poor

thermophysical and transport property at the specified coolant temperature, which led to lower heat transfer coefficient; and 3) the frontal air velocity being lower at the given air inlet temperature thereby decreasing the capacity of the system.

To conclude, the agreements between the model predicted and the measurement results were within acceptable limits considering all measurement constraints, as amply demonstrated, and the selection process of appropriate heat transfer and pressure loss coefficients. Hence, the numerical models are very useful and could be used to design, select components and evaluate medium-temperature secondary coolant refrigeration systems for supermarkets as further explained in Section 8.1.4 below.

#### **8.1.4. Application of secondary coolant model for supermarket refrigeration systems**

The application of the newly developed numerical models of medium-temperature secondary coolant refrigeration system components and the overall refrigeration system could be used to retrofit an existing medium-temperature direct expansion refrigeration system or completely design a new medium-temperature secondary coolant refrigeration system. An exercise of step-by-step system design and component selection was thoroughly carried out in this project. It was also demonstrated that defrost period, defrosting heat input and the time span required to fully defrost the display cabinet air-coils have been accurately determined which could lead to potential energy savings and prevention of product deterioration. However, presently the author suggests the use of only Monopropylene and Monoethylene glycol/water mixtures as secondary coolants in these models since the new frost property correlations were developed based on these secondary coolants. It is believed that frost characteristics and distribution may be affected by the types of secondary coolants used in the air-coils. Unlike the experimental results which showed that COP of the Monopropylene glycol/water based medium-temperature secondary coolant refrigeration system was 1.33, the simulated results on a typical supermarket showed that COP of the system could be as high as 1.75.



## **8.2. Recommendations for future research works**

The following sections discuss the author's recommendations for future extensive investigation in relation to cascade refrigeration systems, improvement in frost correlations and medium-temperature secondary coolant refrigeration systems.

### **8.2.1. Cascade refrigeration system**

The following additional works are recommended for cascade refrigeration systems having evaporating temperatures as low as  $(-50^{\circ}\text{C})$ ; and condensing temperatures as high as  $40^{\circ}\text{C}$  temperatures.

- Experimental investigation on the performance of high-temperature circuit of a cascade refrigeration system using ammonia (R717), propane (R290), propylene (R1270), ethanol and R404A in combination with carbon dioxide (R744) in the low-temperature circuit of the refrigeration system.
- Experimental investigation on the performance of cascade condensers using several types of heat exchangers such as plate, shell-and-plate or shell-and-tube heat exchangers to couple the low-and high-temperature circuits. There is limited research work on heat transfer coefficients of refrigerants in cascade condensers. It is hence imperative to develop a representative correlation for heat transfer coefficient of various natural refrigerants.
- There is no research work to date on frost property correlations developed on actual evaporators for two-phase flow conditions. Hence, development of frost property correlations is of vital importance to make cascade refrigeration systems energy-efficient.
- Development of a robust numerical model which can serve a refrigeration engineer as a guide to evaluate the performance of cascade refrigeration systems for better design and selection of components. These models should be validated against measurements collected from lab-scale test rigs or supermarket establishments.

- Application of the new thermodynamic correlations to real supermarket cascade refrigeration systems to realize the energy saving potential of the optimum thermodynamic parameters to be calculated using the correlations.
- Conducting a separate study to warrant conceptualizing and evaluate all the related matters such as social, environmental and economic benefits of the cascade supermarket refrigeration systems.

### **8.2.2. Improvement in frost property correlations for flat-finned tube air coils**

The present frost property correlations for medium-temperature secondary coolant air-coils can be highly improved if the following gaps in research are further investigated.

- Distribution of frost on fins relative to tubes as a function of frost-surface interface temperatures.
- The effect of air-coil geometry such as fin spacing, fin thickness, tube diameter, air coil dimensions (height, width and depth) including the construction material on frost property characteristics and distribution.
- The effect of air flow pattern on frost property characteristics and distribution on the air coil surfaces.
- The effect of secondary coolant characteristics on frost property characteristics and distribution on the air coil surfaces.
- Thermal boundary layers and the three-dimensional transport phenomena (radial) as compared to the two-dimensional effects (thickness and parallel flow) in the flat fin geometry.
- The effect of thermal radiation on frost property characteristics and distribution on the air coil surfaces.
- The effect of frost minimizing coatings of air-coils (which possibly slow down frost formation) on frost property characteristics and distribution on the air coil surfaces.

### **8.2.3. Improvements in medium-temperature secondary coolant refrigeration systems**

The performance of the medium-temperature secondary coolant refrigeration systems may be further improved if the following areas are thoroughly investigated.

- Pressure drops of different circulating secondary coolants in distribution lines. This could be achieved by measuring pressures using high precision transmitters at various points of the system at the prevailing temperature. It is to be noted that, under the current project, the total pressure drop in the secondary coolant system was calculated based on loss coefficients in fittings and manifolds developed using water but not secondary coolants.
- Refrigerant pressure drops in sub-cooler, condenser and intermediate heat exchangers (brazed plate heat exchangers). The pressure transmitters under the current project were unable to precisely measure the pressure drops across these plate heat exchangers. Hence, high precision transmitters will be mandatory if any future investigation on refrigerant pressure drops is to be carried out.
- There is limited research work on heat transfer coefficients of refrigerant in intermediate heat exchangers, especially, in brazed plate heat exchangers. It is required to develop a representative correlation for heat transfer coefficients of various refrigerants.
- The performance of natural refrigerants both in the primary and secondary circuits of secondary coolant systems should be experimentally investigated.
- A lot of work to needs be done on the reconfiguration air coil geometry such as fin spacing, fin thickness, tube diameter, air-coil dimensions (height, width and depth) including the construction material in order to enhance the effectiveness of the heat exchanger. It is worth noting that the average effectiveness of the test coil under the current project was only 6%, whereas it was only 4.1% for the simulated display cabinet air-coil.
- Additional research is needed to apply the frost correlations on real supermarket secondary coolant display cabinets operating at medium-temperature in order to analyse the energy saving potential of the newly developed frost property correlations.

- Finally, extensive research work is necessary for cost estimates of a typical supermarket secondary coolant refrigeration system based on quotes from various suppliers and installation contractors through applying the present model for design and selection of system components.

# References

- [1] B. A. Nagengast, "A historic look at CFC refrigerants," *ASHRAE Journal*, pp. 37-39, 1988.
- [2] M. Orphelin, D. Marchio, and S. L. D'Alanzo, "Are there optimum temperature and humidity set points for supermarkets?," *ASHRAE Transactions* vol. 105(1), 1999.
- [3] V. C. Mei, F. C. Chen, R. E. Domitrovic *et al.*, "Warm liquid defrosting for supermarket refrigerated display cases," *ASHRAE Transactions*, vol. 108 (1), pp. 669-672, 2002.
- [4] G. Haile-Michael, "Analysis of low-temperature supermarket refrigeration systems," Thesis (ME, Mechanical Engineering)--University of Auckland, 2005., 2005.
- [5] S. A. Tassou, J. S. Lewis, Y. T. Ge *et al.*, "A review of emerging technologies for food refrigeration applications," *Applied Thermal Engineering*, vol. 30, no. 4, pp. 263-276, 2010.
- [6] K. Wang, M. Eisele, Y. Hwang *et al.*, "Review of secondary loop refrigeration systems," *International Journal of Refrigeration*, vol. 33, pp. 212-234, 2010.
- [7] K. G. Christensen, and P. Bertilsen, "Refrigeration systems in supermarkets with propane and CO<sub>2</sub>— energy consumption and economy," in *International Congress of Refrigeration*, Washington D.C., 2003, pp. 1-10.
- [8] D. H. Walker, and V. D. Baxter, "Analysis of advanced, low-charge refrigeration for supermarkets," *ASHRAE Transactions*, vol. 109 (1), pp. 285-292, 2003.
- [9] EES, "Engineering Equation Solver," fChart Software, Inc., 2010.
- [10] H. M. Getu, and P. K. Bansal, "Simulation model of a low-temperature supermarket refrigeration system," *HVAC and R Research*, vol. 12, no. 4, pp. 1117-1139, 2006.
- [11] H. M. Getu, and P. K. Bansal, "Modeling and performance analyses of evaporators in frozen-food supermarket display cabinets at low temperatures," *International Journal of Refrigeration*, vol. 30, no. 7, pp. 1227-1243, 2007.
- [12] C. Chaichana, L. Aye, and W. W. S. Charters, "Natural working fluids for solar-boosted heat pumps," *International Journal of Refrigeration*, vol. 26, no. 6, pp. 637-643, 2003.
- [13] H. M. Getu, "The cascade supermarket refrigeration system at The Warehouse," Auckland, 2006, pp. 1-4.

- [14] I. Wilson, and D. Maier, "Carbon dioxide for use as a refrigerant," in *Innovative Equipment and Systems for Comfort and Food Preservation*, The University of Auckland , New Zealand, 2006, pp. 305-311.
- [15] E. B. Ratts, and J. S. Brown, "A generalized analysis for cascading single fluid vapor compression refrigeration cycles using an entropy generation minimization method," *International Journal of Refrigeration*, vol. 23, no. 5, pp. 353-365, 2000.
- [16] S. Sawalha, "Using CO<sub>2</sub> in supermarket refrigeration," *ASHRAE Journal* vol. 47, no. 8, pp. 26-30, 2005.
- [17] T. S. Lee, C. H. Liu, and T. W. Chen, "Thermodynamic analysis of optimal condensing temperature of cascade-condenser in CO<sub>2</sub>/NH<sub>3</sub> cascade refrigeration systems," *International Journal of Refrigeration* vol. 29, pp. 1100-1108, 2006.
- [18] S. Bhattacharyya, S. Mukhopadhyay, A. Kumar *et al.*, "Optimization of a CO<sub>2</sub>-C<sub>3</sub>H<sub>8</sub> cascade system for refrigeration and heating," *International Journal of Refrigeration*, vol. 28, no. 8, pp. 1284-1292, 2005.
- [19] P. K. Bansal, and S. Jain, "Cascade systems: Past, present, and future," *ASHRAE Transactions*, vol. 113 (1), pp. 245-252, 2007.
- [20] P. K. Bansal, "Emergence of CO<sub>2</sub> refrigerant for low temperature refrigeration systems," in *The International Technical Conference, ACRECONF 2007 on "Challenges to Sustainability" in Air Conditioning and Refrigeration*, Plenary paper, Delhi (India), 2007, pp. 42 – 52.
- [21] P. K. Bansal, "CO<sub>2</sub> as a low temperature refrigerant: Fundamentals and Applications, ," in *Proceedings of 4th International Conference on Cooling and Heating Technologies*, Key note invited paper, Jinhae City (Korea), 2008, pp. 77 – 86.
- [22] P. K. Bansal, "Status of CO<sub>2</sub> as a mainstream low temperature refrigerant: Fundamentals, trends and opportunities," in *13th Brazilian Congress of Thermal Sciences and Engineering Conference (ENCIT-2010)*, Key note invited paper, Uberlandia (Brasil), 2010, pp. 12.
- [23] J. Iragorri, Y.-X. Tao, and S. Jia, "A critical review of properties and models for frost formation analysis," *HVAC and R Research*, vol. 10, no. 4, pp. 393-420, 2004.

- [24] Y. X. Tao, R. W. Besant, and K. S. Rezkallah, "A mathematical model for predicting the densification and growth of frost on a flat plate," *International Journal of Heat and Mass Transfer*, vol. 36, no. 2, pp. 353-363, 1993.
- [25] H. M. Getu, and P. K. Bansal, "Limitations of existing frost property correlations," in *The 22nd International Conference of Refrigeration*, Beijing, P.R. China, 2007.
- [26] Y. Mao, Besant, R.W., and Rezkallah, K.S "A method of measuring frost density using flush-mounted removable disks," *ASHRAE Transactions*, vol. 97(1), pp. 26-30, 1991.
- [27] R. W. Besant, Rezkallah, K.S., Mao, Y., and Falk, J., "Measuring of frost thickness using a laser beam and light meter," *ASHRAE Transactions*, vol. 96 (1), pp. 519-522, 1990.
- [28] Y. Mao, R. W. Besant, and H. Chen, "Frost characteristics and heat transfer on a flat plate under freezer operating conditions: Part I, Experimentation and correlations," *ASHRAE Transactions*, vol. 105 (A), pp. 231-251, 1999.
- [29] Y. B. Lee, and S. T. Ro, "Frost formation on a vertical plate in simultaneously developing flow," *Experimental Thermal and Fluid Science*, vol. 26, no. 8, pp. 939-945, 2002.
- [30] Y. B. Lee, and S. T. Ro, "An experimental study of frost formation on a horizontal cylinder under cross flow," *International Journal of Refrigeration*, vol. 24, no. 6, pp. 468-474, 2001.
- [31] L. Thomas, H. Chen, and R. W. Besant, "Measurement of frost characteristics on heat exchanger fins, Part I: Test facility and instrumentation," *ASHRAE Transactions*, vol. 105 (A), pp. 283-293, 1999.
- [32] K. Ogawa, N. Tanaka, and M. Takeshita, "Performance improvement of plate fin-and-tube heat exchangers under frosting conditions," *ASHRAE Transactions*, vol. 99 (1), pp. 762-774, 1993.
- [33] S. N. Kondepudi, and D. L. O'Neal, "Effects of different fin configurations on the performance of finned-tube heat exchangers under frosting conditions," *ASHRAE Transactions*, vol. 2, pp. 439-444, 1990.
- [34] W.-M. Yan, H.-Y. Li, and Y.-L. Tsay, "Thermofluid characteristics of frosted finned-tube heat exchangers," *International Journal of Heat and Mass Transfer*, vol. 48, no. 15, pp. 3073-3080, 2005.

- [35] Z. Liu, H. Wang, X. Zhang *et al.*, “An experimental study on minimizing frost deposition on a cold surface under natural convection conditions by use of a novel anti-frosting paint. Part I. Anti-frosting performance and comparison with the uncoated metallic surface,” *International Journal of Refrigeration*, vol. 29, no. 2, pp. 229-236, 2006.
- [36] D.-K. Yang, K.-S. Lee, and D.-J. Cha, “Frost formation on a cold surface under turbulent flow,” *International Journal of Refrigeration*, vol. 29, no. 2, pp. 164-169, 2006.
- [37] K.-S. Lee, W.-S. Kim, and T.-H. Lee, “A one-dimensional model for frost formation on a cold flat surface,” *International Journal of Heat and Mass Transfer*, vol. 40, no. 18, pp. 4359-4365, 1997.
- [38] A. Z. Sahin, “An analytical study of frost nucleation and growth during the crystal growth period,” *Heat and Mass Transfer*, vol. 30, pp. 321-330, 1995.
- [39] C. P. Tso, Y. C. Cheng, and A. C. K. Lai, “An improved model for predicting performance of finned tube heat exchanger under frosting condition, with frost thickness variation along fin,” *Applied Thermal Engineering*, vol. 26, no. 1, pp. 111-120, 2006.
- [40] Y. X. Tao, and R. W. Besant, “Prediction of spatial and temporal distributions of frost growth on a flat plate under forced convection,” *Journal of Heat Transfer*, vol. 115, pp. 278-281, 1992.
- [41] K. A. R. Ismail, and C. S. Salinas, “Modeling of frost formation over parallel cold platesModélisation de la formation de givre sur les plaques froides parallèles,” *International Journal of Refrigeration*, vol. 22, no. 5, pp. 425-441, 1999.
- [42] H. Chen, L. Thomas, and R. W. Besant, “Modeling frost characteristics on heat exchanger fins: Part I. Numerical model,” *ASHRAE Transactions*, vol. 106 (A), pp. 357-367, 2000.
- [43] H. Chen, L. Thomas, and R. W. Besant, “Measurement of frost characteristics on heat exchanger fins, Part II: Data and analysis,” *ASHRAE Transactions*, vol. 105(2), 1999.
- [44] G. S. Kazachki, and D. K. Hinde, “Secondary coolant systems for supermarkets,” *ASHRAE Journal*, vol. 48, no. 9, pp. 34-46, 2006.
- [45] D. H. Walker, *Development and demonstration of an advanced supermarket refrigeration/HVAC system*, 62X-SX363C, vol. Final Analysis Report, Foster-Miller, Inc., Waltham, MA 02451, 2001.



- [46] W. T. Horton, "Simulation model of a low-temperature supermarket refrigeration system," PhD Thesis, Purdue University, 2002.
- [47] A. J. Chapman, *Heat transfer*, 4th ed., New York, London: Macmillan; Collier Macmillan, 1984.
- [48] S. W. Inlow, and E. A. Groll, "Analysis of secondary-loop refrigeration systems using carbon dioxide as a volatile secondary refrigerant," *HVAC and R Research*, vol. 2, no. 2, pp. 107-121, 1996.
- [49] T. P. McDowell, J. W. Mitchell, and S. A. Klein, "Investigation of ammonia-secondary fluid systems in supermarket refrigeration systems," *ASHRAE Transactions*, vol. 101 (2), pp. 486-496, 1995.
- [50] B. Purkayastha, and P. K. Bansal, "An NTU- $\epsilon$  model for alternative refrigerants," *International Journal of Refrigeration* vol. 21(5) pp. 381-397, 1998.
- [51] B. Purkayastha, and P. K. Bansal, "An experimental study on HC290 and a commercial liquefied petroleum gas (LPG) mix as suitable replacements for HCFC22," *International Journal of Refrigeration*, vol. 21, no. 1, pp. 3-17, 1998.
- [52] N. Instruments, "NI Vision Builder for Automated Inspection Software V2.6," Texas, 2005.
- [53] J. P. Holman, and W. J. Gajda, *Experimental methods for engineers*, 5th ed., New York: McGraw-Hill, 1989.
- [54] C. Haglund Stignor, P. Fahlen, and B. Sunden, "Design of different types of secondary loop cooling systems in supermarkets - comparison of energy use and costs," in The 22nd International Conference of Refrigeration, Beijing, P.R. China, 2007.
- [55] H. M. Getu, and P. K. Bansal, "Thermodynamic analysis of an R744-R717 cascade refrigeration system," *International Journal of Refrigeration*, vol. 31, no. 1, pp. 45-54, 2008.
- [56] T. Wich, M. W. Browne, and P. K. Bansal, "Design and modeling of new egg-crate type forced flow evaporators in domestic refrigerators," *ASHRAE Transactions* vol. 107(2) pp. 204-213, 2001.
- [57] J. Antony, *Design of Experiment for Engineers and Scientists*: Butterworth-Heinemann, 2003.

## References

---

- [58] C. Samprit, and S. H. Ali, *Regression Analysis by Example*: John Wiley & Sons, Inc., 2006.
- [59] N. H. Kim, B. Youn, and R. L. Webb, "Air-side heat transfer and friction correlations for plain fin-and-tube heat exchangers with staggered tube arrangements," *Journal of Heat Transfer*, vol. 121, no. 3, pp. 662-667, 1999.
- [60] G. Nellis, and S. A. Klein, *Heat transfer*, Cambridge ; New York: Cambridge University Press, 2009.
- [61] B. S. Petukhov, "Heat transfer and friction in turbulent pipe flow with variable physical properties " *Advances in heat transfer*, vol. 6, pp. 503-564, 1970.
- [62] V. Gnielinski, "New equations for heat and mass transfer in turbulent pipe and channel flow," *Chem Eng* vol. 16, pp. 359-368, 1976.
- [63] E. A. D. Saunders, *Heat Exchangers: selection, design & construction*, p.^pp. 184, Harlow, U.K.: Longman Scientific & Technical, 1988.
- [64] G. A. Longo, "Refrigerant R134a condensation heat transfer and pressure drop inside a small brazed plate heat exchanger," *International Journal of Refrigeration*, vol. 31, no. 5, pp. 780-789, 2008.
- [65] G. A. Longo, and A. Gasparella, "Refrigerant R134a vaporisation heat transfer and pressure drop inside a small brazed plate heat exchanger," *International Journal of Refrigeration*, vol. 30, no. 5, pp. 821-830, 2007.
- [66] T. Kuppan *Heat exchanger design hand book*, p.^pp. 357 – 364: Marcel Dekker, Inc. New York, 2000.
- [67] R. A. Buonopane, and R. A. Troupe, "A study of the effects of internal rib and channel geometry in rectangular channels, Part I: Pressure drop & Part II: Heat transfer," *AIChE*, pp. 585-596 1969.
- [68] J. Marriott, "Where and how to use plate heat exchangers," in *Process Heat Exchange*, Chemical Engineering Magazine McGraw-Hill, New York, 1979, pp. 156-162.
- [69] T. Dutto, J. C. Blaise, and T. Benedic, "Performances of brazed plate heat exchanger set in heat pump," in *Proceedings of the 18th International Congress of Refrigeration*, Montreal, Canada, 1991, pp. 1284-1288.

- [70] P. Fernando, B. Palm, P. Lundqvist *et al.*, "Propane heat pump with low refrigerant charge: design and laboratory tests," *International Journal of Refrigeration*, vol. 27, no. 7, pp. 761-773, 2004.
- [71] American Society of Heating Refrigerating and Air-Conditioning Engineers., "The ASHRAE Handbook CD," American Society of Heating, Refrigerating and Air-Conditioning Engineers, 2001, p. 1 computer optical disc.
- [72] P. Popovic, and H. N. Shapiro, "Semi-empirical method for modeling a reciprocating compressor in refrigeration systems," *ASHRAE Transactions*. pp. 367-382.
- [73] G. Haile-Michael, "Analysis of low-temperature supermarket refrigeration systems," Thesis (ME, Mechanical Engineering)--The University of Auckland, Auckland, 2005.
- [74] Y. T. Ge, and S. A. Tassou, "Mathematical modelling of supermarket refrigeration systems for design, energy prediction and control," in *Proceedings of the Institution of Mechanical Engineers, Part A: Journal of Power and Energy*, 2000, pp. 101-114.
- [75] A. Andrusenko, M. Bellstedt, and A. Arkal, "Ammonia and CO2 combined package systems for commercial and industrial applications," in *9th IIR Gustav Lorentzen Conference*, Sydney, Australia, 2010.
- [76] A. Amikhailov, and H. O. Matthiesen, "Comparative analysis of secondary CO2 systems and water based brines in industrial and commercial refrigeration applications," in *9th IIR Gustav Lorentzen Conference*, Sydney, Australia, 2010.
- [77] E. Granryd, "Optimum flow rates in indirect systems," in *The 22nd International Conference of Refrigeration*, Beijing, P.R. China, 2007.
- [78] VSX, "Spaix Quick&Easy," VSX-VOGEL SOFTWARE V2.2, 2005.
- [79] Bitzter, "Bitzer Software Version 5.3.0.2," Bitzer, 2010.
- [80] V. Minea, "Energy efficiency of a supermarket refrigeration/heat recovery system with secondary fluids," in *The 22nd International Conference of Refrigeration*, Beijing, P.R. China, 2007.
- [81] D. B. Van, *Advanced Supermarket Refrigeration/Heat Recovery Systems*, IEA Annex 26, Final Report Volume 1 - Executive Summary, Oak Ridge National Laboratory, 2003.

# Appendix A

Table A.1 Schedule of secondary coolant system components.

<b>I. WATER-LOOP</b>		
<b>COMPONENT</b>	<b>MODEL</b>	<b>SPECIFICATION</b>
Water pump	PEDROLLO PKM70/1	Flow = 5-50 l/min; Head = 62-18 m; Power = 0.6 kW
Water cooler	NQAC400	Flow = 1510 l/sec; Power (two fans) = $2 \times 1.3 \times 230 = 598\text{W}$
Water-cooled condenser	B25 SWEP Compact brazed heat exchanger	Number of plates (NP) = 20 $d \times w \times h = 51 \text{ mm} \times 117 \text{ mm} \times 479 \text{ mm}$
Sub-cooler	B8 SWEP Compact brazed heat exchanger	Number of plates (NP) = 12 $d \times w \times h = 31 \text{ mm} \times 72 \text{ mm} \times 278 \text{ mm}$
Brine drain sump	Custom made	Volume = $l \times w \times h = 0.59 \text{ m} \times 0.42 \text{ m} \times 0.3 \text{ m}$

<b>II. PRIMARY-LOOP</b>		
<b>COMPONENT</b>	<b>MODEL</b>	<b>SPECIFICATION</b>
Intermediate heat exchanger	B25 SWEP Compact brazed heat exchanger	Number of plates (stainless steel) = 16 $d \times w \times h = 42 \text{ mm} \times 117 \text{ mm} \times 479 \text{ mm}$
Accumulator	Virginia VA54-7SRD	
Compressor	ZR462-TFD-230 Copeland Scroll type	Displacement volume = $63 \text{ cm}^3/\text{rev}$ ; power = 2.66 kW
Receiver	N/A	Capacity = 7 kg
Filter	Castel 4016/3	
Sight glass	Danfoss SGI 10	
Thermostatic expansion valve	Flica TMVX	R22 (+15/-45°C)
Manual needle valve	1/4" BSPT connections	

<b>III. SECONDARY-LOOP</b>		
<b>COMPONENT</b>	<b>MODEL</b>	<b>SPECIFICATION</b>
Brine pump	DAB KPS 30/16 M	Flowrate = $0.2\text{--}2.1 \text{ m}^3/\text{h}$ ; Head = 32.5 m; Power = 0.47 kW
Test coil	Custom made	Size = $d \times w \times h = 0.076 \text{ m} \times 0.4027 \text{ m} \times 0.274 \text{ m}$
Pre-cooler	Custom made	Size = $d \times w \times h = 0.260 \text{ m} \times 0.740 \text{ m} \times 0.285 \text{ m}$
Water drain sump	Custom made	Volume = $l \times w \times h = 0.4 \text{ m} \times 0.1 \text{ m} \times 0.4 \text{ m}$

Table A.2 Schedule of pipes and bends for secondary coolant system test rig.

<b>I. WATER-LOOP</b>		
<b>TYPE</b>	<b>SPECIFICATION</b>	<b>REMARK</b>
Copper pipe	OD = 19mm; Length =1.3m	Between cooler and drain sump
Rubber hose	ID = 25.4mm; Length =0.4m	Between sump and pump
Rubber hose	OD =25.4mm; Length =1.8m	Between pump and sub-cooler
Rubber hose	OD =25.4mm; Length =0.3m	Between sub-cooler and condenser
<b>II. PRIMARY-LOOP</b>		
<b>Liquid line</b>		
Copper pipe	OD = 10mm; Length = 1.5 m	Between condenser and sub-cooler
Stainless steel pipe	OD = 6.6mm; Length = 0.4m	Between sub-cooler and expansion valve
Bends (90°)	OD = 10mm	Ten bends
<b>Suction line</b>		
Copper pipe	OD = 19mm; Length = 1.0 m	Between Intermediate heat exchanger and compressor
Copper pipe	OD = 19mm; Length =0.45m	Between expansion valve and intermediate heat exchanger
Bends (90°)	OD = 19mm	Six bends
<b>III. SECONDARY-LOOP</b>		
Copper pipe	OD = 19mm; Length = 2.0 m	Between intermediate heat exchanger and test coil
Copper pipe	OD = 19mm; Length = 1.2m	Between test coil and pre-cooler
Copper pipe	OD = 19mm; Length = 2.0 m	Between pre-cooler and drain sump
Copper pipe	OD = 16mm; Length = 1.3 m	Between drain sump and intermediate heat exchanger
Bends (90°)	OD = 19 mm	Six bends

Table A.3 Schedule of pipe and duct insulation for secondary coolant system test rig.

<b>I. PRIMARY-LOOP</b>		
<b>TYPE</b>	<b>SPECIFICATION</b>	<b>REMARK</b>
<b>Liquid line</b>		
No insulation		
<b>Suction line</b>		
Indaflex	3/4"x1"; Length = 1.0 m (k=0.036W/mK)	Between Intermediate heat exchanger and compressor
Indaflex	3/4"x1"; Length =0.45m	Between expansion valve and intermediate heat exchanger
<b>II. SECONDARY-LOOP</b>		
Indaflex	3/4"x1"; Length = 2.0 m	Between intermediate heat exchanger and test coil
Indaflex	3/4"x1"; Length = 1.2m	Between test coil and pre-cooler
Indaflex	3/4"x1"; Length = 2.0 m	Between pre-cooler and drain sump
Indaflex	3/4"x5/8"; Length = 1.3 m	Between drain sump and intermediate heat exchanger
<b>III. DUCT INSULATION</b>		
Thermobreak	Thickness = 1" (25mm) (k=0.032W/mK)	

Table A.4 Detailed geometrical parameters and construction materials of plate heat exchangers.

<b>Geometrical parameters</b>	<b>Condenser (B25 SWEP)</b>	<b>Intermediate heat exchanger (B25 SWEP)</b>	<b>Sub-cooler (B8 SWEP)</b>
Flow length [mm]	479	479	278
Width [mm]	117	117	72
Channel size, a [mm]	2	2	2
Channel pitch, p [mm]	8	8	2
Plate thickness [mm]	0.9	1	1.3
Total number of plates	20	16	12
Port diameter [mm]	24	24	16
Number of ports per fluid	2	2	2
Refrigerant-side number of channels counted along the depth of the PHX	9	7	5
Water/coolant-side number of channels counted along the depth of the PHX	10	8	6
<b>Plate construction material</b>			
Parts in contact with fluid	AISI 316	AISI 316	AISI 316
Parts not in contact with fluid	AISI 304	AISI 304	AISI 304
Connection material	AISI 316	AISI 316	AISI 316
Brazing material	Pure copper	Pure copper	Pure copper

# Appendix B

Table B.1 Schedule of temperature sensors for frosted test coil fins and air stream.

<b>Test coil fin surface temperatures</b>			
<b>Sensor label on test coil</b>	<b>Sensor type</b>	<b>Position of sensor on frosted test coil fin surface</b>	<b>Polynomial expression for true temperature of the sensor</b>
FinTemp[1]	T-type thermocouple	Left fin trailing edge at the bottom in the air flow direction	$T_{true} = 0.976 \cdot T_{indicated} - 0.0184$
FinTemp[2]	T-type thermocouple	Middle fin trailing edge at the bottom in the air flow direction	$T_{true} = 0.9999 \cdot T_{indicated} + 0.1512$
FinTemp[3]	T-type thermocouple	Right fin trailing edge at the bottom in the air flow direction	$T_{true} = T_{indicated} + 0.1471$
FinTemp[4]	T-type thermocouple	Right fin leading edge at the bottom in the air flow direction	$T_{true} = 1.0008 \cdot T_{indicated} + 0.1687$
FinTemp[5]	T-type thermocouple	Middle fin leading edge at the bottom in the air flow direction	$T_{true} = 1.0009 \cdot T_{indicated} + 0.1682$
FinTemp[6]	T-type thermocouple	Left fin leading edge at the bottom in the air flow direction	$T_{true} = 1.0007 \cdot T_{indicated} + 0.1507$
FinTemp[7]	T-type thermocouple	Left fin trailing edge at the middle in the air flow direction	$T_{true} = 1.0004 \cdot T_{indicated} + 0.1464$
FinTemp[8]	T-type thermocouple	Middle fin trailing edge at the middle in the air flow direction	$T_{true} = 1.0014 \cdot T_{indicated} + 0.1621$
FinTemp[9]	T-type thermocouple	Right fin trailing edge at the middle in the air flow direction	$T_{true} = 1.0016 \cdot T_{indicated} + 0.1607$
FinTemp[10]	T-type thermocouple	Right fin leading edge at the middle in the air flow direction	$T_{true} = 1.0017 \cdot T_{indicated} + 0.1675$
FinTemp[11]	T-type thermocouple	Middle fin leading edge at the middle in the air flow direction	$T_{true} = 1.002 \cdot T_{indicated} + 0.1657$
FinTemp[12]	T-type thermocouple	Left fin leading edge at the middle in the air flow direction	$T_{true} = 0.9985 \cdot T_{indicated} + 0.1502$
FinTemp[13]	T-type thermocouple	Left fin trailing edge at the top in the air flow direction	$T_{true} = 1.0004 \cdot T_{indicated} + 0.1344$
FinTemp[14]	T-type thermocouple	Middle fin trailing edge at the top in the air flow direction	$T_{true} = 0.9993 \cdot T_{indicated} + 0.1357$
FinTemp[15]	T-type thermocouple	Right fin trailing edge at the top in the air flow direction	$T_{true} = 0.9996 \cdot T_{indicated} + 0.1409$
FinTemp[16]	T-type thermocouple	Right fin leading edge at the top in the air flow direction	$T_{true} = 0.9992 \cdot T_{indicated} + 0.154$
FinTemp[17]	T-type thermocouple	Middle fin leading edge at the top in the air flow direction	$T_{true} = 0.9988 \cdot T_{indicated} + 0.1288$
FinTemp[18]	T-type thermocouple	Left fin leading edge at the top in the air flow direction	$T_{true} = 0.9999 \cdot T_{indicated} + 0.1326$
<b>Air temperature sensors</b>			
FinTemp[21]	T-type thermocouple	Test coil air inlet temperature	$T_{true} = 1.0058 \cdot T_{indicated} - 0.0684$
FinTemp[22]	T-type thermocouple	Test coil air outlet temperature	$T_{true} = 1.0053 \cdot T_{indicated} - 0.0829$

## Appendix B

Table B.2 Schedule of temperature sensors for frosted test coil tubes.

TubeTemp[1]	T-type thermocouple	Left of bottom tube, row-2, in the air flow direction	$T_{true} = 1.024 \cdot T_{indicated} - 0.1641$
TubeTemp[2]	T-type thermocouple	Middle of bottom tube, row-2, in the air flow direction	$T_{true} = 1.007 \cdot T_{indicated} - 0.1327$
TubeTemp[3]	T-type thermocouple	Right of bottom tube, row-2, in the air flow direction	$T_{true} = 1.0053 \cdot T_{indicated} - 0.1507$
TubeTemp[4]	T-type thermocouple	Right of bottom tube, row-1, in the air flow direction	$T_{true} = 0.9986 \cdot T_{indicated} - 0.0285$
TubeTemp[5]	T-type thermocouple	Middle of bottom tube, row-1, in the air flow direction	$T_{true} = 1.0077 \cdot T_{indicated} - 0.1017$
TubeTemp[6]	T-type thermocouple	Left of bottom tube, row-1, in the air flow direction	$T_{true} = 1.0054 \cdot T_{indicated} - 0.1475$
TubeTemp[7]	T-type thermocouple	Left of middle tube, row-2, in the air flow direction	$T_{true} = 1.0049 \cdot T_{indicated} - 0.148$
TubeTemp[8]	T-type thermocouple	Middle of middle tube, row-2, in the air flow direction	$T_{true} = 1.0044 \cdot T_{indicated} - 0.1406$
TubeTemp[9]	T-type thermocouple	Right of middle tube, row-2, in the air flow direction	$T_{true} = 1.0053 \cdot T_{indicated} - 0.1339$
TubeTemp[10]	T-type thermocouple	Right of middle tube, row-1, in the air flow direction	$T_{true} = 0.9986 \cdot T_{indicated} - 0.0285$
TubeTemp[11]	T-type thermocouple	Middle of middle tube, row-1, in the air flow direction	$T_{true} = 1.006 \cdot T_{indicated} - 0.1194$
TubeTemp[12]	T-type thermocouple	Left of middle tube, row-1, in the air flow direction	$T_{true} = 1.0065 \cdot T_{indicated} - 0.0957$
TubeTemp[13]	T-type thermocouple	Left of top tube, row-2, in the air flow direction	$T_{true} = 1.0046 \cdot T_{indicated} - 0.1606$
TubeTemp[14]	T-type thermocouple	Middle of top tube, row-2, in the air flow direction	$T_{true} = 1.0042 \cdot T_{indicated} - 0.1568$
TubeTemp[15]	T-type thermocouple	Right of top tube, row-2, in the air flow direction	$T_{true} = 1.004 \cdot T_{indicated} - 0.1453$
TubeTemp[16]	T-type thermocouple	Right of top tube, row-1, in the air flow direction	$T_{true} = 0.9986 \cdot T_{indicated} - 0.0285$
TubeTemp[17]	T-type thermocouple	Middle of top tube, row-1, in the air flow direction	$T_{true} = 1.0039 \cdot T_{indicated} - 0.1258$
TubeTemp[18]	T-type thermocouple	Left of top tube, row-1, in the air flow direction	$T_{true} = 1.0044 \cdot T_{indicated} - 0.1131$



Table B.3 Schedule of secondary coolant system temperature and pressure sensors.

<b>Temperature sensors</b>			
<b>Sensor label on test rig</b>	<b>Sensor type</b>	<b>Position of sensor in the secondary coolant system</b>	<b>Polynomial expression for true temperature of the sensor</b>
RTD[1]	RTD	Coolant temperature at intermediate heat exchanger inlet	$T_{true} = 0.9986 \cdot T_{indicated} - 0.0285$
RTD[2]	RTD	Coolant temperature at intermediate heat exchanger outlet	$T_{true} = 0.999 \cdot T_{indicated} - 0.0199$
RTD[3]	RTD	Condenser water inlet temperature	$T_{true} = 1.001 \cdot T_{indicated} + 0.0462$
RTD[4]	RTD	Condenser water outlet temperature	$T_{true} = 0.9972 \cdot T_{indicated} + 0.0122$
RTD[5]	RTD	Sub-cooler water inlet temperature	$T_{true} = 0.9971 \cdot T_{indicated} + 0.0654$
RTD[6]	RTD	Sub-cooler water outlet temperature	$T_{true} = 0.9965 \cdot T_{indicated} + 0.0827$
T[7]	K-type thermocouple	Sub-cooler refrigerant outlet temperature	$T_{true} = 1.0162 \cdot T_{indicated} - 0.2971$
RTD[8]	RTD	Expansion valve refrigerant inlet temperature	$T_{true} = 0.9954 \cdot T_{indicated} + 0.0662$
RTD[9]	RTD	Refrigerant temperature at intermediate heat exchanger inlet	$T_{true} = 0.9983 \cdot T_{indicated} + 0.01$
RTD[10]	RTD	Refrigerant temperature at intermediate heat exchanger outlet	$T_{true} = 0.9981 \cdot T_{indicated} + 0.0188$
RTD[11]	RTD	Refrigerant temperature at compressor inlet	$T_{true} = 0.9992 \cdot T_{indicated} - 0.0257$
RTD[12]	RTD	Refrigerant temperature at compressor outlet	$T_{true} = 0.9987 \cdot T_{indicated} + 0.0145$
RTD[13]	RTD	Refrigerant temperature at condenser inlet	$T_{true} = 0.9975 \cdot T_{indicated} + 0.0512$
RTD[14]	RTD	Refrigerant temperature at condenser outlet	$T_{true} = 0.9917 \cdot T_{indicated} - 0.0126$
RTD[15]	RTD	Refrigerant temperature at sub-cooler inlet	$T_{true} = 0.9917 \cdot T_{indicated} - 0.0126$
FinTemp[19]	T-type thermocouple	Coolant temperature at test coil inlet	$T_{true} = 1.0077 \cdot T_{indicated} - 0.0192$
FinTemp[20]	T-type thermocouple	Coolant temperature at test coil outlet	$T_{true} = 1.008 \cdot T_{indicated} - 0.0146$
<b>Pressure sensors</b>			
<b>Sensor label on test rig</b>	<b>Sensor type</b>	<b>Position of sensor in the secondary coolant system</b>	<b>Polynomial expression for true pressure of the sensor</b>
P[16]	Pressure Transducer	Refrigerant pressure at compressor outlet	$P_{true} = 0.9863 \cdot P_{indicated} + 0.0574$
P[17]	Pressure Transducer	Refrigerant pressure at condenser outlet	$P_{true} = 1.0093 \cdot P_{indicated} - 0.0374$
P[18]	Pressure Transducer	Refrigerant pressure at expansion valve outlet	$P_{true} = 1.0118 \cdot P_{indicated} - 0.0077$
P[19]	Pressure Transducer	Refrigerant pressure at intermediate heat exchanger outlet	$P_{true} = 1.0196 \cdot P_{indicated} - 0.0584$
P[20]	Pressure Transducer	Refrigerant pressure at sub-cooler outlet	$P_{true} = 0.9948 \cdot P_{indicated} - 0.0148$

Table B.4 Schedule of secondary coolant system flowmeters and wattmeters.

<b>WATER-LOOP</b>			
<b>Instrument</b>	<b>Model</b>	<b>Specification</b>	<b>Polynomial expression for true value of the instrument</b>
Flowmeter	Fischer and Porter Precision Bore Flowrator Tube No. FP I-35-G-10/83 Model No. 10A3567XA	Rotameter	$\dot{m}_{true} = 0.2613 \cdot \dot{m}_{indicated} + 0.0869$
<b>PRIMARY-LOOP</b>			<b>Polynomial expression for true value of the instrument</b>
Flowmeter	Remote flow transmitter Model No. RFT9712 and Flow sensor Model No. DS025S119SS	Microprocessor-based mass flow transmitter used in conjunction with a Micro Motion flow sensor	$\dot{m}_{true} = 0.976 \cdot \dot{m}_{indicated} - 0.0184$
<b>SECONDARY-LOOP</b>			<b>Polynomial expression for true value of the instrument</b>
Flowmeter	Flow transducer RS stock No. 257-133	Flow range: 1.5-30 litres/min Pulse per litre : 1200 pulses/litre	Mono-propylene glycol/water mixture
			$\dot{m}_{true} = 0.8993 \cdot \dot{m}_{indicated} + 0.1597$
			Mono-ethylene glycol/water mixture
			$\dot{m}_{true} = 1.0442 \cdot \dot{m}_{indicated} + 0.2062$
<b>PRIMARY- &amp; SECONDARY-LOOP</b>			
Wattmeter	LEM HEME-Analyst 2000P	Clip-on measuring instrument	Factory calibrated
Wattmeter	Fluke 434 3-Phase Power Quality Analyzer	Records all values in a three phase system	Factory calibrated

## Appendix C

Table C.1 Intermediate heat exchanger measurements for mono-propylene glycol/water mixture (52%/48% by weight).

Description		Test number				
		1	2	3	9	10
Intermediate heat exchanger refrigerant inlet temperature	[°C]	-23.5	-21.7	-20.1	-22.4	-21.0
Maximum variation in intermediate heat exchanger refrigerant inlet temperature	[°C]	±1.3	±0.8	±1.1	±0.8	±0.9
Intermediate heat exchanger refrigerant outlet temperature	[°C]	-24.5	-22.7	-20.6	-23.3	-21.9
Maximum variation in intermediate heat exchanger refrigerant outlet temperature	[°C]	±0.8	±0.6	±1.2	±0.9	±1.0
Intermediate heat exchanger refrigerant inlet pressure	[bar] abs	2.19	2.51	2.48	2.24	2.36
Maximum variation in intermediate heat exchanger refrigerant inlet pressure	[kPa]	±30.0	±23.0	±10.0	±10.0	±10.0
Intermediate heat exchanger refrigerant outlet pressure	[bar] abs	2.04	2.33	2.34	2.11	2.27
Maximum variation in intermediate heat exchanger refrigerant outlet pressure	[kPa]	±20.0	±21.0	±8.0	±7.0	±11.0
Intermediate heat exchanger coolant inlet temperature	[°C]	-11.7	-9.9	-9.0	-12.2	-10.5
Maximum variation in intermediate heat exchanger coolant inlet temperature	[°C]	±0.7	±0.9	±1.1	±0.7	±0.7
Intermediate heat exchanger coolant outlet temperature	[°C]	-17.7	-16.6	-14.1	-16.8	-15.5
Maximum variation in intermediate heat exchanger coolant outlet temperature	[°C]	±1.2	±0.5	±1.2	±0.6	±0.3
Intermediate heat exchanger refrigerant mass flowrate	[kg/min]	1.17	1.31	1.34	1.77	1.79
Maximum variation in intermediate heat exchanger refrigerant mass flowrate	[kg/min]	±0.8	±0.3	±0.4	±0.03	±0.08
Intermediate heat exchanger coolant mass flowrate	[kg/min]	10.89	11.7	11.94	12.62	12.98
Maximum variation in intermediate heat exchanger coolant mass flowrate	[kg/min]	±0.3	±0.33	±0.31	±0.18	±0.17
Refrigerant-side rate of heat transfer	[W]	3156	3492	3412	4706	4737
Coolant-side rate of heat transfer	[W]	3763	4520	3513	3342	3741

Table C.2 Thermostatic expansion valve measurements for mono-propylene glycol/water mixture (52%/48% by weight).

Description		Test number				
		1	2	3	9	10
Thermostatic Expansion Valve refrigerant inlet temperature	[ <sup>0</sup> C]	27.5	29.6	35.7	29.7	30.7
Maximum variation in Thermostatic Expansion Valve refrigerant inlet temperature	[ <sup>0</sup> C]	±0.2	±0.4	±0.5	±0.2	±0.3
Thermostatic Expansion Valve refrigerant outlet temperature	[ <sup>0</sup> C]	-23.5	-21.7	-20.1	-22.4	-21.0
Maximum variation in Thermostatic Expansion Valve refrigerant outlet temperature	[ <sup>0</sup> C]	±0.9	±0.5	±0.8	±0.7	±0.9
Thermostatic Expansion Valve refrigerant inlet pressure	[bar] abs	12.48	13.39	15.23	13.28	13.58
Maximum variation in Thermostatic Expansion Valve refrigerant inlet pressure	[kPa]	±90	±90	±120	±100	±130
Thermostatic Expansion Valve refrigerant outlet pressure	[bar] abs	2.19	2.51	2.48	2.24	2.36
Maximum variation in Thermostatic Expansion Valve refrigerant outlet pressure	[kPa]	±30.0	±23.0	±10.0	±10.0	±10.0
Thermostatic Expansion Valve refrigerant mass flowrate	[kg/min]	1.17	1.31	1.34	1.77	1.79
Maximum variation in thermostatic Expansion Valve refrigerant mass flowrate	[kg/min]	±0.8	±0.3	±0.4	±0.03	±0.08

Table C.3 Condenser measurements for mono-propylene glycol/water mixture (52%/48% by weight).

Description		Test number				
		1	2	3	9	10
Condenser refrigerant inlet temperature	[°C]	120.1	118.2	133.1	116.3	114.8
Maximum variation in condenser refrigerant inlet temperature	[°C]	±1.7	±6.1	±8.5	±7.3	±4.3
Condenser refrigerant outlet temperature	[°C]	30.8	33.2	39.8	33.5	34.1
Maximum variation in condenser refrigerant outlet temperature	[°C]	±0.4	±0.4	±0.5	±0.4	±1.0
Condenser refrigerant inlet pressure	[bar] abs	n/a	n/a	n/a	n/a	n/a
Maximum variation in condenser refrigerant inlet pressure	[kPa]	n/a	n/a	n/a	n/a	n/a
Condenser refrigerant outlet pressure	[bar] abs	12.6	13.49	14.63	13.43	13.69
Maximum variation in condenser refrigerant outlet pressure	[kPa]	±10	±30	±20	±10	±50
Condenser water inlet temperature	[°C]	27.9	29.9	36.4	30.5	30.8
Maximum variation in condenser water inlet temperature	[°C]	±0.3	±0.5	±0.6	±0.2	±0.8
Condenser water outlet temperature	[°C]	31.3	33.6	40.3	33.7	34.1
Maximum variation in condenser water outlet temperature	[°C]	±0.4	±0.4	±0.5	±0.2	±0.8
Condenser refrigerant mass flowrate	[kg/min]	1.17	1.31	1.34	1.77	1.79
Maximum variation in condenser refrigerant mass flowrate	[kg/min]	±0.8	±0.3	±0.4	±0.03	±0.08
Condenser water mass flowrate	[kg/min]	22.3	22.56	22.56	24.65	25.27
Maximum variation in condenser water mass flowrate	[kg/min]	±0.0	±0.0	±0.0	±0.0	±0.0
Refrigerant-side rate of heat transfer	[W]	4877	5343	5527	7164	7178
Water-side rate of heat transfer	[W]	5252	5783	6098	5443	5778

## Appendix C

Table C.4 Subcooler measurements for mono-propylene glycol/water mixture (52%/48% by weight).

Description		Test number				
		1	2	3	9	10
Subcooler refrigerant inlet temperature	[ <sup>0</sup> C]	30.63	32.92	38.87	32.67	33.34
Maximum variation in subcooler refrigerant inlet temperature	[ <sup>0</sup> C]	±0.2	±0.3	±0.4	±0.3	±0.8
Subcooler refrigerant outlet temperature	[ <sup>0</sup> C]	28.0	30.08	36.76	30.55	30.8
Maximum variation in subcooler refrigerant outlet temperature	[ <sup>0</sup> C]	±0.2	±0.5	±0.5	±0.2	±0.8
Subcooler refrigerant inlet pressure	[bar] abs	12.6	13.49	15.63	13.43	13.69
Maximum variation in subcooler refrigerant inlet pressure	[kPa]	±10	±30	±20	±10	±50
Subcooler refrigerant outlet pressure	[bar] abs	12.48	13.39	15.23	13.28	13.58
Maximum variation in subcooler refrigerant outlet pressure	[kPa]	±90	±90	±120	±100	±130
Subcooler water inlet temperature	[ <sup>0</sup> C]	27.89	29.76	36.46	30.52	30.75
Maximum variation in subcooler water inlet temperature	[ <sup>0</sup> C]	±0.3	±0.4	±0.4	±0.2	±0.7
Subcooler water outlet temperature	[ <sup>0</sup> C]	27.95	30.04	36.57	30.6	30.86
Maximum variation in subcooler water outlet temperature	[ <sup>0</sup> C]	±0.3	±0.4	±0.4	±0.3	±0.7
Subcooler refrigerant mass flowrate	[kg/min]	1.17	1.31	1.34	1.77	1.79
Maximum variation in subcooler refrigerant mass flowrate	[kg/min]	±0.8	±0.3	±0.4	±0.03	±0.08
Subcooler water mass flowrate	[kg/min]	22.3	22.56	22.56	24.65	25.27
Maximum variation in subcooler water mass flowrate	[kg/min]	±0.0	±0.0	±0.0	±0.0	±0.0
Refrigerant-side rate of heat transfer	[W]	66	80	63	81	98
Water-side rate of heat transfer	[W]	93	438	172	136	193

Table C.5 Test coil and pre-cooler measurements for mono-propylene glycol/water mixture (52%/48% by weight).

TEST COIL MEASUREMENTS						
Description		Test number				
		1	2	3	9	10
Test coil air inlet dry bulb temperature	[°C]	-0.8	-0.2	0.1	-2.9	-1.0
Maximum variation in test coil air inlet dry bulb temperature	[°C]	±0.8	±0.8	±0.8	±0.8	±0.8
Test coil air outlet dry bulb temperature	[°C]	-1.9	-1.1	-0.6	-4.3	-2.2
Maximum variation in test coil air outlet dry bulb temperature	[°C]	±0.8	±0.8	±0.8	±0.8	±0.8
Test coil air inlet dew point temperature	[°C]	-0.9	-0.3	-0.1	-3.7	-1.3
Maximum variation in test coil air inlet dew point temperature	[°C]	±0.6	±0.6	±0.6	±0.6	±0.6
Test coil air outlet dew point temperature	[°C]	-1.9	-1.1	-0.6	-4.7	-2.2
Maximum variation in test coil air outlet dew point temperature	[°C]	±0.6	±0.6	±0.6	±0.6	±0.6
Test coil air inlet pressure	[kPa] abs	101.8	101.4	101.4	101.1	101.6
Maximum variation in test coil air inlet pressure	[kPa]	±0.0	±0.0	±0.0	±0.0	±0.0
Test coil air pressure drop	[kPa] abs	0.204	0.176	0.188	0.027	0.057
Maximum variation in test coil air pressure drop	[kPa]	±0.0	±0.0	±0.0	±0.0	±0.0
Test coil coolant inlet temperature	[°C]	-16.9	-14.8	-13.8	-16.6	-15.1
Maximum variation in test coil coolant inlet temperature	[°C]	±0.6	±0.5	±1.1	±1.1	±1.1
Test coil coolant outlet temperature	[°C]	-15.8	-14.1	-13.1	-16.0	-14.5
Maximum variation in test coil coolant outlet temperature	[°C]	±0.5	±0.7	±0.7	±0.6	±0.5
Test coil air mass flowrate	[kg/min]	12.58	16.73	15.62	13.77	14.10
Maximum variation in test coil air mass flowrate	[kg/min]	±0.3	±0.3	±0.3	±0.3	±0.3
Test coil coolant mass flowrate	[kg/min]	10.89	11.7	11.94	12.62	12.98
Maximum variation in test coil coolant mass flowrate	[kg/min]	±0.3	±0.33	±0.31	±0.18	±0.17
Air-side rate of heat transfer	[W]	378	417	280	456	430
Coolant-side rate of heat transfer	[W]	688	471	481	435	448

PRE-COOLER MEASUREMENTS						
Description		Test number				
		1	2	3	9	10
Pre-cooler coolant inlet temperature	[°C]	-15.8	-14.1	-13.1	-16.0	-14.5
Maximum variation in pre-cooler coolant inlet temperature	[°C]	±0.5	±0.7	±0.7	±0.6	±0.5
Pre-cooler coolant outlet temperature	[°C]	-11.7	-9.9	-9.0	-12.2	-10.5
Maximum variation in pre-cooler coolant outlet temperature	[°C]	±0.7	±0.9	±1.1	±0.7	±0.7
Pre-cooler coolant mass flowrate	[kg/min]	10.89	11.7	11.94	12.62	12.98
Maximum variation in pre-cooler coolant mass flowrate	[kg/min]	±0.3	±0.33	±0.31	±0.18	±0.17
Air-side rate of heat transfer	[W]	n/a	n/a	n/a	n/a	n/a
Coolant-side rate of heat transfer	[W]	2564	2825	2817	2754	2984

Table C.6 Compressor and coolant pump measurements for mono-propylene glycol/water mixture (52%/48% by weight).

Description		Test number				
		1	2	3	9	10
Compressor refrigerant inlet temperature	[°C]	-18.0	-15.7	-15.3	-17.5	-16.5
Maximum variation in compressor refrigerant inlet temperature	[°C]	±0.5	±0.3	±0.7	±0.5	±0.7
Compressor refrigerant outlet temperature	[°C]	124.3	121.9	136.2	119.3	117.5
Maximum variation in compressor refrigerant outlet temperature	[°C]	±2.0	±6.5	±9.0	±7.7	±4.5
Compressor refrigerant inlet pressure	[bar] abs	2.04	2.33	2.34	2.11	2.27
Maximum variation in compressor refrigerant inlet pressure	[kPa]	±20.0	±21.0	±8.0	±7.0	±11.0
Compressor refrigerant outlet pressure	[bar] abs	n/a	n/a	n/a	n/a	n/a
Maximum variation in compressor refrigerant outlet pressure	[kPa]	n/a	n/a	n/a	n/a	n/a
Compressor refrigerant mass flowrate	[kg/min]	1.17	1.31	1.34	1.77	1.79
Maximum variation in compressor refrigerant mass flowrate	[kg/min]	±0.8	±0.3	±0.4	±0.03	±0.08
Coolant pump coolant mass flowrate	[kg/min]	10.89	11.7	11.94	12.62	12.98
Maximum variation in coolant pump coolant mass flowrate	[kg/min]	±0.3	±0.33	±0.31	±0.18	±0.17
Compressor power consumption	[W]	2075	2250	2450	2200	2250
Maximum variation in compressor power consumption	[W]	±75	±50	±50	±0.0	±50
Coolant pump power consumption	[W]	328	334	329	327	327
Maximum variation in coolant pump power consumption	[W]	±3.5	±7	±2	±0.0	±0.0



# Appendix D

Table D.1 Intermediate heat exchanger measurements for mono-ethylene glycol/water mixture (42%/58% by weight).

Description		Test number				
		4	5	6	7	8
Intermediate heat exchanger refrigerant inlet temperature	[°C]	-22.2	-21.1	-13.9	-19.7	-19.2
Maximum variation in intermediate heat exchanger refrigerant inlet temperature	[°C]	±0.9	±0.5	±0.9	±0.7	±1.0
Intermediate heat exchanger refrigerant outlet temperature	[°C]	-22.1	-22.4	-14.8	-20.6	-19.5
Maximum variation in intermediate heat exchanger refrigerant outlet temperature	[°C]	±1.8	±0.6	±0.5	±0.8	±1.6
Intermediate heat exchanger refrigerant inlet pressure	[bar] abs	2.29	2.4	2.95	2.38	2.41
Maximum variation in intermediate heat exchanger refrigerant inlet pressure	[kPa]	±10	±0.0	±0.0	±10	±10
Intermediate heat exchanger refrigerant outlet pressure	[bar] abs	2.15	2.23	n/a	n/a	n/a
Maximum variation in intermediate heat exchanger refrigerant outlet pressure	[kPa]	±10	±0.0	n/a	n/a	n/a
Intermediate heat exchanger coolant inlet temperature	[°C]	-15.7	-15.2	-5.3	-12.2	-12.4
Maximum variation in intermediate heat exchanger coolant inlet temperature	[°C]	±0.7	±0.9	±0.4	±0.8	±1.0
Intermediate heat exchanger coolant outlet temperature	[°C]	-19.6	-19.0	-10.5	-16.6	-16.5
Maximum variation in intermediate heat exchanger coolant outlet temperature	[°C]	±0.6	±0.7	±0.3	±0.7	±0.9
Intermediate heat exchanger refrigerant mass flowrate	[kg/min]	1.258	1.326	1.672	1.471	1.905
Maximum variation in intermediate heat exchanger refrigerant mass flowrate	[kg/min]	±0.23	±0.02	±0.04	±0.05	±0.04
Intermediate heat exchanger coolant mass flowrate	[kg/min]	16.05	16.07	19.51	19.16	19.11
Maximum variation in intermediate heat exchanger coolant mass flowrate	[kg/min]	±0.1	±0.1	±0.1	±0.2	±0.2
Refrigerant-side rate of heat transfer	[W]	3403	3507	4614	4101	5036
Coolant-side rate of heat transfer	[W]	3456	3374	5678	4676	4345

## Appendix D

Table D.2 Thermostatic expansion valve measurements for mono-ethylene glycol/water mixture (42%/58% by weight).

Description		Test number				
		4	5	6	7	8
Thermostatic Expansion Valve refrigerant inlet temperature	[°C]	27.6	30.8	27.8	24.5	31.5
Maximum variation in Thermostatic Expansion Valve refrigerant inlet temperature	[°C]	±0.2	±0.1	±0.3	±0.3	±0.3
Thermostatic Expansion Valve refrigerant outlet temperature	[°C]	-22.2	-21.1	-13.9	-19.7	-19.2
Maximum variation in Thermostatic Expansion Valve refrigerant outlet temperature	[°C]	±0.9	±0.5	±0.3	±0.7	±1.0
Thermostatic Expansion Valve refrigerant inlet pressure	[bar] abs	11.76	13.49	13.09	11.66	14.16
Maximum variation in Thermostatic Expansion Valve refrigerant inlet pressure	[kPa]	±50	±10	±20	±20	±10
Thermostatic Expansion Valve refrigerant outlet pressure	[bar] abs	2.15	2.21	2.95	2.35	2.38
Maximum variation in Thermostatic Expansion Valve refrigerant outlet pressure	[kPa]	±10	±0.0	±0.0	±10	±10
Thermostatic Expansion Valve refrigerant mass flowrate	[kg/min]	1.258	1.326	1.672	1.471	1.905
Maximum variation in thermostatic Expansion Valve refrigerant mass flowrate	[kg/min]	±0.23	±0.02	±0.04	±0.05	±0.04

Table D.3 Condenser measurements for mono-ethylene glycol/water mixture (42%/58% by weight).

Description		Test number				
		4	5	6	7	8
Condenser refrigerant inlet temperature	[°C]	115.4	119.0	96.5	99.2	117.9
Maximum variation in condenser refrigerant inlet temperature	[°C]	±2.0	±3.7	±0.8	±2.4	±4.7
Condenser refrigerant outlet temperature	[°C]	30.9	34.3	32.7	28.5	35.7
Maximum variation in condenser refrigerant outlet temperature	[°C]	±0.4	±0.1	±0.3	±0.5	±0.3
Condenser refrigerant inlet pressure	[bar] abs	n/a	n/a	n/a	n/a	n/a
Maximum variation in condenser refrigerant inlet pressure	[kPa]	n/a	n/a	n/a	n/a	n/a
Condenser refrigerant outlet pressure	[bar] abs	12.68	13.76	13.32	11.94	14.21
Maximum variation in condenser refrigerant outlet pressure	[kPa]	±20	±0.0	±9.2	±10	±10
Condenser water inlet temperature	[°C]	28.0	31.1	28.2	25.0	32.3
Maximum variation in condenser water inlet temperature	[°C]	±0.3	±0.2	±0.3	±0.4	±0.3
Condenser water outlet temperature	[°C]	31.5	34.8	32.5	28.6	36.0
Maximum variation in condenser water outlet temperature	[°C]	±0.2	±0.1	±0.3	±0.3	±0.2
Condenser refrigerant mass flowrate	[kg/min]	1.258	1.326	1.672	1.471	1.905
Maximum variation in condenser refrigerant mass flowrate	[kg/min]	±0.23	±0.02	±0.04	±0.05	±0.04
Condenser water mass flowrate	[kg/min]	23.34	23.60	24.65	24.65	24.65
Maximum variation in condenser water mass flowrate	[kg/min]	±0.0	±0.0	±0.0	±0.0	±0.0
Refrigerant-side rate of heat transfer	[W]	5160	5387	6347	5803	7640
Water-side rate of heat transfer	[W]	5659	6050	7343	6146	6320

## Appendix D

Table D.4 Subcooler measurements for mono-ethylene glycol/water mixture (42%/58% by weight).

Description		Test number				
		4	5	6	7	8
Subcooler refrigerant inlet temperature	[°C]	30.95	34.13	32.89	28.48	35.15
Maximum variation in subcooler refrigerant inlet temperature	[°C]	±0.3	±0.1	±0.3	±0.5	±0.3
Subcooler refrigerant outlet temperature	[°C]	28.12	31.36	28.17	24.96	32.44
Maximum variation in subcooler refrigerant outlet temperature	[°C]	±0.2	±0.1	±0.3	±0.3	±0.2
Subcooler refrigerant inlet pressure	[bar] abs	12.68	13.76	13.32	11.94	14.24
Maximum variation in subcooler refrigerant inlet pressure	[kPa]	±20	±0.0	9.2	±10	±10
Subcooler refrigerant outlet pressure	[bar] abs	11.76	13.49	13.09	11.66	14.16
Maximum variation in subcooler refrigerant outlet pressure	[kPa]	±50	±10	±20	±20	±10
Subcooler water inlet temperature	[°C]	27.85	31.00	28.10	24.96	32.33
Maximum variation in subcooler water inlet temperature	[°C]	±0.2	±0.1	±0.2	±0.3	±0.3
Subcooler water outlet temperature	[°C]	28.10	31.28	28.28	25.08	32.44
Maximum variation in subcooler water outlet temperature	[°C]	±0.2	±0.1	±0.2	±0.3	±0.3
Subcooler refrigerant mass flowrate	[kg/min]	1.258	1.326	1.672	1.471	1.905
Maximum variation in subcooler refrigerant mass flowrate	[kg/min]	±0.23	±0.02	±0.04	±0.05	±0.04
Subcooler water mass flowrate	[kg/min]	23.34	23.60	24.65	24.65	24.65
Maximum variation in subcooler water mass flowrate	[kg/min]	±0.0	±0.0	±0.0	±0.0	±0.0
Refrigerant-side rate of heat transfer	[W]	76	79	169	109	112
Water-side rate of heat transfer	[W]	404	458	307	205	188

Table D.5 Test coil and pre-cooler measurements for mono-ethylene glycol/water mixture (42%/58% by weight).

TEST COIL MEASUREMENTS						
Description		Test number				
		4	5	6	7	8
Test coil air inlet dry bulb temperature	[°C]	-4.5	-2.5	4.9	-0.4	-1.7
Maximum variation in test coil air inlet dry bulb temperature	[°C]	±0.8	±0.8	±0.8	±0.8	±0.8
Test coil air outlet dry bulb temperature	[°C]	-5.8	-4.0	3.7	-1.6	-2.8
Maximum variation in test coil air outlet dry bulb temperature	[°C]	±0.8	±0.8	±0.8	±0.8	±0.8
Test coil air inlet dew point temperature	[°C]	-4.7	-2.6	4.6	-1.5	-2.1
Maximum variation in test coil air inlet dew point temperature	[°C]	±0.6	±0.6	±0.6	±0.6	±0.6
Test coil air outlet dew point temperature	[°C]	-5.8	-4.0	3.7	-2.4	-3.2
Maximum variation in test coil air outlet dew point temperature	[°C]	±0.6	±0.6	±0.6	±0.6	±0.6
Test coil air inlet pressure	[kPa] abs	101.4	101.1	100.5	100.9	100.5
Maximum variation in test coil air inlet pressure	[kPa]	±0.0	±0.0	±0.0	±0.0	±0.0
Test coil air pressure drop	[kPa] abs	0.088	0.299	0.141	0.174	0.180
Maximum variation in test coil air pressure drop	[kPa]	±0.0	±0.0	±0.0	±0.0	±0.0
Test coil coolant inlet temperature	[°C]	-19.0	-17.9	-10.4	-16.1	-16.2
Maximum variation in test coil coolant inlet temperature	[°C]	±0.6	±0.7	±1.1	±1.1	±1.1
Test coil coolant outlet temperature	[°C]	-18.6	-17.1	-9.6	-15.6	-15.7
Maximum variation in test coil coolant outlet temperature	[°C]	±0.6	±0.7	±0.3	±0.7	±0.8
Test coil air mass flowrate	[kg/min]	15.45	13.67	17.08	16.61	16.55
Maximum variation in test coil air mass flowrate	[kg/min]	±0.3	±0.3	±0.3	±0.3	±0.3
Test coil coolant mass flowrate	[kg/min]	16.05	16.07	19.51	19.16	19.11
Maximum variation in test coil coolant mass flowrate	[kg/min]	±0.1	±0.1	±0.1	±0.2	±0.2
Air-side rate of heat transfer	[W]	485	536	579	503	500
Coolant-side rate of heat transfer	[W]	323	708	868	529	527

PRE-COOLER MEASUREMENTS						
Description		Test number				
		4	5	6	7	8
Pre-cooler coolant inlet temperature	[°C]	-18.6	-17.1	-9.6	-15.6	-15.7
Maximum variation in pre-cooler coolant inlet temperature	[°C]	±0.6	±0.7	±0.3	±0.7	±0.8
Pre-cooler coolant outlet temperature	[°C]	-15.7	-14.2	-5.3	-12.2	-12.4
Maximum variation in pre-cooler coolant outlet temperature	[°C]	±0.7	±0.9	±0.4	0.8	±1.0
Pre-cooler coolant mass flowrate	[kg/min]	16.05	16.07	19.51	19.16	19.11
Maximum variation in pre-cooler coolant mass flowrate	[kg/min]	±0.1	±0.1	±0.1	±0.2	±0.2
Air-side rate of heat transfer	[W]	n/a	n/a	n/a	n/a	n/a
Coolant-side rate of heat transfer	[W]	2844	2849	5138	3984	3856

Table D.6 Compressor and coolant pump measurements for mono-ethylene glycol/water mixture (42%/58% by weight).

Description		Test number				
		4	5	6	7	8
Compressor refrigerant inlet temperature	[°C]	-18.2	-21.0	-10.4	-15.8	-15.6
Maximum variation in compressor refrigerant inlet temperature	[°C]	±1.0	±2.8	±0.5	±0.7	±0.9
Compressor refrigerant outlet temperature	[°C]	119.2	122.5	98.6	102.1	120.5
Maximum variation in compressor refrigerant outlet temperature	[°C]	±2.2	±3.8	±0.9	±2.6	±5.0
Compressor refrigerant inlet pressure	[bar] abs	2.15	2.23	n/a	n/a	n/a
Maximum variation in compressor refrigerant inlet pressure	[kPa]	±10	±0.0	n/a	n/a	n/a
Compressor refrigerant outlet pressure	[bar] abs	n/a	n/a	n/a	n/a	n/a
Maximum variation in compressor refrigerant outlet pressure	[kPa]	n/a	n/a	n/a	n/a	n/a
Compressor refrigerant mass flowrate	[kg/min]	1.258	1.326	1.672	1.471	1.905
Maximum variation in compressor refrigerant mass flowrate	[kg/min]	±0.23	±0.02	±0.04	±0.05	±0.04
Coolant pump coolant mass flowrate	[kg/min]	16.05	16.07	19.51	19.16	19.11
Maximum variation in coolant pump coolant mass flowrate	[kg/min]	±0.1	±0.1	±0.1	±0.2	±0.2
Compressor power consumption	[W]	2233	2320	2225	2000	2260
Maximum variation in compressor power consumption	[W]	±133	±120	±25	±100	±140
Coolant pump power consumption	[W]	351	310	327	327	327
Maximum variation in coolant pump power consumption	[W]	±24	±11	±0.0	±0.0	±0.0

# Appendix E

Table E.1 List of cabinets fed by Circuit A.

BRANCH NUMBER	CABINET SECTION NUMBER	BRANCH DESCRIPTION	CABINETS & EVAPORATORS NUMBER	CABINETS & EVAPORATORS MANUFACTURER	CABINETS OR EVAPORATOR MODEL NUMBER	EVAPORATING TEMPERATURE (°C)	COOLING DUTY (kW)
BR29	1	Produce Multideck Cabinet	1x3.87m	HUSSMAN	D5-LE	-8.0	5.01
BR30	1	Produce Multideck Cabinet	1x2.45m	HUSSMAN	D5-LE	-8.0	3.34
BR30	1	Produce Multideck Cabinet	1x2.45m	HUSSMAN	D5-LE	-8.0	3.34
BR30	2	Produce Multideck Cabinet	1x2.45m	HUSSMAN	D5-LE	-8.0	3.34
BR31	1	Produce Multideck Cabinet	1x2.45m	HUSSMAN	C2.5 NXLE	-8.0	4.35
BR31	2	Produce Multideck Cabinet	1x2.45m	HUSSMAN	C2NX-LE	-8.0	4.35
BR32	1	Produce Multideck Cabinet	1x2.45m	HUSSMAN	D5-LE	-8.0	3.34
BR32	2	Produce Multideck Cabinet	1x2.45m	HUSSMAN	D5-LE	-8.0	3.34
BR32	3	Produce Multideck Cabinet	1x45" IS MITRE	HUSSMAN	D5-LE	-8.0	1.98
BR32	4	Produce Multideck Cabinet	1x2.45m	HUSSMAN	D5-LE	-8.0	3.34
BR33	1	Lunch to Go Cabinet	1x3.75m	ARNEG	BERLINO 2 SL 100/216 2C	-8.0	5.90
BR33	2	Drinks to Go Cabinet	1x3.75m	ARNEG	BERLINO 2 SL 100/216 2C	-8.0	5.90
BR35	1	Wine Cabinet	1x3.75m	ARNEG	BERLINO 2 SL 100/216 2C	-8.0	5.90
BR35	2	Wine Cabinet	1x3.75m	ARNEG	BERLINO 2 SL 100/216 2C	-8.0	5.90
BR36	1	Beer Cabinet	1x3.75m	ARNEG	BERLINO 2 SL 100/216 2C	-8.0	5.90

Table E.2 List of cabinets fed by Circuit B.

BRANCH NUMBER	CABINET SECTION NUMBER	BRANCH DESCRIPTION	CABINETS & EVAPORATORS NUMBER	CABINETS & EVAPORATORS MANUFACTURER	CABINETS OR EVAPORATOR MODEL NUMBER	EVAPORATING TEMPERATURE (°C)	COOLING DUTY (kW)
BR7	1	Dairy Cabinet	1x2.50m	ARNEG	BERLINO 2 SL 100/218 2C	-8.0	3.93
BR8	1	Delicatessen	1x2.45m	TYLER	NLM	-10.0	0.60
BR28	1	Home Meal Replacement Cabinet	1x3.87m	HUSSMAN	RGSSFP	-8.0	5.20
BR34	1	Salads to Go Cabinet	1x3.75m	ARNEG	BERLINO 2 SL 100/218 2C	-8.0	5.90
BR34	2	Salads to Go Cabinet	1x2.50m	ARNEG	BERLINO 2 SL 100/218 2C	-8.0	3.93
BR34	3	Salads to Go Cabinet	1x2.50m	ARNEG	BERLINO 2 SL 100/218 2C	-8.0	3.93
BR37	1	Wine Cabinet	1x2.50m	ARNEG	BERLINO 2 SL 100/218 2C	-8.0	3.93
BR37	2	Wine Cabinet	1x2.50m	ARNEG	BERLINO 2 SL 100/218 2C	-8.0	3.93
BR38	3	Pet Food Cabinet	1x2.50m	ARNEG	RIO M1	-10.0	4.80
BR39	1	Milk Cabinet	1x3.75m	ARNEG	BERLINO 2 FC 110/205	-10.0	8.60
BR40	1	Milk Cabinet	1x3.75m	ARNEG	BERLINO 2 FC 110/205	-10.0	8.60



Table E.3 List of cabinets fed by Circuit C.

BRANCH NUMBER	CABINET SECTION NUMBER	BRANCH DESCRIPTION	CABINETS & EVAPORATORS NUMBER	CABINETS & EVAPORATORS MANUFACTURER	CABINETS OR EVAPORATOR MODEL NUMBER	EVAPORATING TEMPERATURE (°C)	COOLING DUTY (kW)
BR2	1	Dairy cabinet	1x3.76m	ARNEG	BERLINO 2 SL 100/218 2C	-8.0	5.90
BR2	2	Dairy cabinet	1x3.76m	ARNEG	BERLINO 2 SL 100/218 2C	-8.0	5.90
BR3	1	Dairy Cabinet	1x3.76m	ARNEG	BERLINO 2 SL 100/218 2C	-8.0	5.90
BR3	2	Dairy Cabinet	1x3.76m	ARNEG	BERLINO 2 SL 100/218 2C	-8.0	5.90
BR4	1	Dairy Cabinet	1x1.875m	ARNEG	BERLINO 2 SL 100/216 2C	-8.0	2.95
BR5	1	Dairy Cabinet	1x2.50m	ARNEG	BERLINO 2 SL 100/218 2C	-8.0	3.93
BR5	2	Dairy Cabinet	1x3.75m	ARNEG	BERLINO 2 SL 100/216 2C	-8.0	5.90
BR6	1	Dairy Cabinet	1x3.75m	ARNEG	BERLINO 2 SL 100/216 2C	-8.0	5.90
BR6	2	Dairy Cabinet	1x3.75m	ARNEG	BERLINO 2 SL 100/216 2C	-8.0	5.90
BR9	1	Delicatessen	1x3.87m	TYLER	NLM	-10.0	0.65
BR10	1	Delicatessen	1x2.45m	TYLER	NLM	-10.0	0.60
BR11	1	Delicatessen	1x2.45m	TYLER	NLM	-10.0	0.60
BR14	1	Cheese Cabinet	1x1.90m	AFINOX	MURALE	-10.0	2.03
BR25	1	HANG SELL Cabinet	1x3.67m	HUSSMAN	D5NLE	-6.0	5.50
BR26	1	Pizza Service Cabinet	1x2.45m	HUSSMAN	RGSSFP	-8.0	3.50
BR27	1	Sushi Service Cabinet	1x1.80m	HUSSMAN	MES	-10.0	1.50

Table E.4 List of cabinets fed by Circuit D.

BRANCH NUMBER	CABINET SECTION NUMBER	BRANCH DESCRIPTION	CABINETS & EVAPORATORS NUMBER	CABINETS & EVAPORATORS MANUFACTURER	CABINETS OR EVAPORATOR MODEL NUMBER	EVAPORATING TEMPERATURE (°C)	COOLING DUTY (kW)
BR1	1	Dairy Cabinet	1x1.875m	ARNEG	BERLINO 2 SL 100/216 2C	-8.0	2.95
BR12	1	Delicatessen	1x2.45m	TYLER	NLM	-10.0	0.60
BR13	1	Cheese Cabinet	1x2.45m	TYLER	NNG	-7.0	1.31
BR15	1	Cheese Cabinet	1x2.50m	ARNEG	BERLINO 2 SL 100/216 2C	-8.0	3.93
BR1	1	Dairy Cabinet	1x1.875m	ARNEG	BERLINO 2 SL 100/216 2C	-8.0	2.95
BR12	1	Delicatessen	1x2.45m	TYLER	NLM	-10.0	0.60
BR13	1	Cheese Cabinet	1x2.45m	TYLER	NNG	-7.0	1.31
BR15	1	Cheese Cabinet	1x2.50m	ARNEG	BERLINO 2 SL 100/216 2C	-8.0	3.93

Table E.5 List of cabinets fed by Circuit E.

BRANCH NUMBER	CABINET SECTION NUMBER	BRANCH DESCRIPTION	CABINETS & EVAPORATORS NUMBER	CABINETS & EVAPORATORS MANUFACTURER	CABINETS OR EVAPORATOR MODEL NUMBER	EVAPORATING TEMPERATURE (°C)	COOLING DUTY (kW)
BR16A	1	Cake Cabinet	1x1.20m	COSSIGA	GT12	NA	INTIGR AL
BR16B	1	Cake Cabinet	1x1.20m	COSSIGA	GT12	NA	INTIGR AL
BR17	1	Meat Cabinet	1x3.67m	HUSSMAN	IMPACT D5-LE MEAT	-8.5	5.77
BR18	1	Meat Cabinet	1x3.67m	HUSSMAN	IMPACT D5-LE MEAT	-8.5	5.77
BR18	2	Meat Cabinet	1x3.67m	HUSSMAN	IMPACT D5-LE MEAT	-8.5	5.77
BR19	1	Meat Cabinet	1x2.45m	HUSSMAN	IMPACT D5-LE MEAT	-8.5	3.85
BR19	2	Meat Cabinet	1x45" IS MITRE	HUSSMAN	IMPACT D5-LE MEAT	-8.5	0.80
BR19	3	Meat Cabinet	1x2.45m	HUSSMAN	IMPACT D5-LE MEAT	-8.5	3.85
BR19	4	Meat Cabinet	1x45" OS MITRE	HUSSMAN	IMPACT D5-LE MEAT	-8.5	2.20
BR20	1	Meat Cabinet	1x3.57m	HUSSMAN	IMPACT D5-LE MEAT	-8.5	5.77
BR21	1	Meat Service Cabinet	1x3.57m	TYLER	NLM	-8.0	0.85
BR22	1	Meat Service Cabinet	1x3.87m	TYLER	NLM	-8.0	0.85
BR48		Shelf Fish Cabinet	1x1.20m	HUSSMAN	NEGCH	0.0	1.00

Table E.6 List of cool rooms fed by separate Refrigerant Circuit.

BRANCH NUMBER	CABINET SECTION NUMBER	BRANCH DESCRIPTION	CABINETS & EVAPORATORS NUMBER	CABINETS & EVAPORATORS MANUFACTURER	CABINETS OR EVAPORATOR MODEL NUMBER	EVAPORATING TEMPERATURE (°C)	COOLING DUTY (kW)
BR41		Bakery Cool Room	1x	PATTON	BM28	-4.0	2.06
BR42		Cool Room	1x	PATTON	BM28	-4.0	1.96
BR43		Dairy Cool Room	1x	PATTON	BM66	-4.0	5.71
BR44		Meat Cool Room	1x	PATTON	PM95K	-6.0	7.88
BR45		Produce Cool Room	1x	PATTON	PM160	0.0	11.97
BR46		Fish Cool Room	1x	PATTON	BM37K	-6.0	2.96
BR47		Delicatessen Raw Cool Room	1x	PATTON	BM37	-4.0	2.80

## *List of publications*

---

### **1. Journal papers**

- [1] H. M. Getu, and P. K. Bansal, “New frost property correlations for a flat-finned-tube heat exchanger,” *International Journal of Thermal Sciences*, vol. 50, pp. 544- 557, 2011.
- [2] H. M. Getu, and P. K. Bansal, “Thermodynamic analysis of an R744-R717 cascade refrigeration system,” *International Journal of Refrigeration*, vol. 31, no. 1, pp. 45-54, 2008.
- [3] H. M. Getu, and P. K. Bansal, “Modeling and performance analyses of evaporators in frozen-food supermarket display cabinets at low temperatures,” *International Journal of Refrigeration*, vol. 30, no. 7, pp. 1227-1243, 2007.
- [4] H. M. Getu, and P. K. Bansal, “Simulation model of a low-temperature supermarket refrigeration system,” *HVAC and R Research*, vol. 12, no. 4, pp. 1117-1139, 2006.

### **2. Conference papers**

- [1] H. M. Getu, and P. K. Bansal, “Limitations of existing frost property correlations,” in *The 22nd International Conference of Refrigeration*, Beijing, P.R. China, 2007.
- [2] H.M. Getu, and P.K. Bansal, “Modelling of supermarket display cabinet evaporators at low-temperatures: a review,” in *Refrigeration Science and Technology, Proceedings, IIR-IRHACE Conference, Innovative Equipment and Systems for Comfort and Food Preservation*, the University of Auckland, pp 213-220, 2006,
- [3] H.M. Getu, and P.K. Bansal, “Effect of store relative humidity on a low-temperature supermarket refrigeration system,” in *Refrigeration Science and Technology, Proceedings, IIR-IRHACE Conference, Innovative Equipment and Systems for Comfort and Food Preservation*, the University of Auckland; pp 443-450, 2006.

## *Vita*

---

Getu Haile-Michael was born in Addis Ababa, Ethiopia on July 28, 1972. He received his Bachelor of Science in Mechanical Engineering from Addis Ababa University, Faculty of Technology in 1997. He then continued his postgraduate studies and received Postgraduate Diploma in Geothermal Energy Technology – Specialization in Utilization and Production of Geothermal Resources; and Master of Engineering Degree (thesis) with first class honors – Specialization in Mechanical Engineering from The University of Auckland, New Zealand in 2002 and 2005, respectively. He immediately started his PhD study in 2005 at the Department of Mechanical Engineering, The University of Auckland, New Zealand. He now works for Snowy Mountains Engineering Corporation (SMEC) as an expert of hydro-mechanical works of dams, canals, tunnels and hydro power plants based in Melbourne Office, Australia.

His research interests are supermarket refrigeration systems, building services, geothermal energy technology, hydro power and cavitation–silt erosion of steel linings of dam bottom outlets and power intakes.